Titre: Title:	Contributions to Modeling and Simulation of HVAC Cables Using Field Test Results
Auteur: Author:	Maria Isabel Silva Lafaia Simoes
Date:	2016
Type:	Mémoire ou thèse / Dissertation or Thesis
Référence: Citation:	Silva Lafaia Simoes, M. I. (2016). Contributions to Modeling and Simulation of HVAC Cables Using Field Test Results [Thèse de doctorat, École Polytechnique de Montréal]. PolyPublie. https://publications.polymtl.ca/2350/

UNIVERSITÉ DE MONTRÉAL

CONTRIBUTIONS TO MODELING AND SIMULATION OF HVAC CABLES USING FIELD TEST RESULTS

MARIA ISABEL SILVA LAFAIA SIMÕES

DÉPARTEMENT DE GÉNIE ÉLECTRIQUE

ÉCOLE POLYTECHNIQUE DE MONTRÉAL

THÈSE PRÉSENTÉE EN VUE DE L'OBTENTION

DU DIPLÔME DE PHILOSOPHIAE DOCTOR

(GÉNIE ÉLETRIQUE)

OCTOBRE 2016

UNIVERSITÉ DE MONTRÉAL

ÉCOLE POLYTECHNIQUE DE MONTRÉAL

Cette thèse intitulée:

CONTRIBUTIONS TO MODELING AND SIMULATION OF HVAC CABLES USING FIELD TEST RESULTS

présentée par : SILVA LAFAIA SIMÕES Maria Isabel

en vue de l'obtention du diplôme de : Philosophiae Doctor

a été dûment acceptée par le jury d'examen constitué de :

M. KARIMI Houshang, Ph. D., président

M. MAHSEREDJIAN Jean, Ph. D., membre et directeur de recherche

Mme. CORREIA DE BARROS Maria Teresa, Ph. D., membre et codirecteur de recherche

M. KOCAR Ilhan, Ph. D., membre et codirecteur de recherche

M. REZAEI-ZARE Afshin, membre

M. RACHIDI Farhad, Ph. D., membre externe

DEDICATION

Aos meus pais, ao meu irmão, à minha madrinha.

To my parents, to my brother, to my godmother.

ACKNOWLEDGEMENTS

There are many people to whom I owe gratitude:

To my main supervisor Dr. Jean Mahseredjian for giving me the opportunity of this PhD project, for the friendship and the trust.

To Dr. Akihiro Ametani for his constant support, orientation and encouragement.

To my co-supervisor Dr. Teresa Correia de Barros who made the first contact that allowed me to start this PhD and who continued to support me even at distance.

To my co-supervisor Dr. Ilhan Koçar for the valuable discussions and advise.

To Réseaux de Transport d'Électricité, RTE-France for the financing and for providing the field test results that triggered this PhD project.

To National Grid, UK for providing valuable field tests.

To Polytechnique Montréal for the financial support.

To all the department colleagues that I have met during my PhD. To those who already left: Hani, Lyes, Jean-Nicolas, Mar Jan, Andy and Steve. To those who will continue: Ming, Aramis, Haoyan, Jesus, Miguel, Anton, Louis, Aboutaleb, Fidji. For those who were always there: Thomas and Baki. Also to my office colleagues Kevin and Maxime. I will keep all of you in my memory.

To Lise, for her support and friendship since my arrival to Montreal.

To Thomas for his support and patience, especially during the writing of the thesis.

Finally, a special thanks to my parents and to my brother for their constant support and encouragement and for always believing in me.

RÉSUMÉ

L'intérêt pour les câbles de transmission de puissance a augmenté au cours des dernières années avec des projets ayant lieu partout dans le monde. Cette tendance a motivé le développement de modèles de câble plus précis utilisés dans la simulation des transitoires électromagnétiques. Cette thèse aborde les différents domaines d'action associés à la modélisation et à la simulation des câbles à haute tension en courant alternative.

Le premier champ d'action est la validation de modèles de câbles pour la simulation de transitoires électromagnétiques. La validation est basée sur des essais disponibles en tenant compte des différents paramètres et équipements.

L'approche typique pour l'analyse des résultats d'essais consiste à extraire l'atténuation et la vitesse de l'onde ainsi que l'impédance caractéristique et à comparer ces valeurs à ceux du modèle. Cette approche permet de vérifier qu'un modèle de câble est précis, mais ne donne pas des indications sur les sources de divergence lorsque les résultats de l'essai et de la simulation ne sont pas en accord.

Cette thèse présente une nouvelle approche pour la validation d'un modèle de câble pour la simulation des transitoires électromagnétiques, basée sur des résultats d'essais sur le terrain. L'innovation consiste à extraire les paramètres par unité de longueur du câble à partir des formes d'onde mesurées, plutôt que d'extraire seulement l'atténuation, la vitesse et l'impédance caractéristique. Ces données supplémentaires fournissent une base additionnelle pour l'analyse des résultats de l'essai et de la simulation.

Le deuxième champ d'action de cette thèse est l'étude du phénomène de décharge naturelle des câbles. Bien que très peu d'essais de décharge se trouvent dans la littérature, ce phénomène est un sujet important pour les ingénieurs qui réalisent des tests sur des câbles à haute tension et pendant des travaux d'entretien. Récemment, le sujet de décharge a été le sujet de nouvelles considérations par certains gestionnaires de réseaux qui utilisent les câbles pour réguler la tension du réseau. Cette thèse contribue à l'étude des caractéristiques de décharge des câbles de type 'papier imprégné d'huile sous pression' à 275 kV. Les facteurs qui influent sur le phénomène, à savoir la capacité du câble, les résistances de fuite de l'isolation des câbles et des isolateurs externes, sont clairement identifiés et des valeurs typiques sont fournis. À partir de ces valeurs, le temps requis pour décharger un câble pour obtenir une tension en dessous des limites de sécurité (25 V selon IEC

60479-1) est calculé. Un facteur de correction pour tenir compte de l'impact de l'humidité relative de l'air sur la résistance de fuite des isolants externes est proposé. Les résultats de cette étude peuvent être appliqués pour la conception des protections de câble et l'évaluation de la nécessité d'installer un équipement de décharge.

Le troisième champ d'action de cette thèse est l'étude des câbles à écrans transposés. Les longs câbles à haute tension en courant alternatif ont souvent des écrans transposés et mis à la terre pour maximiser la performance du câble et empêcher le claquage de son isolation. Le comportement des systèmes à écrans transposés est plus complexe que dans les cas sans transposition à cause des réflexions crées aux points de jonction des écrans. Des équivalents homogènes peuvent être utilisés pour permettre la modélisation des câbles indépendamment du nombre de sections et ainsi surmonter les problèmes de simulation des systèmes avec un nombre élevé de sections.

Dans cette thèse, les différences entre les méthodes appliquées de transposition de câbles sont d'abord présentées et l'impact de la mise à la terre et de la transposition des écrans sur les caractéristiques de propagation du câble analysé. Des modèles de câbles à écrans transposés utilisant des équivalents homogènes sont comparés. En particulier, il est démontré qu'une représentation par équivalent homogène n'est pas suffisamment précise ni dans le domaine temporel, ni dans le domaine de la fréquence, car un tel modèle ne peut pas tenir compte de la superposition des différents modes créés par des courants circulant dans les écrans et qui affectent la réponse du câble. Une méthode générale pour le calcul des caractéristiques de propagation des systèmes de transmission non homogènes, y compris les câbles à écrans transposes, est démontrée dans cette thèse. La méthode utilise seulement la réponse en circuit ouvert du câble étudié. Enfin, une méthode à un seul terminal pour localiser des défauts dans des câbles à écrans transposés est aussi présentée. La méthode utilise la réponse en fréquence et la vitesse de propagation du câble. Cette étude de câbles à écrans transposés peut être utile dans des simulations de transitoires électromagnétiques, des études harmoniques et dans la localisation des défauts dans les câbles à haute tension en courant alternatif.

Les différentes études présentées dans cette thèse sont basées sur les caractéristiques modales de propagation, ainsi que sur les réponses dans les domaines temporel et fréquentiel des câbles. Des essais de terrain effectués par RTE-France et par National Grid (UK) fournissent la base de validation avec le logiciel EMTP.

ABSTRACT

The interest towards power transmission cables has increased in the recent years with projects taking place all over the world. This trend has motivated research for better understanding of phenomena associated with cables as well for more accurate cable models used in the simulation of electromagnetic transients (EMTs). This thesis addresses the different fields of action associated with the modeling and simulation of HVAC cables.

The first field of action is the validation of cable models for the simulation of EMT's. The most reliable validation method is based on comparison with field test results performed on actual cable system. Typically, the analysis of field test results consists of extracting the wave attenuation, velocity and surge impedance and comparing to those of the cable model. Although this approach allows verifying the cable model, it gives little insight into the sources of divergence when field test and simulations do not agree. This thesis presents a new method for validating a cable model for simulation of EMT's based on surge field test results. The innovation consists of extracting per-unit-length (PUL) cable parameters from the measured waveforms, rather than simply extracting attenuation, velocity and characteristic impedance. This approach provides a broader base for analyzing field test and simulation results.

The second field of action is the study of cable natural discharge. Although very few test results of cable charging and discharging can be found in the literature, this phenomenon is a matter of concern to cable engineers particularly when performing tests and during maintenance work. Recently, the charging/discharging phenomenon has received renewed consideration from utilities when using high-voltage (HV) cables for voltage control during periods of light load which requires nightly switching of cables. This thesis investigates discharging characteristics of 275 kV POF cables based on field and laboratory tests. The factors affecting the phenomenon, i.e. cable capacitance, leakage resistances of cable insulation and external insulators, are identified and typical values are provided. From these values, the time required to discharge a cable to safe voltage limits (25 V according to IEC 60479-1) is calculated. A correction factor to account for the impact of relative air humidity on the leakage resistance of external insulators is proposed. The results of this study can be applied to the design of cable protections and to evaluate the need for special discharge equipment.

The third field of action is the investigation of cross-bonded cables. Long HVAC cables have their sheaths cross-bonded and grounded to improve cable performance and prevent breakdown of cable insulation. The response of cross-bonded systems is more complicated compared to no-bonding systems because the sheaths change phase throughout the cable route and because bonding points create complicated traveling wave phenomena. To overcome the computational burden of simulating long cross-bonded systems, homogeneous equivalents can be used to enable modeling of cross-bonded cables independently of the number of major sections. In this thesis, the differences between alternative bonding methods are highlighted and studied. The impact of sheath grounding and sheath cross-bonding on the propagation characteristics of the cable is explained. Alternative models for cross-bonded systems, using homogeneous equivalents are compared. It is shown that a full homogeneous equivalent cannot accurately model a cross-bonded cable neither in time domain nor in frequency domain because it cannot account for mode superposition caused by currents circulating in the sheaths. A general method for calculating the propagation characteristics of cross-bonded cables, is proposed. The method uses only the open-circuit response of the system. Finally, a single-terminal method to locate faults in cross-bonded cables based on frequency response and characteristic wave velocity is demonstrated.

The different analysis presented in this thesis are based on the modal propagation characteristics, time-domain and frequency-domain responses of the different cable systems. Field tests carried out by RTE-France and by National Grid (UK) are used to validate EMTP simulations.

TABLE OF CONTENTS

LIST OF TABLES

LIST OF FIGURES

LIST OF SYMBOLS AND ABBREVIATIONS

α	Per-unit-length wave attenuation
AC	Alternate current
β	Per-unit-length phase shift
c	Wave velocity
C'	Per-unit-length shunt capacitance
CIGRÉ	Conseil International des Grands Réseaux Électriques
CMDCF	Cable model data calculation function
DC	Direct current
EMT	Electromagnetic transients
EMTP-RV	Electromagnetic Transients Program, Revised Version
EPDM	Ethylene propylene diene monomer
EPR	Ethylene propylene rubber
ESDD	Equivalent salt deposit density
f_0	Fundamental resonant frequency
G'	Per-unit-length shunt conductance
$\bar{\gamma}$	Per-unit-length propagation factor
$\bar{\mathbf{\Lambda}}$	Matrix of modal per-unit-length propagation factors
HDPE	High-density poly-ethylene
HV	High voltage
HVAC	High-voltage, alternate current
IEEE	Institute of Electrical and Electronics Engineers
IEC	International Electrotechnical Commission
L'	Per-unit-length series inductance

λ	Electromagnetic wavelength
OF	Oil-filled
OHL	Overhead line
POF	Pressurized-oil-filled
PT	Pipe-type
PUL	Per-unit-length
R'	Per-unit-length series resistance
RC	Parallel resistive-capacitive lumped circuit
RLC	Resistive-inductive-capacitive lumped circuit
RTE	Réseaux de Transport d'Electricité
SC	Single-core
τ	Propagation time delay
$\bar{\mathbf{T}}_\mathbf{i}$	Current transformation matrix
TSO	Transmission system operator
$\bar{\mathbf{T}}_\mathbf{v}$	Voltage transformation matrix
XLPE	Cross-linked poly-ethylene
$\bar{Y}'$	Per-unit-length shunt admittance
$\bar{Z}'$	Per-unit-length series impedance
$\bar{Z}_c$	Characteristic impedance
Z_{in}	Input impedance

LIST OF APPENDICES

CHAPTER 1 INTRODUCTION

1.1 Motivation

The interest towards power transmission cables has increased in the recent years with projects taking place all over the world [1]-[6]. For example, Denmark plans to entirely underground the 132-150 kV grid [3]. France is another notable case with a number of projects undergoing and planned for the next ten years for reinforcing the connection to peripheral regions [5], linking to off-shore wind parks and for interconnecting to neighbour countries [6].

This trend has motivated the development of more accurate cable models for computer simulation [7],[9]-[14] used for electromagnetic transient (EMT) studies, cable fault location and harmonic studies. Accurate simulations require adequate models that account for the frequency dependency of cable's per-unit-length (PUL) parameters.

Sophisticated cable/line models have been developed in the recent years [7],[9]-[14]. In some cases, the models are compared based on simulations only [7],[12]. A more reliable validation is based on comparison with field test results performed on the real cable system [8],[10],[14]-[20]. Typically, the analysis of field test results consists of extracting wave attenuation, velocity and surge impedance, and comparing to those of the cable model. Only rarely, the field test results are used to estimate the PUL parameters [17],[18],[20].

Although very few test results of cable charging and discharging can be found in the literature [21]-[23] this phenomenon has been a concern to cable engineers specially when performing tests and during maintenance work [1],[24]-[27]. Recently, the charging/discharging phenomenon has received renewed attention from utilities when using high-voltage (HV) cables for voltage control during periods of light load which require nightly switching of cables [28].

Long HVAC cables have their sheaths cross-bonded and grounded. This improves cable performance by reducing sheath currents, thus improving cable ampacity, and by reducing sheath voltage to prevent breakdown of cable insulation. Transposition of cores may also be used to further reduce sheath currents [29]. The first studies concerning cross-bonded cables were published in the 60's and continued steadily until end of the 80's motivated by new cable projects [15],[30],[43].

Recently, interest toward transmission cables and particularly cross-bonded systems is renewed [14],[16],[20],[44]-[82] thanks to new projects [1]-[6].

The response of cross-bonded systems is more complicated compared to no-bonding systems because the sheaths change phase throughout the cable route and because bonding points create complicated reflection phenomena. The first publications concerning cross-bonded cables used long and cumbersome equations and approximate lumped parameter models to calculate power frequency and transient responses [30]-[33]. Due to the complexity of the studies and limited computer resources at the time, studies were generally limited to one major section and to the first incident wave [30]-[33].

To overcome limitations in computer resources (not so important with modern computers) for the study of long cross-bonded systems, a homogeneous equivalent was derived to enable modeling of cross-bonded cables independently of the number of major sections [34]-[36] (a comprehensive derivation of the equivalent is given in [15]). The homogeneous equivalent option is available in various EMT-type software and it is generally considered as the only method for evaluating the propagation constants (e.g. attenuation and velocity) of cross-bonded cables. As emphasized in this thesis, the homogeneous equivalent model has several limitations for transient studies as it does not represent the reflections from bonding points nor the impedance of bonding wires and it cannot calculate sheath over-voltages within major sections. However, if bonding wires can be neglected, the homogeneous equivalent is thought to be accurate in frequency domain. The homogeneous equivalent is still used in frequency domain analysis [44] but recent transient studies opted for discrete modeling of each minor section [14],[16],[20],[45]-[47].

1.2 Contributions

The contributions of this thesis can be divided into the following categories.

Validation of cable models for transient studies based on field test results

The typical approach when validating cable models from field test results is to calculate the propagation constants (attenuation, velocity and characteristic impedance) from the measured waveforms and to compare them with simulation results obtained with the cable model. Although this approach is useful to verify that the model is accurate, it gives little insight into the sources of divergence when field test and simulation results do not agree. One objective of this thesis is to develop an alternative approach for model validation based on field test results between field test and the simulation results. The proposed new approach is applied to a field test carried out by the French Transmission System Operator (TSO) Réseau de Transport d'Electricité – RTE on a 225 kV underground cable and used to validate the cable model of EMTP-RV (EMT simulation tool).

Investigation of cable discharge, calculation of typical discharge times

Another contribution of this thesis is the investigation of parameters that affect the discharge of HVAC cables. The time required to discharge the cable to a safe voltage level (25 V according to IEC 60479-1) is of particular interest. Typical values for the leakage resistance of cable insulation as well as the leakage resistance of external insulators connected to the cable will be calculated. A correction factor to account for the influence of air humidity on the leakage resistance of external insulators will be proposed. The developments will be mostly based on the results of a field test of cable discharge carried out in 2015 by UK National Grid on a 275 kV pressurized-oil-filled (POF) cable of 21 km length and courteously gave permission to use the test results in this thesis.

These contributions are useful for designing cable protections and for evaluating the need for special discharge equipment when using power cables for voltage control in the network.

Modeling and simulation of long cross-bonded cables

One contribution of the thesis is to clarify the differences between the different bonding methods applied to HVAC cables, in particular the difference between normal-bonded (e.g. submarine) and cross-bonded cables (e.g. France, Denmark, Japan, UK). The comparison will be based on the propagation characteristics (attenuation and velocity), frequency domain and time domain responses of the different cable systems. A clear knowledge of the propagation characteristics is relevant for EMT analysis [10],[14]-[20],[24],[28],[33]-[38],[48]-[52],[62],[63],[69],[70],[72]-[78],[83] fault detection [45]-[47] and harmonic analysis [44] involving cross-bonded cables

Another contribution of this thesis is that it investigates and makes clear the impact of non-uniformities, in particular the grounding and the cross-bonding of the sheaths. Grounding of sheaths is a technique often used both in normal-bonded and cross-bonded cables which is somehow analogous to the grounding of the shield wires in overhead lines. Even though there are several articles studying the impact of shield wire grounding in OHL's, there is no similar literature studying the impact of grounding of cable sheaths and this thesis is intended to fill that gap. The mechanism through which the cross-bonding and the sheath currents affect the cable response will be clarified.

Another contribution is the study of different modeling methods for long cross-bonded cables, including both homogeneous and non-homogeneous equivalents. The alternative models will be compared based on frequency and time domain responses, particularly on the simulation of a field test carried out on RTE 225 kV cross-bonded cable with 64 km and 17 major sections.

The exact-pi circuit can be used to accurately calculate the propagation constants (attenuation and velocity) of a uniform structure, e.g. a minor section. It will be demonstrated that the exact-pi circuit representation can still be used for non-uniform structures such as cross-bonded cables under certain conditions. These calculations eliminate the need to find a homogeneous equivalent for the system.

Finally, a single-terminal method for locating faults on cross-bonded cables will be proposed.

1.3 Thesis outline

This thesis is composed of seven chapters and one appendix.

- CHAPTER 1 – INTRODUCTION, explains the background motivating this PhD project, highlights its objectives and contributions and summarizes the chapters' content.
- CHAPTER 2 – THEORETICAL BACKGROUND, contains the theory essential to understand the content of this thesis. This includes transmission line theory of single-phase and multi-phase systems, modal theory, as well as propagation characteristics and frequency and time responses of homogeneous cable systems.
- CHAPTER 3 – FIELD TESTS ON UNDERGROUND CABLES, presents a series of field and laboratory tests carried out on underground cables. This includes surge and energising tests carried out by RTE-France on a 225 kV XLPE underground cable and a discharge test carried out by National Grid, UK on a 275 kV OF cable.
- CHAPTER 4 – CALCULATION OF PUL CABLE PARAMETERS, presents a method for calculating the PUL parameters of cable systems based on field test results. The calculation of PUL resistance, inductance and capacitance are applicable to surge tests while the calculation of PUL conductance requires measurements of cable discharge.
- CHAPTER 5 – SIMULATION OF FIELD TESTS, contains simulation of field tests presented in Chapter 3 carried out in EMTP-RV and validation of cable models.
- CHAPTER 6 – CROSS-BONDED CABLES, contains a comparison of different cross-bonded cables in comparison to normal-bonded systems based on the distribution and characteristics of modal components, frequency and time-domain responses.
- CHAPTER 7 – CONCLUSION, presents the main conclusions of this thesis, the list of publications which derived from it and possible future developments based on this work.
- APPENDIX – FORMULAS FOR CABLE PUL PARAMETER CALCULATIONS, presents the theoretical formulas used in EMTP-RV to calculate PUL cable matrices for single-core and for pipe-type cables. It also shows the required modification to input data necessary to model stranded cores, semi-conducting screens and HDPE tubes. These are the features required for the simulations in Chapter 5.

CHAPTER 2 THEORETICAL BACKGROUND

This chapter covers the theory essential to understanding the content of the thesis. Single-phase telegrapher's equations are introduced in first place as they provide the basis for explaining the transient behavior of cables. Even though a cable always has more than one conductor, i.e. at least a core and a sheath, single-phase theory is still useful to explain the response of the cable to a specific propagation mode, with the approximating assumption of full mode decoupling.

Per-unit-length (PUL) parameters, as well as propagation factor, attenuation, phase shift, propagation velocity and characteristic impedance are defined from the telegrapher's equations. The application of voltage and current boundary conditions to the solution of telegrapher's equations leads to the definition of the exact-pi model in frequency domain. The exact-pi model combined with the lossless system approximation can be used to obtain an expression for resonant frequencies at which the line input impedance becomes very low, i.e. close to a short-circuit, or very high, i.e. close to an open-circuit. Resonant frequencies can be expressed in terms of the wavelength and the length of the transmission system.

Multi-phase theory is then introduced to cover the typical multi-conductor transmission systems. In this case, the telegrapher's equations become matrix coupled equations because of the coupling between the system conductors. A solution to the equations is possible through diagonalization using voltage and current transformation matrices which columns relate to the eigenvectors of the system.

Diagonalization of the telegrapher's equations allows separately studying each propagation mode in the transmission system, with the approximate assumption of full mode decoupling. Analysis of the system eigenvectors gives information on the distribution of modes, i.e. which current loop corresponds to each mode. The analysis will cover the simple single-phase single-core (SC) cable, the three-phase SC cable and the three-phase pipe-type (PT) cable.

Whereas eigenvectors give information on the modal loops, eigenvalues contain the characteristics of each mode, i.e. attenuation and phase shift, or alternatively propagation velocity. The difference between propagation characteristics of SC and PT cables will be clarified.

Frequency responses of input impedance for the two cable systems and for different energising conditions are investigated. Core, sheath and pipe application of zero-sequence or inter-phase

(differential) energising are considered. Resonant conditions are verified and expressed in terms of the modal wavelengths and the length of the cable.

Finally, the time-domain response of SC and PT cables are analyzed for the cases of energising from infinite and finite power networks.

2.1 Single-phase theory

Single-phase transmission line theory is introduced in this section to provide the basis for explaining the transient behavior of cables A single-phase transmission line can be modeled as an infinite series of elements shown in Figure 2.1.

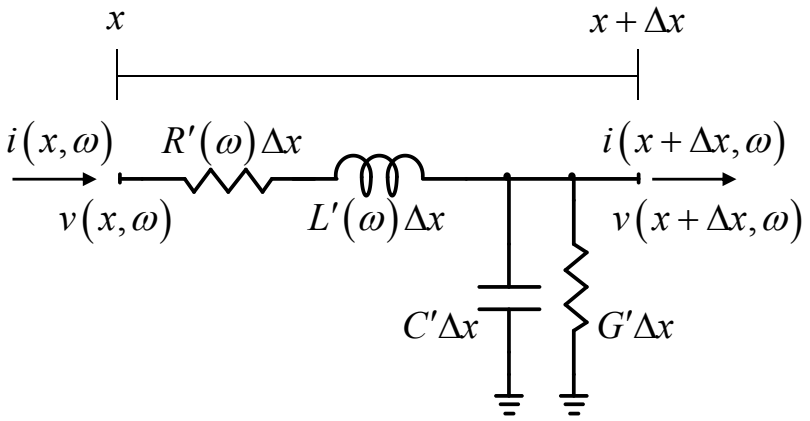

Figure 2.1 Model of an infinitesimal length of transmission line.

Based on Figure 2.1, the voltage and current in an infinitesimal length of transmission line are described in frequency-domain by the following equations

$$\frac{d\bar{V}(x,\omega)}{dx} = -\left(R'(\omega) + j\omega L'(\omega)\right)\bar{I}(x,\omega) = -\bar{Z}'(\omega)\bar{I}(x,\omega) \tag{2.1}$$

$$\frac{d\bar{I}(x,\omega)}{dx} = -\left(G' + j\omega C'\right)\bar{V}(x,\omega) = -\bar{Y}'(\omega)\bar{V}(x,\omega) \tag{2.2}$$

where a bar is used to indicate complex quantities and $\omega = 2\pi f$ is the angular frequency. Taking the derivative of (2.1) and (2.2) with respect to x results into

$$\frac{d^2\bar{V}}{dx^2} = \bar{Z}'\bar{Y}'\bar{V} = \bar{\gamma}^2\bar{V} \tag{2.3}$$

$$\frac{d^2\bar{I}}{dx^2} = \bar{\gamma}^2\bar{I} \tag{2.4}$$

$\bar{\gamma}$ is the propagation constant defined as

$$\bar{\gamma} = \sqrt{\bar{Z}'\bar{Y}'} = \sqrt{(R' + j\omega L')(G' + j\omega C')} = \alpha + j\beta \tag{2.5}$$

where α and β are the attenuation and phase shift constants.

The general solution of (2.3) and (2.4) is

$$\bar{V}(x,\omega) = \bar{V}^+ e^{-\bar{\gamma}x} + \bar{V}^- e^{\bar{\gamma}x} \tag{2.6}$$

$$\bar{I}(x,\omega) = \frac{1}{\bar{Z}_c}\left(\bar{V}^+ e^{-\bar{\gamma}x} - \bar{V}^- e^{\bar{\gamma}x}\right) \tag{2.7}$$

where $\bar{Z}_c$ is the characteristic impedance defined as

$$\bar{Z}_c = \sqrt{\frac{R' + j\omega L'}{G' + j\omega C'}} \tag{2.8}$$

In the case of a lossless system, the time domain forms of (2.6) and (2.7) are as follows

$$v(x,t) = v^+(x - ct) + v^-(x + ct) \tag{2.9}$$

$$i(x,t) = i^+(x - ct) + i^-(x + ct) \tag{2.10}$$

where c is the propagation velocity calculated from the frequency and the phase shift as

$$c = \frac{\omega}{\beta} \tag{2.11}$$

Equations (2.6) and (2.7) are converted to the well-known delay equations by using the values of voltage and current at the line terminals, i.e. $\bar{V}_0 = \bar{V}(x = 0, \omega)$, $\bar{V}_l$ and $\bar{I}_0$, $\bar{I}_l$ (both currents entering the system), resulting into

$$\bar{V}_0 - \bar{Z}_c\bar{I}_0 = \left(\bar{V}_l + \bar{Z}_c\bar{I}_l\right)e^{-\bar{\gamma}l} \tag{2.12}$$

$$\bar{V}_0 + \bar{Z}_c\bar{I}_0 = \left(\bar{V}_l - \bar{Z}_c\bar{I}_l\right)e^{\bar{\gamma}l} \tag{2.13}$$

By using hyperbolic functions, the above equations can be rewritten to have the sending end quantities $\bar{V}_0$ and $\bar{I}_0$ expressed in terms of the receiving end $\bar{V}_l$ and $\bar{I}_l$ as

$$\bar{V}_0 = \cosh(\bar{\gamma} l)\bar{V}_l - \bar{Z}_c \sinh(\bar{\gamma} l)\bar{I}_l \tag{2.14}$$

$$\bar{I}_0 = \frac{1}{\bar{Z}_c}\sinh(\bar{\gamma} l)\bar{V}_l - \cosh(\bar{\gamma} l)\bar{I}_l \tag{2.15}$$

or in matrix form

$$\begin{bmatrix} \bar{V}_0 \\ \bar{I}_0 \end{bmatrix} = \begin{bmatrix} A & B \\ C & D \end{bmatrix} \begin{bmatrix} \bar{V}_l \\ \bar{I}_l \end{bmatrix} \tag{2.16}$$

where $A = -D = \cosh(\bar{\gamma} l), B = -\bar{Z}_c \sinh(\bar{\gamma} l), C = (\bar{Z}_c)^{-1} \sinh(\bar{\gamma} l)$. The above formulation allows to establish the pi-equivalent model with a series branch $\bar{Z}_{\pi s}$ and two shunt branches $\bar{Z}_{\pi g}$ as illustrated in Figure 2.2 with

$$\bar{Z}_{\pi s} = \bar{Z}_c \sinh(\bar{\gamma} l) \tag{2.17}$$

$$\bar{Z}_{\pi g} = \frac{\bar{Z}_c}{\tanh(\bar{\gamma} l/2)} \tag{2.18}$$

It is emphasized here that the actual parameters (PUL) are frequency dependent and the exact-pi formulation can be achieved if the pi-equivalent is calculated at each frequency using frequency dependent parameters.

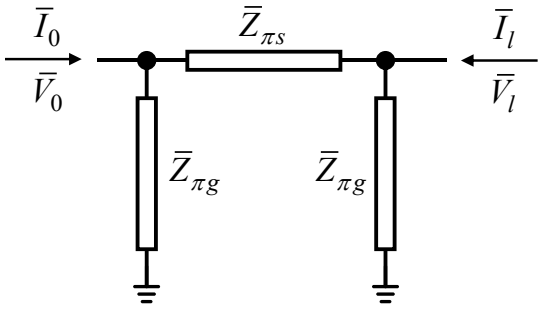

Figure 2.2 PI-equivalent model of a transmission line.

Finally, the voltage and current at a distance x between the two line terminals are given as

$$\bar{V}(x) = \frac{\bar{V}_0 + \bar{Z}_c \bar{I}_0}{2} e^{-\bar{\gamma} x} + \frac{\bar{V}_l + \bar{Z}_c \bar{I}_l}{2} e^{\bar{\gamma} x} \tag{2.19}$$

$$\bar{I}(x) = \frac{\bar{V}_0 + \bar{Z}_c \bar{I}_0}{2\bar{Z}_c} e^{-\bar{\gamma} x} - \frac{\bar{V}_l + \bar{Z}_c \bar{I}_l}{2\bar{Z}_c} e^{\bar{\gamma} x} \tag{2.20}$$

Assuming a lossless line ($R'=0$) and a lossless insulation ($G'=0$), $\bar{Z}_c$ in (2.8) becomes purely resistive, i.e. $Z_c=\sqrt{L'/C'}$, and $\bar{\gamma}$ in (2.5) becomes a simple phase shift, i.e. $\bar{\gamma}=j\omega\sqrt{L'C'}=j\beta$. The propagation velocity defined in (2.11) can thus be written as $c=1/\sqrt{L'C'}$. Accordingly, the branches for the exact-pi model become

$$\bar{Z}_{\pi s-lossless}=jZ_c\sin\left(2\pi l/\lambda\right) \tag{2.21}$$

$$\bar{Z}_{\pi g-lossless}=-jZ_c/\tan\left(\pi l/\lambda\right) \tag{2.22}$$

where λ is the wavelength defined as

$$\lambda=\frac{2\pi}{\beta} \tag{2.23}$$

The above definition of λ is general, i.e. it does not require lossless conditions.

In (2.22), $\bar{Z}_{\pi g-lossless}$ may become zero if $\pi l/\lambda=\pi/2,\,3\pi/2,\,5\pi/2,...$ and infinity if $\pi l/\lambda=0,\,\pi,\,2\pi,....$ These conditions correspond to resonant frequencies in which the input impedance of the transmission line is near to a short-circuit or an open-circuit, respectively (in reality, because every system has losses, the resonant impedances never reach zero nor infinite). Resonance occurs at frequencies for which line length is a multiple of a quarter wavelength, i.e.

$$l=\frac{\lambda}{4}\rightarrow Z_{in}=0$$

$$l=2\frac{\lambda}{4}\rightarrow Z_{in}=\infty$$

$$l=3\frac{\lambda}{4}\rightarrow Z_{in}=0$$

...

where the wavelength λ is monotonously decreasing with frequency.

To illustrate the above, consider the 100 km overhead line described in Table 2.1. Figure 2.3 shows the positive sequence impedance and it is clear that resonant peaks of minimum and maximum impedance occur at frequencies multiple of one another. The result in Figure 2.3 is the same using an exact-PI or a wide-band line model.

Table 2.1 Data of a 230 kV overhead line with 100 km length.

Ph.	Horizontal distance [m]	Vertical height [m]	Other data:
A	-10	20	Phase/ground wire DC resistance $2\times10^{-8}\,\Omega/\text{km}$
B	10	20	Phase/shield wire outside diameter $5\text{cm}/3\text{cm}$
C	-7	20	Earth resistivity $100\,\Omega\text{-m}$
GW	7	29	Total line length $100\,\text{km}$

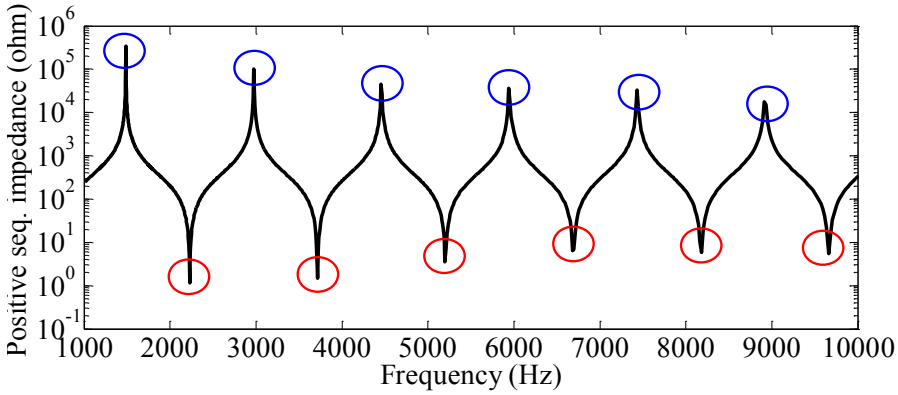

Figure 2.3 Positive sequence impedance of a 230 kV 100 km overhead line.[1]

2.2 Multi-phase theory

In the case of a multi-phase system, as it is the case of transmission cables, equations (2.3) and (2.4) are rewritten as

$$\frac{d^2\,\bar{\mathbf{V}}}{dx^2} = \bar{\mathbf{Z}}'\bar{\mathbf{Y}}'\bar{\mathbf{V}} \tag{2.24}$$

$$\frac{d^2\,\bar{\mathbf{I}}}{dx^2} = \bar{\mathbf{Y}}'\bar{\mathbf{Z}}'\bar{\mathbf{I}} \tag{2.25}$$

The products $\bar{\mathbf{Z}}'\bar{\mathbf{Y}}'$ and $\bar{\mathbf{Y}}'\bar{\mathbf{Z}}'$ are full matrices because of the coupling between the phases. Using eigenvalue theory, it is possible to transform the two above equations from phase-domain to modal

[1] Circuit: CableSimulation_Files\NonHomogeneous_LinesCables\EMTP_Files\Circuit2.ecf

domain [48]. The voltages and currents in phase and modal domain are related through transformation matrices $\bar{\mathbf{T}}_\mathbf{v}$ and $\bar{\mathbf{T}}_\mathbf{i}$ as

$$\bar{\mathbf{V}} = \bar{\mathbf{T}}_\mathbf{v}\bar{\mathbf{V}}^m \tag{2.26}$$

$$\bar{\mathbf{I}} = \bar{\mathbf{T}}_\mathbf{i}\bar{\mathbf{I}}^m \tag{2.27}$$

Applying the above relations to (2.24) and (2.25) results into

$$\frac{d^2\,\bar{\mathbf{V}}^m}{dx^2} = \left(\bar{\mathbf{T}}_\mathbf{v}{}^{-1}\bar{\mathbf{Z}}'\bar{\mathbf{Y}}'\bar{\mathbf{T}}_\mathbf{v}\right)\bar{\mathbf{V}}^m = \bar{\mathbf{\Lambda}}^2\,\bar{\mathbf{V}}^m \tag{2.28}$$

$$\frac{d^2\,\bar{\mathbf{I}}^m}{dx^2} = \left(\bar{\mathbf{T}}_\mathbf{i}{}^{-1}\bar{\mathbf{Y}}'\bar{\mathbf{Z}}'\bar{\mathbf{T}}_\mathbf{i}\right)\bar{\mathbf{I}}^m = \bar{\mathbf{\Lambda}}^2\,\bar{\mathbf{I}}^m \tag{2.29}$$

$$\bar{\mathbf{\Lambda}}^2 = -\left(\bar{\mathbf{T}}_\mathbf{v}{}^{-1}\bar{\mathbf{Z}}'\bar{\mathbf{Y}}'\bar{\mathbf{T}}_\mathbf{v}\right) = \left(\bar{\mathbf{T}}_\mathbf{i}{}^{-1}\bar{\mathbf{Y}}'\bar{\mathbf{Z}}'\bar{\mathbf{T}}_\mathbf{i}\right) \tag{2.30}$$

From the equality in (2.30) it follows that

$$\bar{\mathbf{T}}_\mathbf{v} = \bar{\mathbf{T}}_\mathbf{i}{}^{-T} \tag{2.31}$$

Matrix $\bar{\mathbf{\Lambda}}$ is a diagonal matrix. From (2.30) it follows that the elements in the diagonal of $\bar{\mathbf{\Lambda}}$ are eigenvalues of both matrices $\bar{\mathbf{Z}}'\bar{\mathbf{Y}}'$ and $\bar{\mathbf{Y}}'\bar{\mathbf{Z}}'$ (despite the products not being necessarily equal). From (2.28) it follows that $\bar{\mathbf{T}}_\mathbf{v}$ contains the eigenvectors of $\bar{\mathbf{Z}}'\bar{\mathbf{Y}}'$ while (2.29) shows that $\bar{\mathbf{T}}_\mathbf{i}$ contains the eigenvectors of $\bar{\mathbf{Y}}'\bar{\mathbf{Z}}'$. Contrary to eigenvectors, eigenvalues are uniquely defined.

From (2.26) to (2.31) it is also concluded that

$$\bar{\mathbf{Z}}'^m = \bar{\mathbf{T}}_\mathbf{i}{}^T\bar{\mathbf{Z}}'\bar{\mathbf{T}}_\mathbf{i} \tag{2.32}$$

$$\bar{\mathbf{Y}}'^m = \bar{\mathbf{T}}_\mathbf{v}{}^T\bar{\mathbf{Y}}'\bar{\mathbf{T}}_\mathbf{v} \tag{2.33}$$

and

$$\bar{\mathbf{Z}}_\mathbf{c}{}^m = \bar{\mathbf{T}}_\mathbf{i}{}^T\bar{\mathbf{Z}}_\mathbf{c}\,\bar{\mathbf{T}}_\mathbf{i} \tag{2.34}$$

All these modal-domain matrices depend on the choice of eigenvectors in $\bar{\mathbf{T}}_\mathbf{i}$ and $\bar{\mathbf{T}}_\mathbf{v}$.

The $i-\text{th}$ element in the diagonal of $\bar{\mathbf{\Lambda}}$, which can be expressed as $\bar{\gamma}_i^m$ is identified as the propagation constant of the $i-\text{th}$ mode. With the diagonalization in (2.30), a system of n coupled

phases can be described as a system of n uncoupled modes and each mode can be studied with the theory of single-phase transmission line presented in section 2.1.

2.3 Identification of modal components

2.3.1 Single-phase single-core cable

A single-core cable is composed in its simplest form of a core and a metallic sheath. Hence, analysis of modal components of a single-core (SC) cable requires the application of the multi-phase transmission line theory presented in section 2.2.

Given the coaxial structure of a SC cable, a possible approximate modal transformation is [24]

$$\bar{\mathbf{I}} = \begin{bmatrix} I_{co} \\ I_{sh} \end{bmatrix} = \mathbf{T_i}\bar{\mathbf{I}}^{\mathbf{m}} = \begin{bmatrix} 0 & 1 \\ 1 & -1 \end{bmatrix}\begin{bmatrix} I_1 \\ I_2 \end{bmatrix} \tag{2.35}$$

$$\bar{\mathbf{V}} = \begin{bmatrix} V_{co} \\ V_{sh} \end{bmatrix} = \mathbf{T_v}\bar{\mathbf{V}}^{\mathbf{m}} = \begin{bmatrix} 1 & 1 \\ 1 & 0 \end{bmatrix}\begin{bmatrix} V_1 \\ V_2 \end{bmatrix} \tag{2.36}$$

Subscripts 1 and 2 are used for the two propagation modes. The inverse transformation is

$$\begin{bmatrix} I_1 \\ I_2 \end{bmatrix} = \begin{bmatrix} 1 & 1 \\ 1 & 0 \end{bmatrix}\begin{bmatrix} I_{co} \\ I_{sh} \end{bmatrix}, \mathbf{T_i}^{-1} = \begin{bmatrix} 1 & 1 \\ 1 & 0 \end{bmatrix} = \mathbf{T_v}^T \tag{2.37}$$

$$\begin{bmatrix} V_1 \\ V_2 \end{bmatrix} = \begin{bmatrix} 0 & 1 \\ 1 & -1 \end{bmatrix}\begin{bmatrix} V_{co} \\ V_{sh} \end{bmatrix}, \mathbf{T_v}^{-1} = \begin{bmatrix} 0 & 1 \\ 1 & -1 \end{bmatrix} = \mathbf{T_i}^T \tag{2.38}$$

The above equations highlight the nature of the two propagation modes. From (2.38) it follows that $V_1 = V_{sh}$ which identifies mode 1 as an earth-return mode illustrated in Figure 2.4 (left). Combining (2.37) and (2.38) results into $I_2 = I_{co}$ and $V_2 = V_{co} - V_{sh}$ which makes clear that mode 2 is a coaxial as illustrated in Figure 2.4 (right).

a) Earth-return mode. b) Coaxial mode.

Figure 2.4 Propagation modes in a single-phase single-core cable.

Because of the finite thickness of the sheath, the earth-return and coaxial modes are coupled. The frequency at which mode decoupling is achieved can be determined using the complex penetration depth $\bar{d}_{sh}$ of the sheath and its absolute value d_{sh} defined as

$$\bar{d}_{sh} = \sqrt{\frac{\rho_{sh}}{j\omega\mu_{sh}}}, d_{sh} = \left|\bar{d}_{sh}\right| = \sqrt{\frac{2\rho_{sh}}{\omega\mu_{sh}}} \tag{2.39}$$

where ρ_{sh} and μ_{sh} are the resistivity and magnetic permeability of the sheath. When d_{sh} becomes lesser than the sheath thickness, coaxial and earth-return modes become decoupled i.e. the sheath provides full shielding and the coaxial mode becomes dominant. A so-called critical frequency f_c can be defined as the frequency at which the sheath complex depth magnitude d_{sh} in (2.39) becomes equal to the sheath thickness $d_{sh} = r_{sh-out} - r_{sh-in}$

$$f_c = \frac{\rho_{sh}}{2\pi\,\mu_{sh}\left(r_{sh-out} - r_{sh-in}\right)^2} \tag{2.40}$$

where ρ_{sh} is the sheath resistivity, μ_{sh} the sheath magnetic permeability and r_{sh-out}, r_{sh-in} are the outer and inner sheath radii.

2.3.2 Three-phase single-core cable

A three-phase SC cable has 6 propagation modes, illustrated in Figure 2.5: a zero-sequence sheath mode with return through the earth (earth-return mode), a two-phase and a three-phase inter-sheath modes, a zero-sequence core mode, with return through the sheaths, a two-phase and a three-phase inter-core modes.

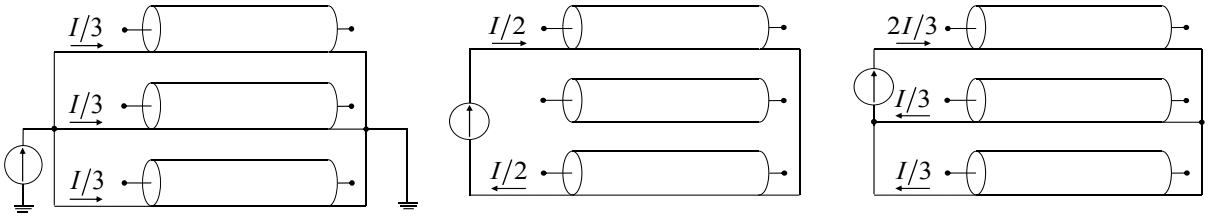

a) zero-sequence sheath mode (earth-return mode)

b) two-phase inter-sheath mode

c) three-phase inter-sheath mode

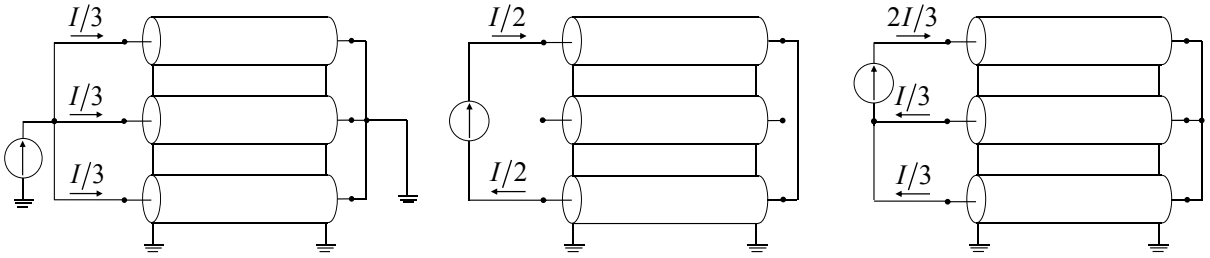

d) zero-sequence core mode e) two-phase inter-core mode f) three-phase inter-core mode

Figure 2.5 Propagation modes in a three-phase single-core cable.

Even though transformation matrices vary continuously with frequency, the following approximate transformations for a three-phase SC cable can be used [24] for a three-phase cable without armour

$$\begin{bmatrix} V_1 \\ V_2 \\ V_3 \\ V_4 \\ V_5 \\ V_6 \end{bmatrix} = \left[\begin{array}{ccc:ccc} 0 & 0 & 0 & 1/3 & 1/3 & 1/3 \\ 0 & 0 & 0 & 1/2 & 0 & -1/2 \\ 0 & 0 & 0 & -1/3 & 2/3 & -1/3 \\ \hdashline 1/3 & 1/3 & 1/3 & 0 & 0 & 0 \\ 1/2 & 0 & -1/2 & 0 & 0 & 0 \\ -1/3 & 2/3 & -1/3 & 0 & 0 & 0 \end{array}\right] \begin{bmatrix} V_{co-a} \\ V_{co-b} \\ V_{co-c} \\ \hdashline V_{sh-a} \\ V_{sh-b} \\ V_{sh-c} \end{bmatrix}, \; f < f_s \tag{2.41}$$

$$\begin{bmatrix} V_1 \\ V_2 \\ V_3 \\ V_4 \\ V_5 \\ V_6 \end{bmatrix} = \left[\begin{array}{ccc:ccc} 0 & 0 & 0 & 1/3 & 1/3 & 1/3 \\ 0 & 0 & 0 & 1/2 & 0 & -1/2 \\ 0 & 0 & 0 & -1/3 & 2/3 & -1/3 \\ \hdashline 1/3 & 1/3 & 1/3 & -1/3 & -1/3 & -1/3 \\ 1/2 & 0 & -1/2 & -1/2 & 0 & 1/2 \\ -1/3 & 2/3 & -1/3 & 1/3 & -2/3 & 1/3 \end{array}\right] \begin{bmatrix} V_{co-a} \\ V_{co-b} \\ V_{co-c} \\ \hdashline V_{sh-a} \\ V_{sh-b} \\ V_{sh-c} \end{bmatrix}, \; f_s < f < f_c \tag{2.42}$$

$$\begin{bmatrix} V_1 \\ V_2 \\ V_3 \\ V_4 \\ V_5 \\ V_6 \end{bmatrix} = \left[\begin{array}{ccc:ccc} 0 & 0 & 0 & 1/3 & 1/3 & 1/3 \\ 0 & 0 & 0 & 1/2 & 0 & -1/2 \\ 0 & 0 & 0 & -1/3 & 2/3 & -1/3 \\ \hdashline 0 & 0 & 1 & 0 & 0 & -1 \\ 1 & 0 & 0 & -1 & 0 & 0 \\ 0 & 1 & 0 & 0 & -1 & 0 \end{array}\right] \begin{bmatrix} V_{co-a} \\ V_{co-b} \\ V_{co-c} \\ \hdashline V_{sh-a} \\ V_{sh-b} \\ V_{sh-c} \end{bmatrix}, \; f > f_c \tag{2.43}$$

where f_c is defined in (2.40) and f_s is given empirically in the following form [24]

$$f_s \approx \frac{\rho_{sh}^{3/4}}{10\pi\,\mu_{sh}\,y\left(r_{sh-out} - r_{sh-in}\right)} \tag{2.44}$$

where y is the separation between phases, ρ_{sh} is the sheath resistivity, μ_{sh} the sheath magnetic permeability and r_{sh-out}, r_{sh-in} are the outer and inner sheath radii.

In (2.41) to (2.43) it is clear that mode 1 is an earth-return mode with $V_1 = (V_{sh-a} + V_{sh-b} + V_{sh-c})/3$. Modes 2 and 3 are respectively two-phase and three-phase inter-sheath modes with $V_2 = (V_{sh-a} - V_{sh-c})/2$ and $V_3 = (2V_{sh-b} - V_{sh-a} - V_{sh-c})/3$.

It is also clear in (2.41) to (2.43) that the nature of modes 4, 5 and 6 changes with frequency. At low frequencies, i.e. $f < f_s$, these modes are pure inter-core modes. For $f_s < f < f_c$, the inter-core modes are accompanied by inter-sheath modes while at high frequencies modes 4, 5 and 6 become pure single-phase coaxial modes, i.e. $V_4 = V_{co-c} - V_{sh-c}$, $V_5 = V_{co-a} - V_{sh-a}$ and $V_6 = V_{co-b} - V_{sh-b}$. In reality, this evolution in the nature of modes is a gradual phenomenon, i.e. it cannot be said that for $f = f_s - \Delta, \Delta << 1$ the propagation modes have a given nature and for $f = f_s + \Delta$ the modes become completely different.

As explained in [49], this interaction between inter-core and inter-sheath modes occurs because the magnetic flux generated by core currents also links the inter-sheath circuit. The result is the excitation of sheath currents which oppose the flux linkage, converting the inter-core mode into both a coaxial and an inter-sheath mode. At low frequencies, the sheath resistance is relatively high and thus sheath currents are weak. As the frequency increases, the sheath resistance becomes relatively smaller compared to the core resistance and hence higher currents flow into the sheaths. At high frequencies the modes become purely coaxial.

The definition of f_s in (2.44) agrees with the above as f_s increases with the sheath resistivity and decreases with the distance between phases (the larger the distance the larger the surface for flux linkage).

2.3.3 Pipe-type cable

In the case of a pipe-type (PT) cable, the three SC cables are enclosed by a metallic pipe. Hence, the earth-return mode V_1 in (2.43) and illustrated in Figure 2.5 is substituted by a pipe-return mode and there will be an additional mode between the pipe and the earth-return path. These modes are illustrated in Figure 2.6. The inter-sheath modes will be the same but will have different

characteristics because instead of earth, the phases will be separated by the pipe inner insulation. An approximate transformation matrix for high frequencies is

$$\begin{bmatrix} V_1 \\ V_2 \\ V_3 \\ V_4 \\ V_5 \\ V_6 \\ V_7 \end{bmatrix} = \left[\begin{array}{ccc:ccc:c} 0 & 0 & 0 & 1/3 & 1/3 & 1/3 & -1 \\ 0 & 0 & 0 & 1/2 & 0 & -1/2 & 0 \\ 0 & 0 & 0 & -1/3 & 2/3 & -1/3 & 0 \\ \hdashline 0 & 0 & 1 & 0 & 0 & -1 & 0 \\ 1 & 0 & 0 & -1 & 0 & 0 & 0 \\ 0 & -1 & 0 & 0 & -1 & 0 & 0 \\ \hdashline 0 & 0 & 0 & 0 & 0 & 0 & 1 \end{array}\right] \begin{bmatrix} V_{co-a} \\ V_{co-b} \\ V_{co-c} \\ \hdashline V_{sh-a} \\ V_{sh-b} \\ V_{sh-c} \\ \hdashline V_p \end{bmatrix}, \; f_c < f \tag{2.45}$$

For frequencies at which the penetration depth of the pipe is smaller than the pipe thickness, i.e.

$$\sqrt{\frac{2\rho_p}{\omega\mu_p}} < r_{p-out} - r_{p-in} \tag{2.46}$$

the pipe can be assumed as of infinite thickness. In that case, there is no earth-return mode and the last row and column in (2.45) are eliminated. Normally (2.46) is verified even at power frequency because of the relatively large thickness and high magnetic permeability of pipes used in PT cables.

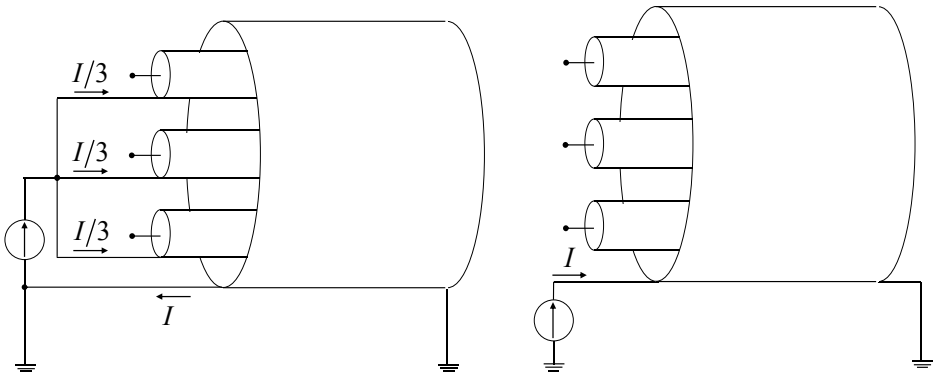

Figure 2.6 Pipe-return and earth-return modes in three-phase pipe-type cable.

2.4 Modal velocity and attenuation

2.4.1 Three-phase single-core cable

Figure 2.7 illustrates a trefoil SC cable which phases are described in Table 2.2.

Table 2.2 Data of a single-core cable.

Parameter	Value
Core conductor	$r_{co-in} = 0,\ r_{co-out} = 28.4\,\text{mm},\ \rho_{co} = 2.84\times10^{-8}\,\Omega/\text{m}$
Core insulation	$\varepsilon_{r_{co-ins}} = 3.23,\ \tan\delta = 0.0008$
Metallic sheath	$r_{sh-in} = 56.4\,\text{mm},\ r_{sh-out} = 57.2\,\text{mm},\ \rho_{sh} = 2.6\times10^{-8}\,\Omega/\text{m}$
Outer insulation	$\varepsilon_{r_{sh-ins}} = 2.5,\ \tan\delta = 0.0008$

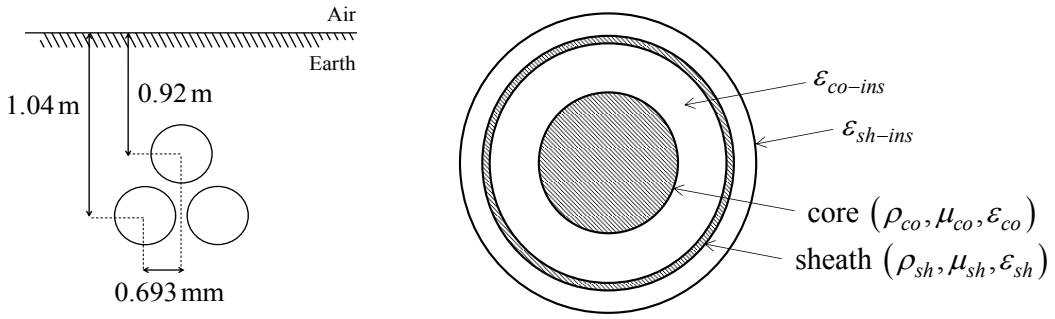

Figure 2.7 Three-phase single-core underground cable.

Figure 2.8 and Figure 2.9 show the modal attenuations and velocities for the cable in Figure 2.7. The values computed at 100 kHz are summarized in Table 2.4.

The earth-return mode is the more attenuated and also the slowest mode. It is also the most frequency-dependent with a constantly rising velocity while the other modes reach a constant value at high frequencies. The high attenuation is due to the high resistivity of soil compared to core and sheath resistivities and the low velocity is due to the high inductance of the earth-return path.

The two inter-sheath modes are highly attenuated at low frequencies because of the influence of the earth-return path, while at high frequencies they become nearly as attenuated as core modes. Inter-sheath modes have at least twice the earth-return velocity and they are largely slower than core modes.

The core modes are the least attenuated because of low resistivity and no influence of earth-return path and they are the fastest propagating modes. The velocity of core modes is given for high frequencies (purely coaxial mode) by

$$c = \frac{c_0}{\sqrt{\varepsilon_r}} \tag{2.47}$$

where ε_r is the relative permittivity of the core insulation. With $c_0 = 300\,\text{m}/\mu\text{s}$ and $\varepsilon_r = 3.23$ in Table 2.2, (2.47) results into $c = 167\ \text{m}/\mu\text{s}$ which agrees with the value in Figure 2.9. The two inter-core modes are initially different from the zero-sequence core mode. They are initially faster and less attenuated.

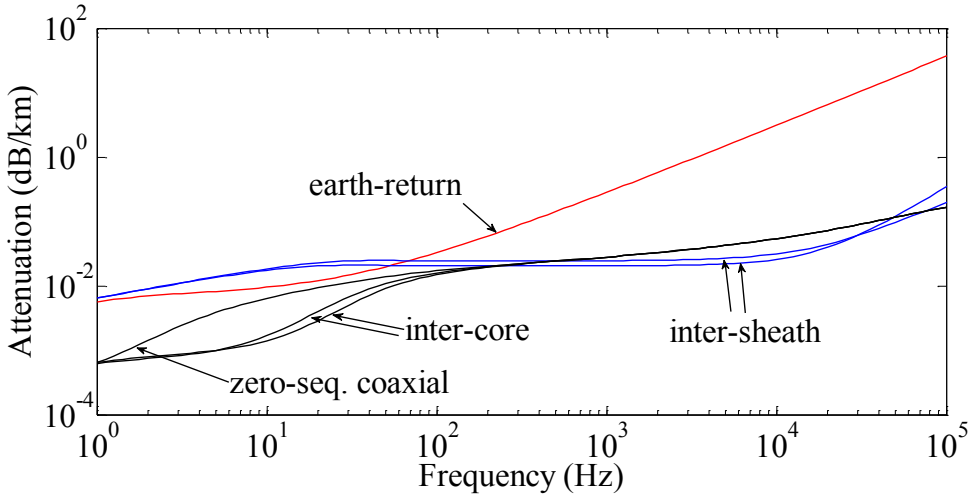

Figure 2.8 Modal attenuation constants of a three-phase single-core cable.[2]

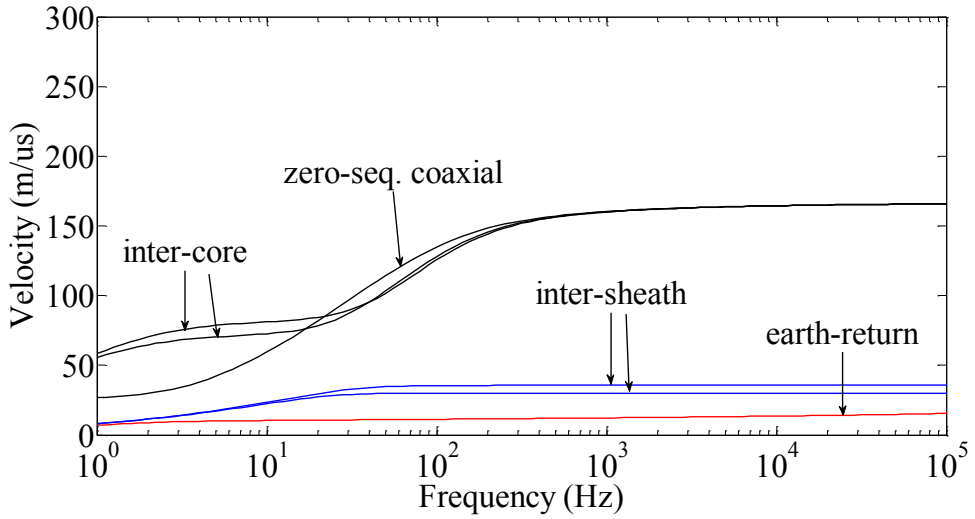

Figure 2.9 Modal velocities of a three-phase single-core cable.[2]

[2] Circuits: CableSimulation_Files\Comparison_SC_PT_cables\ModalComponents\Circuit.ecf
Plotting: CableSimulation_Files\Comparison_SC_PT_cables\ModalComponents\Plots.m

2.4.2 Pipe-type cable

Figure 2.10 shows a PT cable in everything equal to the SC cable in Figure 2.7, except that the three phases are in this case enclosed by a pipe. The data for each phase is given in Table 2.2 and the properties of the pipe are given in Table 2.3 and in Figure 2.10.

Table 2.3 Data of a pipe-type cable.

Parameter	Value
Phases inside pipe	See Table 2.2
Insulation inside pipe	Air: $\varepsilon_r = 1,\ \tan\delta = 0$
Pipe conductor	$r_{p-in} = 150\,\text{mm},\ r_{p-out} = 170\,\text{mm},\ \rho_{sh} = 1.5\times10^{-7}\,\Omega/\text{m},\ \mu_{r_p} = 300$
Pipe outer insulation	$r_{p-ins} = 190\,\text{mm},\ \varepsilon_{r_{p-ins}} = 2.5,\ \tan\delta = 0.0008$

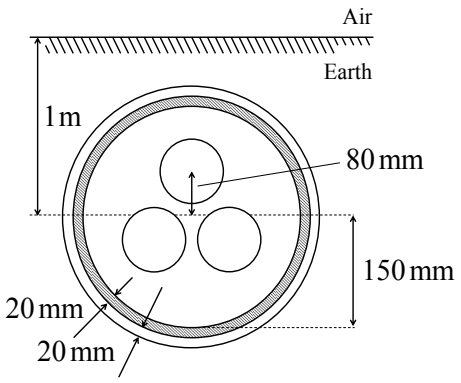

Figure 2.10 Three-phase pipe-type cable.

Figure 2.11 and Figure 2.12 show respectively the modal attenuations and velocities for the PT cable in Figure 2.10 and Table 2.3. Table 2.4 gives the values computed at 100 kHz.

The core modes are exactly equal to those of the three-phase SC cable analyzed in section 2.4.1. This is because the phases of the PT cable are the same as the phases of the 3-phase SC cable and because the core modes are practically not influenced by the media outside the metallic sheath.

A substantial difference relative to the SC cable is that the inter-sheath modes for the PT cable are way less attenuated and faster compared to the inter-sheath modes of the SC cable. The inter-sheath mode velocities in Figure 2.12 are even faster than the core mode velocities and they are close to

light velocity. The reason for this is the pipe being filled with air ($\mu_r = 1$, $\varepsilon_r = 1$). Hence the inter-sheath modes behave nearly as the inter-phase modes of an aerial line.

The zero-sequence sheath mode, i.e. pipe-return mode, is also substantially different from the zero-sequence sheath mode of the SC cable: less attenuated and faster, nearly as much as the PT cable inter-sheath modes. As expected, the pipe-to-earth mode is close to the earth-return mode of the SC cable. Still, it is less attenuated and faster because of the big dimensions of the pipe compared to the dimensions of the sheaths and the larger insulation thickness.

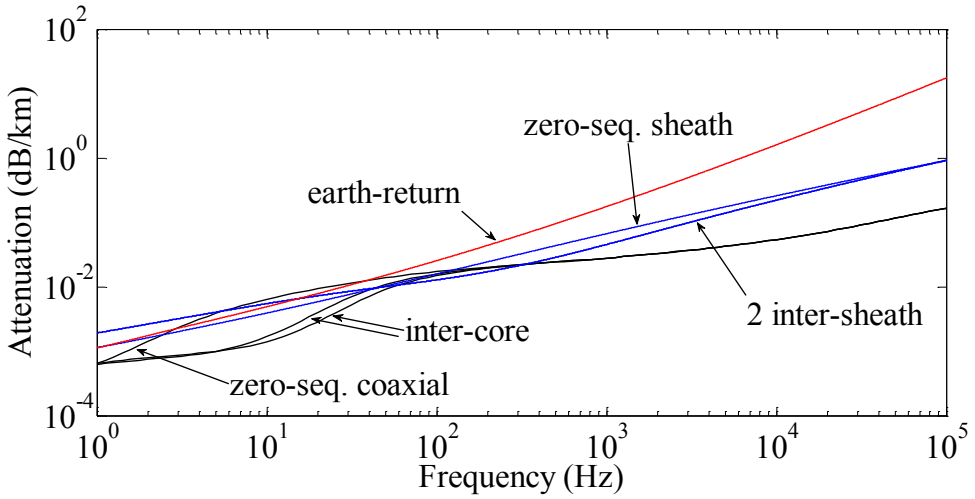

Figure 2.11 Modal attenuation constants for a three-phase pipe-type cable. [2]

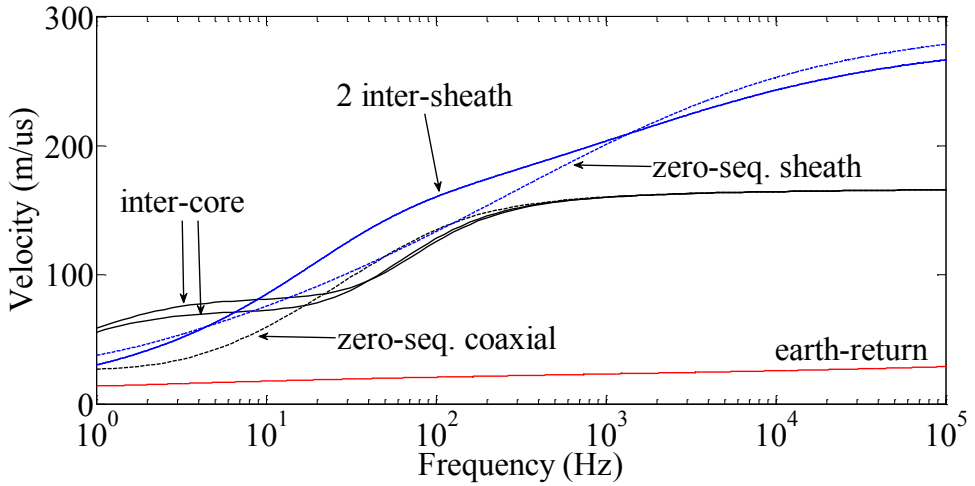

Figure 2.12 Modal velocities for a three-phase pipe-type cable. [2]

Table 2.4 summarizes the modal characteristics of SC and PT cables computed at 100 kHz. It is very clear that both systems have the same response to core modes. However, the response to sheath modes is very different in SC and PT cables. Inter-sheath modes in PT cables have characteristics similar to the modes in overhead lines and they are substantially faster that the same modes in SC cables because of the air gap inside the pipe. On the other hand, the pipe-to-earth modes of the PT cable is similar to the zero-sequence sheath mode in the SC cable because of the strong impact of the earth-return impedance.

Table 2.4 Modal attenuations and velocities for three-phase single-core and pipe-type cables computed at 100 kHz.

Mode	SC cable		PT cable	
	v [m/μs]	α [dB/km]	v [m/μs]	α [dB/km]
Zero-sequence coaxial	166	0.166	166	0.166
2-phase inter-core	166	0.166	166	0.166
3-phase inter-core	166	0.166	166	0.166
Zero-sequence sheath	15.45	37.01	278.6	0.9136
2-phase inter-sheath	35.68	0.346	266.5	0.9136
3-phase inter-sheath	30.14	0.197	266.5	0.9136
Pipe-to-earth	--	--	28.86	17.47

2.5 Frequency-domain responses

This section presents the input impedance response of the SC cable in Figure 2.7 with data in Table 2.2 and the PT cable in Figure 2.10 and Table 2.3 under different energising conditions. In each test the cables are energised with a frequency-varying current source which phasor is written as

$$\bar{I}(f) = e^{j2\pi f} \tag{2.48}$$

with frequency f scanned from 1 Hz to 1 MHz. The cables input impedances are calculated from the amplitude $|V_{src}|$ and phase θ of measured at the source terminals as

$$\bar{Z} = \frac{\bar{V}_{src}(f)}{\bar{I}(f)} = \frac{|V_{src}|e^{j2\pi f + j\theta}}{e^{j2\pi f}} = |V_{src}|e^{j\theta} \tag{2.49}$$

2.5.1 Core energisation

The circuits in Figure 2.13 are used to compare the responses of the SC and the PT cable to different core energising. Each circuit is tested using 1 km and 10 km cable lengths and for open-circuit and short-circuit termination of cores. The sheaths (and pipe for the PT cable) are bonded and grounded at both ends through a resistance $R_g = 5\ \Omega$.

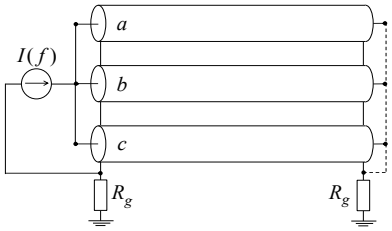

a) Zero-sequence core mode.

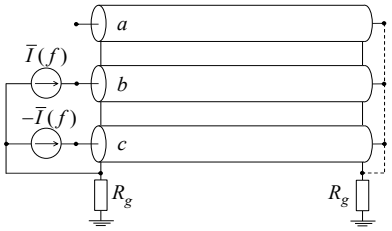

b) Two-phase inter-core mode.

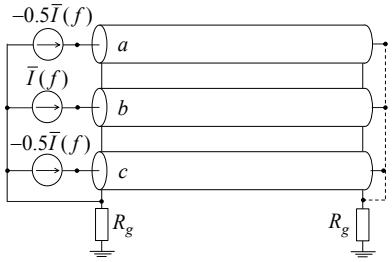

c) Three-phase inter-core mode.

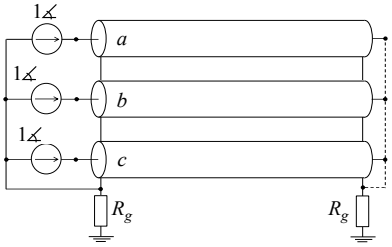

d) Positive-sequence.

Figure 2.13 Circuits for core energising in a single-core cable in frequency domain. The dash line is used to short-circuit the cores at the receiving end.

Figure 2.14 shows the input impedance (magnitude and angle) for open-circuit termination to the four energising schemes in Figure 2.13. The impedance in Figure 2.14 is exactly the same for SC and PT cable.

The minima of impedance in Figure 2.14 correspond to resonant conditions characterized by the cable length being a multiple of a quarter wavelength. The wavelength is defined in (2.23) as a function of the phase shift which is in general different for each propagation mode. However, the resonant frequencies in Figure 2.14 are the same for the four different core energising. The reason for this is that the first resonant frequency is already high enough so that the three core modes as well as the positive sequence (which is a combination of core modes) will have the same modal phase shift. The same is not true for the amplitude of impedances which are different for each case.

As expected, under resonance the impedance amplitude is at a minimum with the phase near to zero. When a 10 km cable is considered (Figure 2.15) the resonant points are observed at frequencies ten times lower than the frequencies of the 1 km cable and the amplitudes of resonant impedances are higher as a result of higher resistance. The linear variation of resonant frequencies with the cable length is not observed for the amplitude of impedances because the phenomenon of skin effect is not linear with frequency.

If the receiving end cores are short-circuited (Figure 2.16) the impedance minima become impedance maxima and vice-versa, compared to the open-circuit case (Figure 2.14). An important difference is that for the short-circuit termination the impedance is minimal at DC and it is given by the DC resistance of the coaxial loop.

Table 2.5 contains the values of the first three resonant frequencies and corresponding impedances for the different core energising schemes. In open-circuit, the resonant frequencies are given as f_0, $3f_0$, $5f_0$,… where f_0 is the fundamental frequency given as

$$f_0 = \frac{c}{4l} \tag{2.50}$$

where c is the propagation velocity and l is the cable length. Using $c = 166\,\mathrm{m/\mu s}$ (Table 2.4) and $l = 1\,\mathrm{km}$ in (2.50) results $f_0 = 41.5\,\mathrm{kHz}$ which agrees with the values in Table 2.5. In the case of cores short-circuited, resonance occurs at $2f_0$, $4f_0$, $6f_0$,…

It can also be observed from Table 2.5 that the input impedance for two-phase energising is 6 times the value for zero-sequence energising, while the impedance for three-phase energising is 4.5 times higher. This is readily explained as follows. Let Z_{co} be the input impedance of one phase. A zero-sequence application energises three phases in parallel, thus $Z_0 = Z_{co}/3$. On the contrary, a two-phase application energises two phases in series, thus $Z_{2-ph} = 2Z_{co} = 2 \times 3 \times Z_0 = 6Z_0$. A three-phase application energises one phase in series with the parallel of the other two, thus $Z_{3-ph} = Z_{co} + Z_{co}/2 = 3Z_{co}/2 = 3 \times 3 \times Z_0/2 = 4.5Z_0$.

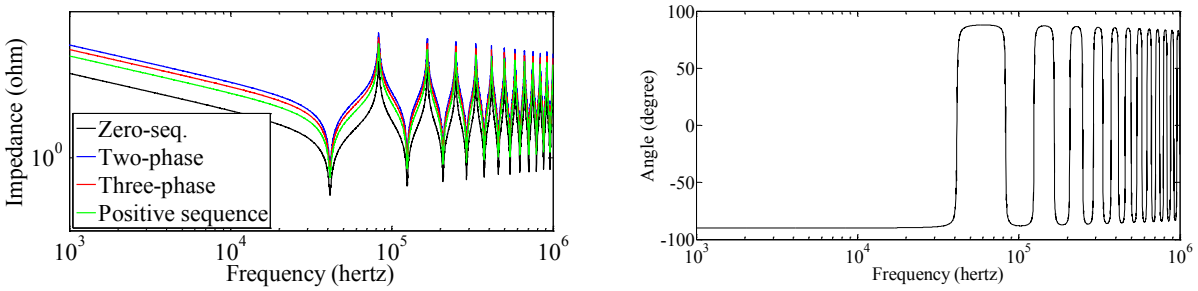

a) Impedance magnitude. b) Impedance angle.

Figure 2.14 Open-circuit response to different core energising on 1 km cable (valid for both single-core and pipe-type systems).[3]

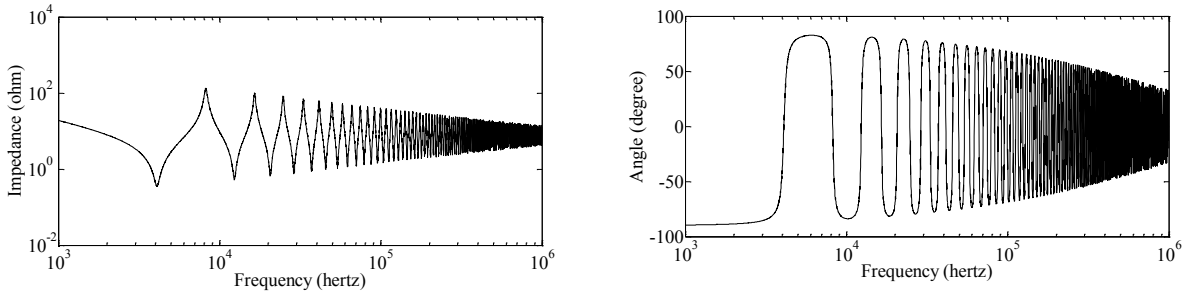

a) Impedance magnitude. b) Impedance angle.

Figure 2.15 Open-circuit response to zero-sequence core excitation on 10 km cable (valid for both single-core and pipe-type systems).[3]

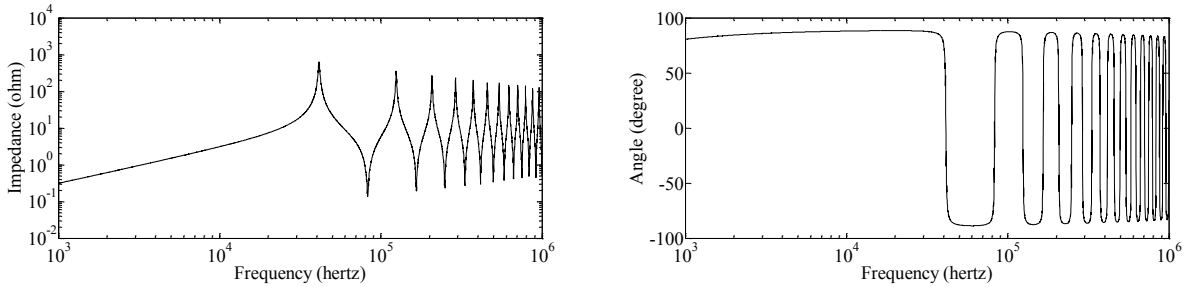

a) Impedance magnitude. b) Impedance angle.

Figure 2.16 Short-circuit response to zero-sequence core excitation on 1 km cable (valid for both single-core and pipe-type). [3]

---

[3] Circuits: CableSimulation_Files\Comparison_SC_PT_cables\ImpedanceResponses\Circuit.ecf

Plotting: CableSimulation_Files\Comparison_SC_PT_cables\ImpedanceResponses\Plots.m

Table 2.5 Resonant frequencies and input impedance of 1 km and 10 km cables for different energising schemes, in open-circuit and short-circuit (single-core and pipe-type cables).

		Open-circuit			Short-circuit		
		f_0	f_1	f_2	f_0	f_1	f_2
1 km	Frequency (kHz)	41.4	124.2	207	82.79	166	250
	Zero-seq. (ohm)	0.09341	0.1659	0.2269	0.1346	0.1972	0.2322
	Two-phase (ohm)	0.5605	0.9951	1.361	0.8076	1.183	1.393
	Three-phase (ohm)	0.4204	0.7463	1.021	0.6057	0.8875	1.045
	Positive-seq.(ohm)	0.2802	0.4975	0.6806	0.4048	0.5917	0.6966
10 km	Frequency (kHz)	4.074	12.36	20.61	8.204	16.56	24.72
	Zero-seq. (ohm)	0.3585	0.5241	0.6829	0.4488	0.5967	0.7115
	Two-phase (ohm)	2.152	3.145	4.098	2.694	3.581	4.269
	Three-phase (ohm)	1.614	2.359	3.074	2.02	2.686	3.202
	Positive-seq. (ohm)	1.076	1.573	2.049	1.347	1.791	2.135

2.5.2 Sheath and pipe energisation

The circuits in Figure 2.17 are simulated in frequency domain to compare the responses of the SC and the PT cables to different sheath energising schemes. Figure 2.18 shows the circuit for pipe energising of the pipe-type cable. The reason why the source is not grounded in circuits b) and c) is to energise each inter-sheath mode without the superposition of additional modes that would be excited in the case of a grounded source [50]. Each simulation is repeated for 1 km and 10 km cable lengths and for open-circuit and short-circuit termination of sheaths and pipe.

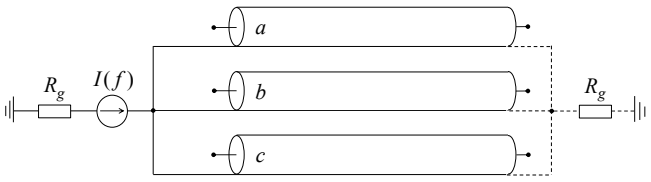

a) Zero-sequence sheath mode.

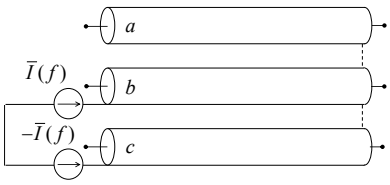

b) Two-phase inter-sheath mode.

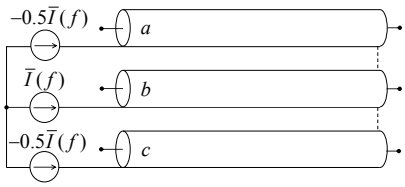

c) Three-phase inter-sheath mode.

Figure 2.17 Circuits for studying the frequency response to different sheath energising of single-core and pipe-type cables.

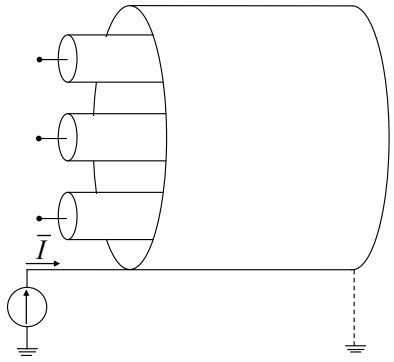

Figure 2.18 Circuit for pipe energising of a pipe-type cable.

In the case of the SC cable, energising a two-phase or a three-phase inter-sheath mode will produce a single propagation mode only if the phases are adequately chosen. Figure 2.19 shows two alternative excitation schemes for a three-phase inter-sheath energising. A pure inter-sheath mode is produced only if the current enters the top phase and returns through the bottom phases. This is because given the symmetry of the system (see Figure 2.7) the two bottom phases will have the same impedance: both are at the same depth and both have two other phases at the same distance. In the case of the PT cable in Figure 2.10 it makes no difference in which phase the current enters first because the pipe provides a shielding to the inner phases and because all the phase are at the same distance from the pipe and from one another in the system of Figure 2.10.

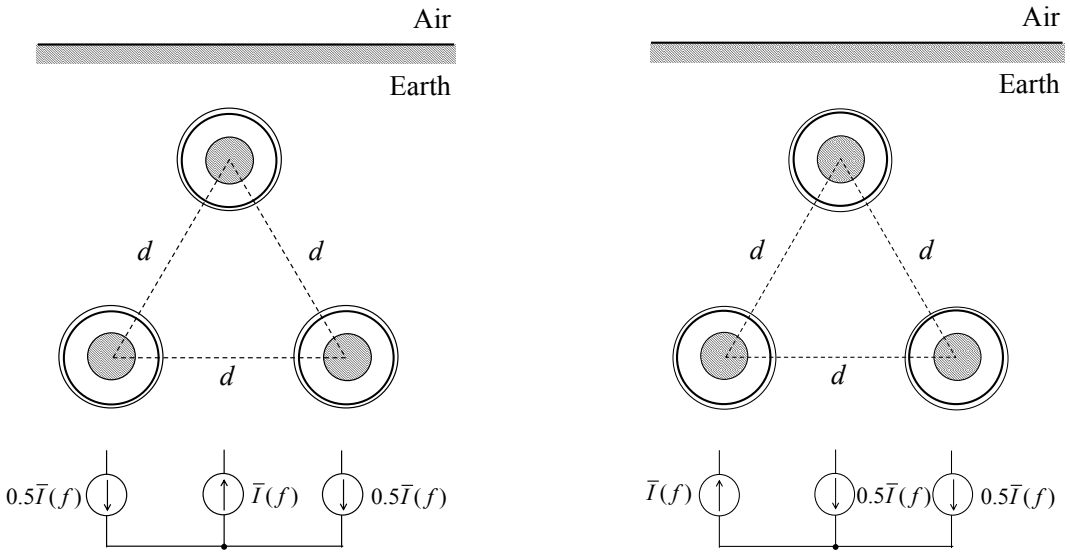

Figure 2.19 Alternative three-phase inter-sheath energising of a single-core cable.

Figure 2.20 shows the response of the 1 km SC cable to different sheath energising. The resonant frequencies for zero-sequence energising are substantially lower and have higher impedance

compared to the cases of inter-sheath energising, as a result of a much lower propagation velocity of the zero-sequence sheath mode and a higher resistance of the earth-return path (see Table 2.4).

Figure 2.21 shows the response of the 1 km PT cable to different sheath and pipe energising. In this case, the zero-sequence sheath energising produces a response similar to the inter-sheath source applications. The response to pipe energising is somehow similar to the zero-sequence sheath energising of the SC cable in Figure 2.20 which is explained by the two energising schemes having the earth as a return path.

The resonant frequencies are the same for the two-phase and three-phase sheath energising of the PT cable because the two inter-sheath modes have the same propagation velocity. The resonant frequencies for zero-sequence energising are slightly different and the magnitude is substantially higher because the pipe having an impedance different to the sheath is involved as a return path.

Table 2.6, showing the first resonant points in both SC and PT cables, confirms the above remarks.

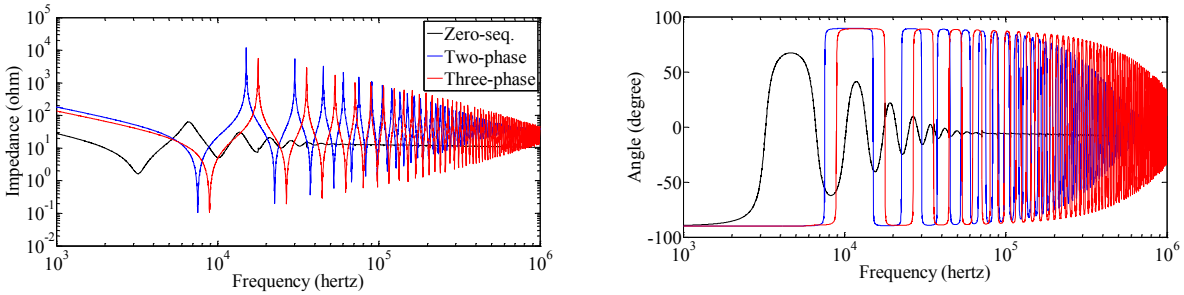

a) Impedance magnitude. b) Impedance angle.

Figure 2.20 Responses of a 1 km single-core cable to different sheath excitations. Receiving end sheaths in open-circuit. [3]

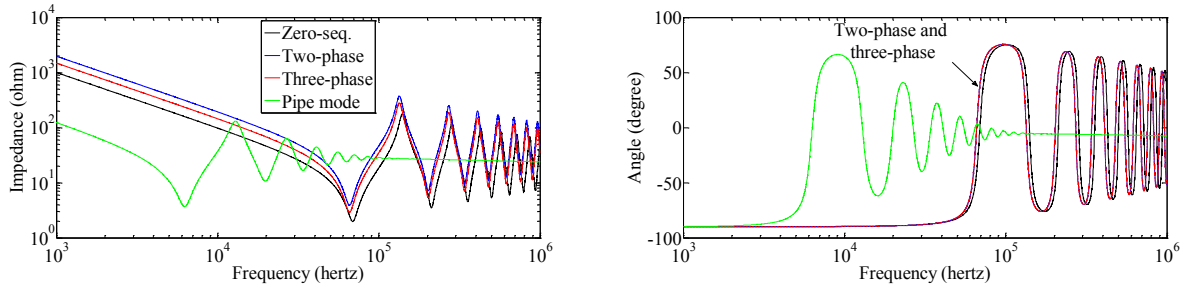

a) Impedance magnitude. b) Impedance angle.

Figure 2.21 Response of 1 km length pipe-type cable to different sheath and pipe excitations. Receiving end sheaths and pipe in open-circuit. [3]

Table 2.6 Resonant frequencies and input impedances of single-core and pipe-type cables for different sheath and pipe energising.

Single-core cable							
		Open-circuit			Short-circuit		
		f_0	f_1	f_2	f_0	f_1	f_2
1 km	Frequency (kHz)	3.206	10.19	17.78	6.668	13.74	21.13
	Zero-seq. (ohm)	1.63	5.015	7.252	3.331	6.534	9.086
	Frequency (kHz)	7.534	22.59	37.58	15.03	30.13	45.19
	Two-phase (ohm)	0.106	0.198	0.3613	0.1428	0.2709	0.4742
	Frequency (kHz)	8.892	26.73	44.67	17.82	35.73	53.58
	Three-phase (ohm)	0.1051	0.191	0.295	0.1787	0.3296	0.3964
10 km	Frequency (kHz)	0.2938	0.9204	1.556	0.6012	1.236	1.884
	Zero-seq. (ohm)	1.608	4.623	7.291	3.109	6.012	8.522
	Frequency (kHz)	0.7534	2.259	3.758	1.503	3.013	4.519
	Two-phase (ohm)	0.9123	0.923	0.9521	0.9169	0.9336	0.9592
	Frequency (kHz)	0.8892	2.673	4.467	1.782	3.573	5.358
	Three-phase (ohm)	0.6984	0.7472	0.7808	0.7208	0.7859	0.8494
Pipe-type cable							
		Open-circuit			Short-circuit		
		f_0	f_1	f_2	f_0	f_1	f_2
1 km	Frequency (kHz)	68.87	211.8	357.3	140	428.5	285.1
	Zero-seq. (ohm)	1.976	3.473	4.493	2.829	4.924	4.017
	Frequency (kHz)	65.61	203.2	342.8	134.3	272.9	411.1
	Two-phase (ohm)	3.893	7.133	9.387	5.747	8.316	10.27
	Frequency (kHz)	65.61	203.2	342.8	134.3	272.9	411.1
	Three-phase (ohm)	2.92	5.349	7.04	4.31	6.237	7.699
	Frequency (kHz)	6.252	19.82	33.88	12.91	26.79	41.02
	Pipe mode (ohm)	3.677	10.69	16.72	7.249	13.88	19.15
10 km	Frequency (kHz)	6.026	19.68	34.12	12.71	26.49	40.55
	Zero-seq. (ohm)	5.755	9.875	12.57	8.146	11.24	13.32
	Frequency (kHz)	5.888	18.58	32.21	12.25	25.41	38.73
	Two-phase (ohm)	9.426	18.26	23.73	14.38	21.21	25.9
	Frequency (kHz)	5.888	18.58	32.21	12.25	25.41	38.73
	Three-phase (ohm)	7.069	13.69	17.8	10.79	15.91	19.43
	Frequency (kHz)	0.561	1.766	3.048	1.161	2.399	3.681
	Pipe mode (ohm)	4.295	11.2	17.14	7.86	14.26	19.48

2.6 Time-domain responses

The SC cable in Figure 2.7, Table 2.2 and the PT cable in Figure 2.10, Table 2.3 are simulated in time domain for an energising transient. The two cable systems have 10 km. The sheaths (and pipe, in the case of the PT cable) are grounded at both ends through 5 Ω resistances. Each cable is separately energised from a 225 kV balanced network at t = 1 ms (all phases). The simulation is carried out for the cases of infinite power network and for finite power network with short-circuit capacity of 7740 MVA with X/R = 7 [51].

Figure 2.22 and Figure 2.23 show respectively the cable receiving end voltages and sending end currents for the energising from an infinite power network. Figure 2.24 and Figure 2.25 show the finite power network case. The results are the same both for the SC cable and for the PT cable. In section 2.4 it was demonstrated that the SC cable and PT cable only show the same characteristics as far as core modes are concerned. Therefore, it can be concluded that only core modes are involved in the waveforms of Figure 2.22 to Figure 2.25.

The frequency of the transient when energising from an infinite power network is higher than for the case of real source. The reason for this is that the network inductance adds up to the cable inductance thus reducing the oscillating frequency.

The oscillations are damped out much faster in the case of infinite power network because in this case the transient has a high frequency. The attenuation of the cable is more important for higher frequencies, as shown in section 2.4. The network impedance limits the transient current, as observed from a comparison of Figure 2.23 and Figure 2.25.

To observe the impact of the closing time, the same energising tests were repeated for the case of non-deterministic switch closing times. The closing time for each pole follows a Gaussian distribution of mean 0.0165 seconds and standard deviation of 0.014 seconds. The maximum overvoltages observed throughout 1000 simulations were +331.6 kV (phase-b) when energising from an infinite source and +355.1 kV (phase-c) for the case of real source. Energising from a real source creates higher overvoltages in all phases. The reason for this is that the infinite source has more power to control the voltage that the real source.

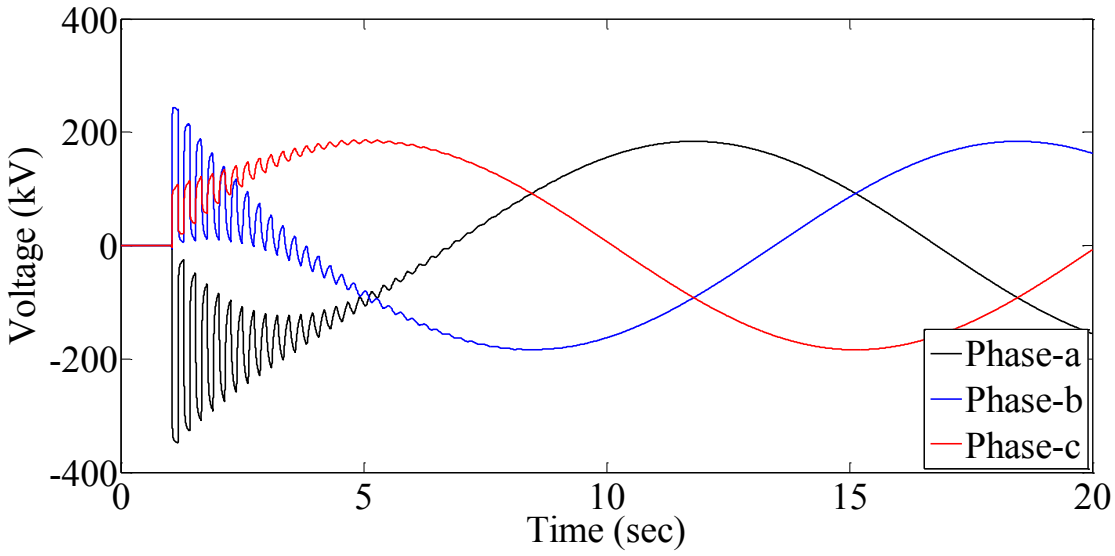

Figure 2.22 Receiving end voltages for energising of a 10 km cable from a 225 kV infinite power network.[4]

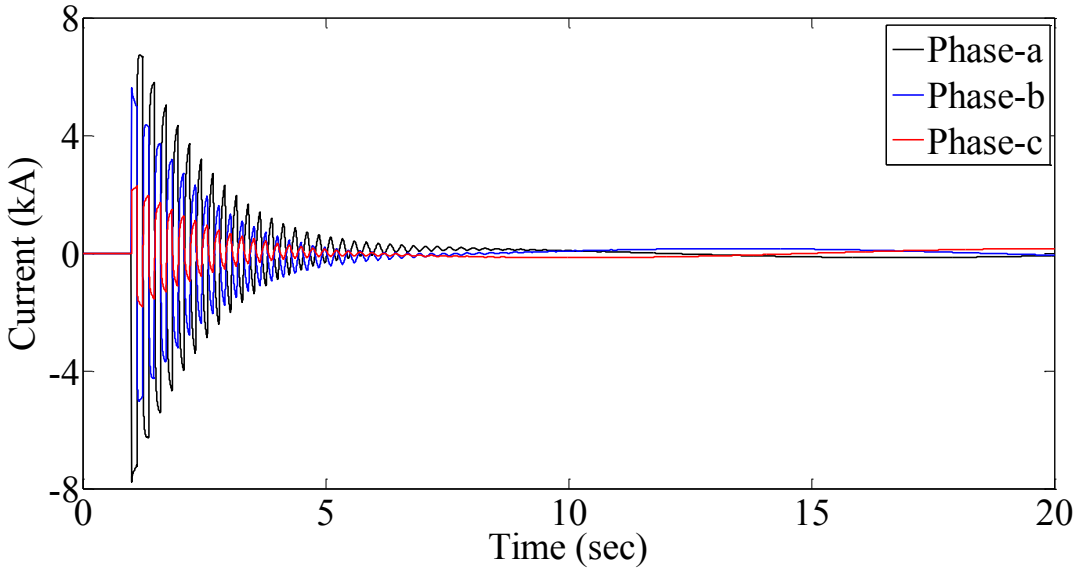

Figure 2.23 Sending end currents for energising of a 10 km cable from a 225 kV infinite power network.[4]

[4] Circuits: CableSimulation_Files\Comparison_SC_PT_cables\TimeResponses\Circuit.ecf

Plotting: CableSimulation_Files\Comparison_SC_PT_cables\TimeResponses\Plots.m

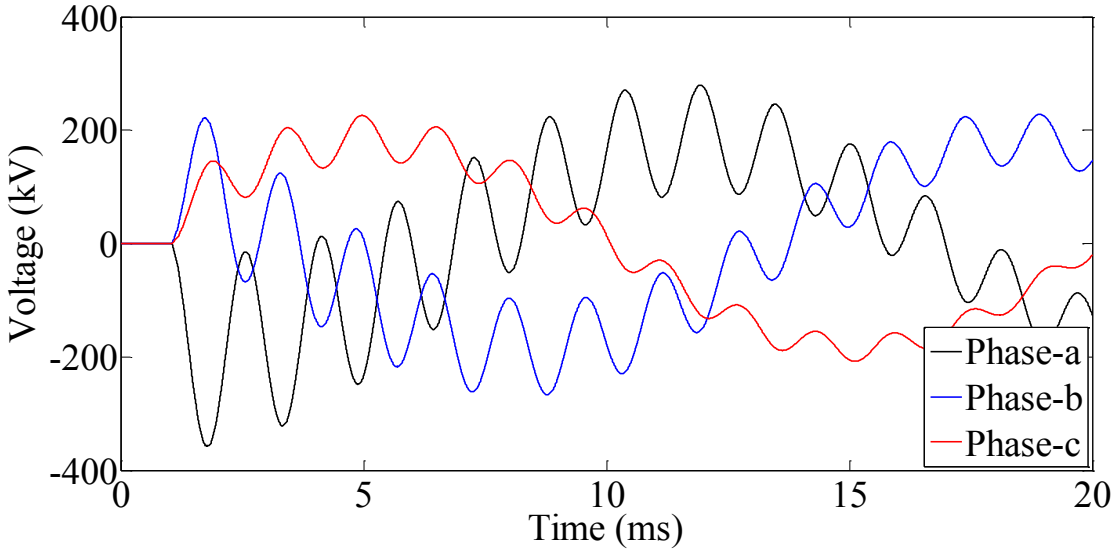

Figure 2.24 Receiving end voltages for energising of a 10 km cable from a 225 kV finite power network. [4]

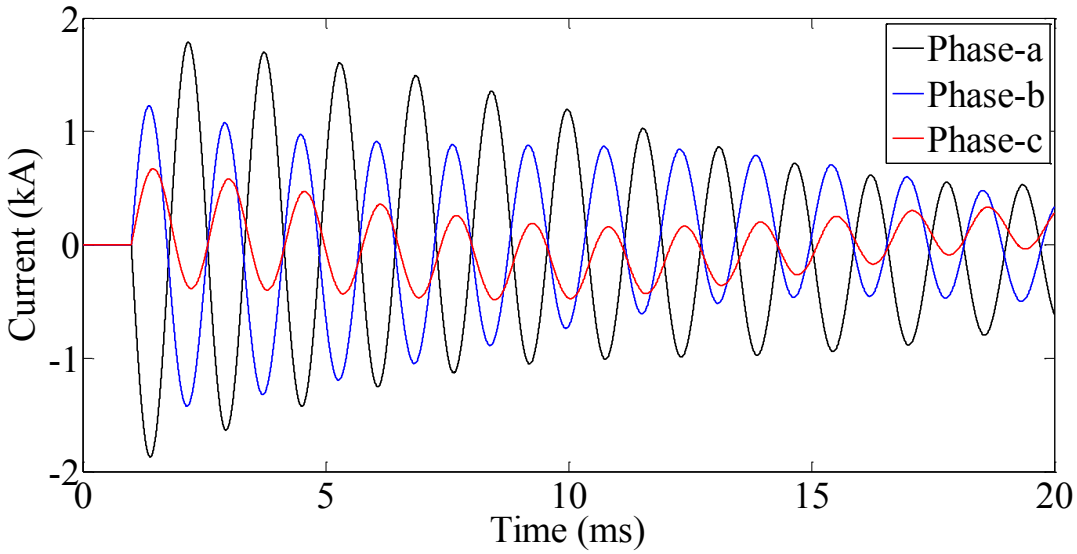

Figure 2.25 Sending end currents for energising of a 10 km cable using a 225 kV source of finite power. [4]

2.7 Conclusion

This chapter presented the theory over which this thesis is based. Per-unit-length impedance and admittance matrices were defined from the Telegrapher's equations. Propagation factor, attenuation, phase shift, propagation velocity and characteristic impedance have been defined. The basis of modal theory was also presented to provide a means of studying any multi-phase system, particularly transmission cables. The PI-model was also introduced to support the definition of wavelength and resonance in the cable.

The nature of modes in a three-phase power cable was explained and a difference between two of the most popular topologies, single-core cable and pipe-type cable, was made clear.

Frequency responses for the two cable systems were investigated for different energising conditions, with focus on resonant conditions. The time-domain responses of single-core and pipe-type cables for an energising test was also analyzed for the cases of infinite and finite power networks.

CHAPTER 3 FIELD TESTS ON UNDERGROUND CABLES

This chapter presents five field and laboratory tests carried out on underground HVAC cables. These field test results provide data for validating the developments presented in the next chapters of this thesis.

3.1 Surge test on RTE 225 kV cross-bonded cable

In 2014, RTE carried out a surge test on a new cable installed in the South East of France between the regions of Boutre and Trans-en-Provence. This is a 225 kV XLPE underground cross-bonded cable with 64 km length and it is one of three underground links that were built to reinforce the connection of the PACA region (Provence-Alpes-Côte d'Azur) to the French grid, previously fed through a single 400 kV overhead link.

The surge test was carried out during the cable construction. Therefore, it was possible to test a separate minor section. A major section was also tested to observe the impact of cross-bonding. Different excitation schemes were used to measure the characteristics of different propagation modes.

The minor section used in this test has 1080 m and uses 2000 mm² core conductors while the major section has 3953 m and uses 2000 mm² and 2500 mm² conductors, as illustrated in Figure 2.26. The cable phases are enclosed by HDPE (high-density poly-ethylene) tubes embedded in concrete. Figure 2.29 shows a sample of a cable phase. Figure 2.30 illustrates the burial layout and Table 2.8 contains the cable data. The complete cable is 64 km long and has 17 major sections with surge arresters protecting the terminal major sections. These are the cable sections closest to aerial lines and thus more prone to overvoltage. The layout of a terminal and an intermediate major sections of the Boutre-Trans cable are illustrated in Figure 2.27 and Figure 2.28. The length of all the cable sections are given in Table 2.7. The cross-bonding joints of the terminal major sections are protected by surge arresters.

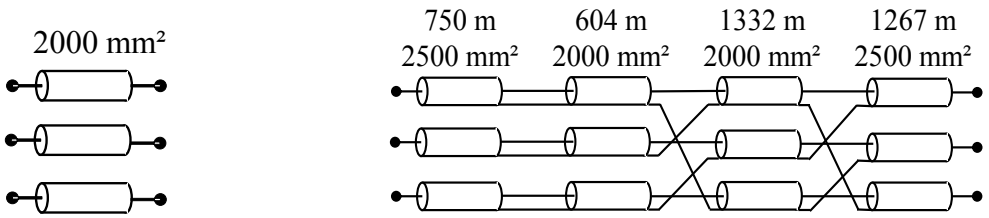

Figure 2.26 Minor and major sections of the RTE 225 kV cable used in the surge field test [20].

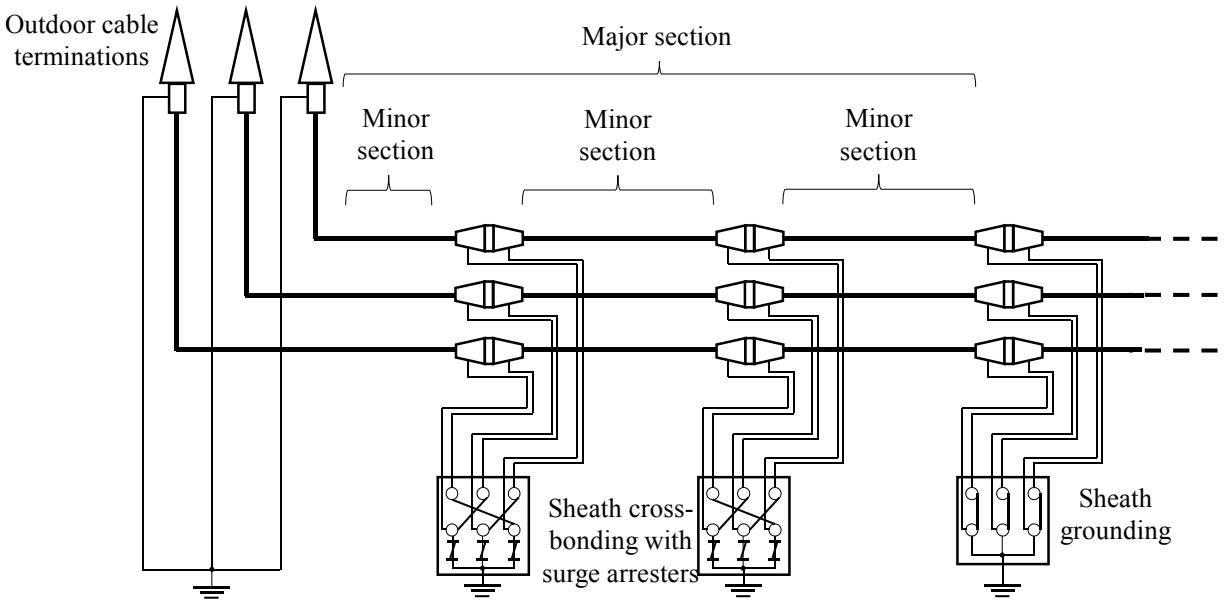

Figure 2.27 Layout of a terminal major section of the RTE 225 kV cable.

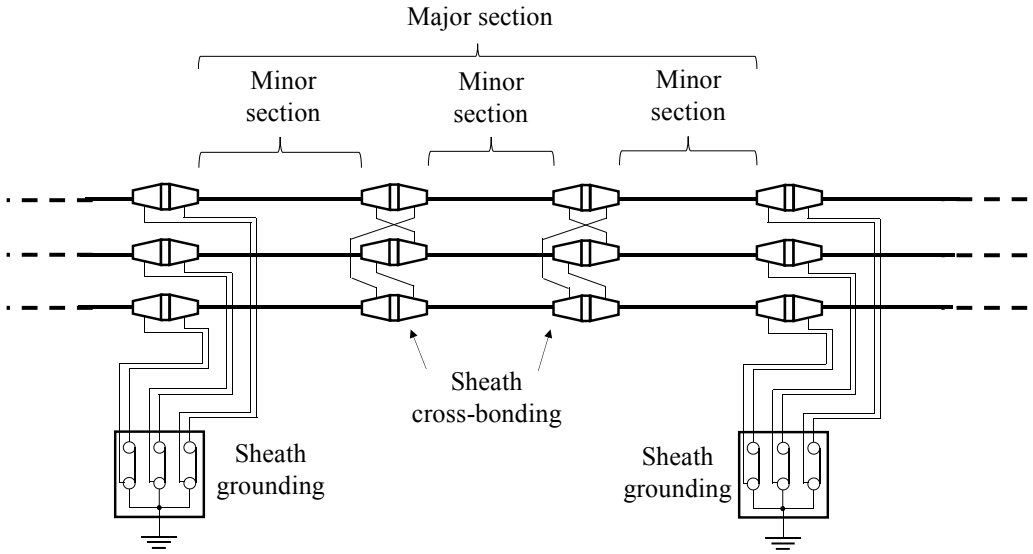

Figure 2.28 Layout of an intermediate major section of the RTE 225 kV cable.

Table 2.7 Length of minor sections in the RTE 225 kV cable.

Major section	Minor section	Section (mm^2)	Length (m)	Major section	Minor section	Section (mm^2)	Length (m)
1 (Boutre)	1	2500	750	11	38	2000	850
	2	2000	604		39	2000	820
	3	2000	1332		40	2000	820
	4	2500	1267		41	2000	860
2	5	2000	1232		42	2500	819
	6	2000	1299		43	2500	810
	7	2000	1300	12	44	2500	970
3	8	2000	820		45	2500	970
	9	2000	917		46	2500	1003
	10	2000	935		47	2500	959
	11	2000	826		48	2000	1039
	12	2000	827		39	2000	912
	13	2000	826	13	50	2000	1275
4	14	2000	1282		51	2000	1275
	15	2000	1300		52	2500	1193
	16	2000	1300	14	53	2500	1300
5	17	2000	820		54	2500	1200
	18	2000	820		55	2500	676
	19	2000	820		56	2500	650
	20	2000	820	15	57	2500	1200
	21	2000	820		58	2500	1193
	22	2000	820		59	2500	600
6	23	2000	820		60	2500	630
	24	2000	771	16	61	2500	585
	25	2000	770		62	2500	610
7	26	2000	1093		63	2500	600
	27	2000	985		64	2500	600
	28	2000	985		65	2500	594
8	29	2000	1056		66	2500	612
	30	2000	1060	17 (Trans)	67	2000	820
	31	2000	1070		68	2000	820
9	32	2000	1040		69	2500	830
	33	2000	1045				
	34	2000	1080				
10	35	2000	992				
	36	2500	930				
	37	2500	930				

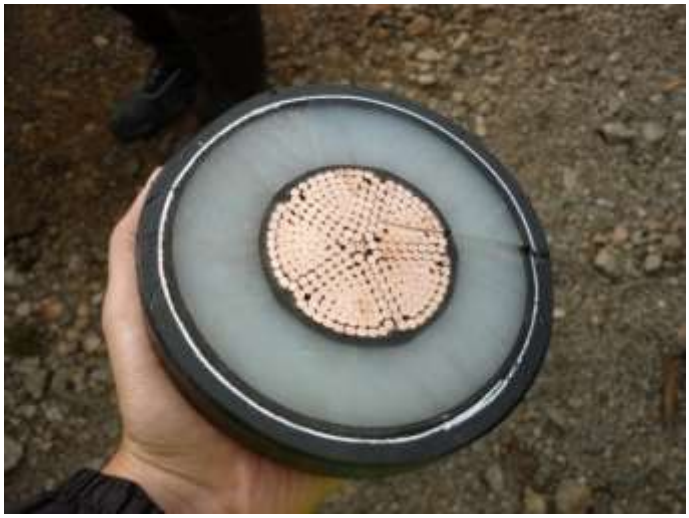

Figure 2.29 Sample of the RTE 225 kV cable with 2000 mm² enamelled copper cores.

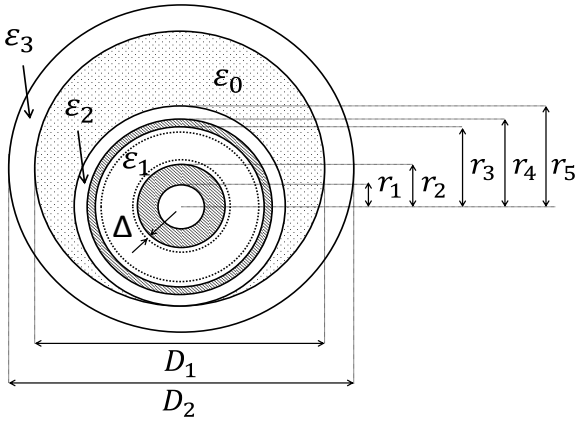

Figure 2.30 Layout of one phase of the RTE 225 kV cable [20].

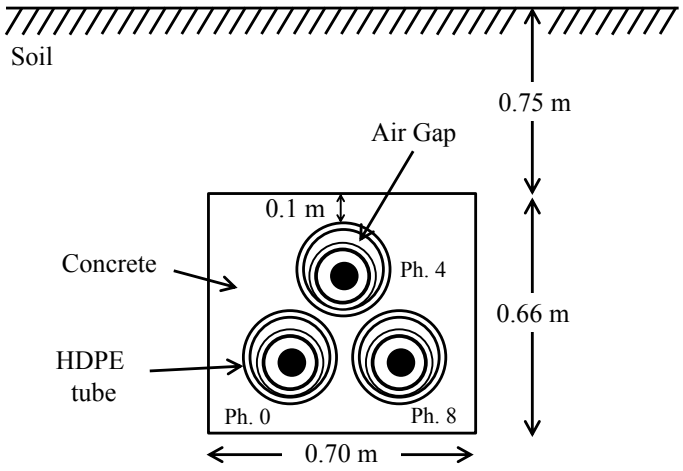

Figure 2.31 Layout of the three phases of the RTE 225 kV cable buried on earth [20].

Table 2.8. Data for RTE 225 kV cable [20].

Parameter	2000 mm^2 cable	2500 mm^2 cable
Core conductor ($r_1 = 0$.)	$r_{2n} = 34.5$ mm* $r_2 = 28.4$ mm** $\rho = 1.76\times10^{-8}$ Ωm	$r_{2n} = 37.1$ mm* $r_2 = 31.9$ mm** $\rho = 1.76\times10^{-8}$ Ωm
Semiconductor screen 1	$\Delta = 3$ mm (thickness)	
Core insulation	$\varepsilon_{r1} = 2.5$, $\tan\delta = 0.0008$	
Semiconductor screen 2	$\Delta = 3$ mm (thickness)	
Metallic sheath	$r_3 = 56.4$ mm $r_4 = 57.2$ mm $\rho = 2.84\times10^{-8}$ Ωm	$r_3 = 59.9$ mm $r_4 = 60.7$ mm $\rho = 2.84\times10^{-8}$ Ωm
Outer insulation	$r_5 = 62.2$ mm $\varepsilon_{r2} = 2.5$ $\tan\delta = 0.001$	$r_5 = 65.7$ mm $\varepsilon_{r2} = 2.5$ $\tan\delta = 0.001$
HDPE tubes	$D_1 = 198.5$ mm, $D_2 = 225$ mm $\varepsilon_{r3} = 2.5$, $\tan\delta = 0.001$	

* Nominal radius of core conductor.

** Corrected core radius accounting for effective section of wires in the strand (appendix A.4.1).

The surge applied to the cable is a 2 kV 1.2/50 μs impulse. The impulse generator (IG) used in the field test was a Haefely Axos 5 with an output impedance of 2 Ω. Waveforms were measured on a WaveJet 324A oscilloscope using PHV1000 voltage probes and Pearson 110 current probes with bandwidths of 400 MHz and 20 MHz respectively. IG and oscilloscope are shown in Figure 2.32 and the probes are shown in Figure 2.33.

The sites where the field test was performed are shown in Figure 2.34 and Figure 2.35 for the minor and major sections, respectively. Grounding rods had to be installed next to the two terminals of the minor section and the receiving end of the major section, for protection of equipment and operators. The major section sending end is located in a substation where a grounding network is available. The DC values of grounding impedance are 30 Ω (measured) for the remote areas and 5 Ω (provided by RTE) for the substation [20].

Figure 2.32 Haefely Axos 5 impulse generator and WaveJet 324A oscilloscope.

Figure 2.33 PHV1000 voltage probe and Pearson 110 current probe.

Figure 2.34 Sending and receiving end sites for surge field test of a minor section of the RTE 225 kV cable.

Figure 2.35 Sending and receiving end sites for surge field test of a major section of the RTE 225 kV cable.

3.1.1 Testing on a minor section

3.1.1.1 Core-to-ground application

The circuits in Figure 2.36 were used in the field test to apply an impulse to the core of a minor section and measure the sheath voltage of the same phase. The two circuits are for the case of all sheaths open-circuited and for the case of sheaths grounded, except the measured sheath.

The sheath voltages for the two cases are shown in Figure 2.37. Given the high attenuation of the waveforms in the figure, it is clear that the mode observed is an earth-return mode. However, there is also a contribution of a coaxial mode which can be observed from the period of the peaks in the voltage waveforms in Figure 2.37. Using the cable length and the time between the second and third peaks (12.6 μs), the propagation velocity is calculated as $2\times1080/12.6=171\,\mathrm{m/\mu s}$ which is close to the coaxial mode velocity calculated from the light velocity $c_0=300\,\mathrm{m/\mu s}$ and the cable insulation permittivity $\varepsilon_r=3.23$ (Table 2.8) as $c=c_0/\sqrt{\varepsilon_r}=300/\sqrt{3.23}=167\,\mathrm{m/\mu s}$.

In Figure 2.37, the voltage corresponding to the sheaths being grounded is lower and becomes negative after a certain point as a result of negative reflections transmitted from grounded terminals.

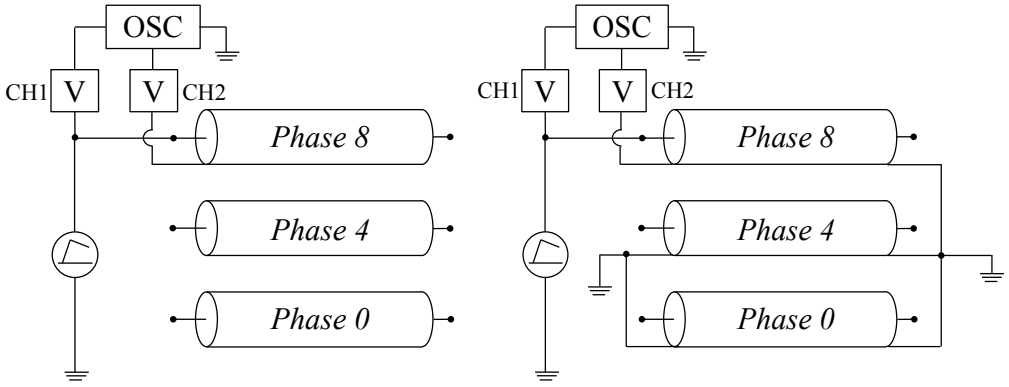

Figure 2.36 Field test circuits for core-to-ground application on a minor section: a) sheaths open; b) sheaths grounded.

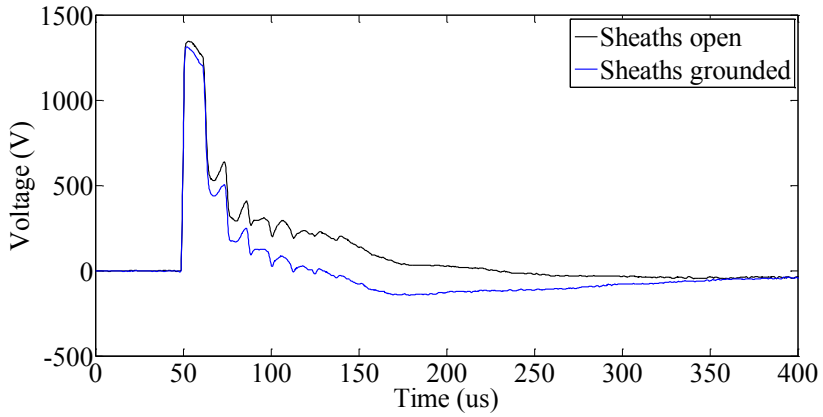

Figure 2.37 Sending end sheath voltage for core-to-ground surge application on a minor section. [5]

3.1.1.2 Core-to-sheath application

Figure 2.38 illustrates the circuit used in the field test to apply a surge between the core and sheath of a phase in a minor section. The three sheaths and the two non-used cores were grounded together with the surge tester.

The core voltage and current at the sending end and the core voltage at the receiving end were measured and are shown in Figure 2.39 to Figure 2.41, respectively. If the initial peak values of voltage and current are used to calculate the surge impedance, the following value is obtained $Z_s = 1752/68.74 = 25\,\Omega$ which agrees with the formula for coaxial mode surge impedance

[5] Data files: CableSimulation_Files\FieldTestSimulation_RTECable\Data_FieldTest\Minor section

$$Z_s = \frac{1}{2\pi}\sqrt{\frac{\mu_0}{\varepsilon_0\varepsilon_r}}\log\left(\frac{r_3}{r_2}\right) = \frac{60}{\sqrt{3.23}}\log\left(\frac{56.4}{28.4}\right) = 22.9\,\Omega \tag{3.1}$$

Where $(2\pi)^{-1}\sqrt{\mu_0/\varepsilon_0} = 60\ \Omega$, $\varepsilon_r = 3.23$, $r_2 = 28.4\,\text{mm}$ and $r_3 = 56.4\,\text{mm}$ are cable parameters given in Table 2.8.

An oscillation period of 27.4 μs can be clearly observed form Figure 2.39 to Figure 2.41. Using the cable length, the propagation velocity is calculated as

$$c = \frac{c_0}{\sqrt{\varepsilon_r}} = \frac{300}{\sqrt{3.23}} = 158\,\text{m/μs} \tag{3.2}$$

where $c_0 = 300\,\text{m/μs}$. This velocity corresponds to a coaxial mode of propagation.

The sending end voltage does not follow exactly the surge tester. The spikes observed are caused by the inductance of the wire connecting to the tester and the fast variation of current.

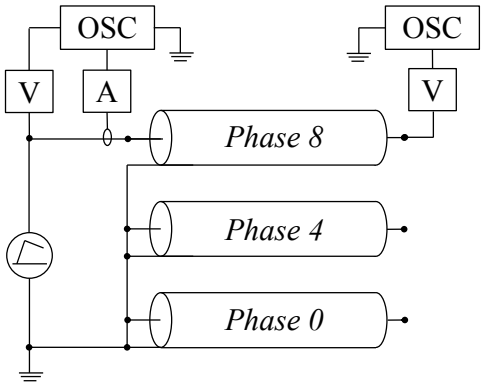

Figure 2.38 Surge test circuit for core-to-sheath application on a minor section [20].

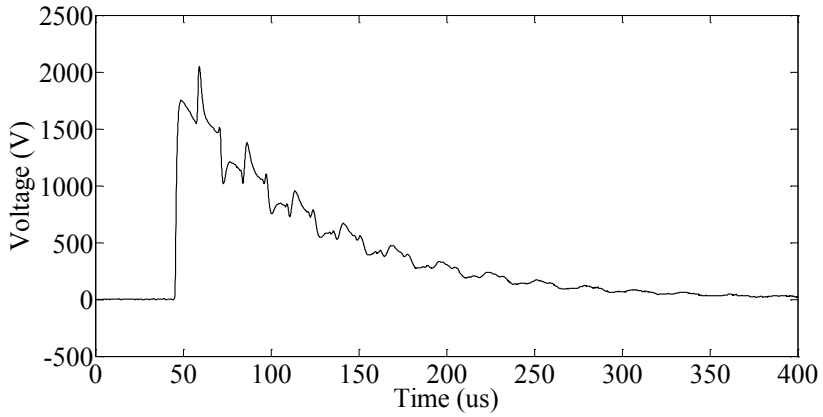

Figure 2.39 Sending end core voltage for core-to-sheath surge application on a minor section.[5]

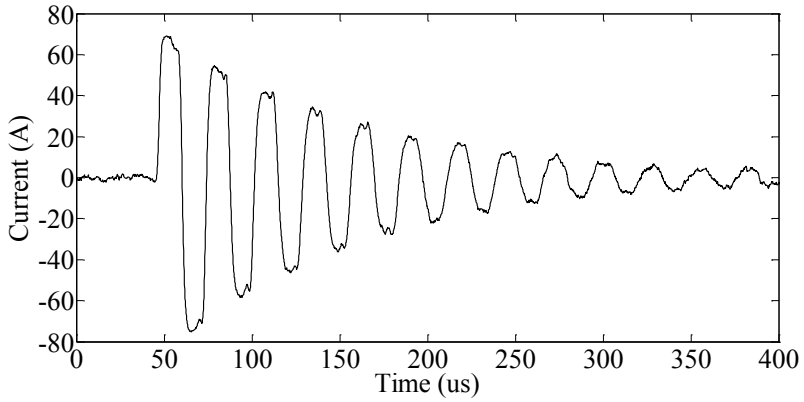

Figure 2.40 Sending end core current for core-to-sheath surge application on a minor section.[5]

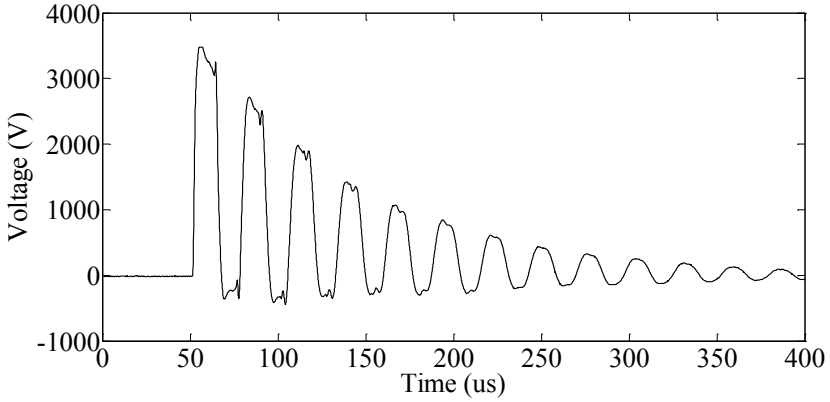

Figure 2.41 Receiving end core voltage for core-to-sheath surge application on a minor section.[5]

3.1.1.3 Two-phase inter-sheath application

The circuit in Figure 2.42 was used in the field tests to apply a surge between two sheaths of a minor section. The surge tester current and the sheath voltages at the sending and receiving ends are shown in Figure 2.43 to Figure 2.45. The receiving end voltage for phase-8 in Figure 2.45 is approximately double of that at the sending end in Figure 2.44, as expected.

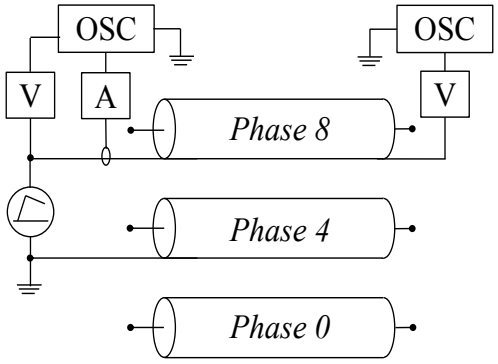

Figure 2.42 Surge test circuit for two-phase inter-sheath application on a minor section.[5]

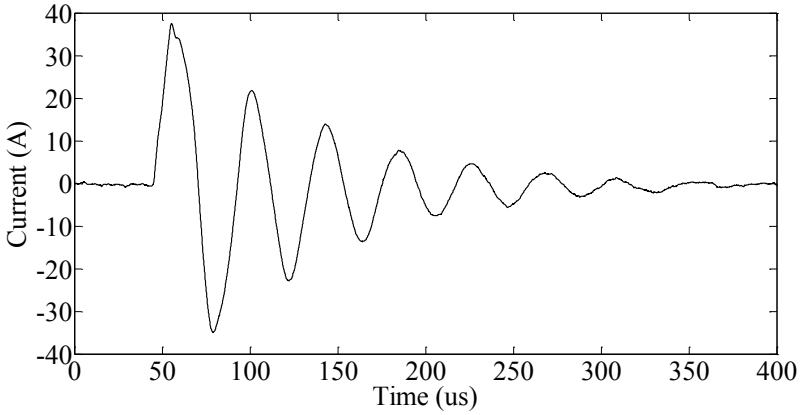

Figure 2.43 Sending end current for 2-phase inter-sheath surge application on a minor section.[5]

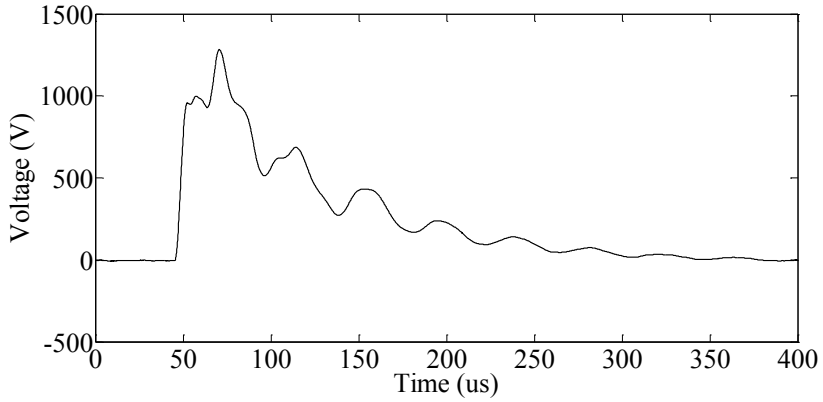

Figure 2.44 Sending end voltage for 2-phase inter-sheath surge application on a minor section.[5]

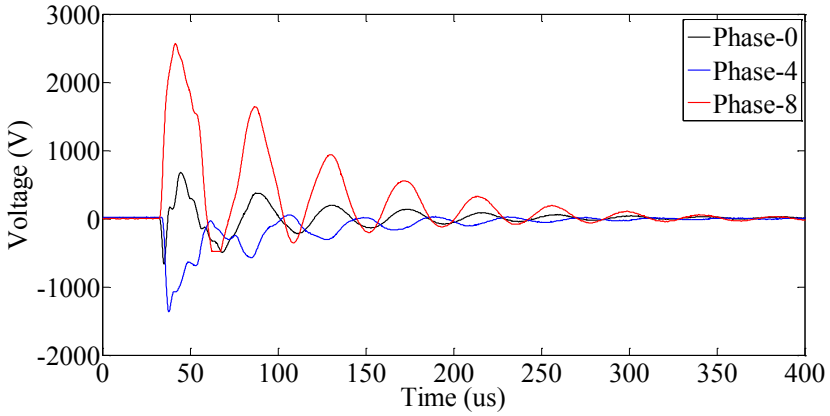

Figure 2.45 Receiving end voltages for 2-phase inter-sheath surge application on a minor section.[5]

3.1.1.4 Three-phase inter-sheath application

The circuit in Figure 2.46 was used in the field test apply a surge between the three sheaths of a minor section. The waveforms measured at sending and receiving ends are shown in Figure 2.47 to Figure 2.49.

The period of oscillations of the current and voltage waveforms is approximately 38 μs. Using the cable length, the propagation velocity is calculated as $c = 4 \times 1080/38 = 114\,\text{m}/\mu\text{s}$. The surge impedance is calculated from the initial peaks of voltage and current in Figure 2.47 and Figure 2.48 as $Z_c = 1221/49.01 = 24.91\ \Omega$.

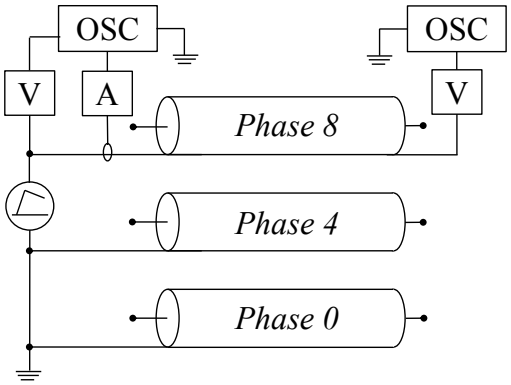

Figure 2.46 Surge test circuit for three-phase inter-sheath application on a minor section [20].

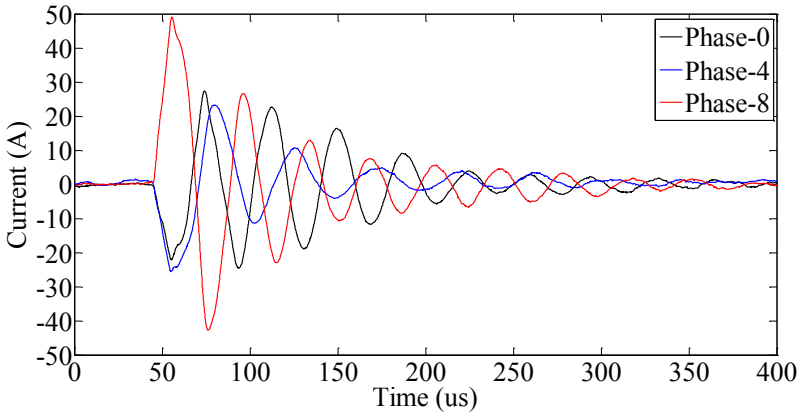

Figure 2.47 Sending end current for 3-phase inter-sheath surge application on a minor section.[5]

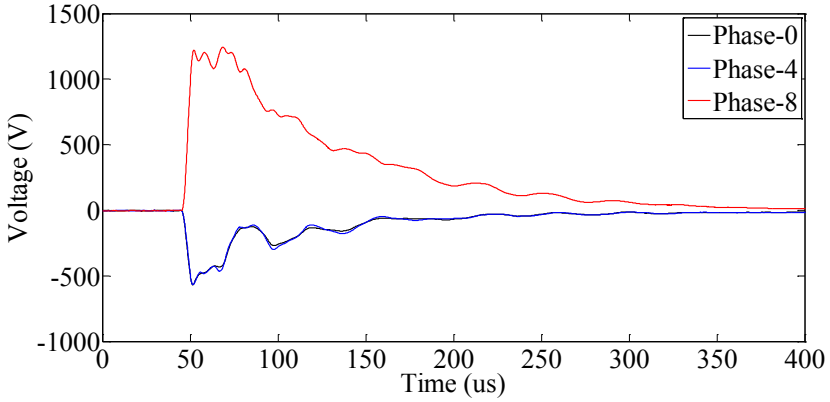

Figure 2.48 Sending end voltages for 3-phase inter-sheath surge application on a minor section.[5]

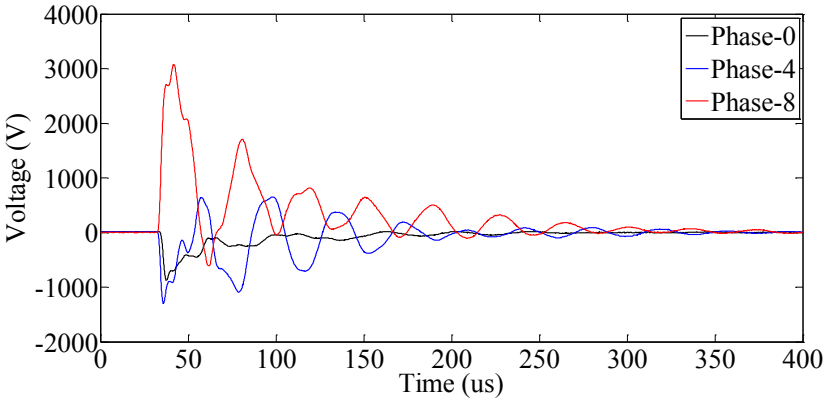

Figure 2.49 Receiving end voltages for 3-phase inter-sheath surge application on a minor section.[5]

3.1.1.5 Sheath-to-ground application

The circuit in Figure 2.50 was used in the field test to apply a surge between the sheaths of a minor section and the ground, with the receiving end sheaths grounded. The measured surge tester current is given in Figure 2.51 which shows clearly a high attenuation mostly due to the high impedance of the return path.

The earth-return mode of propagation was further investigated in the field test using the circuits of Figure 2.52, in which a surge is applied between the ground and one, two and three sheaths respectively, with the sheaths in the receiving end open-circuited. The sheath voltages measured at the receiving end of the minor section are shown in Figure 2.53 to Figure 2.55, respectively. The maximum voltage in phase-8 is 1149 V, 750 V and 623 V for surge applied between one sheath and the earth, two sheaths and the earth, and finally three sheaths and the earth, respectively.

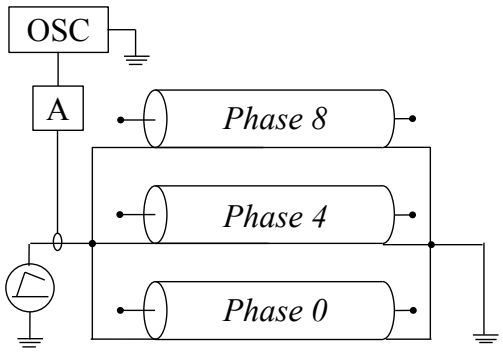

Figure 2.50 Surge test circuit for zero-sequence sheath application on a minor section with receiving end grounded [20].

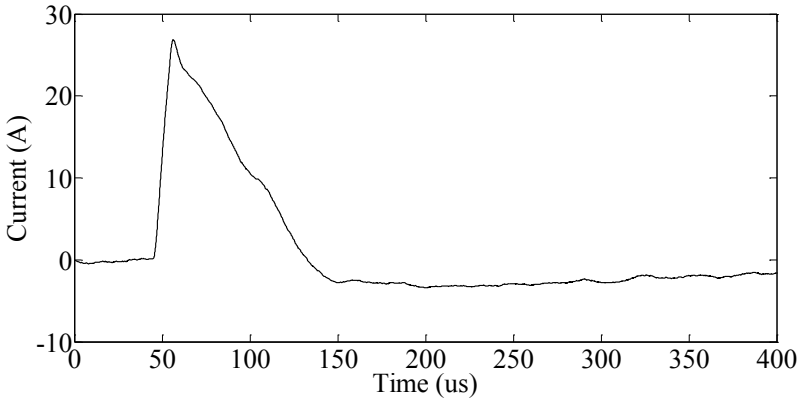

Figure 2.51 Sending end current for zero-sequence surge application on the sheaths of a minor section with the receiving end grounded.[5]

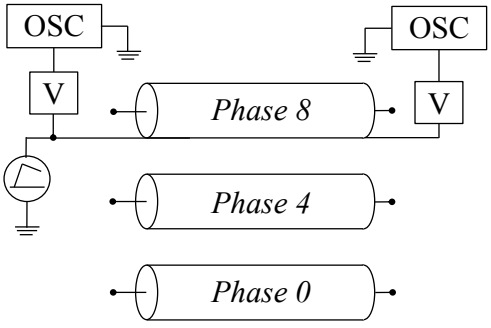

a) single-phase application.

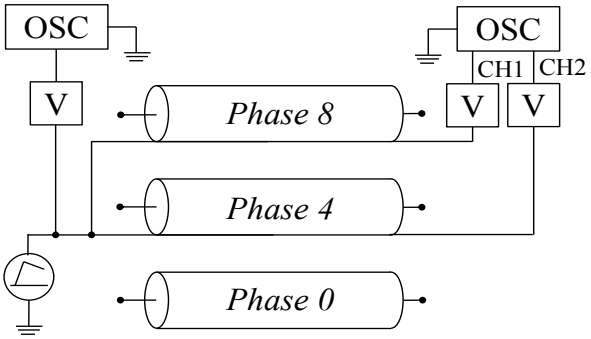

b) two-phase application.

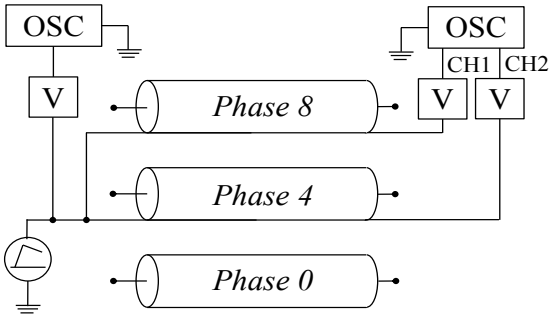

c) three-phase application.

Figure 2.52 Surge test circuit for zero-sequence sheath application on a minor section with receiving end open.

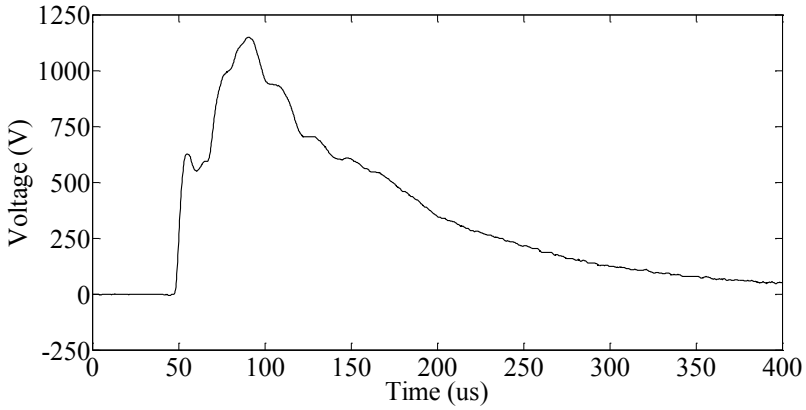

Figure 2.53 Receiving end voltages for surge application on one sheath of a minor section with the receiving end in open-circuit.[5]

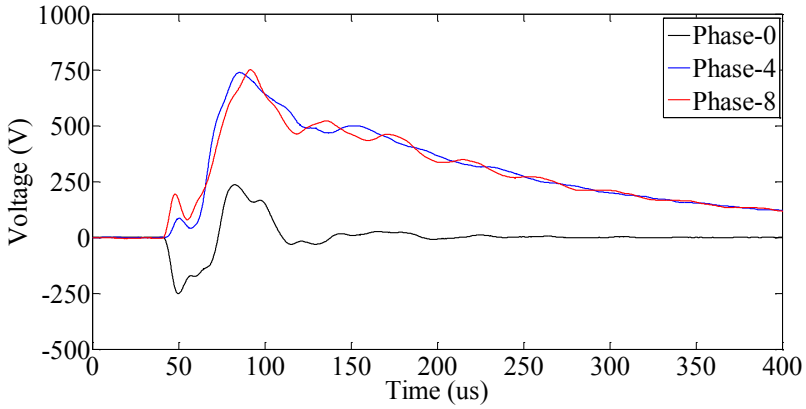

Figure 2.54 Receiving end voltages for surge application on two sheaths of a minor section with the receiving end in open-circuit.[5]

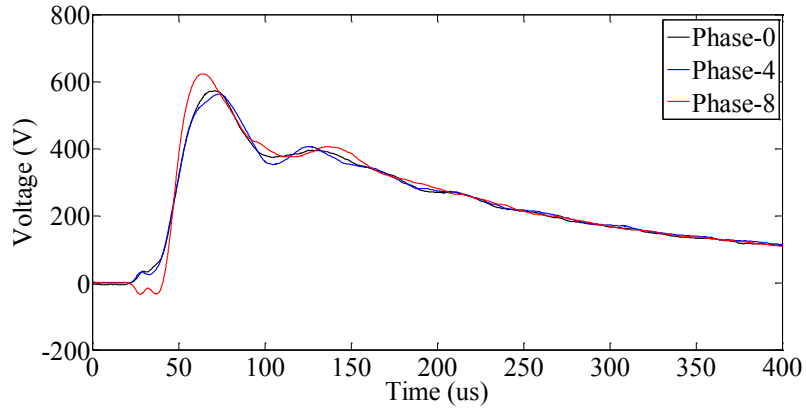

Figure 2.55 Receiving end voltages for surge application on three sheaths of a minor section with the receiving end in open-circuit.[5]

3.1.2 Testing on a major section

3.1.2.1 Core-to-sheath application

Figure 2.56 shows the circuit used in the field test to apply a surge between core and sheath of one phase of the major section. The three sheaths and the unused cores are grounded together with the surge tester. The test was repeated for the three phases.

Figure 2.57 and Figure 2.58 show the current and voltage measured on the energised core for the three surge applications. All phases have nearly the same response. The measured oscillations have a period of 100 μs. Using the cable length, the velocity is calculated as

$c = 4 \times 3953/100 = 158\,\mathrm{m/\mu s}$.

The surge impedance is calculated using the initial peaks of voltage and current in each phase $Z_{sa} = 1699/75.43 = 22.52\,\Omega$, $Z_{sb} = 1697/73.16 = 23.20\,\Omega$ and $Z_{sc} = 1688/72.75 = 23.20\,\Omega$. The average of the three values is $22.9\,\Omega$.

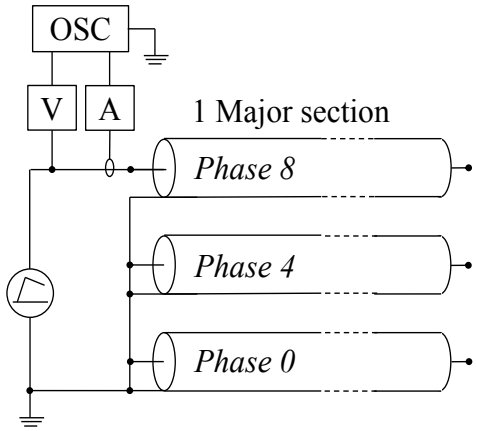

Figure 2.56 Surge test circuit for core-to-sheath application on a major section [20].

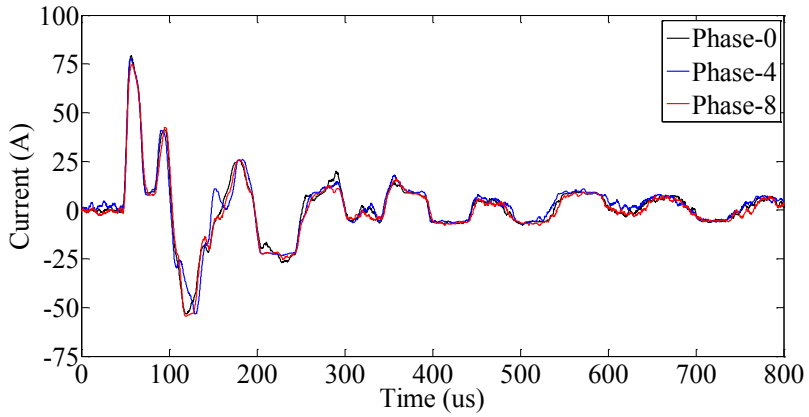

Figure 2.57 Sending end current for core-to-sheath surge application on a major section.[6]

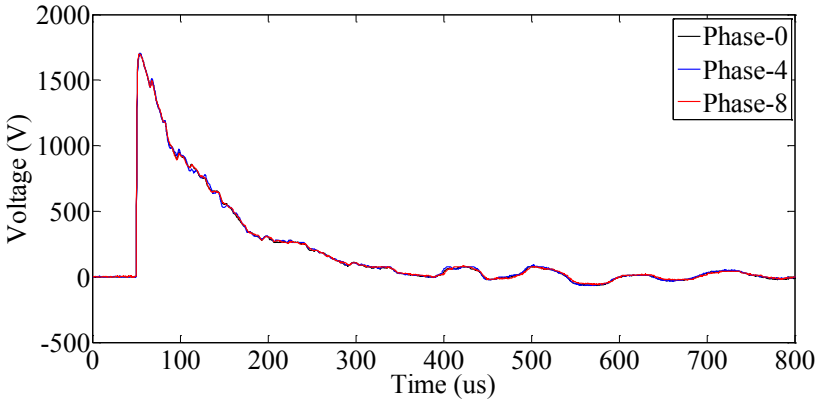

Figure 2.58 Sending end voltage for core-to-sheath surge application on a major section.[6]

3.1.2.2 Two-phase inter-sheath application

The circuit in Figure 2.59 was used in the field test to apply a surge between two sheaths of a major section, with the sheaths at the receiving end bonded together. The test was repeated for surge applied between phase-8 and phase-4, phase-0 and phase-4, and between phase-8 and phase-0. The current measured at the surge tester and the sending end sheath and core voltages are shown in Figure 2.60 to Figure 2.68 for the three surge applications. The propagation velocity calculated from the oscillating period in Figure 2.61 and the cable length is $c = 4 \times 3953/120 = 132\,\mathrm{m/\mu s}$.

[6] Data files: CableSimulation_Files\FieldTestSimulation_RTECable\Data_FieldTest\Major section

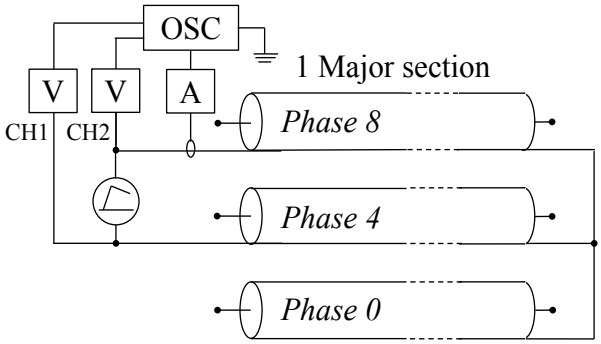

Figure 2.59 Surge test circuit for two-phase inter-sheath application on a major section.

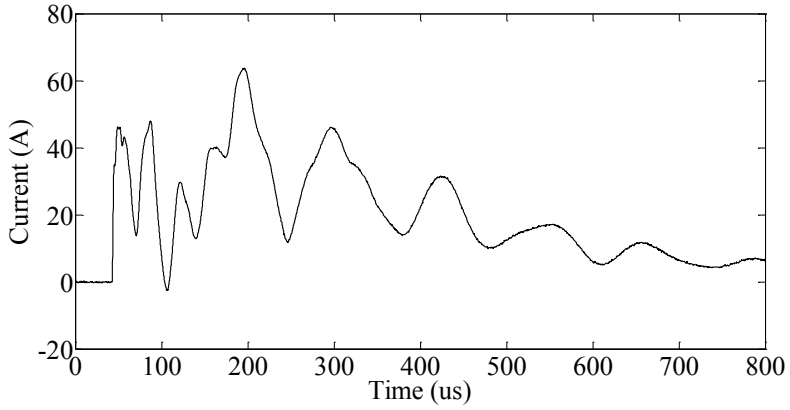

Figure 2.60 Sending end current for surge application between phase-8 and phase-4 sheaths of a major section.[6]

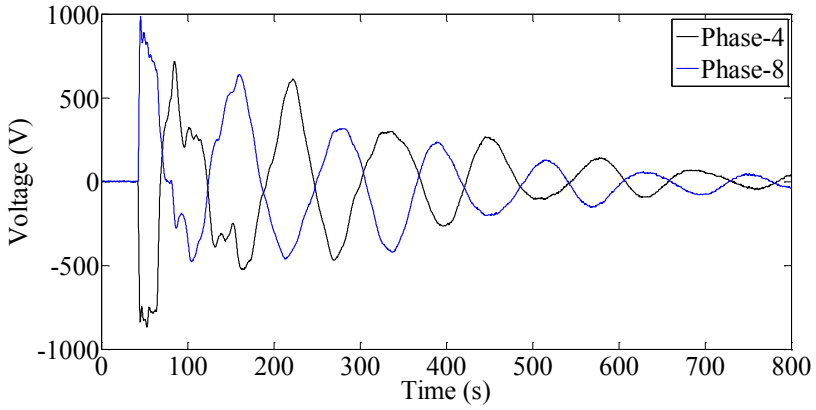

Figure 2.61 Sending end core voltages for surge application between phase-8 and phase-4 sheaths of a major section.[6]

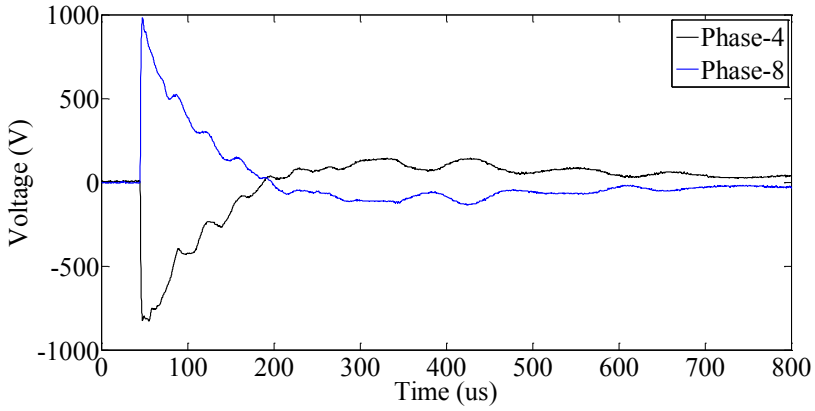

Figure 2.62 Sending end sheath voltages for surge application between phase-8 and phase-4 sheaths of a major section.[6]

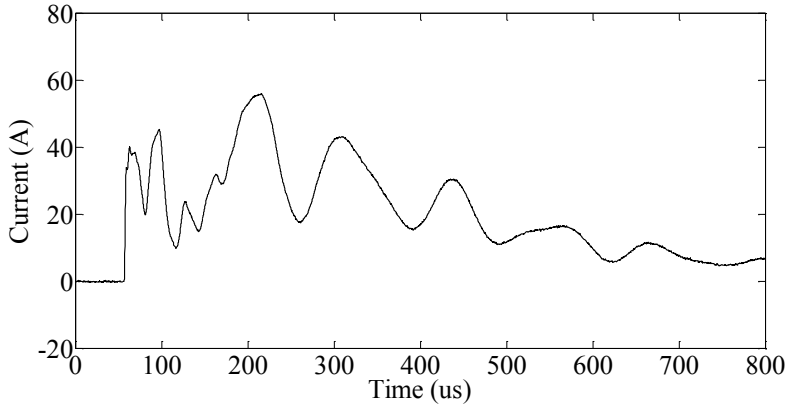

Figure 2.63 Sending end current for surge application between phase-0 and phase-4 sheaths of a major section.[6]

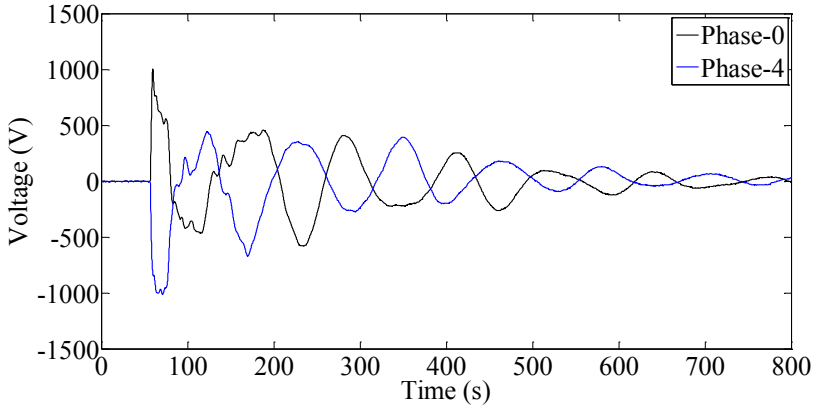

Figure 2.64 Sending end core voltages for surge application between phase-0 and phase-4 sheaths of a major section.[6]

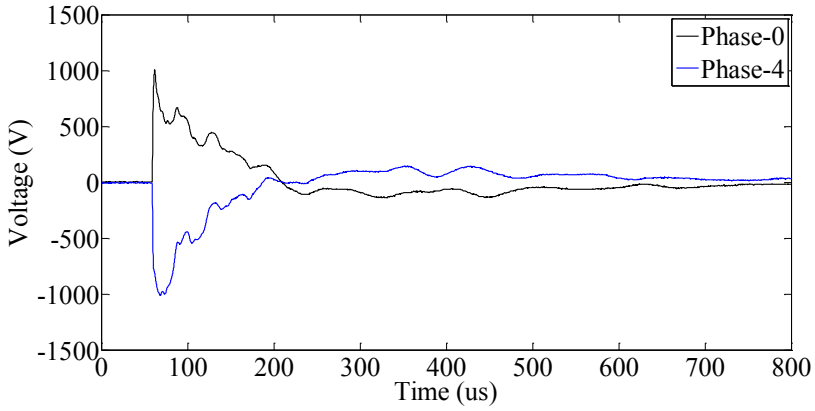

Figure 2.65 Sending end sheath voltages for surge application between phase-0 and phase-4 sheaths of a major section.[6]

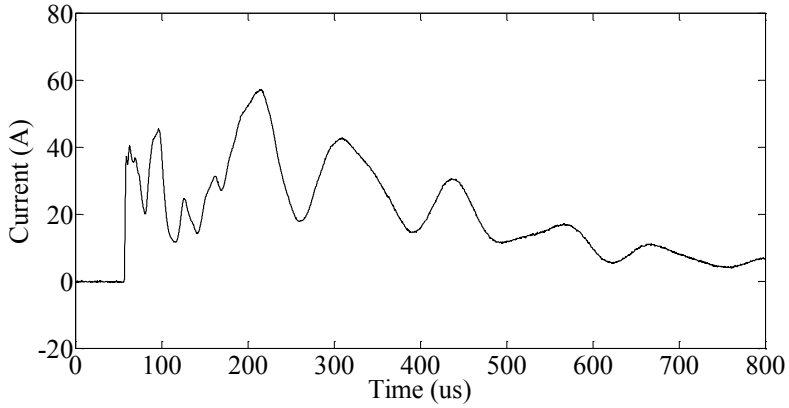

Figure 2.66 Sending end current for surge application between phase-8 and phase-0 sheaths of a major section.[6]

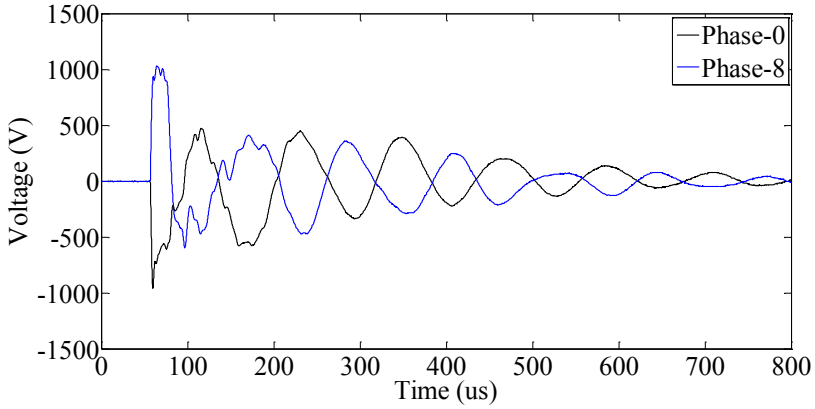

Figure 2.67 Sending end core voltages for surge application between phase-8 and phase-0 sheaths of a major section.[6]

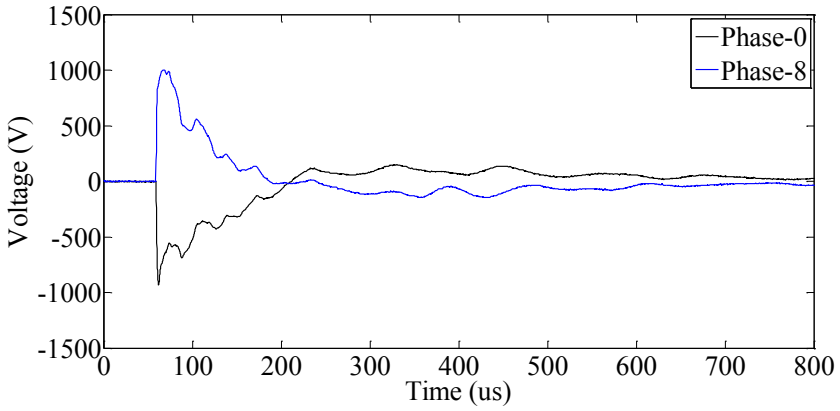

Figure 2.68 Sending end sheath voltages for surge application between phase-8 and phase-0 sheaths of a major section.[6]

3.1.2.3 Three-phase inter-sheath application

The circuit in Figure 2.69 was used in the field test to apply a surge between the sheaths of a major section, with the sheaths at the receiving end bonded together. The surge tester current and the sending end core and sheath voltages are shown in Figure 2.70 to Figure 2.72. These results are similar to the case of surge applied between two sheaths, presented in the previous section.

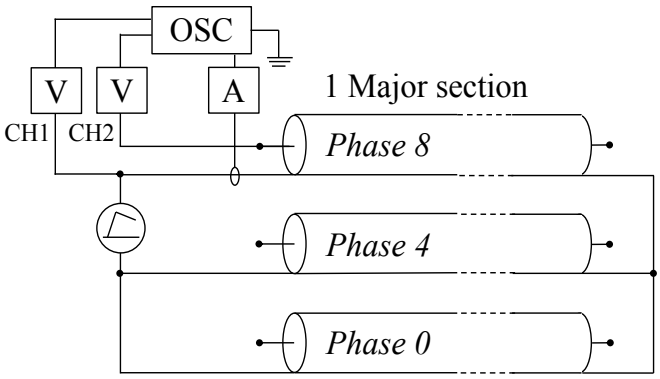

Figure 2.69 Surge test circuit for three-phase inter-sheath application on a major section.

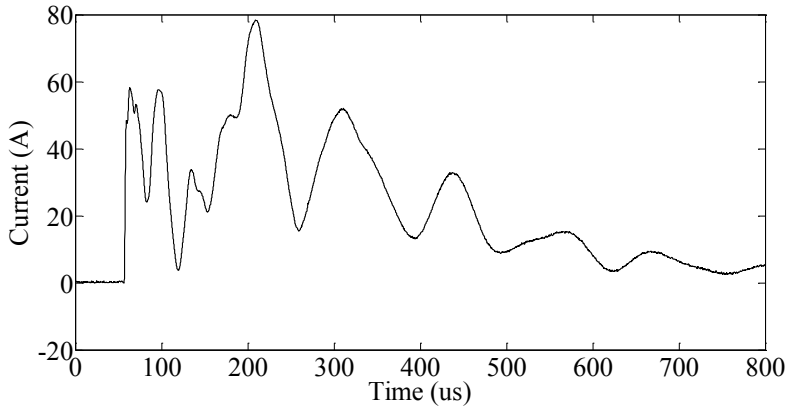

Figure 2.70 Sending end current for surge application between the three sheaths of a major section.[6]

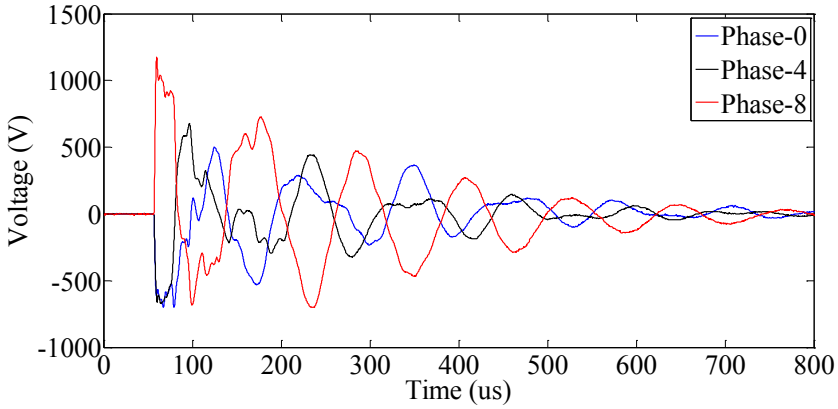

Figure 2.71 Sending end core voltages for surge application between the three sheaths of a major section.[6]

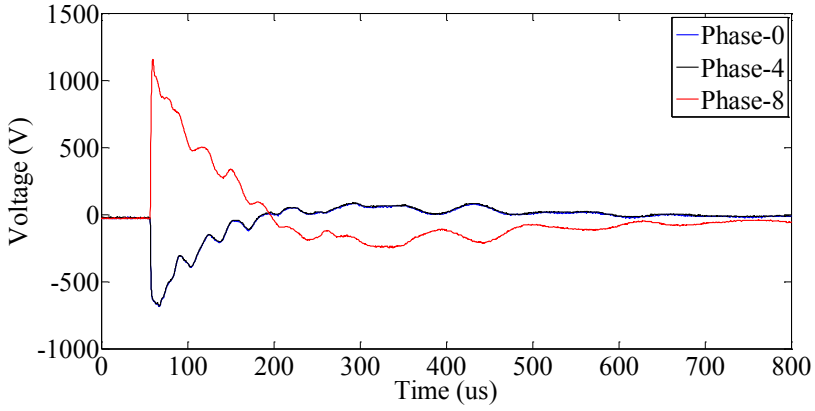

Figure 2.72 Sending end sheath voltages for surge application between the three sheaths of a major section.[6]

3.1.2.4 Sheath-to-ground application

The three circuits in Figure 2.73 were used in the field test to measure the response of a major section to a surge applied between the three sheaths and the ground. The test was repeated with the sheaths at the receiving end open-circuited, bonded, and grounded, respectively. The current of the surge tester and the sheath voltage at the sending end are shown in Figure 2.74 and Figure 2.75.

The cases of open-ended sheaths and short-circuited sheaths have very similar results, with a positive voltage wave reflection arriving around the 225 μs. Using this value and the cable length, the propagation velocity is calculated as $c = 2 \times 3953/225 = 35\,\mathrm{m/\mu s}$. This positive voltage reflection is accompanied by a negative current reflection, as observed in Figure 2.75.

This reflections transmitted from the receiving end is not observed in the cases of sheath grounded at the receiving end because the attenuation is higher in this case.

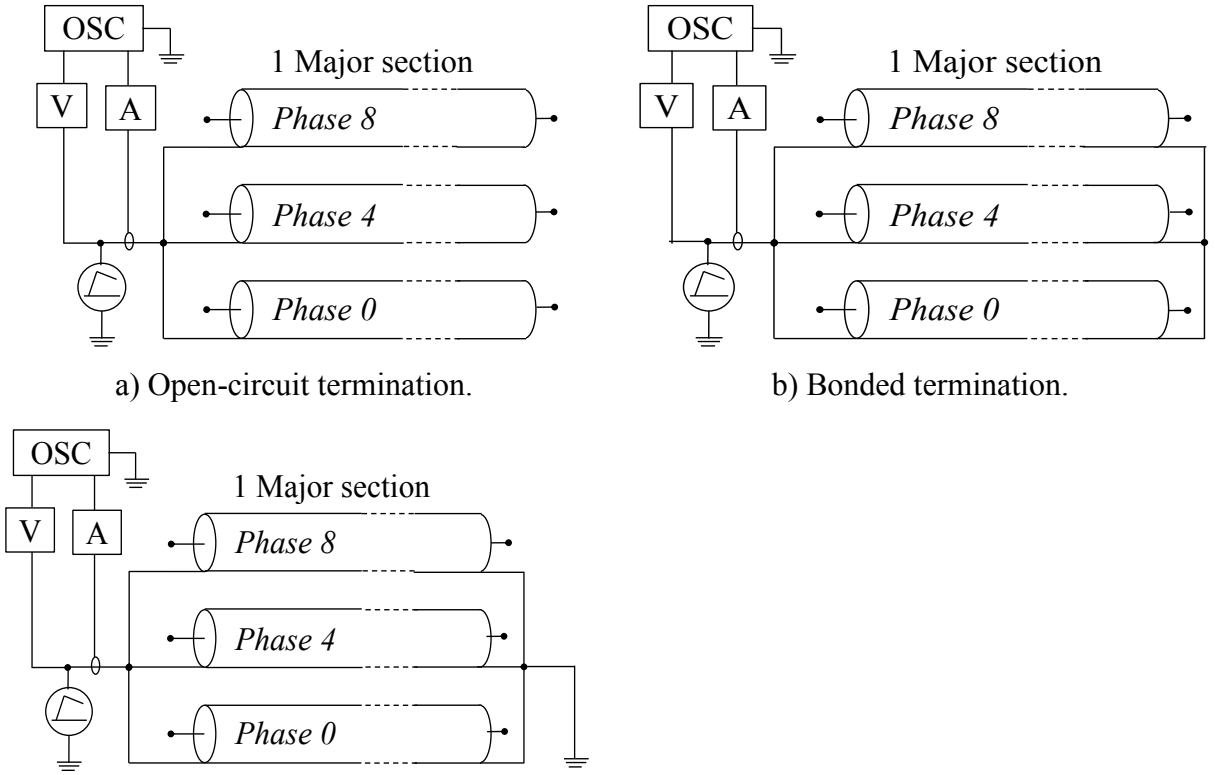

a) Open-circuit termination.

b) Bonded termination.

c) Grounded termination.

Figure 2.73 Surge test circuit for zero-sequence sheath application on a major section.

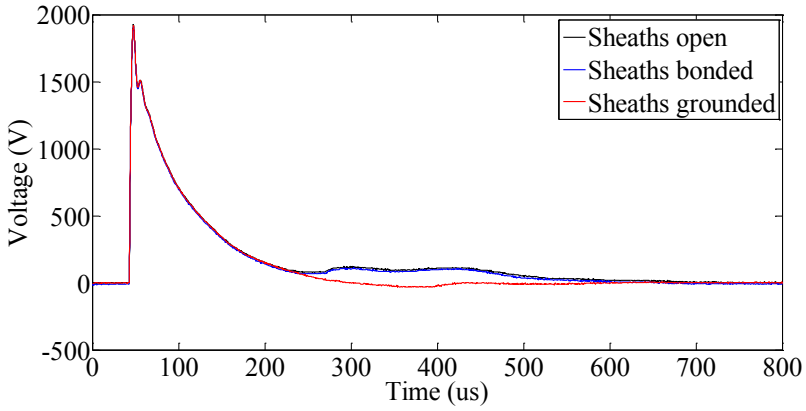

Figure 2.74 Sending end sheath voltages for zero-sequence surge application to the sheaths of a major section for different sheath terminations.[6]

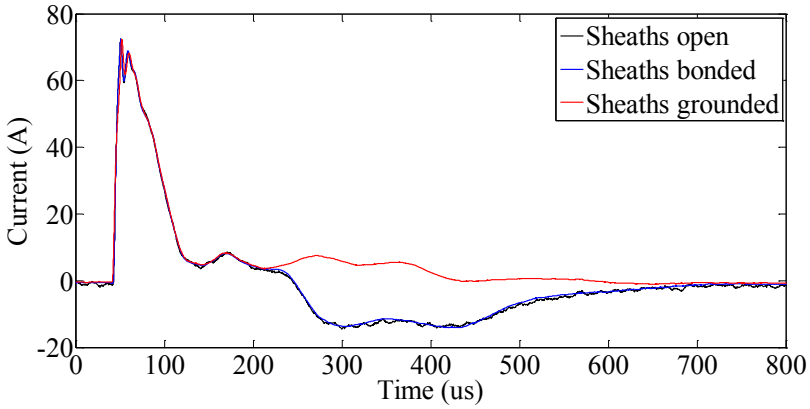

Figure 2.75 Sending end currents for zero-sequence surge application to the sheaths of a major section for different sheath terminations.[6]

3.2 Energising test on RTE 225 kV cross-bonded cable

A test for energising the full RTE 225 kV cable was carried out before the cable was put in service. The sending end is in the substation of Boutre with a short-circuit capacity of 7740 MVA and the receiving end is in the substation of Trans (Trans-en-Province) with a capacity of 4194 MVA. Both substations have X/R ≈ 7. A shunt compensator of 80 Mvar and 175 kW is located at the Trans substation terminal. In the test, the cable was first energised from the substation of Boutre, with the far end open-circuited. The cable was then energised from the substation of Trans. The closing times are t = 4.5 ms, t = 6 ms and t = 6 ms for phase-a, phase-b and phase-c, respectively. Only the compensation at Trans is connected during the field test. This is illustrated in Figure 2.76.

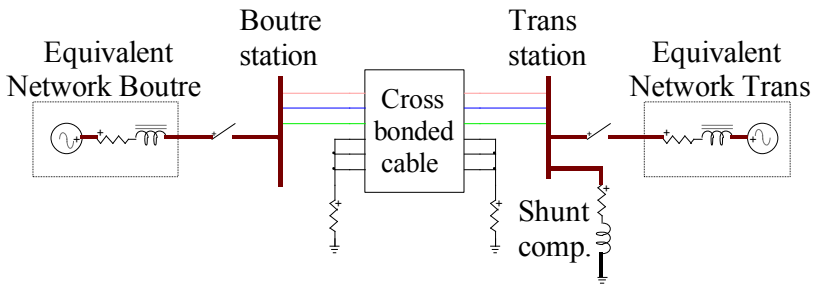

Figure 2.76 Field test circuit for energising the RTE 225 kV cable [51].

3.2.1 Energising from Boutre substation

Figure 2.77 shows the first second of the current and voltage measurements when the cable was energised at the Boutre substation. Figure 2.78 and Figure 2.79 show the initial transients in greater detail. The current initially drawn by the cable is very high. Phase-8 has an initial peak of 3533 A which damps out to 776 A after about 5 cycles (100 ms). The maximum currents in the other phases were 3210 A in phase-0 and 3151 A in phase-4. It is also observed that the voltage reaches steady-state much faster than the current, which does not attain steady-state during the measurement.

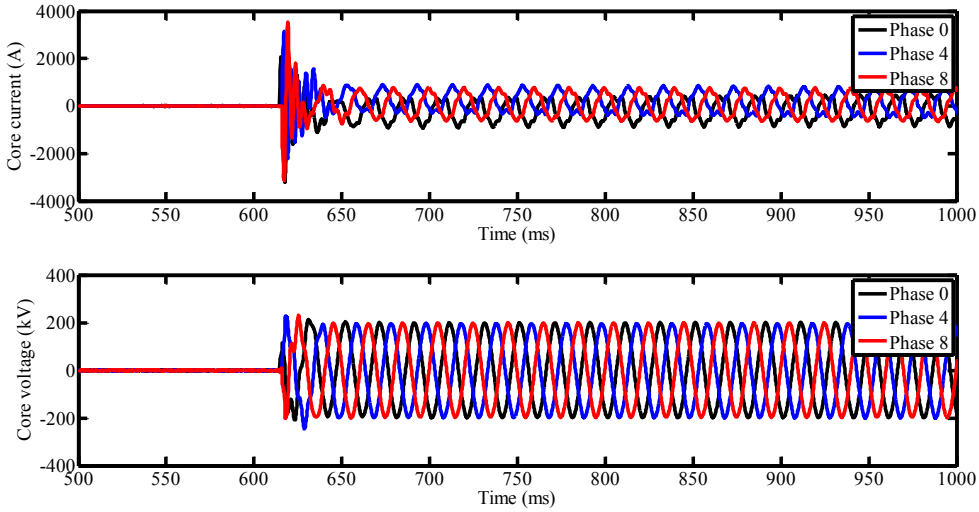

Figure 2.77 Currents and voltages during energising of RTE 225 kV cable from the substation of Boutre.[7]

[7] Plotting: CableSimulation_Files\EnergisingTest_RTECable\Measured_data\Plot.m

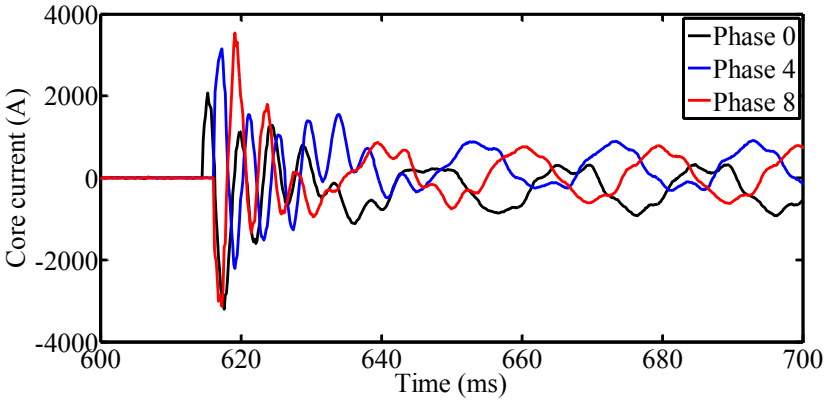

Figure 2.78 Initial transient currents during energising of RTE 225 kV cable from the substation of Boutre.[7]

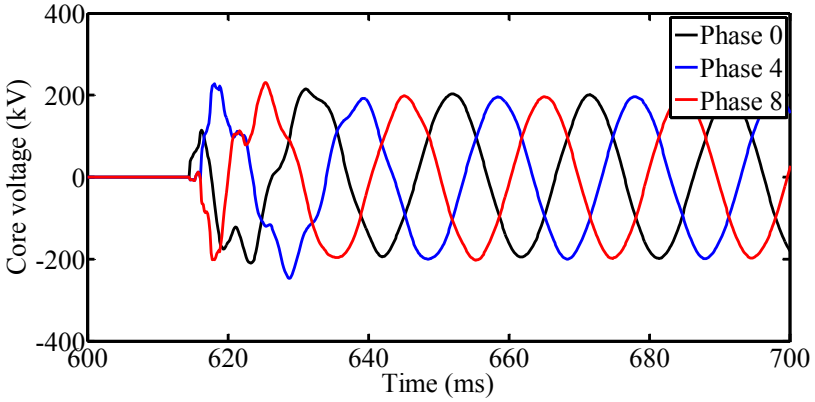

Figure 2.79 Initial transient voltages during energising of RTE 225 kV cable from the substation of Boutre.[7]

3.2.2 Energising from Trans substation

Figure 2.80 shows the currents and voltages measured during the energising of the cable from the Trans substation. The source is applied at t = 648.3 ms for phase-a, t = 646.7 ms for phase-b and t = 648ms for phase-c. More detailed current waveforms are shown in Figure 2.81. The currents have a decaying DC component due to the shunt compensation. Despite this, the phenomenon of zero-missing current is not observed. After energising, the voltages are reduced from 1.09 pu to 1.04 pu which shows that the network absorbed part of the reactive power generated by the cable.

Data: CableSimulation_Files\EnergisingTest_RTECable\Measured_data\Measured.mat

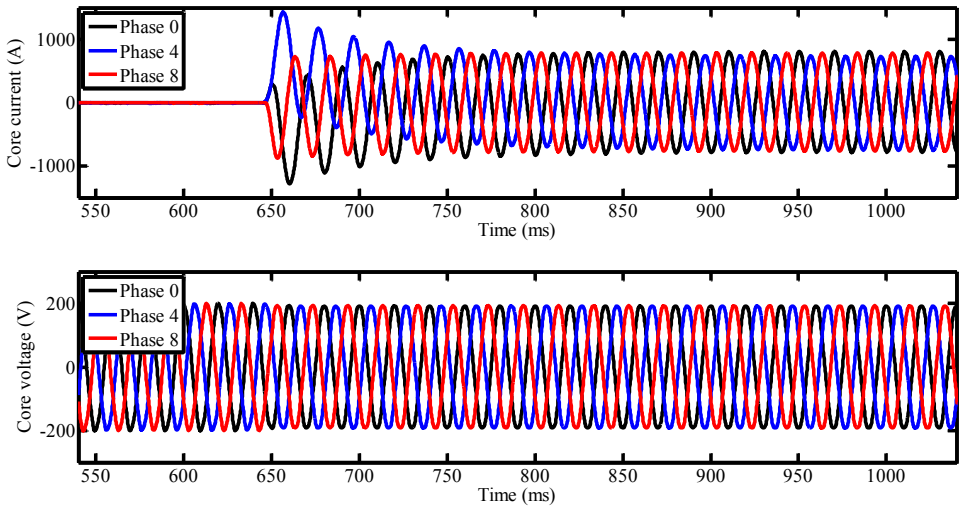

Figure 2.80 Currents and voltages during energising of RTE 225 kV cable from the substation of Trans.[7]

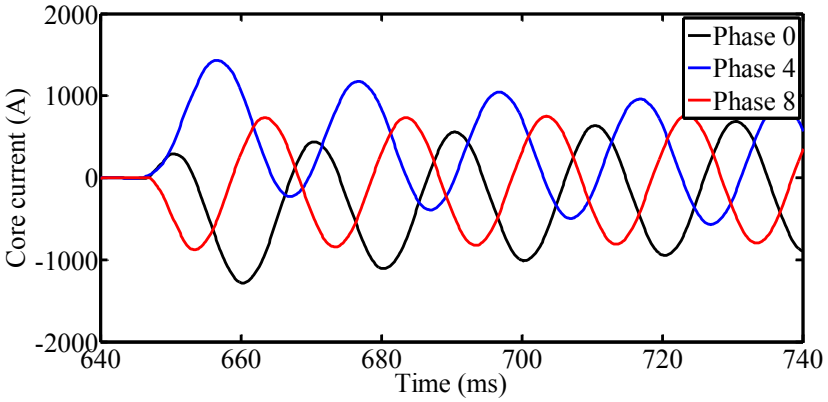

Figure 2.81 Initial transient currents during energising of RTE 225 kV cable from the substation of Trans.[7]

3.3 Discharge test of a 275 kV pipe-type pressurized oil-filled cable in Japan

A field test for commissioning of an underground 275 kV pipe-type pressurized-oil-filled (PT-POF) cable with 20 km length was performed in Japan in 1971. At that time, the 275 kV PT-POF cable installation was a first-time experience. The field test was thus intended to give a basis for the creation of standards for PT-POF cables in Japan. The field test involved a series of measurements: characteristics of oil behavior, DC voltage withstand, surge propagation,

thermal/mechanical behavior of steel pipes, etc. [21]. Cable charging and discharging characteristics were also measured.

3.3.1 Test setup and cable data

Other than the measured results, a significant contribution of [21] is that the leakage currents of components used in the test are given, which are necessary for estimating the corresponding leakage resistances. These parameters allow theoretical calculations and simulation of the charging and discharging processes. Although the cable capacitance is easily calculated from the cross-section geometry and the insulation permittivity, the leakage currents of insulator poles, bushing and cable insulation are not available in general and are very difficult to measure or to estimate theoretically.

The description of the tested cable is given in Table 2.9. According to the test description and theoretical analysis in [21], the cable is charged through a resistance R_0 for 1 hour up to a certain voltage using a DC voltage generator. The cable is then switched off and slowly discharges due to leakage current in its insulation and in the components connected to it. After 88 minutes, a forced discharge leads the cable voltage to zero. The three cores are bonded together and the sheaths are grounded at both terminals. The following values are given in [21]

$I_0 = 3\,\text{mA}$, generator rated current,

$V_{\max} = 414\,\text{kV}$, maximum cable voltage,

$I_{ext} = 0.6\,\text{mA}$, leakage of external components at $V_{\max}$,

$R'_{cable} = 22\,\text{G}\Omega\text{-km}$, cable leakage resistance (inverse of per-unit-length shunt conductance G'_{cable} in S/km),

$R_W = 30\,\text{M}\Omega$, resistor used to force full discharge of the cable,

$V_{\min} = 250\,\text{kV}$, voltage just before the forced discharge.

Table 2.9. Data of 275 kV PT-POF cable in Japan [21],[52]

Core conductor inner radius	0 mm	Core conductor resistivity	$1.728 \cdot 10^{-8}$ Ω-m
Core conductor outer radius	23.65 mm	Screen resistivity	$73 \cdot 10^{-8}$ Ω-m
Screen inner radius	43.65 mm	Pipe resistivity	$10 \cdot 10^{-8}$ Ω-m
Screen outer radius	44.65 mm	Pipe permeability	300 μ_0
Cable outer radius	46.65 mm	Core/screen/pipe insulation permittivity	3.7 ε_0
Pipe inner radius	127.3 mm	Semiconducting layers thickness	3 mm
Pipe outer radius	133.7 mm	Burial depth	2.5 m

The above data together with the description and theoretical analysis in [21] lead to the circuit in Figure 2.82. The remaining unknown values in the circuit can be easily calculated as follows. The charging resistance is $R_0 = V_{\max}/I_0 = 138\,\mathrm{M\Omega}$. $R_{ext} = V_{\max}/I_{ext} = 690\,\mathrm{M\Omega}$ is the leakage resistance of the external circuit, assumed in this study as equally distributed on both sides of the switch ($R_{ext1} = R_{ext2} = 2R_{ext} = 1380\,\mathrm{M\Omega}$). The total cable leakage resistance is calculated as

$$R_{cable} = R'_{cable}/nl \tag{3.3}$$

where $R'_{cable} = 22\,\mathrm{G\Omega\text{-}km}$, $l = 20\,\mathrm{km}$ and $n = 3$ phases in parallel, resulting into

$R_{cable} = 367\ \mathrm{M\Omega}$. The total capacitance of the cable is calculated as

$$C_{cable} = nl\,C'_{cable} \tag{3.4}$$

$$C'_{cable} = \frac{2\pi\varepsilon_0\varepsilon_r}{\log_e\left(r_{out}/r_{in}\right)} \tag{3.5}$$

where $\varepsilon_r = 3.7$ is the relative permittivity of core insulation, $r_{out} = 40.65\,\mathrm{mm}$ and $r_{in} = 26.65\,\mathrm{mm}$ are respectively the external and internal radii of insulation in Table 2.9, resulting into $C_{cable} = 29.3\,\mu\mathrm{F}$.

The switch S_0 is closed at $t = 0$ to charge the cable and opens at $t = 60\,\mathrm{min}$, letting the cable discharge. S_W is closed (S_0 is now open) at $t = 148\,\mathrm{min}$ forcing the total discharge of the cable.

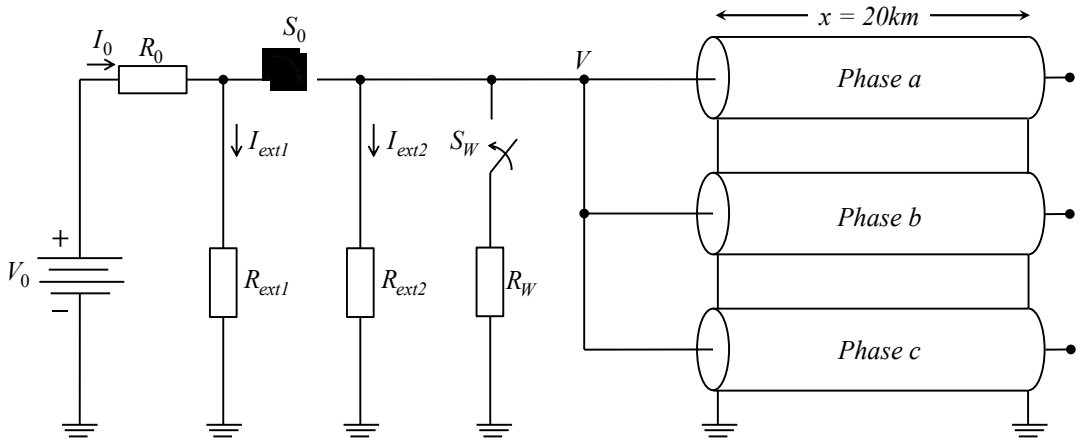

a) Field test circuit.

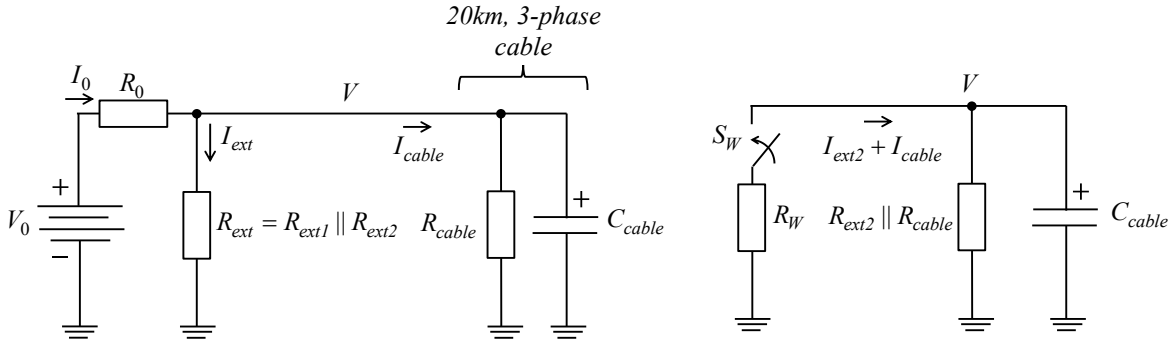

b) Approximate equivalent circuits for charging; c) and discharging.

Figure 2.82 Estimated circuit for field testing on a 275 kV PT-POF cable in Japan [52].

3.3.2 Measured discharge voltage

The measured voltage characteristic of the cable during charging and discharging is shown in Figure 2.83.

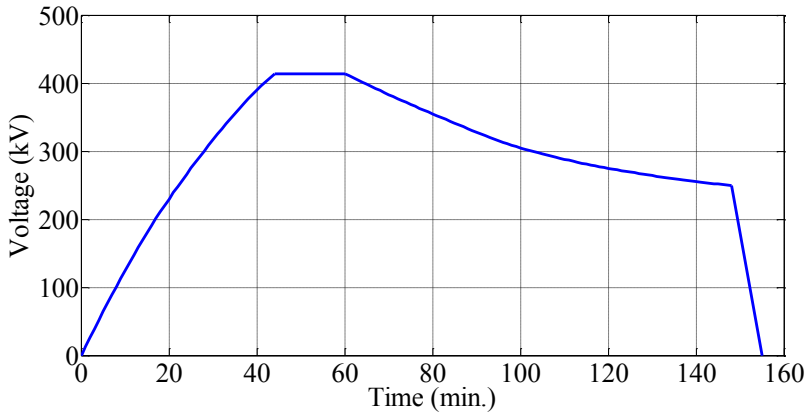

Figure 2.83 Field test of 275kV PT-POF cable in Japan (reproduced with permission from the measured result in [21]).[8]

As the first approximation, the result in Figure 2.83 can be explained using the equations of an *RC* circuit. This approximation is explained further in section 4.2. Based on the circuit in Figure 2.82b, the cable response during discharge is

$$v(t) = V_{\max}\, e^{-t/\tau} \tag{3.6}$$

for $60 < t < 148$ min, with $t_1 = 60$ min and $t_2 = 148$ min. The time constant is calculated using the total leakage resistance $R_{total} = R_{ext2} \parallel R_{cable} = 290\,\text{M}\Omega$ and the cable capacitance $C_{cable} = 29.3\,\mu\text{F}$ as

$$\tau = R_{total}\, C_{cable} \tag{3.7}$$

resulting into $\tau = 8483$ s $= 141.38$ min [52].

The time required to discharge the cable from $v(t_1) = 414$ kV to $v(t_2) = 250$ kV is calculated from

$$t_2 - t_1 = \tau \log_e\left(\frac{v(t_1)}{v(t_2)}\right) \tag{3.8}$$

---

[8] Circuits: CableSimulation_Files\CableDischarge\EMTP_Circuits.ecf

Plotting: CableSimulation_Files\CableDischarge\Plot_FieldTests.m

resulting into $t_2 - t_1 = 71.3\,\text{min}$ [52]. This value is too low compared to the 88 minutes of the voltage in Figure 2.83 measured in the field test and it shows that the leakage estimate was incorrect in [21].

3.4 Laboratory test of leakage currents, cable in Japan

In 1970, the same cable manufacturer performing the field test in section 3.3 [21] carried out a laboratory test using 1 m length model cables [22],[23]. The goal of the test was to observe the variation of leakage current with applied voltage and insulation temperature.

3.4.1 Test setup and cable sample

The laboratory test was carried out on specially designed model cables. A copper electrode of 35 mm radius and 1 m length used as core conductor is lapped over by an insulation of oil immersed paper with 125 μm thickness and relative permittivity of 3.6. Four model cables were produced with 0.5, 1, 3 and 5 mm thick insulation. The paper insulation is itself lapped over by a lead tape sheath. The model cables are inserted each into a chamber filled with oil at a pressure of 1 kg/cm^2. The oil temperature is controlled by forced circulation.

The model cables were charged for 20 hours, and then discharged to measure the leakage current of the thin insulation film.

3.4.2 Measured leakage currents

Figure 2.84 shows measured curves of leakage currents as a function of time for insulation temperatures of 20ºC and 80ºC. The three curves in each figure correspond to the initial applied voltages per millimeter of insulation thickness, of 10 kV/mm, 20 kV/mm and 30 kV/mm.

Due to normalization of applied voltage used in [22],[23], the curves in Figure 2.84 are applicable to all four model cables with different insulation thickness. Given the small thickness of the insulation (d varies between 0.5 and 5 mm) in relation to the insulation inner radius ($r_{in} = 35\,\text{mm}$), the electric field strength E (kV/mm) is nearly uniform inside the insulation and can be calculated from the applied voltage V using the relation $V = E\,d$.

Figure 2.84 clearly shows the influence of insulation temperature. The leakage currents for 80 ºC are about 10 times higher than those for 20ºC.

It is also observed in Figure 2.84 that the leakage current decreases with electric field strength E, but the three curves are nearly parallel in Figure 2.84 (left), which indicates that the leakage resistance calculated as $R_{total} = E\,d/I$ is not much dependent on the variation of electric field strength in this case. On the other hand the curves of leakage current for 80 ^{o}C are not parallel. This indicates that the influence of electric field on the value of leakage resistance may be more important at higher temperatures [60].

The test results in Figure 2.84 can be used to estimate the voltage of the model cables during discharge as

$$v(t) = \frac{E_0\,d}{I_0} i(t) \tag{3.9}$$

where E_0 is the initial electric field applied to the model cable, $i(t)$ is the leakage current in Figure 2.84 and I_0 its initial value, and d is the insulation thickness of the model cable. The voltages for the case of 1 mm thick insulation are shown in Figure 2.85, where the impact of temperature on the rate of decay is clearly observed.

The leakage currents in Figure 2.84 have a characteristic given by

$$i(t) = I_0\, e^{-t/\tau} \tag{3.10}$$

where I_0 is the current at $t = 0$. The capacitance for the model cable with 1 mm insulation thickness is calculated from (3.4) and (3.5) with $\varepsilon_r = 3.6$, $r_{in} = 35$ mm, $r_{out} = 36$ mm, $l = 1$ m and $n = 1$, resulting into $C_{cable} = 7.11$ nF. References [22],[23] do not give details on the leakage resistance, but it can be estimated from the cable capacitance and the time constant of the current in Figure 2.84a calculated with the formula in (3.8)

$$\tau = \frac{60 \times (100 - 1)}{\log_e (10/0.1585)} = 1433.2\,\text{s}$$

Using $C_{cable} = 7.11$ nF and $\tau = 1433.2$s in (3.7), $R_{total} = 201.6$ GΩ is found [52]. This value includes the leakage of the model cable and the external circuit. Such a high leakage resistance may be explained by very low losses in paper insulated cables and by the fact that a laboratory test has better conditions (low humidity, low levels of contamination) than a field test [52].

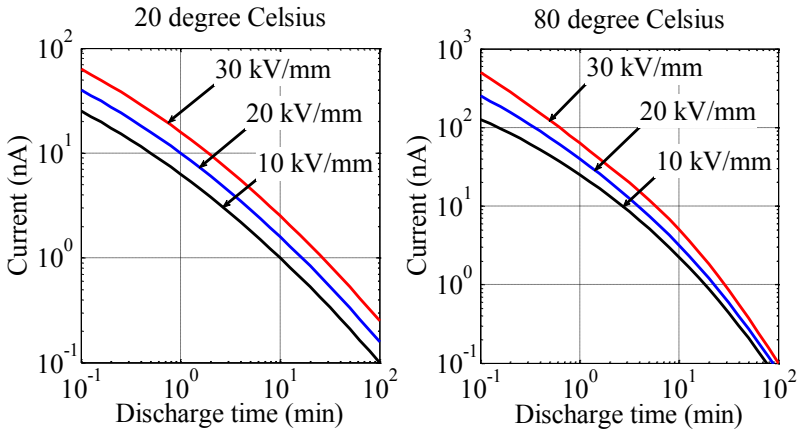

Figure 2.84 Measured leakage currents (reproduced with permission from the measurement results in [22]). [9]

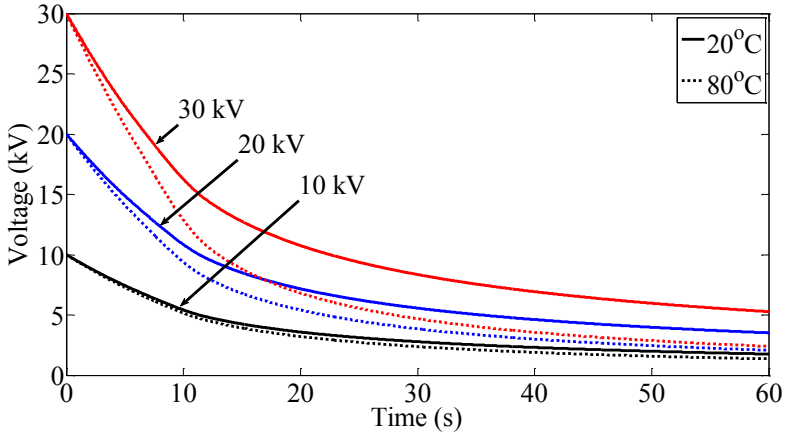

Figure 2.85 Voltage of model cable of 1 mm thick insulation during discharge test for different values of initial applied voltage and temperature [52].[9]

3.5 Discharge test of National Grid, UK 275 kV oil-filled cable

There is very little information in the literature on what is average time required to discharge HV cables to safe voltage levels, without using forced discharge. For this reason, in 2015 National Grid, UK carried out a discharge test on a 275 kV oil-filled (OF) cable with 21 km. Voltage, temperature, pressure and relative humidity of air were simultaneously measured during a total of 10 hours. This allowed studying the impact of these factors on the discharge time of the system.

[9] Plotting: CableSimulation_Files\CableDischarge\Plot_FieldTests.m

3.5.1 Test setup and cable data

Table 2.10 and Figure 2.86 show the details of the 275 kV POF cable with a length of 21 km. The cable is used in a trench with a depth of 1 m. The cable sealing end at ground level is connected to a piece of overhead horizontal busbar with a length of about 13.5 m. The busbar is supported by two vertical insulator poles, each with an axial length (not creepage) of 2.4 m. The capacitance of each cable phase is calculated using the data in Table 2.10, i.e. $\varepsilon_r = 3.8$, $r_{sh-in} = 40\,\text{mm}$, $r_{co-out} = 29.75\,\text{mm}$, and $l = 21\times10^3\,\text{m}$ into (3.4) and (3.5), resulting $C_{cable} = 15.0\,\mu\text{F}$.

The three cable phases are fed by a balanced source reaching 2 pu in phase-c, -1.3 pu in phase-b and -1.6 pu in phase-a. The source is switched off and the voltage in the cable is measured for 10 hours.

Table 2.10. Data of 275 kV POF cable in U.K [28]

Core conductor inner radius	6.8 mm	Core conductor resistivity	$1.724\cdot10^{-8}$ Ω-m
Core conductor outer radius	26.75 mm	Screen resistivity	$21.3\cdot10^{-8}$ Ω-m
Screen inner radius	43.00 mm	Core insulation permittivity	3.8 ε_0
Screen outer radius	47.20 mm		
Semiconducting layers thickness	3 mm	Screen insulation permittivity	8 ε_0
Cable outer radius	51.56 mm	Depth	1 m

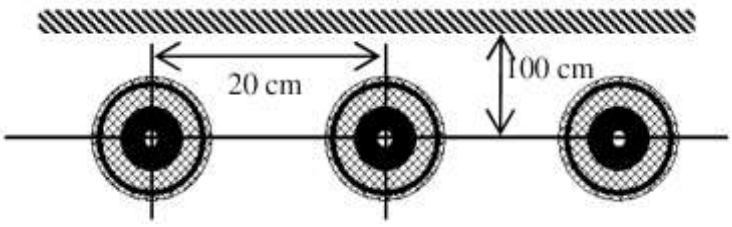

Figure 2.86 Layout of 275kV POF cable in the UK [28].

3.5.2 Measured discharge voltage

Figure 2.87 shows the measured cable voltage during discharge. It took about 8 hours to fully discharge the cable.

The voltage measured in each phase in Figure 2.87 follows a characteristic given by (3.6).

The time constant for discharging each phase can be obtained using any two points t_1 and t_2 of a curve in Figure 2.87 and equation (3.8), resulting $\tau_a = 3.04$ h, $\tau_b = 3.20$ h and $\tau_c = 3.50$ h [52]. The leakage resistances can be estimated using the time constants and the capacitance $C_{cable} = 15.0$ μF in (3.7) giving

$R_{total-a} = 729.8\,\text{M}\Omega$, $R_{total-b} = 768.2\,\text{M}\Omega$, and $R_{total-c} = 840.2\,\text{M}\Omega$. These values include the leakage in the cable and in the external circuit.

In reality, the above leakage resistances are average values based on the initial voltage characteristics in Figure 2.87. Another approach is to estimate the time constant from (3.8), rewritten as

$$\log_e\left(\frac{v(t)}{v(0)}\right) = -\frac{t}{\tau} \tag{3.11}$$

The above equation shows that if the vertical axis in Figure 2.87 is transformed to logarithmic scale, the value of τ can be observed simply from the slope of the voltage characteristic. This is illustrated in Figure 2.88, and it is easily observed that the time constant changed during the test. This is because the humidity in air increased during the test, which caused an increase of the leakage current and a reduction of the time constant.

Figure 2.89 shows temperature, pressure and relative humidity measured during the field test. The humidity increased from 80% to 100%. The impact of this change is that the time constant is reduced from 3.5 hours (initial) to 1.5 hours and the leakage resistance is reduced from $R_{total-c} = 840.2$ MΩ to 360.1 MΩ.

The impact of air humidity is caused by the busbar, insulator poles connected to the cable, as well as the cable sealing ends which are exposed to air.

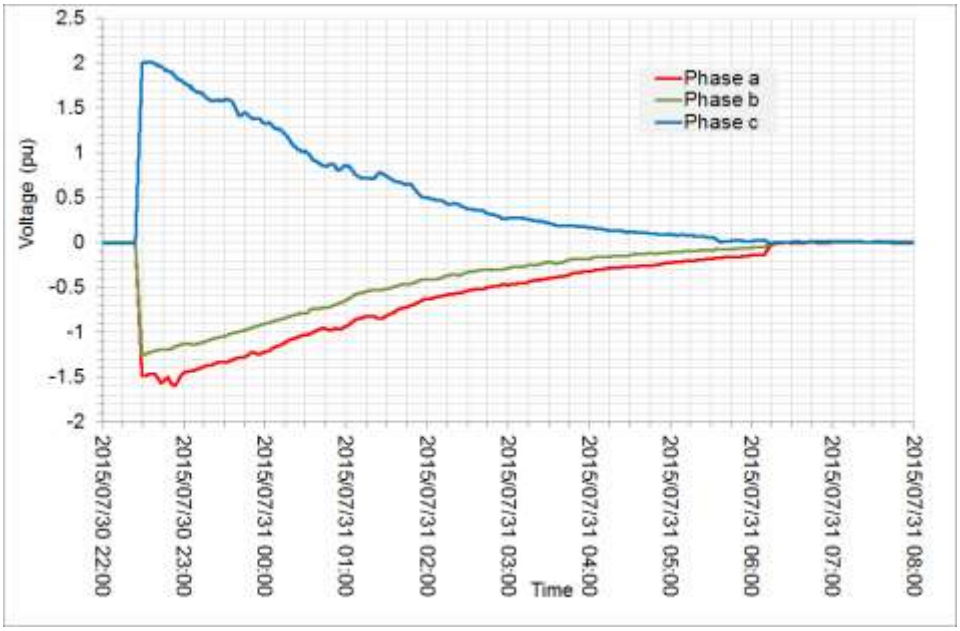

Figure 2.87 Test results of discharge voltage, 275 kV POF cable, courtesy of National Grid, UK [52].[10]

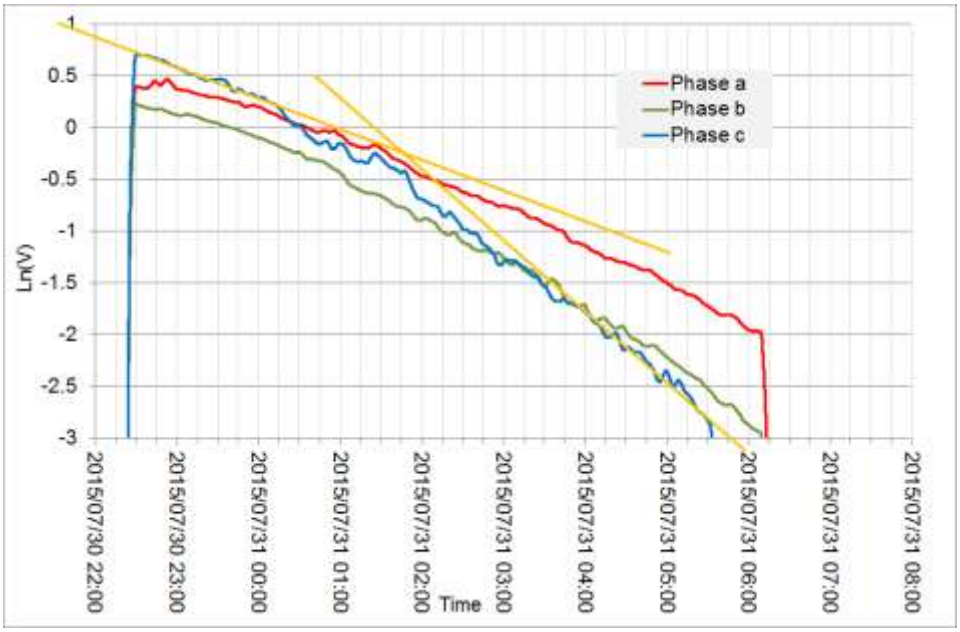

Figure 2.88 Test results of Figure 2.87, logarithmic scale, courtesy of National Grid, UK [52].[10]

[10] Figures : CableSimulation_Files\CableDischarge\UK_MeasuredResults.docx

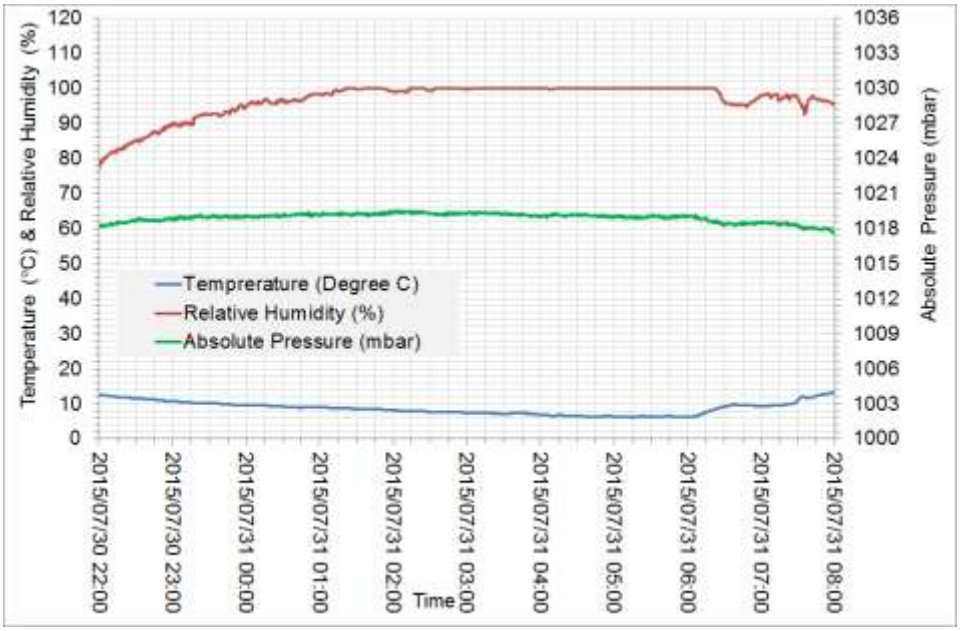

Figure 2.89 Temperature, humidity and absolute pressure measured during the field test by National Grid, UK (courtesy of National Grid) [52].[10]

3.6 Conclusion

This chapter presented five field and laboratory tests on underground HVAC cables.

The first was a surge test conducted by RTE-France on a minor and on a major section of a 225 kV underground XLPE cable. The test which followed CIGRÉ Standards, was intended to observe the cable response to the excitation of different propagation modes and to analyze the impact of sheath cross-bonding.

The second test was an energising test conducted by RTE on the full length of the same cable. The objective was to study the transient voltages and currents observed during a normal switching operation, in particular when reactive compensation is applied.

The third test dates back to 1971 and was carried out in Japan for the commissioning of a 275 kV PT-POF cable with 20 km. The cable voltage was measured during charging and both natural and forced discharging. The fourth test was carried out by the same manufacturer of the 275 kV PT-POF cable. It consisted on a laboratory measurement of the leakage currents of 1 m cable samples under different conditions of temperature and initial applied voltage.

Finally, the fifth test was carried out in 2015 by National Grid, UK on a 275 kV OF cable with 21 km. Not only was the cable voltage measured during discharge but also the temperature and humidity of air during the measurements.

The different test results presented in this chapter will be used in the following sections to validate the developments presented in this thesis.

CHAPTER 4 CALCULATION OF CABLE PER-UNIT-LENGTH PARAMETERS FROM FIELD TEST RESULTS

The main scope of this chapter is demonstrating the calculation of cable per-unit-length parameters based on field test results.

Cable models for transient studies are often analyzed based on simulations only [7],[12]. However, to validate the models it is necessary to compare the simulation results with measurements carried out on the real cable system [8],[10],[14]-[20].

The usual practice when validating cables models for transient studies is to compare the attenuation, propagation velocity and characteristic impedance of measured voltages and currents to the same values calculated using the model. This allows verifying that a model is accurate but gives little insight when deviations between field tests and simulations are observed.

The first section of this chapter demonstrates a method for extracting additional information from results of surge field test, namely the per-unit-length resistance, inductance and capacitance for each mode of propagation. This additional data allows a better identification of the source of deviation between field tests and simulations. The method is applied to a field test presented in section 3.1. The *RLC* parameters evaluated from the field test results are already in modal domain because each energising excited one single specific mode.

The second section of this chapter is dedicated to calculating the per-unit-length conductance, which related to losses inside the cable insulation. This parameter has almost negligible impact during surge or switching transient phenomena but it is determinant during the cable natural discharge, which is a nearly DC phenomenon. In the literature as in this thesis the cable shunt capacitance is often referred to in terms of its inverse, i.e. the leakage resistance of cable insulation. Estimation of the cable leakage resistance is demonstrated based on discharge tests presented in sections 3.3 and 3.5. The impact of leakage in external insulator equipment, usually exposed to air temperature, humidity and contamination, is also made clear. Typical values of discharge time are given. These values depend on the cable capacitance and leakage resistance as well as on the leakage resistance of the external insulators are indicated.

4.1 Evaluating the per-unit-length resistance, inductance and capacitance from surge measurements

Calculating the PUL resistance, inductance and capacitance from a surge test result requires several steps, explained in the following sections. First the field test measured result is approximated by the response of a simple *RLC* lumped circuit. Then the parameters of the lumped circuit are converted into PUL parameters such that the frequency and attenuation on the two systems remains the same. Finally, to be able to compare the parameters extracted from field tests to the cable model parameters it is necessary of transform the field test parameters from modal to phase domain. To be able to calculate the phase domain cable matrices it is required to have field test results for the excitation of all the propagation modes. The method is demonstrated with an example of the field test presented in section 3.1.

4.1.1 Calculation of lumped parameters for equivalent circuits

The cable transient responses shown in section 3.1 can be approximated by the response of simple *RLC* circuits. L-equivalent, PI-equivalent and T-equivalent lumped circuits are alternatives for modeling the cable responses. However, PI-equivalent and T-equivalent have two transient frequencies instead of one and require two-times more information from the measured results to determinate *RLC* parameters. Therefore, L-equivalents as illustrated in Figure 2.90 are used to represent the cable under different transient conditions. To simplify the derivation of analytical responses in Laplace domain [18][53], the field test impulse voltage is approximated by a unit step voltage [20].

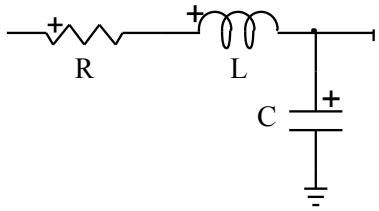

Figure 2.90 L-equivalent circuit (*RLC* circuit) model for cable [20].

The Laplace transform of the current in an L-equivalent circuit and its time-domain form are given by

$$I(s) = \frac{E}{s\left(R + sL + \dfrac{1}{sC}\right)} \tag{4.1}$$

where E is the amplitude of the step function. The initial conditions are zero. The general time-domain form of (4.1) which is also valid for the over-damped condition with $\omega^2 < \alpha^2$ is

$$i(t) = \frac{E}{L\,\omega_d} e^{-\alpha t} \sinh\left(\omega_d t\right) \tag{4.2}$$

where $\alpha = R/(2L)$, $\omega_d = \sqrt{\left|\alpha^2 - \omega^2\right|}$ and $\omega = 1/\sqrt{LC}$.

For the oscillatory condition

$$i(t) = \frac{E}{L\omega_d} e^{-\alpha t} \sin\left(\omega_d t\right), \quad \omega^2 > \alpha^2 \tag{4.3}$$

and for the critically damped condition

$$i(t) = \frac{E}{L} t e^{-\alpha t}, \quad \omega^2 = \alpha^2 \tag{4.4}$$

Given the different forms of time-domain responses in (4.2) to (4.4), different approaches must be used to extract *RLC* parameters according to the nature of the transient responses. For the oscillatory condition, the attenuation is calculated from two current peaks (I_{n-1} and I_n) and the time t_p between them as $\alpha = \ln\left(I_{n-1}/I_n\right)/t_p$ and Z_c is found from the ratio of peak voltage and current. Knowing that the characteristic impedance is also approximately given as $Z_c = \sqrt{L/C}$, it is then possible to extract $L = Z_c/\omega$, $C = 1/\left(\omega Z_c\right)$ and $R = 2L\alpha$.

For the critically damped condition (4.4), the current maximum $I_{\max} = 2E/(eR)$ is reached when $t_{\max} = 1/\alpha$. Thus it is possible to extract $\alpha = 1/t_{\max}$, $R = 2E/\left(eI_{\max}\right)$, $L = R/(2\alpha)$ and $C = 4L/R^2$.

Although the critically damped condition is observed only for a very specific frequency $\omega^2 = \alpha^2$, it is easier to calculate the *RLC* parameters for (4.4) than for the over-damped condition because of the hyperbolic function present in (4.2).

4.1.2 Calculation of per-unit-length parameters from equivalent circuits

The point of calculating L-equivalents which represent the cable transient responses is to validate the parameters output by the cable model data calculation function (CMDCF) [61],[62],[63]. However, lumped parameters of L-equivalents cannot be directly compared to PUL parameters. Wave velocity and propagation delay are concepts that do not apply to lumped-parameter circuits.

Nevertheless, L-equivalents can be converted to distributed-parameter circuits which have the same response under specific conditions. The natural frequency for the L-equivalent is $f = 1/\left(2\pi\sqrt{LC}\right)$ whereas in an actual cable, it is found from $f' = 1/\left(4\ell\right.$, with ℓ being the cable length and when the receiving end is open-circuited. The parameters of a distributed-circuit which has the same transient response as the L-equivalent are calculated by setting the two frequencies f and f' as being equal, which results into [20]

$$L' = \eta L, \quad C' = \eta C \tag{4.5}$$

where L' and C' are the PUL parameters and $\eta = \pi/\left(2\ell\right.$. The same correction applies to the resistance to ensure that attenuation remains the same for lumped and distributed circuits, as demonstrated in appendix B.

4.1.3 Calculation of a transformation matrix

As explained in section 2.2, the parameters of a cable associated to each propagation mode depend upon the transformation matrix used. The *RLC* parameters evaluated from the field test results are already in modal domain because each energising excited one single specific mode. The parameters obtained from the CMDCF are in phase domain or in modal domain using a modal transformation matrix that requires modifying the scaling factor of its eigenvectors.

To know which transformation matrix is associated to the parameters calculated from the field test results, the measured waveforms are compared to the response of a multi-phase constant-parameter (CP) model which uses the PUL values obtained from the field test.

The CP model is defined by the R', L' and C' parameters for each propagation mode and by a constant real transformation matrix [48]. Given that the transients measured in the field test involve relatively high frequencies, a transformation matrix calculated at a high frequency (37 kHz) by the CMDCF can be used. Consider the following notation:

$$\mathbf{I_m} = \mathbf{T_i} \mathbf{I_{ph}}$$
$$\mathbf{I_m} = \begin{bmatrix} I_{co_1} & I_{ish_1} & I_{co_2} & I_{ea} & I_{co_3} & I_{ish_2} \end{bmatrix}^T \tag{4.6}$$
$$\mathbf{I_{ph}} = \begin{bmatrix} I_{c0} & I_{s0} & I_{c4} & I_{s4} & I_{c8} & I_{s8} \end{bmatrix}^T$$

where $\mathbf{I_{ph}}$ and $\mathbf{I_m}$ are the vectors of phase and modal currents at the cable sending end. In $\mathbf{I_{ph}}$, subscripts *c* and *s* are used for core and sheath voltage. The phases are identified by 0, 4 and 8. In $\mathbf{I_m}$ subscripts *co*, *ish* and *ea* are used to identify coaxial, inter-sheath and earth-return modes.

It is well-known that the columns of the above matrix are eigenvectors of the matrix of propagation factors, and that they are not uniquely defined, that means we can multiply an eigenvector by an arbitrary constant and it will still be a valid eigenvector. If we multiply an eigenvector $\mathbf{T_i}$ by a constant *k*, this will affect the series impedance matrix in the following way [20]

$$Z'_m = k\,\mathbf{T_i}^T \mathbf{Z_{ph}}\, k\,\mathbf{T_i} = k^2 \left(\mathbf{T_i}^T \mathbf{Z_{ph}} \mathbf{T_i} \right) = k^2 Z_m \tag{4.7}$$

This will in turn affect the corresponding modal current by $I_m = k^2 Z_m V_m$, where *m* is the propagation mode corresponding to the eigenvector $\mathbf{T_i}$. Therefore, we can calculate which constant to multiply by each eigenvector by comparing the modal current obtained by the L-equivalent and by the multi-phase CP model.

4.1.4 Application to the surge test carried out by RTE

The calculation of PUL cable parameters from field test results is demonstrated with application to the field test presented in section 3.1.

4.1.4.1 Coaxial Mode: Oscillatory

As observed in Figure 2.40 and Figure 2.41, the response of the cable to a coaxial wave is oscillatory. The *RLC* values for the coaxial mode test are calculated below [20]. The parameter

T_{avg} is the period of oscillations, the subscript *avg* stands for average value and the samples of current use the index *n*.

$Z_c = V_{\max} / I_{\max} = 1752/69.07 = 25.37\ \Omega$

$\left(I_{n-1}/I_n\right)_{avg} = 1.273,\ T_{avg} = 27.18\ \mu s,\ \tau_{avg} = 6.80\ \mu s$

$v_{avg} = 158.92\ \text{m}/\mu s,\ f_{avg} = 36.79\ \text{kHz}$

$\alpha = \ln 1.273/27.18\times 10^{-6} = 8888.71\ L = Z_c/(2\pi f) = 0.1098\ \text{mH}/1080\ \text{m}$

$C = 1/(Z_c 2\pi f) = 0.171\ \mu\text{F}/1080\ \text{m}$

$R = 2L\alpha = 1.952\ \Omega/1080\ \text{m}$

To validate the accuracy of *RLC* parameters, the above calculations are compared to the field test result in Figure 2.91. The agreement between field test and the L-equivalent circuit is satisfactory.

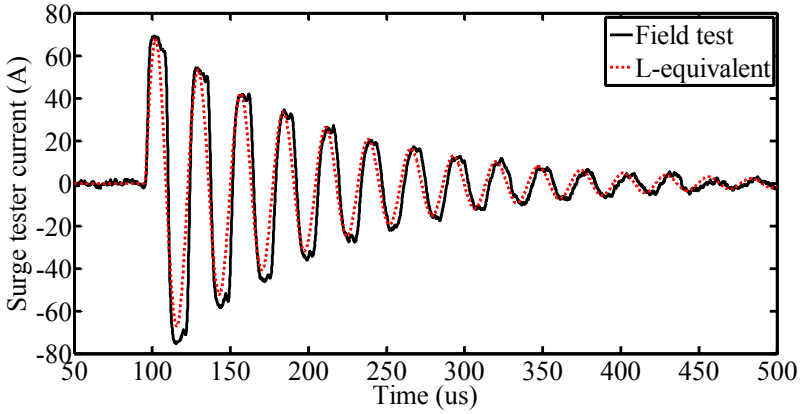

Figure 2.91 Comparison of field test result of coaxial mode current with the response of *RLC* equivalent circuit.[11]

The parameters of the equivalent distributed model (CP model) are calculated by applying the relation in (4.5) resulting into $R' = (\pi/2)1.81 = 2.84\ \Omega/\text{km}$, $L' = (\pi/2)0.102 = 0.160\ \text{mH}/\text{km}$ and

[11] Circuits: CableSimulation_Files\FieldTestSimulation_RTECable\EMTPCirc_MinorSection\Minor_Section.ecf
Plotting: CableSimulation_Files\FieldTestSimulation_RTECable\Plotting\Plotting_MinorSection.m

$C' = (\pi/2)0.158 = 0.249$ μF/km. The current responses for the L-equivalent circuit and the CP-model with these PUL parameters are given in Figure 2.92. As observed in the figure, the frequency and attenuation of the two models are exactly the same. The square-shaped wave of the CP model is due to the fact that it does not account for the frequency dependencies of R' and L'.

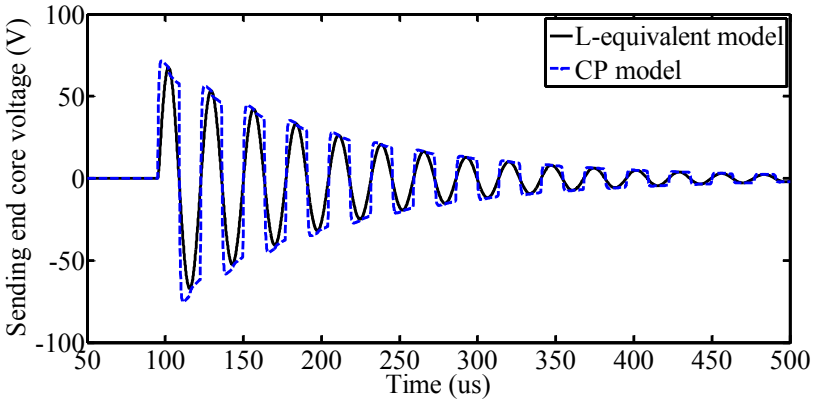

Figure 2.92 Coaxial mode currents using L-equivalent and CP models [20].[11]

4.1.4.2 Inter-Sheath Mode: Oscillatory

Figure 2.43 and Figure 2.45 show that the cable response to inter-sheath waves is oscillatory. The *RLC* values for the inter-sheath mode are thus calculated as [20]

$Z_c = 1221/49.01 = 24.91\ \Omega,\ (I_{n-1}/I_n)_{avg} = 1.791$

$T_{avg} = 36.9\ \mu s,\ \tau_{avg} = 9.23\ \mu s,\ c_{avg} = 117.07$ m/μs

$f_{avg} = 27.10$ kHz, $\alpha = \ln 1.791/36.9\times10^{-6} = 15.793\times10^{3}$ $L = Z_c/(2\pi f) = 0.146$ mH/1080 m

$C = 1/(Z_c 2\pi f) = 0.236$ μF/1080 m

$R = 2L\alpha = 4.61\ \Omega$ / 1080 m

To validate the accuracy of *RLC* parameters, the above calculations are compared to a field test result of inter-sheath mode excitation in Figure 2.93. The agreement between field test results and the L-equivalent circuit results is satisfactory.

The parameters of the equivalent distributed model (CP model) are calculated by applying the relation in (4.5) resulting into $R' = (\pi/2)4.27 = 6.71\ \Omega/\text{km}$, $L' = (\pi/2)0.135 = 0.212$ mH/km and

$C' = (\pi/2)0.219 = 0.344$ μF/km. To validate the accuracy of *RLC* parameters, the above calculations are compared to measurements (minor section) in Figure 2.72. The agreement between field test and the L-equivalent circuit result is satisfactory.

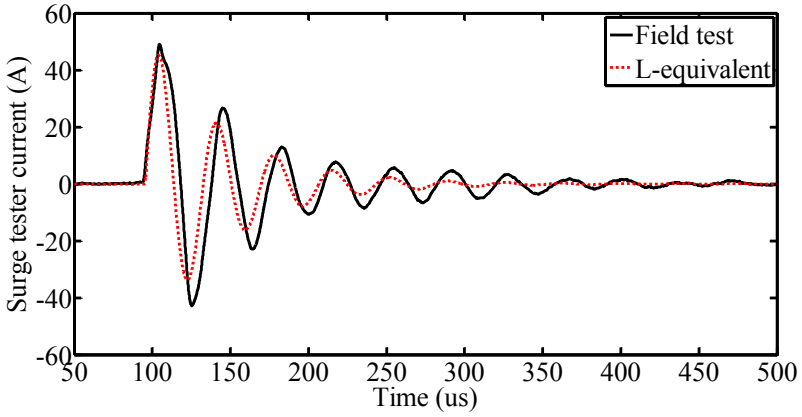

Figure 2.93 Comparison of field test result of inter-sheath mode current with the response of *RLC* equivalent circuit. [11]

4.1.4.3 Earth-Return Mode: Critically Damped

Figure 2.52 and Figure 2.55 show that contrary to coaxial and inter-sheath modes the response of the cable to a pure earth-return wave is non-oscillatory due to the high resistance of the grounding system and earth-return path. The *RLC* values for the earth-return mode are estimated as [20]

$Z_c = 1767/27.04 = 65\ \Omega$

$t_{\max} = 106.7 - 94.9 = 11.8\ \mu s \rightarrow \alpha = 1/t_{\max} = 84.7 \times 10^3$

$I_{\max} = 27.04$ A, $E = 1767$ V $\rightarrow R = 2E/(e\, I_{\max}) = 48.1\ \Omega$/1080 m

$L = R/(2\alpha) = 0.284$ mH/1080 m, $C = 4L/R^2 = 0.491$ μF/1080 m

The parameters of the equivalent distributed model (CP model) are calculated by applying the relation in (4.5) resulting into $R' = (\pi/2)44.54 = 69.96\ \Omega/\text{km}$, $L' = (\pi/2)0.263 = 0.413$ mH/km and $C' = (\pi/2)0.455 = 0.715$ μF/km.

To validate the accuracy of *RLC* parameters, the above calculations are compared to the measurement result of earth-return excitation Figure 2.94. Contrary to the coaxial and inter-sheath

modes, the agreement between field test and the L-equivalent circuit result is not good after the first 50 μs, with the L-equivalent circuit giving a slower decaying current. This is due to the impedance of earth-return and grounding system.

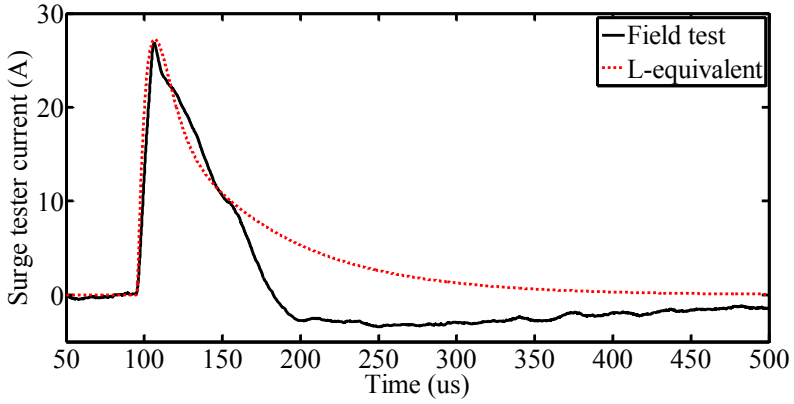

Figure 2.94 Comparison of field test result of earth-return mode current with the response of *RLC* equivalent circuit. [11]

4.1.4.4 Validation against the cable parameter calculation routine of EMTP-RV

The transformation matrix by the CMDCF of EMTP-RV is given by [20]

$$\mathbf{T}_\mathbf{i}^{T} \approx \begin{bmatrix} 0.29 & 0 & 0.41 & 0 & -0.50 & 0 \\ -0.29 & 0.41 & -0.41 & 0.58 & 0.50 & -0.71 \\ -0.58 & 0 & 0.41 & 0 & 0 & 0 \\ 0.58 & -0.82 & -0.41 & 0.58 & 0 & 0 \\ 0.29 & 0 & 0.41 & 0 & 0.50 & 0 \\ -0.29 & 0.41 & -0.41 & 0.58 & -0.50 & 0.71 \end{bmatrix} \begin{matrix} \text{core-0} \\ \text{sheath-0} \\ \text{core-4} \\ \text{sheath-4} \\ \text{core-8} \\ \text{sheath-8} \end{matrix} \tag{4.8}$$

This transformation matrix has to be modified to make sure the multi-phase cable model presents the same responses to each modal excitation as the real cable which responses were measured during the field test.

Figure 2.95 shows the sending end current for the coaxial mode obtained by the L-equivalent and by the CP model using the transformation matrix in (4.8). The frequency and attenuation of the two waveforms is the same but one's amplitude is twice as large as the other's. Following the explanation in section 4.1.3, the correction term for the coaxial mode eigenvectors is $k^2 = 2$. The

dotted line in Figure 2.95 shows the response of the CP model when multiplying the coaxial mode eigenvectors by $k = \sqrt{2}$, which shows the same amplitude as the L-equivalent model.

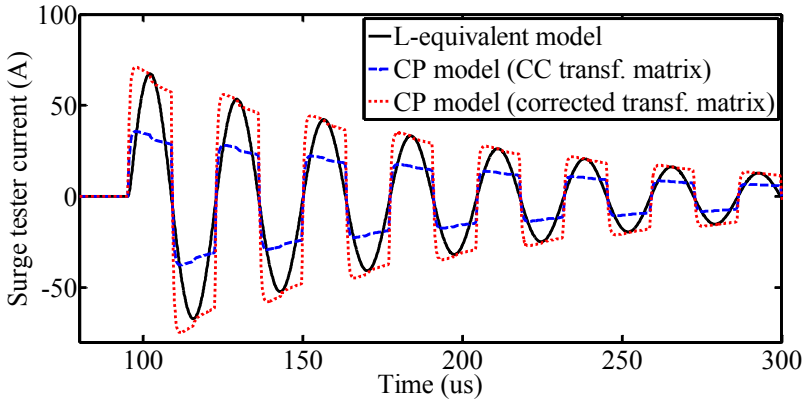

Figure 2.95 Comparison of a coaxial mode current for an L-equivalent model, a constant-parameter (CP) model using the transformation matrix by the cable parameter calculation routine (CC) and a CP model with a corrected transformation matrix [20]. [11]

Applying the same reasoning to the intersheath and the earth-return modes gives the final transformation matrix [20]

$$\mathbf{T}_\mathbf{i}'^{T} \approx \left[\begin{array}{cccccc|l} 0.41 & 0 & 0.58 & 0 & -0.70 & 0 & \text{core-0} \\ -0.41 & 0.50 & -0.58 & 0.32 & 0.70 & -0.87 & \text{sheath-0} \\ -0.82 & 0 & 0.58 & 0 & 0 & 0 & \text{core-4} \\ 0.82 & -1.0 & -0.58 & 0.32 & 0 & 0 & \text{sheath-4} \\ 0.41 & 0 & 0.58 & 0 & 0.70 & 0 & \text{core-8} \\ -0.41 & 0.50 & -0.58 & 0.32 & -0.70 & 0.87 & \text{sheath-8} \end{array}\right] \tag{4.9}$$

Table 2.11 presents the computations of parameters from the EMTP CMDCF and from the field test results. It is observed that the results from the CMDCF for L' and C' are sufficiently accurate and consequently the propagation velocity c and characteristic impedance Z_c agree with field tests. The resistance R' found from field tests is always greater than the one found from the CC. This can be explained with the fact that field test results involve resistances in the measuring system (e.g. source internal resistance, grounding resistance).

Table 2.11. *RLC* parameters calculated from field test results and from EMTP-RV cable model data calculation function (CMDCF) [20].

Mode	Source	$R'(\Omega/\text{km})$	$L'(\text{mH/km})$	$C'(\mu\text{F/km})$
Coaxial f=37 kHz*	Field	2.84	0.160	0.249
	CMDCF	0.352	0.139	0.264
Inter-sheath f=27 kHz*	Field	6.70	0.212	0.343
	CMDCF	0.208	0.203	0.343
Earth-return f=13 kHz*	Field	69.9	0.413	0.609
	CMDCF	13.4	1.16	1.65

* Dominant frequency of transient waveform

4.2 Evaluating the cable insulation leakage resistance from discharge test measurements

As observed in Sections 3.3, 3.4 and 3.5, the time required to discharge a cable depends not only on the leakage of cable insulation but also on the leakage of insulators connected to the cable. The term insulator is used for any system component providing a path for leakage currents, e.g. cable sealing ends, insulator poles, and bushing.

The discharge of distributed-parameter systems, e.g. cables and lines, is in general different from the discharge of lumped-parameter systems, e.g. reactive power compensation capacitor. However, since the phenomenon of cable discharge is very slow, the wavelength will be much larger than the cable length. At 60 Hz, assuming a typical propagation velocity of 150 m/μs, the wavelength is $\lambda = \left(150 \times 10^6\right) \big/ 60 = 2500\,\text{km}$, being even larger for lower frequencies. In such case, the cable is considered as "short" and the response of the cable and insulators connected to it follows the equations of a simple parallel *RC* circuit with time constant given by (3.7).

It must be noted that discharge through a grounding switch, which represents a short circuit across a charged cable, or equipment such as wound voltage transformers would be different to discharge considered in this thesis as in those cases the cable series parameters influence the discharge. Those discharge types are out of the scope of this thesis.

The value of R_{total} in (3.7) depends both on the leakage through the cable insulation and through the insulators connected to the cable. The cable insulation is practically not affected by external

factors, like weather and pollution. On the other hand, insulators (cable sealing ends, insulator poles and bushing) are generally exposed to air and thus are directly affected by humidity and contamination.

This section presents a method for calculating a model of a cable system during discharge. The cable capacitance is calculated directly from the cable data while the cable shunt resistance (or insulation leakage resistance) is calculated from test results of cable discharge. Typical values of cable and insulator parameters are given and allow estimating the discharge time constants based only on the voltage level, cable insulation material (EPR, XLPE, paper insulation) and insulator type (ceramic or composite).

4.2.1 Cable parameters

Cable response during discharge is influenced by its per-unit shunt parameters, i.e. the shunt capacitance in (3.5) and shunt conductance, or more commonly used, the shunt resistance of its insulation

$$R'_{cable} = \frac{1}{G'_{cable}} = \frac{\rho \log_e\left(r_{out}/r_{in}\right)}{2\pi}, R_{cable} = \frac{R'_{cable}}{l} \tag{4.10}$$

where ρ and ε_r are the resistivity and relative permittivity of insulation between core and sheath, r_{in} and r_{out} are the internal and external radii of insulation. The total cable capacitance and shunt resistance are calculated using (3.5) and (4.10) into (3.4) and (3.3), respectively, with l the length of the cable and n the number of phases bonded ($n = 1$ if the phases are not bonded).

Combining (3.3)-(3.5) and (4.10), it is possible to calculate R_{cable} using the cable capacitance and permittivity parameters commonly found in cable datasheets

$$R_{cable} = \frac{\varepsilon_0 \varepsilon_r \rho}{C_{cable}} \tag{4.11}$$

Table 2.12 gives the resistivity and relative permittivity for typical cable insulation [54]-[56]. The capacitance for 275 kV cables is generally within 0.12-0.45 μF/km [57],[58].

Table 2.12. Properties of Cable Insulation Material [52],[54]-[56].

Insulation	EPR	XLPE	Paper (Kapton, Polyimide)
Resistivity	10 GΩ-km	100 GΩ-km	1000—1500 GΩ-km
Relative permittivity	2.5—2.6	2.3—2.5	3.4—3.8

Based on Table 2.12 and typical capacitance values, it is possible to calculate the leakage resistance and leakage current for 275 kV cable systems in Table 2.13. Paper insulated cables have by far the least leakage current.

Table 2.13. Leakage Resistance and Current in 275 kV Cables [52].

	EPR	XLPE	Paper
Leakage Resistance	0.49–1.92 GΩ-km	4.53–18.4 GΩ-km	66.9–280 GΩ-km
Typical values	C=0.35 μF/km, R=0.63 GΩ-km	C=0.25 μF/km, R=8.1 GΩ-km	C=0.45 μF/km, R=74.8 GΩ-km
Leakage Current	0.35 mA/km	0.028 mA/km	0.003 mA/km

4.2.2 Insulator parameters and leakage current

The performance of insulators (cable sealing ends, insulator poles and bushing) is generally evaluated through specific tests under wet and contaminated conditions and it is quantified in terms of equivalent salt deposit density (ESDD) which is used to calculate the dielectric strength of the insulator. These tests are good enough for porcelain and glass insulators, but they are insufficient for composite insulators which, in addition to contamination and moisture, are also affected by aging of the housing material. Furthermore, they do not inform on the leakage current or leakage resistance of the insulator.

The IEEE Working Group on Insulator Contamination proposed an alternative method for evaluating the performance of insulators using measures of surface resistance and published results for three types of insulators: porcelain, ethylene propylene diene monomer (EPDM) and silicone rubber [59]. Table 2.14 shows values of surface resistance measured by the IEEE working group [59]. The surface resistance is expressed in ohm per mm of leakage (or creepage) distance.

It is clear from Table 2.14 that composite insulators (EPDM and silicone) have substantially better performance (higher surface resistance) than porcelain. It is also clear from Table 2.14 that the presence of contaminants in the walls of the insulator greatly reduces its performance.

Table 2.14. Insulator surface resistance per mm of leakage distance (kΩ/mm) [52],[59].

	EPDM	Silicone	Porcelain
Uncontaminated	80 — 210	>5300	3.1—10
Contaminated	0.27 — 5.3	2.7—8	Not Measured

The leakage resistance of an insulator can be obtained as

$$R_{insulator} = R_{surf}\ d_{leakage} \tag{4.12}$$

where R_{surf} is the surface resistance given in Table 2.14 and $d_{leakage}$ is the leakage distance of the insulator. Values of leakage distance are easily found in manufacturer catalogs. For 275 kV insulators the usual values are 5000-7800 mm for composite and 8000-10000 mm for ceramic [64]. Using these values and those in Table 2.14, allows calculating typical values of resistance and leakage current at nominal voltage for 275 kV insulators in Table 2.15.

Table 2.15. Typical Resistance and Leakage Current at Nominal Voltage of 275kV insulators [52].

	EPDM	Silicone	Porcelain
Resistance (MΩ)	400 - 1638	>26500	25 - 100
Leakage current (mA)	0.1 - 0.6	<0.008	2 - 9

4.2.3 Formula and typical values of discharge time constant

The time constant associated with the discharge of cable and surrounding insulators is calculated as

$$\tau = \left(\frac{R_{cable} R_{ext}}{R_{cable} + R_{ext}} \right) C_{cable} \tag{4.13}$$

where R_{cable} and C_{cable} are given in (3.3) and (3.4) and R_{ext} is the leakage resistance of external components calculated as

$$R_{ext} = \left(\sum_{i=1}^{P} \frac{1}{(R_{insulator})_i} \right)^{-1} \tag{4.14}$$

where $\left(R_{insulator}\right)_i$ is the leakage resistance of the i-th insulator and is defined in (4.12) and P is the number of insulator components connected to the cable.

Using the formula for cable discharge voltage in (3.6) with $V_{\max} = V_n\sqrt{2/3}$ the time required to discharge the cable voltage to a safe level (25 V according to IEC 60479-1) is 10τ for 275 kV cables.

Table 2.16 shows time constants τ and time required to discharge the cable to the safe voltage level for different combinations of cables and insulators. These values are based on the typical values of cable insulation and insulator properties shown in Table 2.13 and Table 2.15, respectively. It is worth noting that the most severe cases, i.e. the longest discharge times (lowest leakage currents), are found when the insulators and cable insulation are at their best condition. This is observed in Table 2.16 for paper insulated cables with silicone insulators.

Table 2.16. Typical discharge time constants for 275 kV 20 km cable with cable sealing end [52].

a) Discharge time constants.

		Insulator		
		EPDM	Silicone	Porcelain
Cable Insulation	EPR	3.4 – 3.6 min	3.7 min	1.6 – 2.8 min
	XLPE	17 - 27 min	33 min	2.0 – 6.7 min
	Paper	54 - 170 min	8 - 9 h	3.7 - 14.6 min

b) Time to discharge the cable to safe voltage level.

		Insulator		
		EPDM	Silicone	Porcelain
Cable Insulation	EPR	34 - 36 min	37 min	16 - 28 min
	XLPE	2.8 – 4.5 h	5.5 h	20 min - 1 h
	Paper	9 - 28 h	3.3 - 3.75 days	0.6 - 2.4 h

4.2.4 Correction factor for humidity

The field test results provided by National Grid represent a very important contribution to the study of HVAC cables. Not only they show the evolution of voltage during the discharge of a 275 kV POF cable, a result rarely found in the literature, but they also show the effect of relative humidity, temperature and atmospheric pressure during those measurements, carried out during 10 hours. These results, presented in section 3.5, allow the definition of a correction factor to apply to the

leakage resistance of external insulators to account for a modification in the relative humidity of air. From Figure 2.89 it is observed that the relative humidity increased from 80% to 100%. At the same time, the leakage resistance of external insulators, excluding leakage of cable insulation, measured from the test results, was reduced from 1359.3 MΩ to 430.6 MΩ (see Section 5.3). Let's define h_1 and $R_{ext_{h_1}}$ the initial values of relative humidity and insulator resistance, and h_2 and $R_{ext_{h_2}}$ the values after a change in the relative humidity. In the case of the field test by National Grid, $h_1 = 80\%$, $R_{ext_{h_1}} = 1359.3\,\mathrm{M\Omega}$, $h_2 = 100\%$, and $R_{ext_{h_2}} = 430.6\,\mathrm{M\Omega}$. The correction factor to apply to insulator resistance to account for a modification in the relative humidity is [52]

$$R_{ext_{h_2}} = \frac{h_1}{2.5 h_2} R_{ext_{h_1}} \tag{4.15}$$

4.3 Conclusion

This chapter presented how to calculate the cable PUL parameters based on field test results.

The PUL resistance, inductance and capacitance are rarely calculated from surge tests but they provide a valuable extra backup information that is useful to identify the source of deviations between field tests and simulations. The calculation method was applied to a surge field test by RTE. Coaxial and inter-sheath mode parameters agree well. More deviation was found for the earth-return mode parameters because of the influence of the grounding resistance and the strong frequency dependency of the earth-return mode.

The calculation of the PUL conductance, i.e. the leakage resistance of cable insulation, requires a cable discharge test. The time to discharge a cable is determined by the cable capacitance, which is easily calculated from cable data or found on datasheets, by the leakage resistance of the cable insulation and by the leakage resistance of the insulators connected to the cable. The calculation of these values was demonstrated for two field tests presented in sections 3.3 and 3.5. Typical ranges of properties for cable insulation, cable capacitance and insulator equipment allowed the estimation of the typical discharge times required to lower the cable voltage to safe limits once the cable is out of service. This can go from a few minutes in case of a leaky system to several days if very little leakage is observed. A correction to the leakage resistance of insulators that accounts for changes in the air humidity was defined based on the field test result of section 3.5.

CHAPTER 5 SIMULATION OF FIELD TESTS

This chapter presents simulations carried out in EMTP-RV [65] of the three field tests presented in sections 3.1, 3.3 and 3.5: the surge test carried out by RTE-France on the 225 kV XLPE cable; the discharge test carried out in Japan on a 275 kV POF cable; and the discharge test carried out by National Grid, UK on a 275 kV OF cable. Simulation of the energising test carried out by RTE on the full cable will be shown in CHAPTER 6 to compare different models for cross-bonded cables.

Simulation of the surge test by RTE-France uses a frequency dependent cable model [12],[66],[67] with necessary corrections to account for wired conductors and semiconducting screens. Simulation and field test are compared in the terms of transient waveforms, wave attenuation, velocity and characteristic impedance. These are the usual parameters analyzed when validating a cable model for transient studies. A validation based on the PUL parameters calculated from field tests and EMTP was already demonstrated in section 4.1.4.

Simulation of the discharge tests in Japan and in the UK use simpler lumped RC models using the values of cable capacitance calculated from cable data and leakage resistances of cable insulation and insulators calculated from field tests in section 4.2. Comparison of voltage curves for simulation and field test validates the values estimated in section 4.2.

5.1 Surge test on the RTE 225 kV cross-bonded cable

5.1.1 Data input for cable data calculation function

The RTE 225 kV cable is modeled using a wideband phase-domain model [12],[66],[67]. The dimensions and electromagnetic properties of the cable are shown in Table 2.8. Semiconducting screens, stranded core conductors and the HDPE tubes enclosing each phase are features which cannot be directly handled by the cable model calculation function (CMDCF) in EMT-type software (e.g. EMTP-RV) and require corrections, as explained next.

5.1.1.1 Core and metallic sheath conductors

The metallic sheath of the Boutre-Trans cable is modeled as a hollow cylindrical conductor with resistivity of $2.84\times10^{-8}\,\Omega\text{m}$. The impact of eddy currents due to proximity between sheaths is neglected due to the wide separation between the cable phases.

The core conductor uses stranded enameled copper. The CMDCF can only model solid or hollow cylindrical conductors [61],[62],[63], which requires modifying the resistivity to account for the gaps between the copper wires which reduce the effective section of the core conductor. The core modified resistivity ρ' is calculated from the resistivity of copper $\rho=1.76\times10^{-8}\,\Omega\text{m}$, the core nominal area $A_n=\pi r_{2n}^2$, the actual area of the copper strands $A=\pi r_2^2$ and ρ, r_{2n} and r_2 found in Table 2.8 as in (A.60) (Appendix) resulting into $\rho'=2.6\times10^{-8}\,\Omega\text{m}$ and $\rho'=2.83\times10^{-8}\,\Omega\text{m}$ for the 2000 mm^2 and 2500 mm^2 core cables, respectively.

5.1.1.2 Core insulation and semiconducting screens

Even though cable semiconducting layers have an important impact in the propagation of coaxial waves [68],[69], CMDCF's generally do not offer an automatic way of including them in parameter calculations [61],[62],[63]. The impact of the semiconducting layers affects mostly the shunt admittance [68],[69] and they can be accurately accounted for by modifying the permittivity of the insulation to account for the new thickness as in (A.61), using ε_{r1}, r_2, r_3 and Δ from Table 2.8. The modified values of ε'_{r1} become 3.23 and 3.22 for the 2000 mm^2 and 2500 mm^2, respectively [20].

5.1.1.3 Outer insulation and HDPE tube

Due to the presence of the HDPE tubes, the outer insulation of the sheath is composed of three layers, i.e. the cable outer insulation, the air gap, and the HDPE tube, which are not concentric. To the best of the author's knowledge, no analytical formula of impedance or admittance exists for such a system.

The modeling of the RTE cable used an equivalent sheath insulation which is concentric and has outer radius r_5 (in Table 2.8). The relative permittivity of the equivalent insulation was calculated from the capacitance obtained from field test results of inter-sheath mode capacitance (Table 2.11)

and becomes $\varepsilon_{r2_{eq}} = 0.321$ [20]. A permittivity lower than 1 is a result of representing a non-homogeneous dielectric by an equivalent insulation of smaller dimensions. A cable capacitance calculated through FEM agreed with the capacitance obtained via the field tests [83]. A cable capacitance calculated using the approximated approach in appendix A.4.3 gives 0.339, which is also close to the value calculated from the field test results.

5.1.1.4 Connection wires and cross-bonding points

The connection wires used to connect the surge tester to the minor section had 5 m and those to connect to the major section had 20 m. The wires are modeled by 5 μH and 20 μH inductances [20] (considering 1 μH/m [17]), respectively.

The major section model represents separately each minor section and the sheath cross-bonding wires are modeled through 20 μH inductances [20].

5.1.1.5 Earth-resistivity and grounding resistance

The local soil resistivity measured by RTE is 100 Ωm and the grounding resistance for the measuring circuit is 30 Ω [20].

The grounding resistance is 30 Ω for the remote areas (both terminals of the minor section and receiving end of the major section) and 5 Ω for the substation [20].

5.1.2 Simulation of field tests on a minor section

5.1.2.1 Comparison of propagation constants

The field tests on the minor section are simulated separately for coaxial, inter-sheath and earth-return modes. A comparison between the field tests and simulation results is given in Table 5.1, with V_{init} and I_{init} referring respectively to the initial voltage and current peaks at the cable sending end. The ratio V_{init} / I_{init} allows calculating Z_c. The propagation speeds are found from waveform oscillating periods in EMTP and field tests.

Table 5.1 Field test and simulation results on the RTE 225 kV cable, minor section [20].[5]

Mode	Source	$V_{init}\,(\mathrm{V})$	$I_{init}\,(\mathrm{A})$	$v\,(\mathrm{m/\mu s})$	$Z_c\,(\Omega)$
Coaxial	Field	1752	68.70	157.7	25.5
	EMTP	1769	76.57	159.4	23.1
Inter-sheath	Field	1221	49.01	114	24.9
	EMTP	1067	46.44	111.9	23.0
Earth-return	Field	1767	27.04	63.1	65.3
	EMTP	1868	27.30	35.4	68.4

The values in Table 5.1 can be further validated by comparison with typical range of propagation velocity and surge impedance of coaxial and earth-return modes collected from field tests carried out in Japan on more than twenty cable systems [17],[18],[24]. For the coaxial mode, the velocity is within 137-160 m/μs and the surge impedance is 13-30 Ω, independently of the type of cable. This is reasonable because the characteristics of the coaxial mode are determined by the radii of core and sheath conductors and the relative permittivity of the core insulation. On the contrary, the earth-return mode shows a wide range of values for velocity and surge impedance. The tunnel-installed cable can be compared to an overhead line, and the characteristics of the pipe-type cable are quite dependent on the size of the pipe and the permittivity of the insulation inside the pipe [18]. The velocity can be as high as 150-170 m/μs for tunnel installed cables or as low as 30-70 m/μs in the case of pipe-type and directly buried cables. The surge impedance can be as low as 5 Ω for direct burial and pipe-type, or as high as 100 Ω in the case of tunnel-installed cable.

The measured results in Table 5.1 show a satisfactory agreement with those referred above, and thus it can be concluded that the measured results on the RTE 225 kV cable are within a valid range.

5.1.2.2 Coaxial mode

The setup for this test is given in Figure 5.1. The IG current and the receiving end voltage are compared in Figure 5.2 and Figure 5.3. The initial voltage peak at the sending end (not shown) is 1769 V in EMTP. The values at the receiving end are 3485 V in EMTP and 3480 V in field test, that is, nearly the double of the sending end voltage. This is expected given that the receiving end is open-circuited and the coaxial mode attenuation is in general low. The maximum peak current

is 76.57 A in EMTP and 68.7 A in the field test. The characteristic impedances calculated in Table 5.1 are in agreement with the formula [18],[24]

$$Z_c = \left(60/\sqrt{\varepsilon_\eta}\right)\ln\left(r_3/r_2\right) \tag{5.1}$$

which results into 22.9 Ω. The periods of oscillations are 27.1 μs for EMTP and 27.4 μs for field test and allow calculating the propagation speeds in Table 5.1.

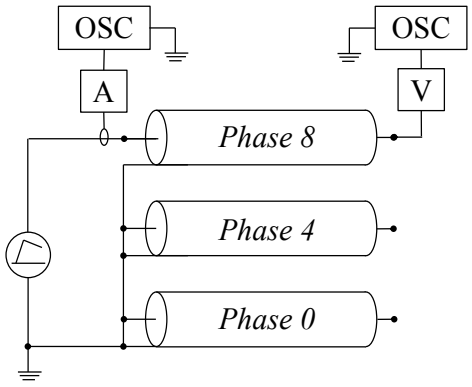

Figure 5.1 Field test setup for coaxial mode excitation in a minor section of the RTE 225 kV cable [20].

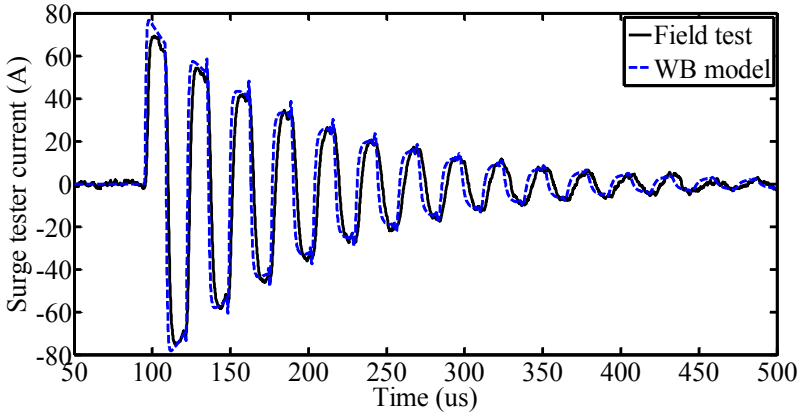

Figure 5.2 Field test and simulation results of coaxial mode current [20]. [11]

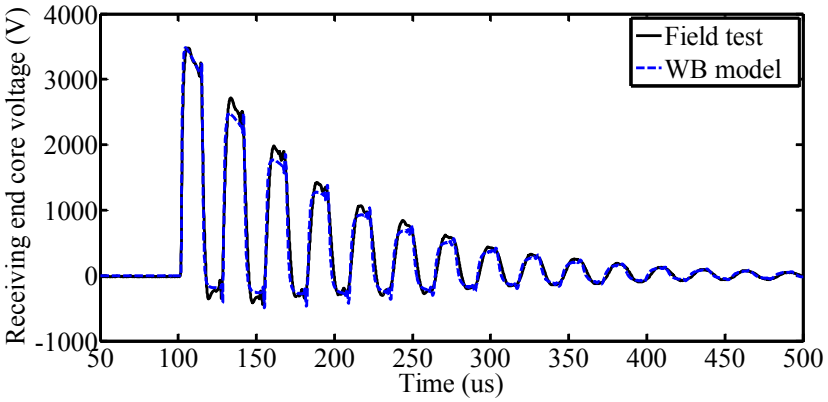

Figure 5.3 Field test and simulation results of receiving end voltage for coaxial mode excitation in minor section [20]. [11]

5.1.2.3 Inter-sheath mode

The setup for this test is given in Figure 5.4. The IG current and the receiving end voltage are shown in Figure 5.5 and Figure 5.6.

The periods of oscillations are estimated from Figure 5.5 as 38.6 μs in EMTP and 38.0 μs in field test, which result into the velocities given in Table 5.1. The agreement between field test and simulation results is sufficiently good, but there is a small difference in propagation velocities that becomes more evident after the second cycle, particularly for the case of the receiving end voltage. Though not shown, the voltage peak measured at the sending end of the metallic sheath, that is, after the lead wire, is 1067 V in EMTP and 1221 V in the field test (see Table 5.1). The voltage difference between sheath-8 and sheath-4 is 1221+551.6=1772.6 V.

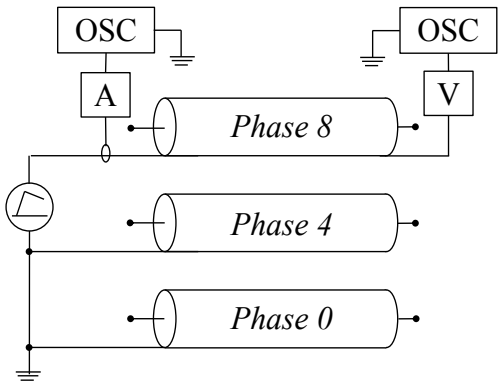

Figure 5.4 Field test setup for inter-sheath excitation in a minor section [20].

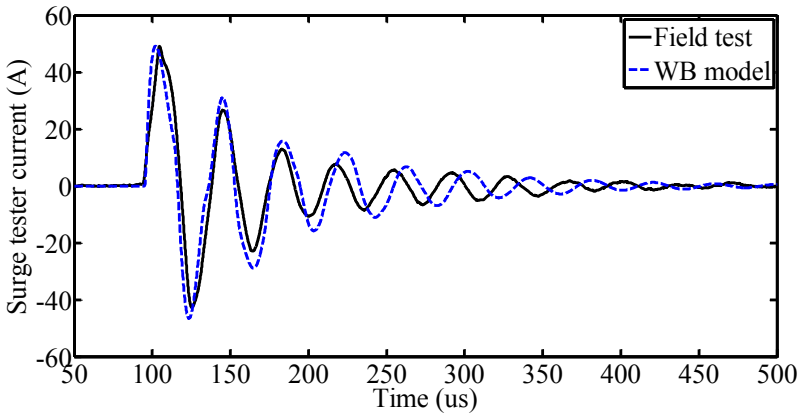

Figure 5.5 Field test and simulation results of sheath current for inter-sheath mode excitation in a minor section [20]. [11]

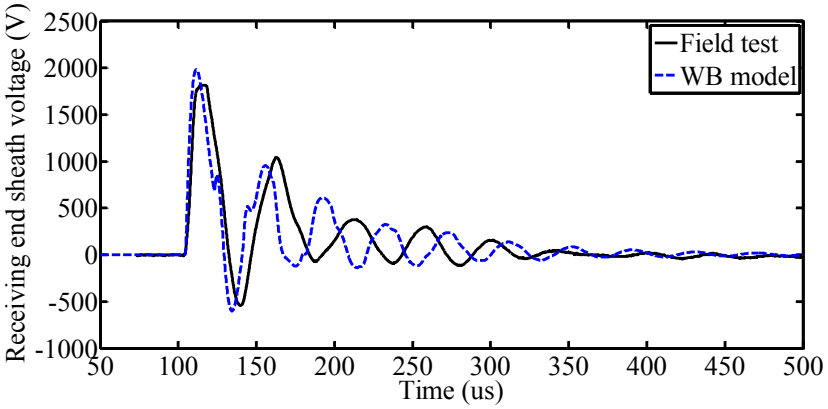

Figure 5.6 Field test and simulation results of receiving end sheath voltage for inter-sheath mode excitation in a minor section [20]. [11]

5.1.2.4 Earth-return mode

The setup for this test is given in Figure 5.7. The IG current is shown in Figure 5.8. The earth-return mode shows an over-damped regime, with no oscillations from which we can calculate the propagation velocity and this had to be estimated approximately from $1/\sqrt{L'C'} = 63.1$ m/μs in field test (see Table 2.11). The agreement between field test and simulation results is good for the current peak but they deviate in the following instants with the simulated current lagging the measured curve.

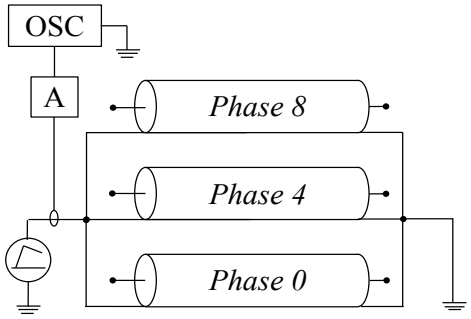

Figure 5.7 Field test setup for earth-return mode excitation in a minor section [20].

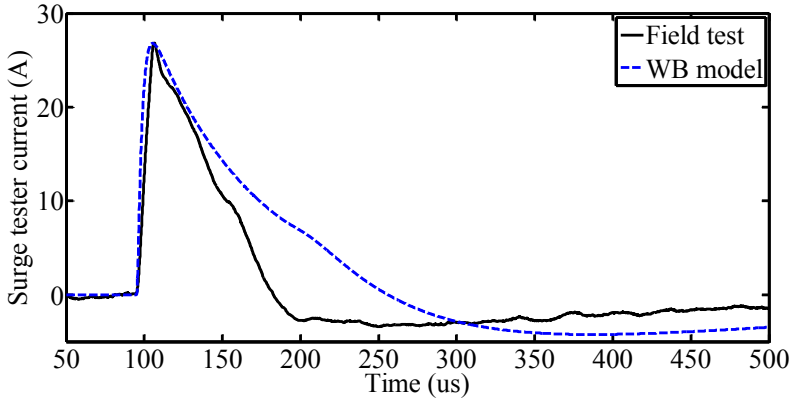

Figure 5.8 Field test and simulation results of sending end current for earth-return mode excitation in a minor section [20]. [11]

5.1.3 Simulation of field tests on a major section

A summary on the comparison between field tests and simulations is presented in Table 5.2.

Table 5.2. Field test and simulation results on the RTE 225 kV cable, major section [20].[5]

Mode	Source	V_{init} (V)	I_{init} (A)	v (m/μs)	Z_c (Ω)
Coaxial	Field	1697	75.36	158	22.97
	EMTP	1615	75.97	142	21.3
Inter-sheath	Field	1817	46	132	39.5
	EMTP	1622.6	46.29	151	35.0
Earth-return	Field	1892	69.5	35.1	27.22
	EMTP	1659	55.97	35.3	29.64

5.1.3.1 Coaxial mode

The setup for this test is given in Figure 5.9. The IG current and the sending end core voltage are shown in Figure 5.10 and Figure 5.11. The voltage results agree well. The current results agree well too in the first peak but they deviate in the following peaks with the measured result lagging the simulated curve.

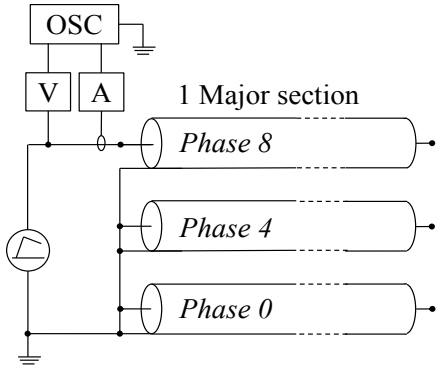

Figure 5.9 Field test setup for coaxial mode excitation in a major section [20].

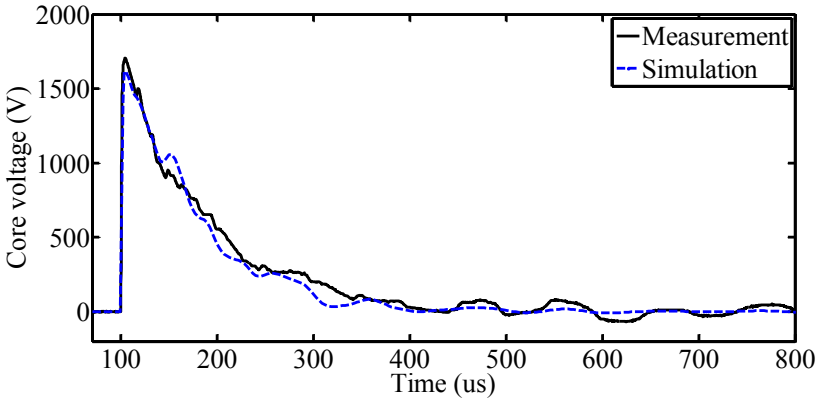

Figure 5.10 Field test and simulation results of core voltage for coaxial mode excitation on a major section [20].[12]

[12] Circuits: CableSimulation_Files\FieldTestSimulation_RTECable\EMTPCirc_MajorSection\Major_Section.ecf
Plotting: CableSimulation_Files\FieldTestSimulation_RTECable\Plotting\Plotting_MajorSection.m

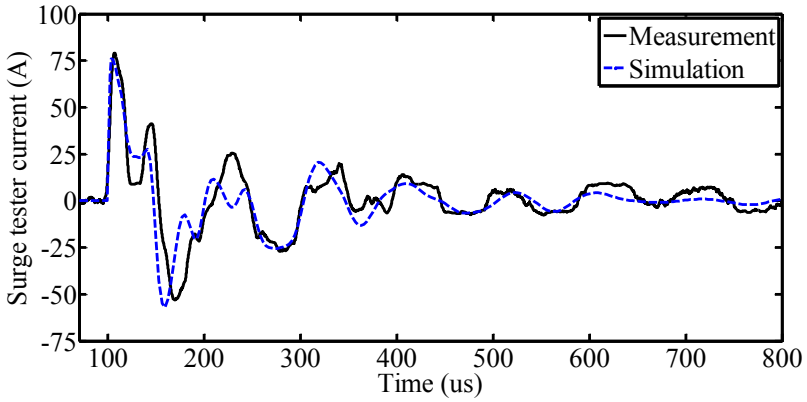

Figure 5.11 Field test and simulation results of IG current for coaxial mode excitation on a major section [20].[12]

5.1.3.2 Inter-sheath mode

The setup for this test is given in Figure 5.12. The sending end core and sheath voltages and the IG current are given in Figure 5.13 and Figure 5.14. It is observed that the core voltages are oscillatory whereas the sheath voltages follow early the voltage of the surge tester. The peak voltage between the two sheaths is obtained from the difference of voltages as 788.9+833.7 = 1622.6 V (1817 V in the field test). The characteristic impedance and velocity found in Table 5.2 are very different from those of the inter-sheath mode on a minor section given in Table 5.1. This is because the propagation modes on a normal-bonded and on a cross-bonded cable are not the same [15],[53],[70]. The agreement between field test and simulation is good, but the measured results lag the simulated curves. Also the simulated sheath voltage is more irregular than the measured result and the simulated IG current is less damped than the measured current.

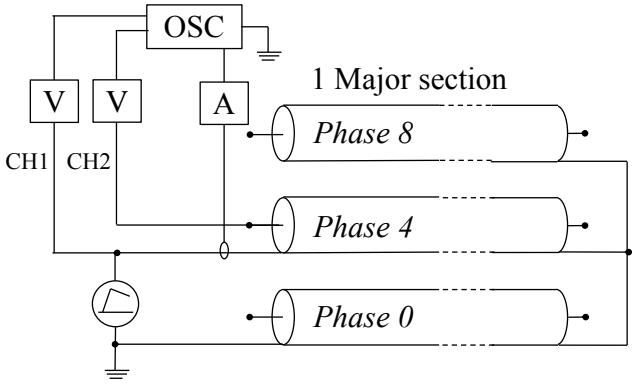

Figure 5.12 Field test setup for inter-sheath excitation in a major section [20].

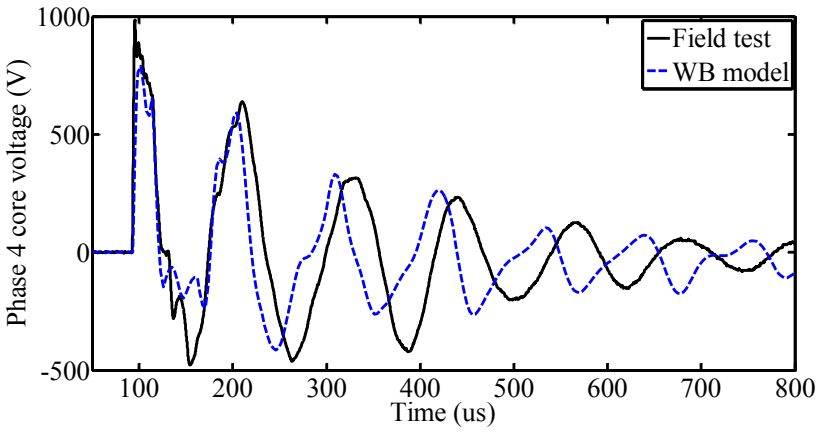

Figure 5.13 Field test and simulation results of phase-4 core voltage for inter-sheath excitation between phases 0 and 4 in a major section [20]. [12]

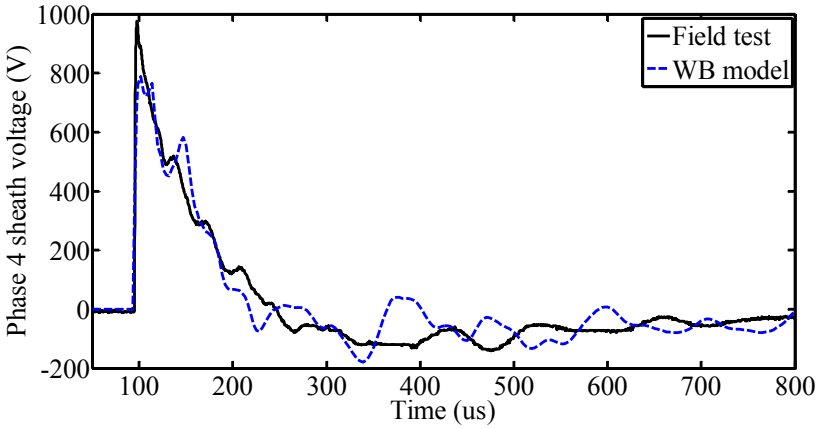

Figure 5.14 Field test and simulation results of phase-4 sheath voltage for inter-sheath excitation between phases 0 and 4 in a major section [20]. [12]

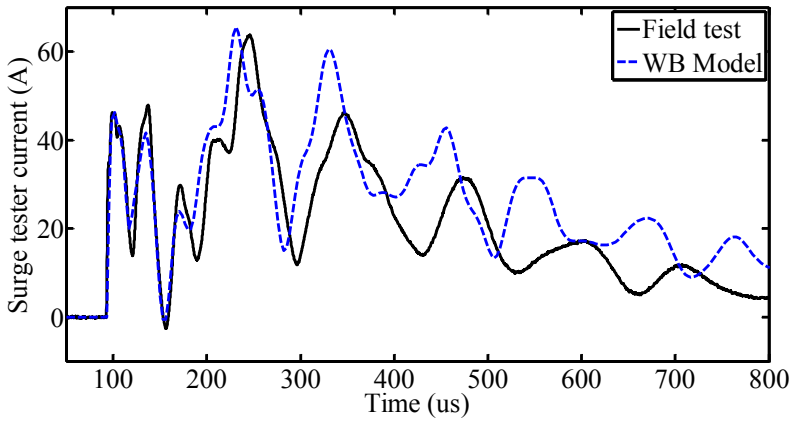

Figure 5.15 Field test and simulation results of IG current for inter-sheath excitation between phases 0 and 4 in a major section [20]. [12]

5.1.3.3 Earth-return mode (sheaths grounded)

The setup for this test is given in Figure 5.16. The IG current and the sending end core voltage are given in Figure 5.17 and Figure 5.18. The voltage curves agree in general but the simulated voltage peak is lower than the measured value. As a consequence, the simulated current peak is lower than the measured value too.

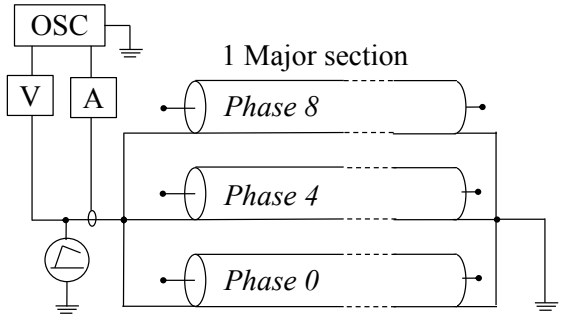

Figure 5.16 Field test setup for earth-return mode excitation in a major section [20].

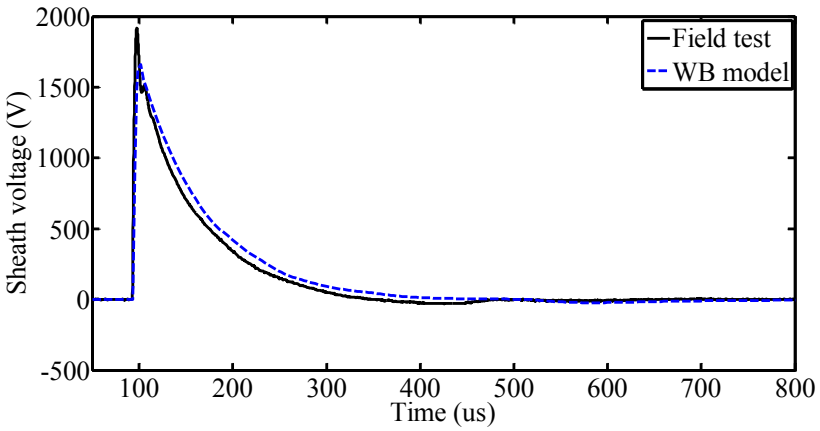

Figure 5.17 Field test and simulation results of sheath voltage for earth-return mode excitation in a major section with sheaths short-circuited [20]. [12]

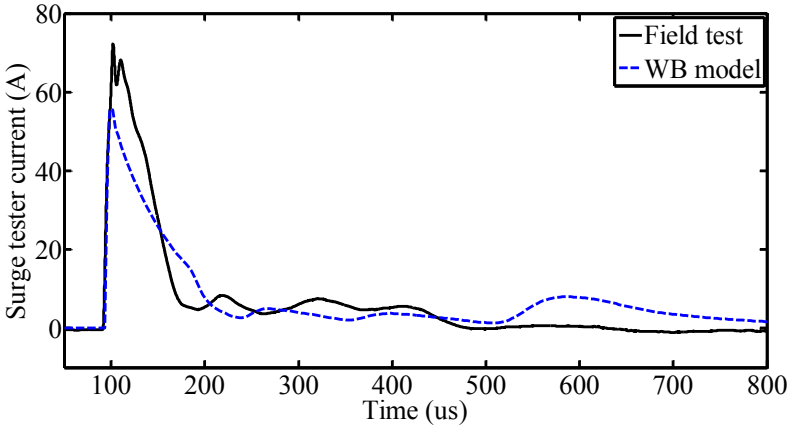

Figure 5.18 Field test and simulation results of IG current for earth-return mode excitation in a major section with sheaths short-circuited [20]. [12]

5.2 275 kV pipe-type pressurized-oil-filled cable in Japan

The paper in which the field test of Figure 2.83 was first published [21] gives estimated values of leakage resistance which result in a discharge time nearly half (49 min) of that observed in the field test (88 min). This means that the leakage in the system was not as severe as estimated and the components presented a resistance higher than expected.

Cable leakage resistance is calculated using half of the resistivity for paper insulation in Table 2.12, i.e. $\rho = 500 \times 10^{12}\ \Omega$-m, together with $n = 3$, $l = 20 \times 10^{3}$ m, $r_{in} = 26.65$ mm and $r_{out} = 40.65$ mm in Table 2.10 into (4.10) and (3.3) resulting into $R_{cable} = 560.0\ \mathrm{M}\Omega$.

The lower value of resistivity is based on typical insulation properties in PT-POF cables of 1970's, which have been improved since then [71].

The leakage resistance of external components is calculated using the surface resistance of EPDM $\rho = 210 \times 10^3\ \Omega/\text{mm}$ in Table 2.14 and a leakage distance of $d_{leak} = 5000\,\text{mm}$ into (4.12) and (4.14) resulting $R_{ext} = R_{insulator} = 1050\,\text{M}\Omega$.

The total leakage resistance is calculated as $R_{total} = R_{cable} \parallel R_{ext} = 365.2\,\text{M}\Omega$. The time constant of the system is obtained using this value and the cable capacitance $C_{cable} = 29.3\,\mu\text{F}$ into (3.8) resulting $\tau = 178.3\,\text{min}$.

The time required to discharge the cable from $v(t_1) = 414\,\text{kV}$ to $v(t_2) = 250\,\text{kV}$ is calculated using $\tau = 178.3\,\text{min}$ into (3.8) as $t_2 - t_1 = 89.9\,\text{min}$. This value is only 5% above the one observed in the field tests (88 min).

The values of leakage resistance for cable insulation and external circuit calculated above, were used to simulate the field test in Figure 2.83. The circuit used to simulate the cable system is shown in Figure 5.19. The 20 km cable is modeled using a parallel *RC* circuit using the parameters of cable insulation for 3 phases in parallel, that is, $C_{cable} = 29.3\,\mu\text{F}$ and $R_{cable} = 560.0\,\text{M}\Omega$. The leakage of external circuit is $R_{ext1} = R_{ext2} = 1050\ \text{M}\Omega$. Other circuit parameters (defined in section 3.3) are

$V_0 = 414\,\text{kV}$, voltage of DC generator,

$R_0 = 138\,\text{M}\Omega$, charging resistance,

$R_W = 30\ \text{M}\Omega$, resistor used for full discharge.

The switch S_0 is closed from $t = 0$ to $t = 60$ min and S_W closes at $t = 148$ min (S_0 being open).

The simulation result in Figure 5.20, agrees with the field test result of Figure 2.83, which validates the modeling approach.

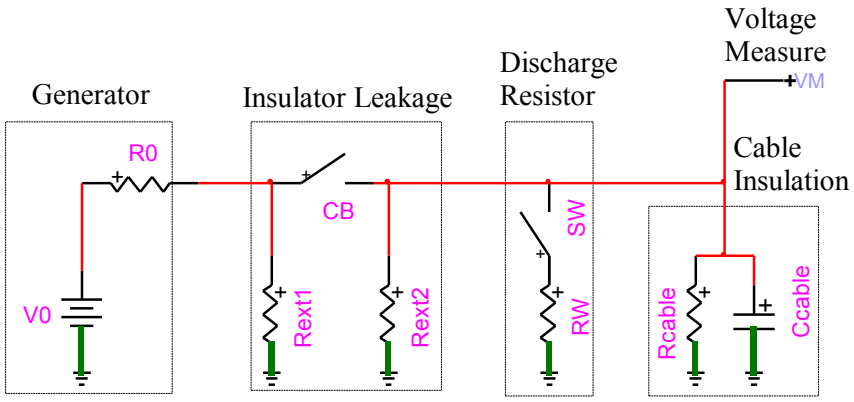

Figure 5.19 Circuit for simulation of field test in Figure 2.82 [52].

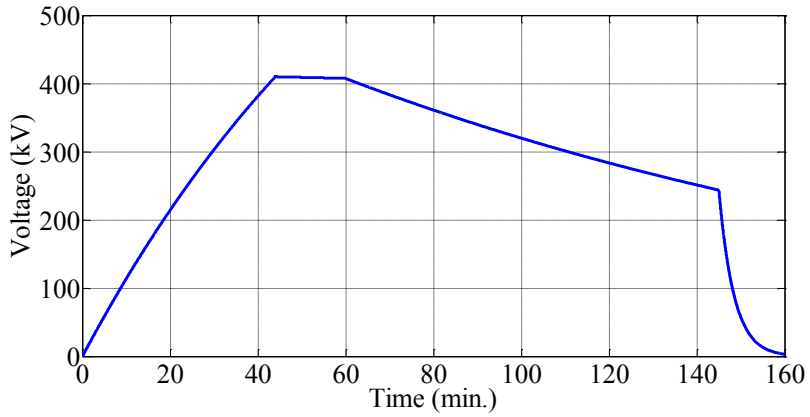

Figure 5.20 Simulation of charging/discharging voltage [52].[13]

5.3 National Grid, UK 275 kV oil-filled cable

From the test result in Figure 2.87 and from the value of cable capacitance, the total leakage resistance of the system has been estimated as 840.2 MΩ for low humidity and 360.1 MΩ for increased humidity. Cable leakage resistance is calculated using (4.10) and (3.3) with the resistivity for paper insulation $\rho = 1000 \times 10^{12}\,\Omega/\mathrm{m}$ in Table 2.12, $l = 21 \times 10^{3}\,\mathrm{m}$, $r_{in} = 29.75\,\mathrm{mm}$ and $r_{out} = 40\,\mathrm{mm}$ in Table 2.10, resulting into $R_{cable} = 2.2\,\mathrm{G}\Omega$.

[13] Circuits: CableSimulation_Files\CableDischarge\EMTP_Circuits.ecf

Plotting: CableSimulation_Files\CableDischarge\Plot_FieldTests.m

The leakage resistance for 3 insulators in parallel (2 insulator poles and cable sealing end) is calculated using $p = 3$, the surface resistance of silicone $\rho = 5300 \times 10^3\ \Omega/\text{mm}$ in Table 2.14 and a leakage distance of $d_{leak} = 5334\,\text{mm}$ (supplied by National Grid) into (4.12) and (4.14) resulting into $R_{ext} = 9.4\,\text{G}\Omega$. With previously found $R_{cable} = 2.2\,\text{G}\Omega$, the total leakage resistance is calculated as $R_{total} = R_{cable} \parallel R_{ext} = 1811.4\,\text{M}\Omega$. This value is about 2 times the value observed in the field tests (840.2 MΩ). However, it must be observed that the calculated insulator resistance considers uncontaminated material. With a total leakage resistance of $R_{total} = 840.2\,\text{M}\Omega$ calculated from the field test in Section 0, the leakage resistance of external components can be re-evaluated from

$$\frac{2200 \times R_{ext}}{2200 + R_{ext}} = 840.2\,\text{M}\Omega,\ R_{ext} = 1359.3\,\text{M}\Omega$$

Using $R_{total} = 360.1\,\text{M}\Omega$ instead of 840.2 MΩ, results into $R_{ext} = 430.6\,\text{M}\Omega$ when humidity rises to 100%.

The field test in Figure 2.87 was simulated using the circuit in Figure 5.21. The cable is modeled with a parallel *RC* circuit using the parameters of its insulation, that is $R_{cable} = 2.2\,\text{G}\Omega$ and $C_{cable} = 15.0\ \mu\text{F}$. The leakage in the external circuit (2 insulator poles and cable bushing) is modeled with a time varying resistance to account for the rise in ambient humidity during the field test. The values for this leakage resistance are given in Table 5.3. The charging resistance is $R_0 = 100\ \text{M}\Omega$ (calculated from the rise time of voltage in Figure 2.87). Figure 5.22 shows the simulated discharge voltage of the cable and the agreement with the field test result in Figure 2.87 is evident.

Table 5.3. Data for the Resistance R(t) in the circuit of Figure 5.21 [52].

Time	0h	0h30	3h15	10h00
Resistance (MΩ)	1359.3	1359.3	430.6	430.6

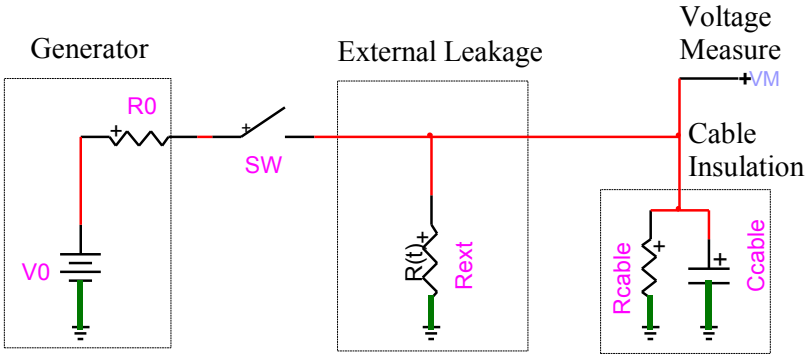

Figure 5.21 Circuit for simulation of discharging of a 275kV POF-cable in the UK [52].

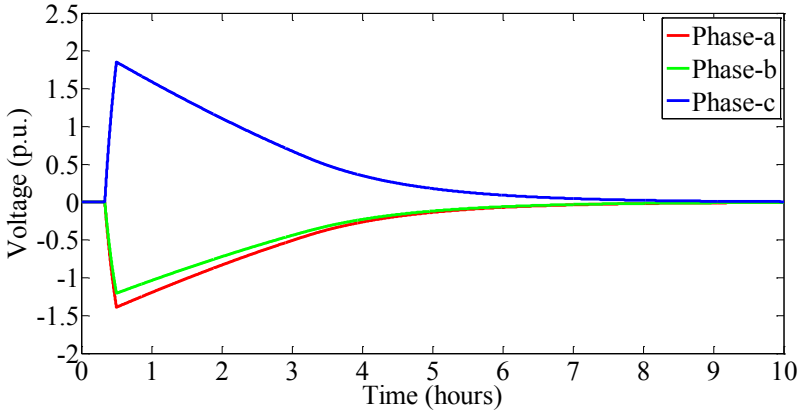

Figure 5.22 Simulation of discharge of a POF-cable in the UK [52].[13]

5.4 Conclusion

This chapter presented the simulation of three field tests performed on underground cables. The first case was a surge test carried out on a 225 kV XLPE underground cable of 64 km. The measurements were carried out on a minor and a cross-bonded major sections of the cable. A wideband cable model was used in the EMTP simulations and the results are in sufficiently good agreement with the field test. The most important differences are observed for the excitation of the earth-return mode, which is highly dependent on frequency, humidity and temperature, and for which the actual test setup conditions are more difficult to identify. The second and third field tests simulated are cable discharge tests carried out on a 275 kV PT-POF cable in Japan and on a 275 kV POF cable in the UK. The cables were modeled by simple parallel *RC* circuits based on the cable capacitance and the leakage resistances of the cable insulation and external insulator equipment. Good agreement was achieved between simulated and field test measured values.

CHAPTER 6 CROSS-BONDED CABLES

This chapter is dedicated to investigating cross-bonded cables used for HVAC power transmission.

At a first stage, different cable bonding methods are analyzed and compared in terms of propagation characteristics (attenuation and velocity), frequency domain and time domain responses. A clear knowledge of the propagation characteristics is extremely relevant for fault detection [45]-[47] and harmonics studies [44] involving cross-bonded cables as they require knowledge of modal propagation velocities.

The impact of non-uniformities, in particular the grounding and the cross-bonding of the sheaths is investigated in detail in this chapter. Grounding of cable sheaths is somehow analogous to the grounding of the shield wires in overhead lines. Even though there are several articles studying the impact of shield wire grounding in OHL's [72]-[76], there is no similar literature studying the impact of sheath grounding on the propagation characteristics of cables. The few references in the literature referring the impact of sheath grounding, consider time domain responses only [14],[77]. The mechanism through which the cross-bonding and the sheath currents affect the cable response is also clarified.

Different modeling of a long cross-bonded cable, including both homogeneous and non-homogeneous equivalents, are compared based on frequency and time domain responses. The models are also compared for the simulation of the field test on a 225 kV cross-bonded cable with 64 km and 17 major sections presented in section 3.2.

A general method for evaluating propagation constants (attenuation and velocity) of non-homogeneous transmission systems, including cross-bonded cables, without requiring any prior knowledge of the system is explained. The method uses the frequency scan of the open-circuit response of the system.

Finally, fault location on cross-bonded systems is discussed and a single-terminal method based on the frequency response of the system is demonstrated.

6.1 Comparison between different bonding methods

The most common cable bonding methods for high voltage cables are illustrated in Figure 6.1. Normal-bonding or no bonding at all is used for short cables and for submarine links. Cross-

bonding by transposition of sheaths is used for example in France, Denmark, and Japan. Sheath cross-bonding with transposition of cores also called Kirke-Searing bonding is used in the U.K. and Japan. Other bonding schemes shown in Figure 6.1 are same-sense and counter-sense transposition of cores and sheaths. Although these are less common bonding schemes, they are considered in this chapter for completeness of the analysis.

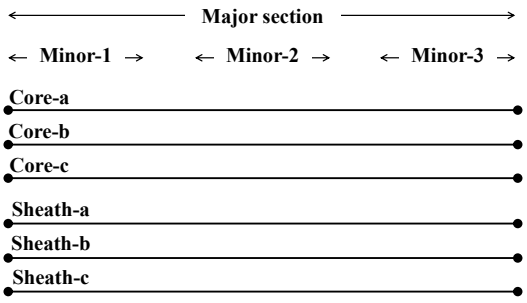

a) normal-bonding of cores and sheaths.

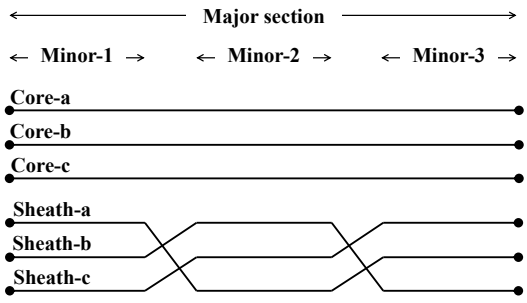

b) cross-bonding of sheaths.

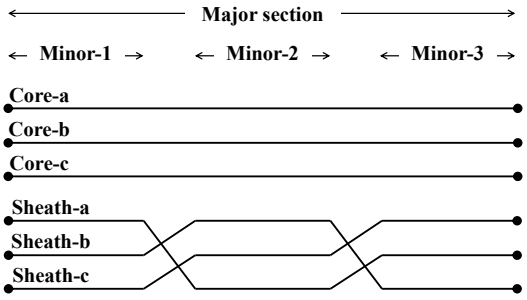

c) transposition of cores, normal-bonding of sheaths.

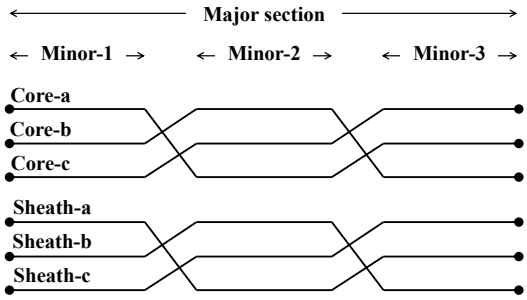

d) same-sense cross-bonding of cores and sheaths.

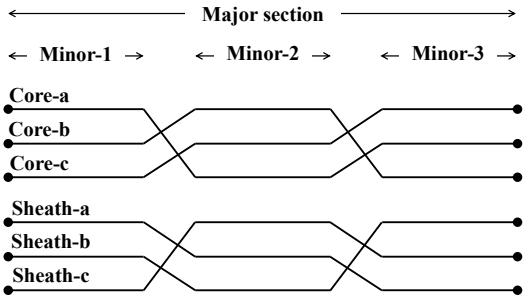

e) counter-sense cross-bonding of cores and sheaths.

Figure 6.1 Power cable bonding schemes.

6.1.1 Propagation characteristics of different bonding schemes

The cable in Figure 6.2 is used as an example to illustrate the differences in propagation characteristics for the different bonding schemes shown in Figure 6.1.

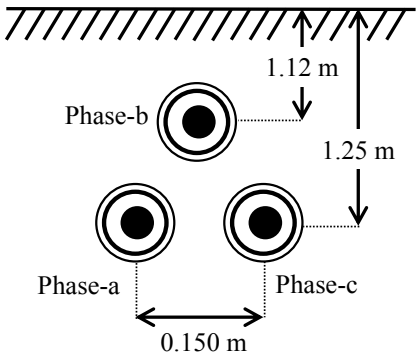

Figure 6.2 Layout of the cable [51].

Table 6.1 Data of a three-phase underground cable [51].

Parameter	Value
Core conductor	$r_1 = 0$, $r_2 = 28.4$ mm, $\rho = 2.6\times10^{-8}$ Ωm
Core insulation	$\varepsilon_{r1} = 3.23$, $\tan\delta = 0.0008$
Metallic sheath	$r_3 = 56.4$ mm, $r_4 = 57.2$ mm, $\rho = 2.84\times10^{-8}$ Ωm
Outer insulation	$r_5 = 62.2$ mm, $\varepsilon_{r2} = 0.321$, $\tan\delta = 0.001$

The nature of propagation modes for the different bonding methods can be observed from the current transformation matrices calculated at a high frequency (1 MHz)

$$\left(\mathbf{T}_\mathbf{i}^N\right)^T = \begin{bmatrix} 0.57 & -0.707 & -0.41 & 0 & 0 & 0 \\ 0.59 & 0 & 0.81 & 0 & 0 & 0 \\ 0.57 & 0.707 & -0.41 & 0 & 0 & 0 \\ -0.57 & 0.707 & 0.41 & 0.81 & 1 & -0.59 \\ -0.59 & 0 & -0.81 & 0.83 & 0 & 1.15 \\ -0.57 & -0.707 & 0.41 & 0.81 & -1 & -0.59 \end{bmatrix} \begin{matrix} \text{core-a} \\ \text{core-b} \\ \text{core-c} \\ \text{sheath-a} \\ \text{sheath-b} \\ \text{sheath-c} \end{matrix} \tag{6.1}$$

$$\left(\mathbf{T}_\mathbf{i}^X\right)^T = \begin{bmatrix} 0.58 & 0.71 & -0.41 & 0 & 0 & 0 \\ 0.58 & 0 & 0.82 & 0 & 0 & 0 \\ 0.58 & -0.71 & -0.41 & 0 & 0 & 0 \\ -0.58 & 0 & 0 & 0.82 & 0.72 & -0.25 \\ -0.58 & 0 & 0 & 0.82 & 0.03 & 0.83 \\ -0.58 & 0 & 0 & 0.82 & -0.75 & -0.58 \end{bmatrix} \tag{6.2}$$

$$\left(\mathbf{T_i}^{K}\right)^{T} = \left[\begin{array}{c|c|c|c|c|c} 0.58 & -0.07 & 0.82 & 0 & 0 & 0 \\ 0.58 & -0.68 & -0.41 & 0 & 0 & 0 \\ 0.58 & 0.74 & -0.41 & 0 & 0 & 0 \\ -0.58 & 0 & 0 & 0.81 & -0.71 & -0.41 \\ -0.58 & 0 & 0 & 0.83 & 0 & 0.81 \\ -0.58 & 0 & 0 & 0.81 & 0.71 & -0.41 \end{array}\right] \tag{6.3}$$

$$\left(\mathbf{T_i}^{SX}\right)^{T} = \left[\begin{array}{c|c|c|c|c|c} 0.58 & 0 & 0.82 & 0 & 0 & 0 \\ 0.58 & 0.77 & -0.14 & 0 & 0 & 0 \\ 0.58 & -0.77 & -0.68 & 0 & 0 & 0 \\ -0.58 & 0 & -0.82 & 0.82 & 1.19 & -0.31 \\ -0.58 & -0.77 & 0.14 & 0.82 & -0.74 & -0.84 \\ -0.58 & 0.77 & 0.68 & 0.82 & -0.45 & 1.15 \end{array}\right] \tag{6.4}$$

$$\left(\mathbf{T_i}^{CX}\right)^{T} = \left[\begin{array}{c|c|c|c|c|c} 0.58 & 0 & 0.78 & 0 & 0 & -0.12 \\ 0.58 & -1.26 & 0.73 & 0 & 0.11 & 0.07 \\ 0.58 & 1.26 & -1.51 & 0 & -0.11 & 0.05 \\ -0.58 & 0.54 & -0.65 & 0.82 & 0.74 & -0.34 \\ -0.58 & -0.54 & 0.32 & 0.82 & -0.74 & -0.50 \\ -0.58 & 0 & 0.32 & 0.82 & 0 & 0.84 \end{array}\right] \tag{6.5}$$

Superscripts used in (6.1) to (6.5) are *N* for normal-bonded, *X* for cross-bonded, *K* for Kirke-Searing, *SX* for same-sense cross-bonding and *CX* for counter-sense cross-bonding. Each matrix column represents an eigenvector and a propagation mode. The first three columns correspond to core modes and the remaining are sheath modes. Both cores and sheaths have a zero-sequence mode, a two-phase mode and a three-phase mode.

The eigenvectors for zero-sequence core and sheath modes are equal for all bonding schemes. On the contrary, inter-phase core and sheath mode eigenvectors are in general different.

One important difference between bonding schemes is observed for the inter-phase core modes. For normal-bonding in (6.1), the two inter-core modes are in fact combinations of single-phase coaxial modes. The same is not observed in (6.2) and (6.3). It is thus concluded that single-phase coaxial modes cannot propagate in cables with cross-bonded of Kirke-Searing bonding method. This is explained by the fact that in these systems, one core is not shield by the same sheath

throughout the length of a major section. Thus, when applying a voltage between the core and sheath of one phase at the sending end a signal will propagate to all the three phases.

Table 6.2 and Table 6.3 shows modal attenuations and velocities calculated at 50 Hz and 1 MHz, respectively, for the cable in Figure 6.2 using the bonding schemes in Figure 6.1. Numbers 1 to 6 are used for the modes and they correspond to the same columns in the matrices of Table 6.2 and Table 6.3. The same numbering is used in Figure 6.3 and Figure 6.4 which show the evolution with frequency of modal attenuations and velocities.

It is clear from Table 6.3 that normal-bonded and same-sense cross-bonded systems have three coaxial modes characterized by the same attenuation and same propagation velocity given by $c/\sqrt{\varepsilon_r} = 300/\sqrt{3.23} = 167\,\mathrm{m/\mu s}$ ($c = 300\,\mathrm{m/\mu s}$ is the light velocity and $\varepsilon_r = 3.23$ is the relative permittivity of the cable insulation). These two systems have in common that the sheaths do not change their phase throughout the cable route.

On the contrary, the systems in which the sheaths change phase (cross-bonded, Kirke-Searing and counter-sense cross-bonded) have two inter-core modes which characteristics are very different from those of a coaxial mode. In this case, they have higher attenuation and lower velocity.

The zero-sequence core and sheath modes are the same for every bonding scheme. Also, as expected, the systems with sheath transposition have two equal inter-sheath modes and the systems with core transposition have two equal inter-core modes.

From the frequency profile of attenuation and velocity in Figure 6.3 and Figure 6.4 it can be observed that the core modes in normal-bonded and same-sense cross-bonded systems change nature as frequency increases. They start as inter-core modes and become coaxial modes after a certain frequency. The frequency at which this occurs is the same as the frequency for which the inter-sheath mode velocities become nearly constant and correspond to the penetration depth on the sheath becoming smaller than the sheath thickness.

The above observations are also valid for the propagation characteristics at 50 Hz, shown in Table 6.2. Although the different bonding schemes still present different characteristics even at power frequency, it could be said that the same-sense cross-bonded system presents a similar response to core modes as the normal-bonded system and the counter-sense cross-bonded system has a similar response as the Kirke-Searing system. Therefore, a same-sense cross-bonded system could be

modeled as a normal-bonded cable and a counter-sense cross-bonded system could be modeled as a Kirke-Searing system without much loss of accuracy.

Table 6.2 Attenuation and velocity of propagation modes for different bonding schemes, 50 Hz.

Bonding	Attenuation α [dB/km]						Velocity v [m/μs]					
	1	2	3	4	5	6	1	2	3	4	5	6
N	17.2	1.64	1.77	12.1	31.3	32.3	103	124	135	18.9	69.0	70.9
X	17.2	1.96	1.96	12.1	29.1	29.1	103	102	110	18.9	64.7	64.7
K	17.2	1.88	1.88	12.1	28.2	30.0	103	106	106	18.9	62.7	66.8
SX	17.2	1.68	1.68	12.1	31.8	31.8	103	129	129	18.9	69.9	69.9
CX	17.2	1.95	1.95	12.1	29.1	29.1	103	106	106	18.9	64.7	64.7

N – normal-bonding; X – cross-bonding; K – Kirke-Searing; SX – same-sense cross-bonding; CX – counter-sense cross-bonding.

Table 6.3 Attenuation and velocity of propagation modes for different bonding schemes, 1 MHz.

Bonding	Attenuation α [dB/km]						Velocity v [m/μs]					
	1	2	3	4	5	6	1	2	3	4	5	6
N	0.65	0.65	0.65	222	0.89	0.78	167	167	167	28.7	101	120
X	0.65	0.88	0.83	222	0.95	0.95	167	108	119	28.7	89.1	89.1
K	0.65	0.83	0.83	222	1.07	0.95	167	113	113	28.7	98.0	82.2
SX	0.65	0.65	0.65	222	0.79	0.79	167	167	167	28.7	109	109
CX	0.65	0.79	0.79	222	0.98	0.98	167	115	115	28.7	88.0	88.0

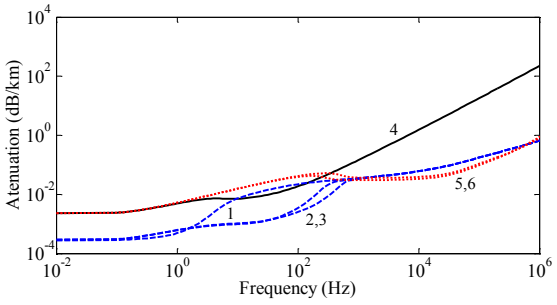

a) normal-bonding of cores and sheaths.

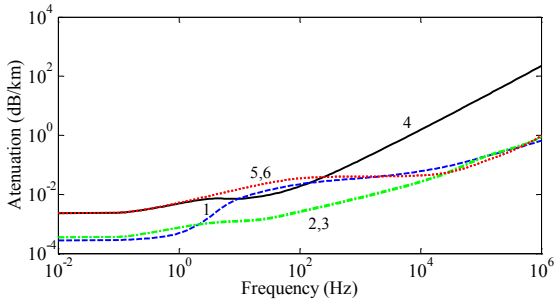

b) cross-bonding of sheaths.

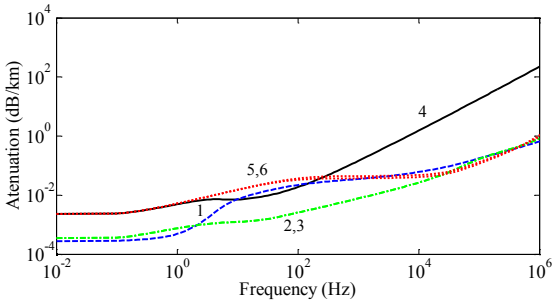

c) transposition of cores, normal-bonding of sheaths.

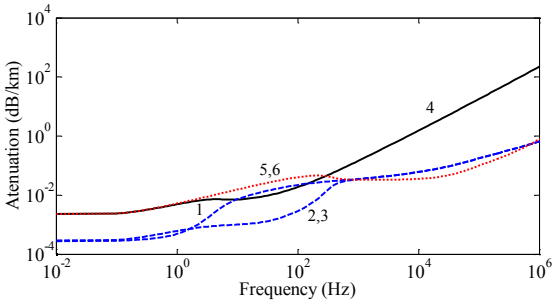

d) same-sense cross-bonding of cores and sheaths.

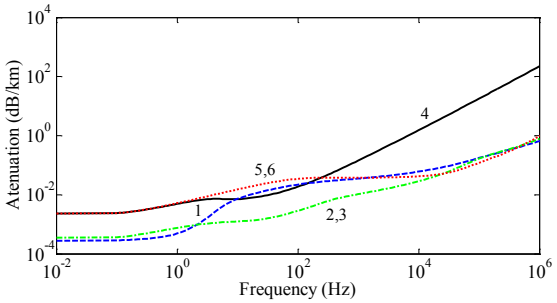

e) counter-sense cross-bonding of cores and sheaths.

Figure 6.3 Mode attenuation for different bonding schemes.

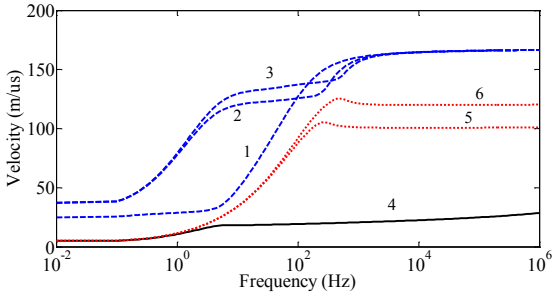

a) normal-bonding of cores and sheaths.

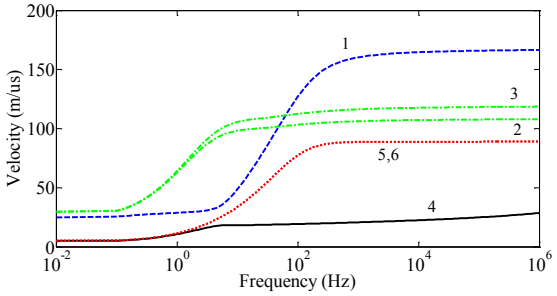

b) cross-bonding of sheaths.

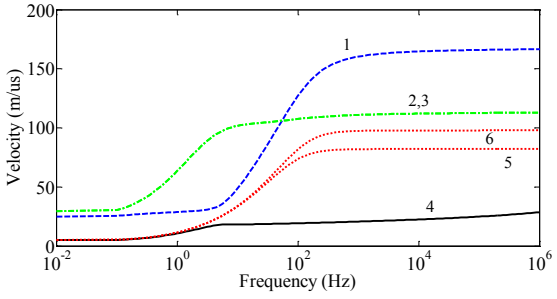

c) transposition of cores, normal-bonding of sheaths.

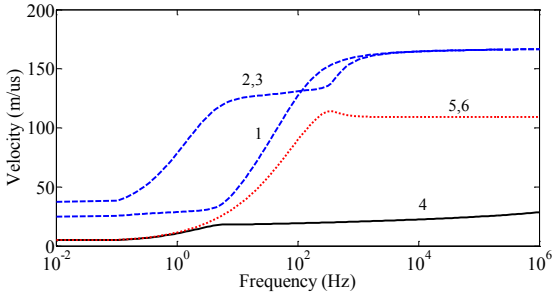

d) same-sense cross-bonding of cores and sheaths.

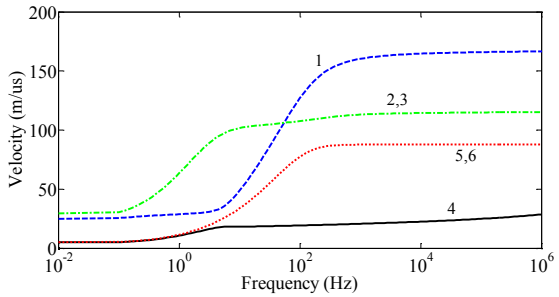

e) counter-sense cross-bonding of cores and sheaths.

Figure 6.4 Mode velocity for different bonding schemes.

6.1.2 Frequency-domain responses

As observed in the previous section, all bonding methods lead to the same zero-sequence modes, both for cores and sheaths. Therefore, the analysis in this section is focused only on inter-core modes to which the bonding methods show a different response.

The circuit in Figure 6.5 is simulated to compare the responses of the cable in Figure 6.2 and Table 6.1 under positive-sequence energising. The responses of 1, 3, 6 and 18 major sections are observed. The simulation is repeated for each of the bonding methods in Figure 6.1. Each major section has a 3 km and is divided into 3 equal minor sections. The sheaths are bonded and grounded at each major section through a resistance $R_g = 5\ \Omega$. The cables are energised with a current source and their input impedance is calculated from the ratio between the voltage and current of the current source of phase-a, as already explained in chapter 2, section 2.5.

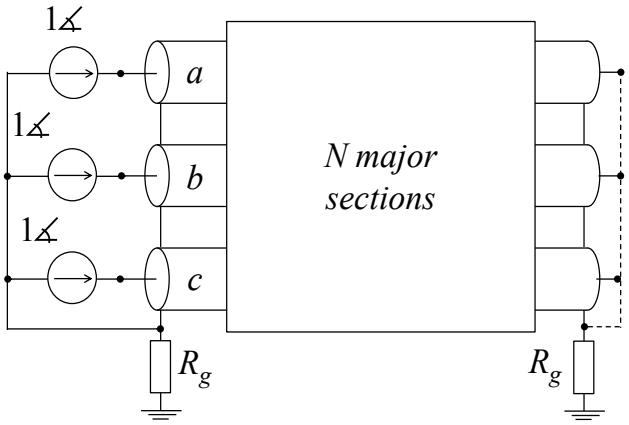

Figure 6.5 Circuit for positive-sequence energising of N major sections. The dashed line represents the short-circuit termination of cores.

Figure 6.6 through Figure 6.10 show the input impedances for 1 major section to a positive-sequence energising. The responses of the normal-bonded cable and the same-sense cross-bonded cable are the same (as already verified in Table 6.2 and Table 6.3) and they have resonance dips occurring at equally spaced frequencies. On the contrary, the responses of cross-bonded, Kirke-Searing and counter-sense cross-bonded systems are irregular because the frequencies of impedance dips are not related and the amplitudes of these dips do not necessarily increase with frequency.

These irregular responses are caused by the sheaths changing phase within each major section and by the different excitation of each phase. The positive-sequence excitation applied to the first minor section gives rise to inter-sheath mode currents which in turn also impact the core voltages in all the phases. The irregular responses of cross-bonded, Kirke-Searing and counter-sense cross-bonded cables are thus caused by the superposition of modes with different propagation constants.

Due to bonding and grounding of sheaths, inter-sheath modes cannot propagate between major sections and their impact is limited to a single major section. The first resonance associated to inter-sheath modes in a cross-bonded cable is calculated from the velocity in Table 6.3 and the length of 1 major section as $f_0 = v/4l = 89.1\times10^6/12000 = 7425\,\text{Hz}$. The impact of inter-sheath modes is thus more noticeable above this frequency [51]. This can be observed in Figure 6.11, showing the positive-sequence excitation of 18 major sections with cross-bonded sheaths: the impedance regular up to the 4th impedance minimum at about 3.6 kHz.

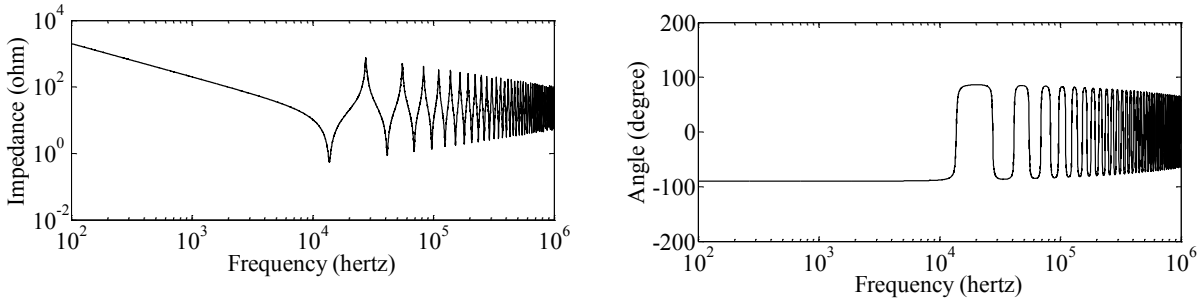

a) Impedance magnitude. b) Impedance angle.

Figure 6.6 Open-circuit input impedance for positive-sequence excitation in 1 major section with normal-bonded sheaths.[14]

[14] CableSimulation_Files\FreqTimeResponses_Crossbonded\FreqDomain_DiffBonding.ecf

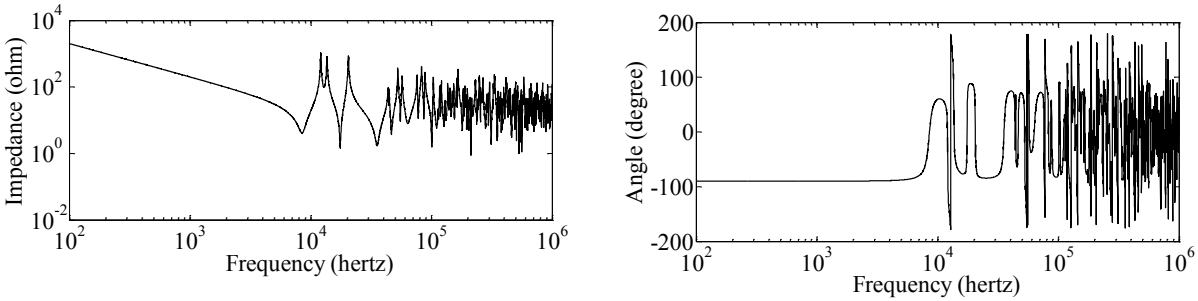

a) Impedance magnitude. b) Impedance angle.

Figure 6.7 Open-circuit input impedance for positive-sequence excitation in 1 major section with cross-bonded sheaths.[14]

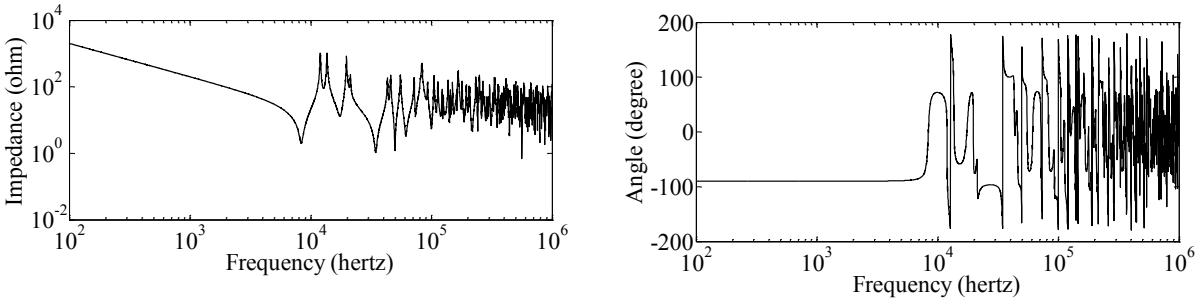

a) Impedance magnitude. b) Impedance angle.

Figure 6.8 Open-circuit input impedance for positive-sequence excitation in 1 major section using the Kirke-Searing bonding method.[14]

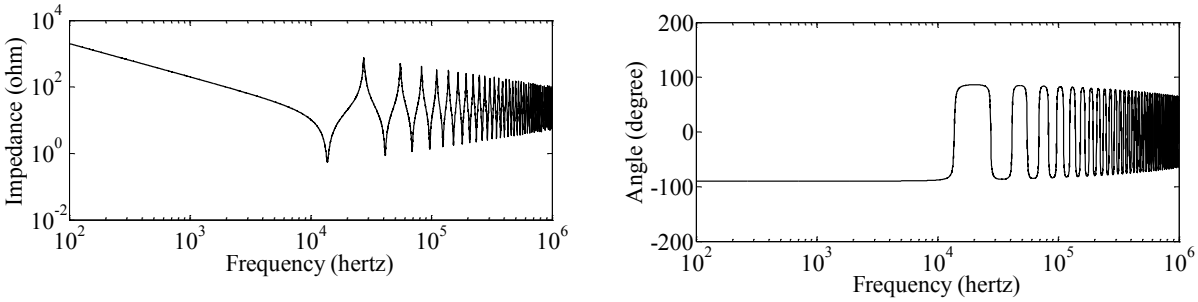

a) Impedance magnitude. b) Impedance angle.

Figure 6.9 Open-circuit input impedance for positive-sequence excitation in 1 major section using same-sense cross-bonding method. [14]

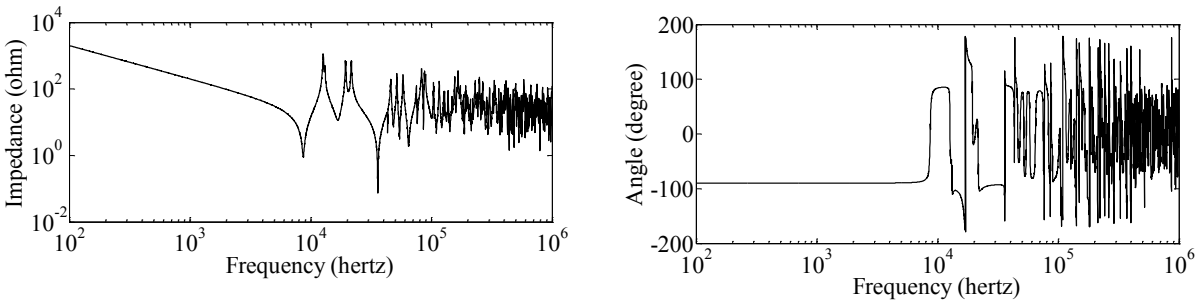

a) Impedance magnitude. b) Impedance angle.

Figure 6.10 Open-circuit input impedance for positive-sequence excitation in 1 major section using counter-sense cross-bonding. [14]

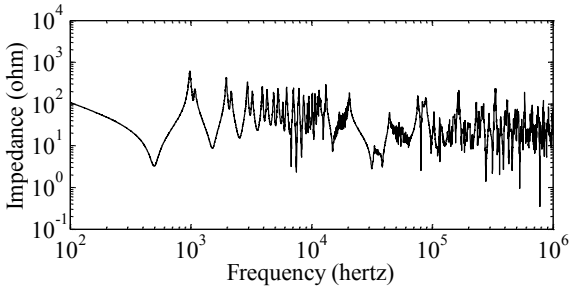

Figure 6.11 Input impedance for positive-sequence excitation of 18 major sections (54 km) with cross-bonded sheaths [51]. [14]

Table 6.4 presents the first resonant frequencies (impedance dips/minima) in the response of normal-bonded and cross-bonded cables for different lengths and for the positive excitation in Figure 6.5. The cable responses using other bonding methods are qualitatively very similar (the same-sense cross-bonding is similar to the case of normal-bonding, and the Kirke-Searing and counter-sense cross-bonding are similar to the cross-bonding method) and they are not shown.

In the normal-bonded cable response, resonant frequencies occur at f_0, $3f_0$, $5f_0$,… where $f_0 = c/4l$ is the so-called fundamental frequency calculated from the cable length l and the inter-core mode velocity $c = 167\times10^6$ m/μs (for 1 major section, $f_0 = 13.9$ kHz, $3f_0 = 41.9$ kHz, $5f_0 = 69.5$ kHz agree with Table 6.4). The same regularity is not observed for the cross-bonded cable in Table 6.4 and the cause is superposition of induced inter-sheath modes to the excited positive-sequence [51], as explained in the previous paragraph.

Table 6.4 Resonant frequencies in open-circuit [kHz] [51]

Major sections	Normal-bonded cable			Cross-bonded cable		
	f_0	f_1	f_2	f_0	f_1	f_2
1	13.8	41.4	68.9	8.41	17.6	35.4
3	4.56	13.8	23.0	3.01	8.56	15.3
6	2.28	6.84	11.4	1.51	4.50	7.38
18	0.73	2.26	3.79	0.50	1.50	2.54

6.1.3 Time-domain responses

The cable in Figure 6.2 having 18 major sections and 54 km is simulated in time domain for the bonding methods in Figure 6.1. Each major section is divided into 3 equal minor sections. The sheaths are bonded and grounded at each major section through 5 Ω resistances. A 225 kV balanced network applies a voltage to the cable at t = 0 ms.

Figure 6.12 shows the voltage of phase-b receiving end. The transient starts at different times for the three bonding methods because of different propagation velocities, reported in Table 6.3. It is also observed that the cross-bonded and transposed cables present initially small amplitude high frequency oscillations due to multiple reflections between the receiving end and the closest cable junction.

To observe the impact of the closing time, the same energising tests were repeated for the case of non-deterministic switch closing times. The closing time for each pole follows a Gaussian distribution of mean 0.016 seconds and standard deviation of 0.014 seconds. The maximum overvoltages observed throughout 50 simulations were 461.2 kV (phase-c) for the normal-bonded cable, 474.3 kV (phase-b) for the cross-bonded cable and 540.3 kV (phase-c) for the cable with transposed cores. Thus, the transposed cable appears to be the most prone to overvoltage, as already observed in Figure 6.12.

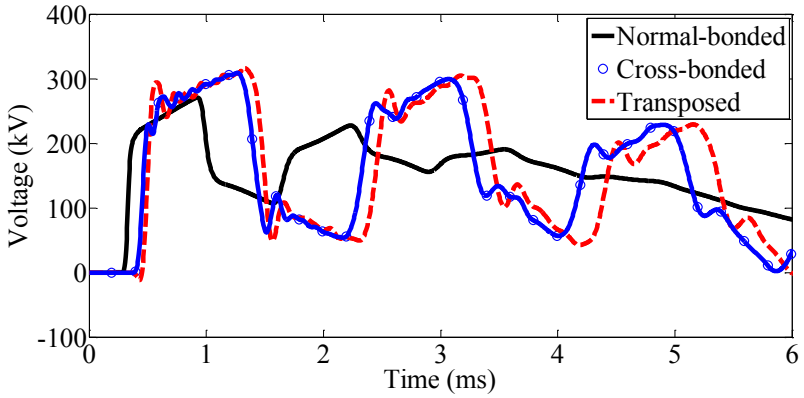

Figure 6.12 Phase-b receiving end voltage for energization of 18 major sections (54 km) with a 225 kV balanced infinite power network [51].[15]

6.2 Impact of non-uniformities in cross-bonded cables

Underground cables are often modeled as a continuous homogeneous structures. However, real cable systems are in general not uniform due to many factors. Some of the most common causes of non-uniformity are cable terminations and joints, non-uniform burial depth, sheath cross-bonding, core transposition, and sheath grounding.

The following sections investigate impact of sheath grounding and sheath cross-bonding on the response of underground cables.

6.2.1 Impact of sheath grounding

6.2.1.1 The analogous case of overhead lines

Cable sheaths as well as OHL shield wires are normally grounded at several points throughout their route. In OHL's, the shield wires protect the phase conductors from lightning. In underground cables, the sheath is designed to shield the phase conductor against external noise/interference and to provide a return path for fault currents.

Even though shield wires and sheaths are not used to transmit power, they have an impact on the overall response of the system because of induction from the phase conductors. The impact of

[15] CableSimulation_Files\FreqTimeResponses_Crossbonded\TimeDomain_DiffBonding.ecf

shield wire grounding on the OHL's response has been studied in many publications [72]-[76] while the impact of sheath grounding has not been so thoroughly studied.

In OHL's, the grounding of shield wires represents a non-uniformity of the system which introduces abrupt changes in the cable characteristics, i.e. propagation factor and characteristic impedance [72]-[76]. This phenomenon, also referred to as standing-wave effect [72],[74], is a result of resonance and it occurs for frequencies at which the length between grounding points is a multiple of half electromagnetic wavelength [72]-[74].

The abrupt changes in the line characteristic functions are in fact the result of a superimposition of the "main" propagation mode, i.e. the mode flowing through the whole line length, with another propagation mode flowing between two grounding points. The contribution of a mode to the overall line response is magnified as the mode becomes resonant [72], i.e. as the length between the grounding points approaches a multiple of half mode wavelength. In general, the modes which are more affected by the shield wire grounding are those of higher attenuation because they are the most influenced by the earth-return path [72].

Due to practical constraints, the distance between OHL towers (where shield wires are grounded) is rarely uniform. This non-uniformity in grounding lengths has the effect of damping out the magnitude of the spikes introduced by the shield wire grounding in the OHL propagation functions [74]. The reason for this is that in the case of regular grounding the modes propagating between each two grounding points become resonant at the same frequency and their influence is summed up, whereas in the irregular case these modes are resonant at different frequencies.

For the case of regular grounding lengths, a non-uniform soil resistivity or non-uniform tower footing resistance have no impact on the resonant frequencies [75]. However, for a higher tower footing resistance the spikes observed in the propagation functions is not as evident [76] because it is as if the grounding became an open-circuit.

The following example illustrates the above findings of existing publications. Consider an OHL described by the data in Table 6.5. The circuits in Figure 6.13 represent a zero-sequence and an inter-phase excitations applied to the overhead line which shield wire is grounded at 4 points. The length of the OHL is 1.2 km. Both cases of regular grounding lengths, i.e. $L_{g1} = L_{g2} = L_{g3} = 400$ m , and irregular lengths $L_{g1} = L_{g3} = 350$ m, $L_{g2} = 500$ m are considered.

Figure 6.14 and Figure 6.15 shows the attenuation for the two excitation schemes of Figure 6.13. Abrupt changes in attenuation are observed at certain frequencies. The zero-sequence mode (earth-return mode) is much more affected by the inter-phase mode. However, even a small perturbation in the grounding lengths is enough to damp out these irregularities in the attenuation of the OHL.

Table 6.5 Data for an overhead transmission line with one shield wire.

Ph.	Horizontal distance [m]	Vertical height [m]	Other data:
A	-10	14	Phase/ground wire DC resistance $2\times10^{-8}\,\Omega$/km
B	10	14	Phase/shield wire outside diameter 5cm/3cm
C	0	14	Earth resistivity 100Ω-m
GW	0	25	Total line length 1.2km

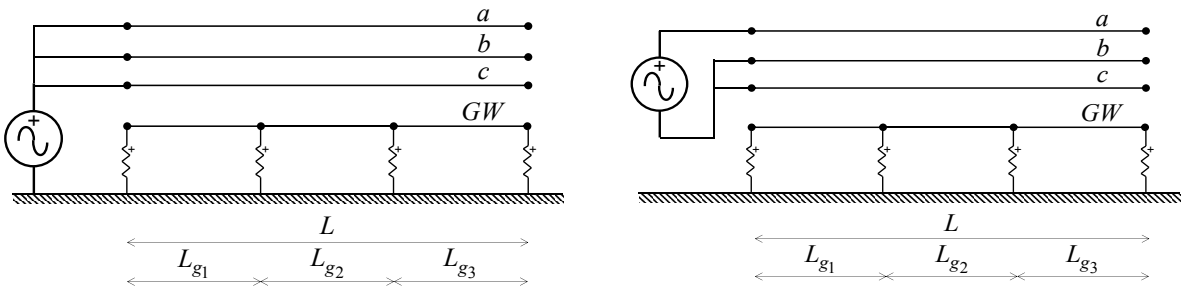

a) Zero-sequence energising. b) Inter-phase energising.

Figure 6.13 Circuits for energising an overhead line having a shield wire.

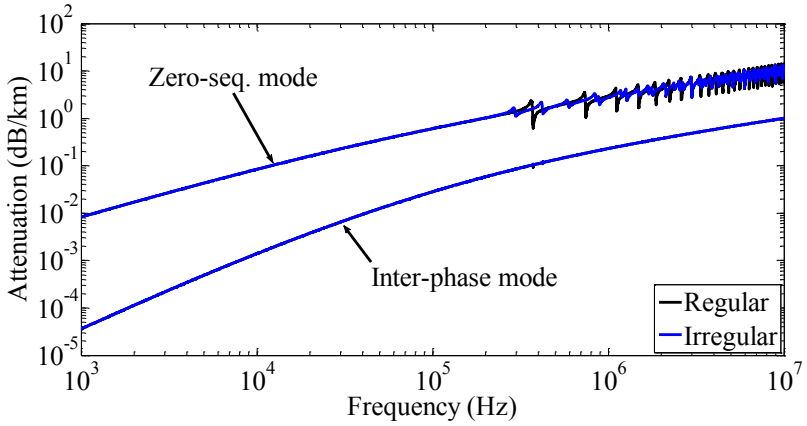

Figure 6.14 Zero-sequence and inter-phase attenuation of an overhead line with one shield wire for regular and irregular separation between towers.[16]

[16] Circuit: CableSimulation_Files\NonHomogeneous_LinesCables\EMTP_Files\Circuit.ecf

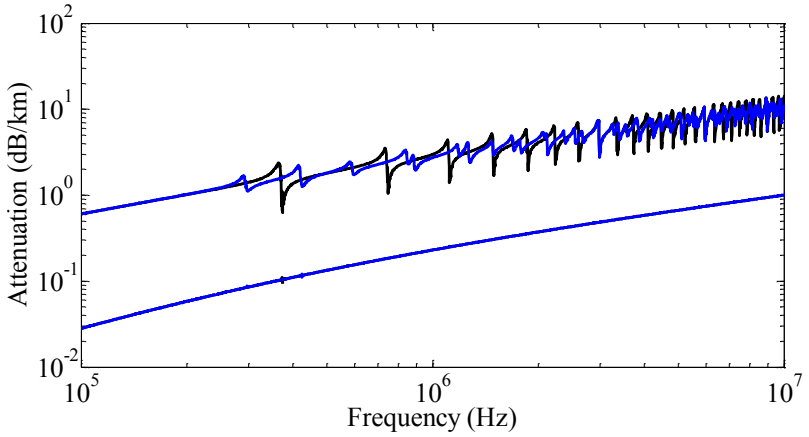

Figure 6.15 Zoomed characteristics of zero-sequence and inter-phase attenuation of an overhead line with one shield wire for regular and irregular separation between towers. [16]

6.2.1.2 Normal-bonded cables

Contrary to OHL's, underground cables with normal-bonded sheaths are not affected by grounding of sheaths as far as the propagation of core modes is concerned. The reason for this is that the first critical frequency, i.e. the frequency for which the length between grounding points is exactly half wavelength, is high enough so that a pure coaxial mode was already developed in the cable.

A pure coaxial mode is achieved when the penetration depth of the sheath conductor becomes lesser than the sheath thickness. Above the frequency for which the penetration depth is equal to the sheath thickness any current flowing into a phase conductor will fully return through the sheath of the same phase, and the return path is the inner sheath surface. Any phenomenon affecting the outer sheath surface has no impact on this propagation. Sheath grounding, which uses the sheath outer surface, has thus no impact on the propagation of the coaxial mode.

This conclusion is illustrated with the following example. Consider a normal-bonded underground cable described by the data in Table 6.6. The circuits in Figure 6.13 can be used to represent a zero-sequence and an inter-phase source application to the normal-bonded cable if the shield wire is replaced by the sheaths. The cable has the same length as the OHL, i.e. 1.2 km. As for the example

---

Plotting: CableSimulation_Files\NonHomogeneous_LinesCables\EMTP_Files\Plots_from_VOC.m

of OHL, both cases of regular grounding lengths, i.e. $L_{g1} = L_{g2} = L_{g3} = 400$ m, and irregular lengths $L_{g1} = L_{g3} = 350$ m, $L_{g2} = 500$ m are considered.

Figure 6.16 show the attenuation of the cable for the two excitation schemes of Figure 6.13. Contrary to the OHL (see Figure 6.15), no abrupt changes are observed in the attenuations of a normal-bonded cable.

Table 6.6 Data of an underground cable.

Ph.	Horizontal distance [m]	Burial depth [m]	Other data:
A	-0.25	1	Core: $\rho_c = 2\times10^{-8}\,\Omega$-m, $r_{c-in} = 0, r_{c-out} = 24$ mm
B	0.25	1	Sheath: $\rho_s = 2\times10^{-8}\,\Omega$-m, $r_{s-in} = 56$ mm, $r_{s-out} = 57$ mm
C	0	1	Insulation: $\varepsilon_{r1} = \varepsilon_{r2} = 2.5, \tan\delta_1 = \tan\delta_2 = 0.0008, r_{ext} = 60$ mm
			Earth resistivity $100\,\Omega$-m, Total length 1.2 km

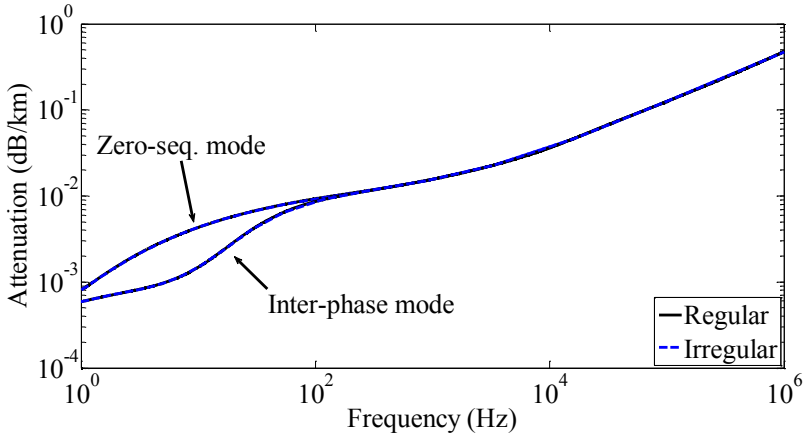

Figure 6.16 Zero-sequence and inter-phase attenuation of a normal-bonded cable with the sheaths grounded at each major section. [16]

6.2.1.3 Cross-bonded cables

As demonstrated in section 6.1.2, cross-bonded cables have a completely different response to inter-phase excitation, compared to normal-bonded structures. Because a sheath changes phase twice inside each major section, it cannot succeed to shield any of the phase conductors. For the same reason, single-phase coaxial modes cannot propagate in a cross-bonded cable and an inter-phase mode will not become a coaxial mode above a certain frequency, as observed for normal-bonded cables. On the other hand, three-phase zero-sequence coaxial mode propagation is not

affected by the cross-bonding because the same current flows in all cores and comes back in all sheaths.

The same example of the previous section using the cable described in Table 6.6 is used to demonstrate the impact of sheath grounding in cross-bonded cables. The excitation circuits in Figure 6.13 (with the ground wire replaced by the sheaths) are applied to the cross-bonded cable. Once again the cable has 1.2 km and both cases of regular and irregular grounding lengths are considered.

Figure 6.17 through Figure 6.20 represents the attenuation of the cable for the cases of: a) zero-sequence core excitation; b) inter-phase excitation with regular grounding lengths, i.e. all major sections having 400 m; c) inter-phase excitation for 350 m – 500 m – 350 m major sections; and d) inter-phase excitation for 300 m – 600 m – 300 m major sections.

As mentioned above, the response to a zero-sequence excitation is not affected at all by sheath grounding and the attenuation is the same as that of a normal-bonded cable. On the other hand, the attenuations in the case of inter-phase excitation are extremely irregular above a certain frequency, much more irregular than in the case of an OHL shown in Figure 6.15. On the other hand, irregular grounding lengths does not have a clear effect on the attenuation as it had for the case of an OHL and the three cases in Figure 6.20 have nearly the same characteristics.

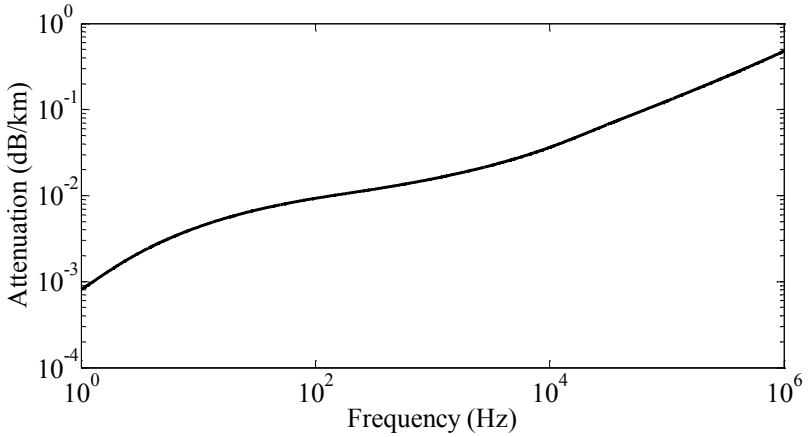

Figure 6.17 Zero-sequence attenuation of a cross-bonded cable. [16]

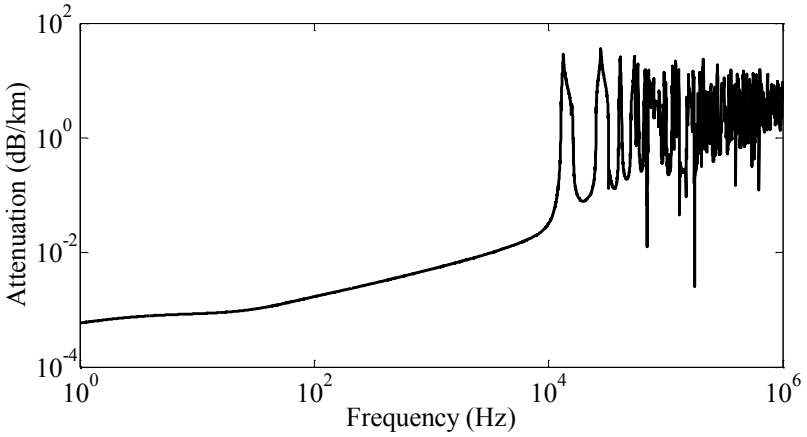

Figure 6.18 Inter-phase attenuation of a cross-bonded cable with the sheaths cross-bonded at regular lengths (400 m, 400 m, 400 m). [16]

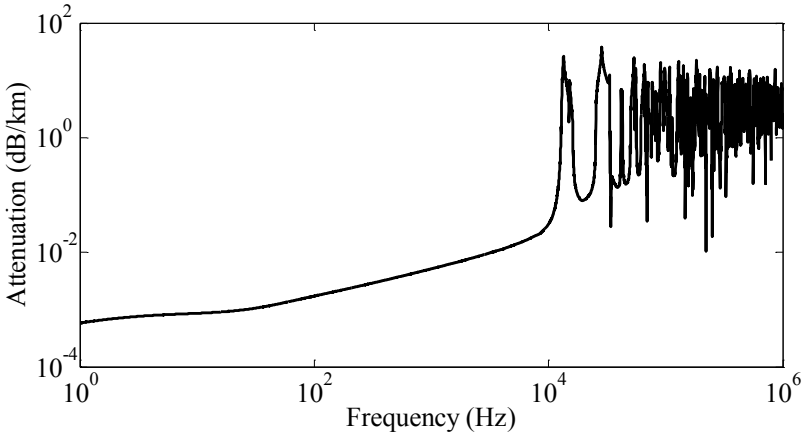

Figure 6.19 Inter-phase attenuation of a cross-bonded cable with the sheaths cross-bonded at irregular lengths (350 m, 500 m, 350 m). [16]

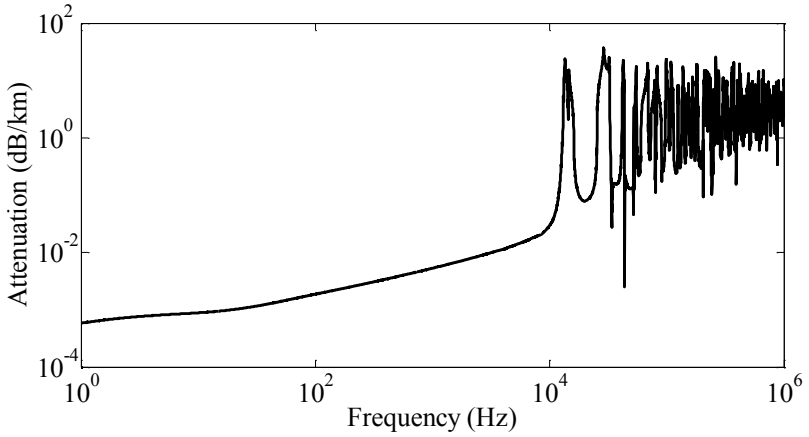

Figure 6.20 Inter-phase attenuation of a cross-bonded cable with the sheaths cross-bonded at irregular lengths (300 m, 600 m, 300 m). [16]

In case the grounding of sheath uses a high resistance, the attenuation characteristics of the cross-bonded cable are exactly equal to those in Figure 6.20. This shows that what affects the cable response is not particularly the grounding but it is the bonding of the sheaths together at the end of the major section. On the other hand, the irregularities in Figure 6.20 would not exist if the sheaths were not cross-bonded as in the case of the normal-bonded cable.

Contrary to OHL's for which all the conductor modes have nearly the same velocity, in an underground cable all the modes have different velocities. Two equal inter-core modes can be achieved through core transposition. In the same way, two equal inter-sheath modes can be achieved through sheath transposition. However, inter-core modes cannot in general be equal to the inter-sheath modes. Thus, wavelengths which are defined from the modal velocities will be different for the inter-core and the inter-sheath modes.

At the same time, the non-uniformities of the core conductors are not the same as the non-uniformities of the sheaths. For example, the sheaths are grounded at each major section. The cores are grounded eventually at the receiving end. Thus, the length which is involved in the resonance phenomenon will be different whether inter-core or inter-sheath modes are considered.

The conclusion of the two previous paragraphs is that multiple resonances will be observed, some related to inter-sheath modes, others related to inter-core modes and the result is a completely irregular characteristics of the cable's response.

6.2.2 Impact of sheath cross-bonding

As observed in section 6.1, cross-bonded cables have in general a different behavior both in frequency and in time-domain compared to normal-bonded cables [50]. In section 6.2.1.3 it was further observed that sheath grounding has impact on the response of the cable to inter-phase excitation only in the case where the sheaths are cross-bonded.

In a cross-bonded system, inter-core currents give rise to inter-sheath currents. The two circuits in Figure 6.21 are used to investigate the impact of sheath currents in a cross-bonded cable. As in a real system, the sheaths are grounded at the receiving end. The cable system is the same used in section 6.1.

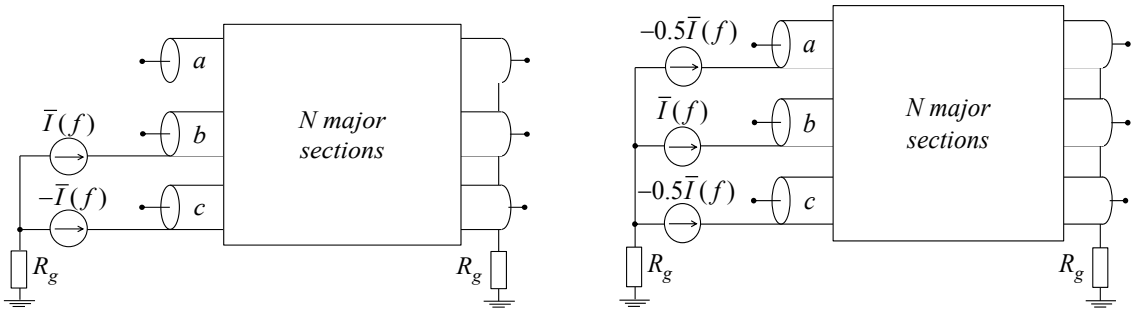

Figure 6.21 Two-phase and three-phase inter-sheath excitation of N major sections.

The responses of the cross-bonded cable to the two excitations in Figure 6.21 are shown in Figure 6.22 and Figure 6.23, respectively. It is readily observed in these figures that the responses of 1 major section to inter-sheath excitations are very similar to the responses to inter-core energising in Figure 6.7 and Figure 6.8.

The responses of 1 and 18 major sections in Figure 6.22 and Figure 6.23 are very similar too. This is a result of bonding the three sheaths at each major section. The three sheath voltages are exactly the same at those points and thus no inter-sheath mode can be transmitted from one major section to the other. The small differences in the responses of 1 and 18 major sections are due to transmission through the core conductors.

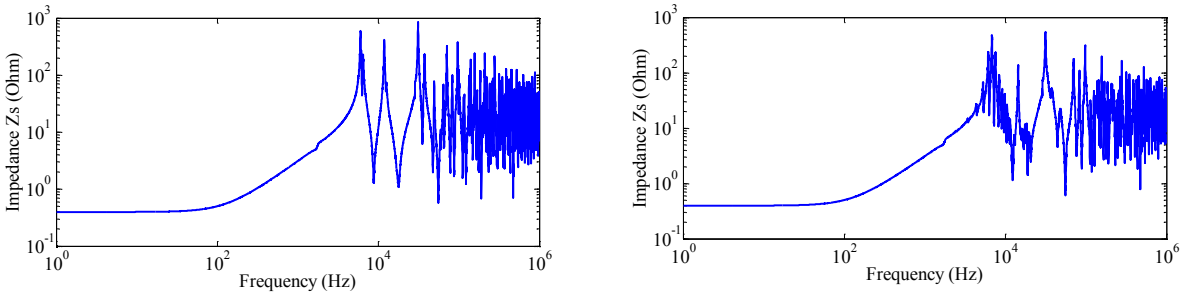

a) One major section. b) 18 major sections.

Figure 6.22 Short-circuit input impedance for two-phase inter-sheath excitation in a cross-bonded cable. [14]

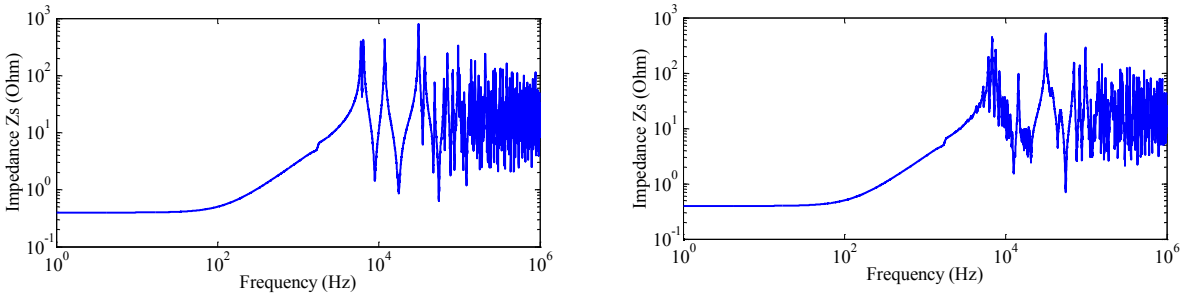

a) One major section. b) 18 major sections.

Figure 6.23 Short-circuit input impedance for three-phase inter-sheath excitation in a cross-bonded cable. [14]

The above phenomenon together with the results from sections 6.1.1 and 6.2.1.3 show that sheath cross-bonding and consequently sheath currents have an important impact on the cable response, in particular at high frequencies. Inter-phase excitation of cross-bonded cables always induces inter-sheath currents.

The existence of inter-sheath modes which circulate within each major section is also observed from points in the frequency response of the cable which are repeatedly observed for all cable lengths and both for short-circuit or open-circuit terminations.

For example, Table 6.7 shows the inter-core mode impedances (obtained in section 6.1.1) as well as inter-sheath mode impedances calculated at 166.7 kHz. Both for inter-core and inter-sheath modes, the impedance at 166.7 kHz does not change with the length of the cable. This results from a phenomenon occurring on the first major section only. The inter-core impedance corresponds to

an open-circuit resonance, whereas the inter-sheath impedance corresponds to a short-circuit resonance. This means that the highest sheath currents induce the highest core voltages.

Table 6.7. Inter-core and inter-sheath mode impedances of a cross-bonded cable at 166.7 kHz.

Recv. end	Major sections	Inter-core excitation		Inter-sheath excitation	
		Two-phase (Ω)	Three-phase (Ω)	Two-phase (Ω)	Three-phase (Ω)
Open-circuit	1	476.2	482.6	n.a.	n.a.
	3	473.4	477.3	n.a.	n.a.
	6	473.4	477.3	n.a.	n.a.
	18	473.3	477.3	n.a.	n.a.
Short-circuit	1	470.4	472	6.672	4.424
	3	473.3	477.3	6.124	3.607
	6	473.3	477.3	6.087	3.595
	18	473.3	477.3	6.088	3.595

At 166.7 kHz the wavelength of the coaxial mode is

$$\lambda_c = c_{co}/f = \left(166.7\times10^6\right)\Big/\left(166.7\times10^3\right) = 1000\,\text{m}$$

where $c_{co} = 166.7\times10^6$ m/s is the coaxial velocity in Table 6.3 and $f = 166.7\times10^3$ Hz is the resonant frequency. The wavelength of an inter-sheath mode is

$$\lambda_{sh} = c_{sh}/f = \left(89.1\times10^6\right)\Big/\left(166.7\times10^3\right) = 535\,\text{m}$$

Interestingly, at 166.7 kHz the length of a major section is 6 times $\lambda_c/2$ and about 11 times $\lambda_{sh}/2$. This shows that the response of a cross-bonded cable to an inter-core excitation has a strong contribution of different modes and it is irregular because the different modes become resonant at different frequencies that are not necessarily multiples of one another.

6.3 Modeling of cross-bonded cables

The most straightforward way for modeling cross-bonded cables is by modeling each minor section separately (**discrete model**) [14],[16],[20],[44]-[47]. This approach can be cumbersome and result in long simulations if the number of cable sections to model is very large.

In alternative, a whole major section can be modeled by a single **homogeneous equivalent** with the three bonded sheaths represented as a single conductor [15],[34]-[36]. Despite clear gains in computation time, the homogeneous equivalent does not allow calculating sheath over-voltages within major sections and has limitations which affect the accuracy of time and frequency domain simulations. Previous studies made clear the importance of modeling bonding wires impedance [16], non-uniform length of minor sections [32], and reflections caused by discontinuities at bonding points during a transient [16],[20],[47]. As this section will show, even without accounting for bonding wire impedances, the homogenous equivalent may not be sufficiently accurate in frequency domain.

In this section, four alternative models for cross-bonded cables are compared based on frequency and time domain responses, including the simulation of a field test.

6.3.1 Alternative models

Figure 6.24 through Figure 6.27 illustrate the different models for a cross-bonded cables with *N* major sections: **Model 1**, the most accurate, models each minor section separately; **Model 2** represents each major section by a homogeneous equivalent; **Model 3** uses homogeneous equivalents for all except the first and last major sections; **Model 4** uses discrete modeling of the two major sections at each terminal. An approach similar to model 1 had already been investigated for OHL's with ground wires [78].

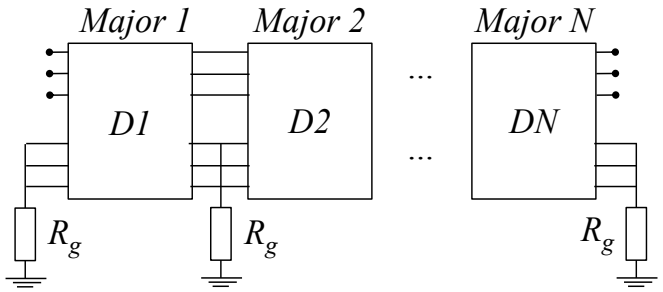

Figure 6.24 Model 1 for a cable with N major sections – discrete modeling of each major section [51].

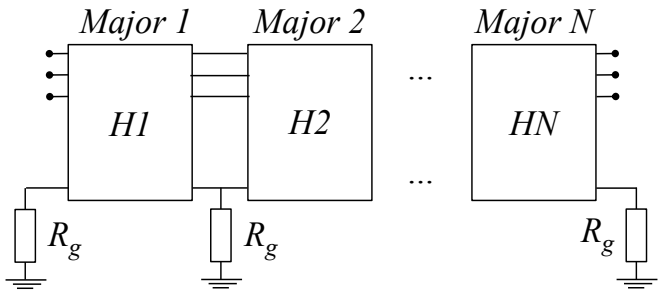

Figure 6.25 Model 2 for a cable with N major sections – each major section modeled with a homogeneous equivalent [51].

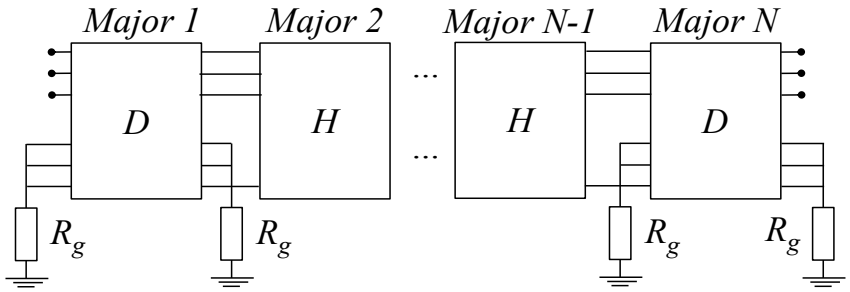

Figure 6.26 Model 3 for a cable with N major sections – discrete modeling of terminal major sections only [51].

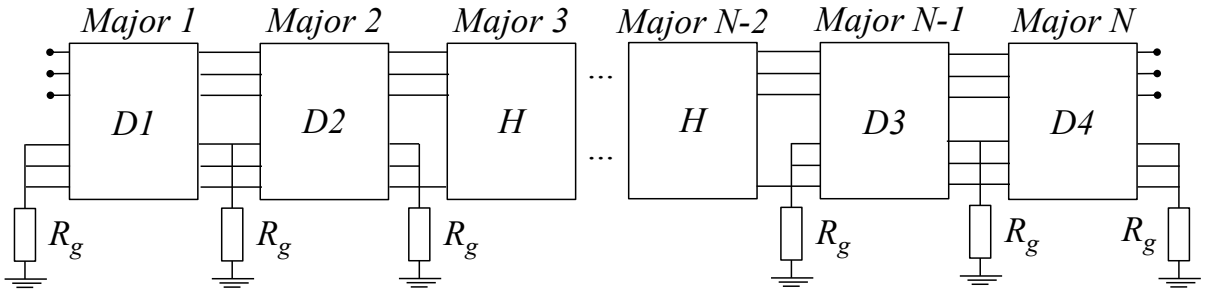

Figure 6.27 Model 4 for a cable with N major sections – discrete modeling of 2 major sections at each terminal [51].

6.3.2 Frequency responses

Figure 6.31 shows the response of the alternative models of a cross-bonded cable with layout in Figure 6.2 and 18 major sections of 3 km each to the excitation in Figure 6.5 (right). All models give the same result up to about 7425 Hz, corresponding to resonance between the inter-sheath mode component and 1 major section, as explained in section 6.2.2. Above this frequency, mode

superposition strongly affects the frequency responses. Model 3 and model 4 can account for this phenomenon and they show good agreement with model 1. Instead, model 2 has a response similar to a normal-bonded cable and it cannot represent the mode superposition caused by induced by sheath currents. Thus, if the cross-bonding is simply neglected and the cable is modeled with a single section the response will be the same as that of a homogeneous model (model 2).

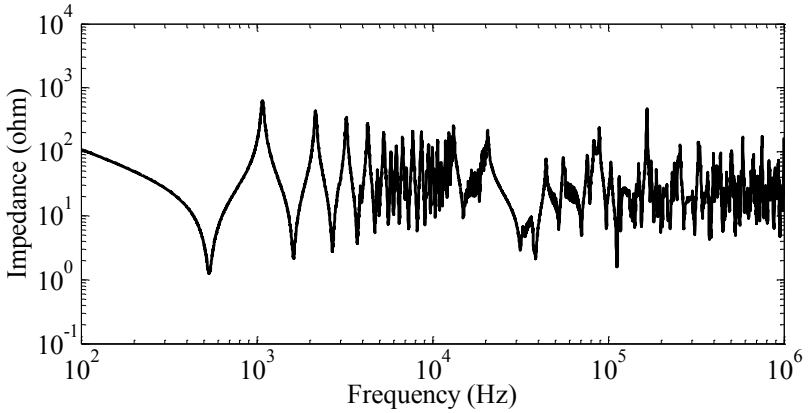

Figure 6.28 Input impedance for 3-phase excitation in 18 major sections (54 km) of a cross-bonded cable using model 1 in Figure 6.24 [51].[15]

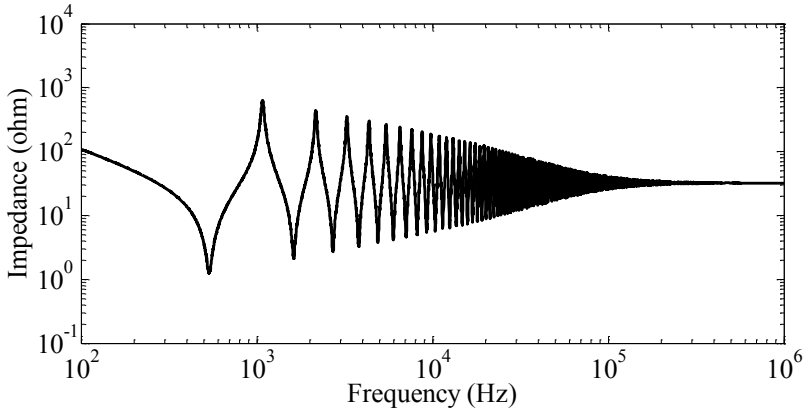

Figure 6.29 Input impedance for 3-phase excitation in 18 major sections (54 km) of a cross-bonded cable using model 2 in Figure 6.25 [51]. [15]

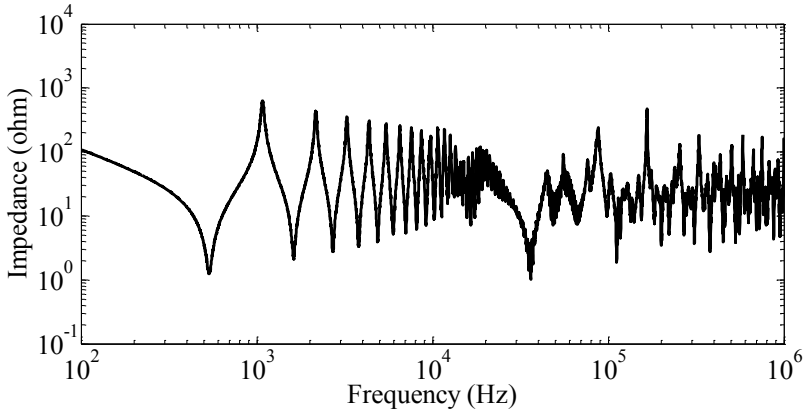

Figure 6.30 Input impedance for 3-phase excitation in 18 major sections (54 km) of a cross-bonded cable using model 3 in Figure 6.26 [51]. [15]

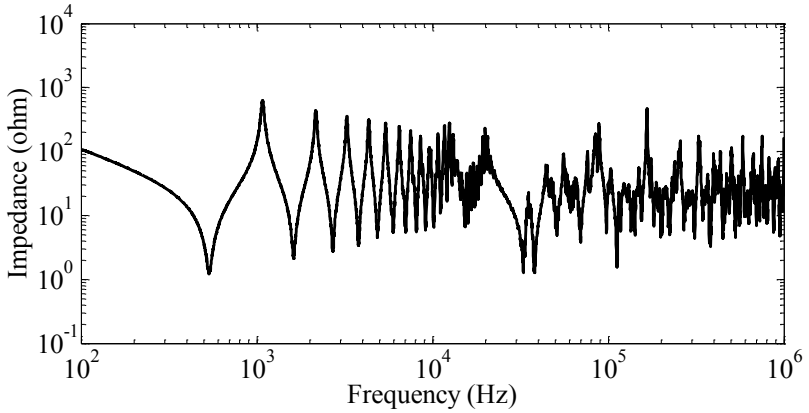

Figure 6.31 Input impedance for 3-phase excitation in 18 major sections (54 km) of a cross-bonded cable using model 4 in Figure 6.27 [51]. [15]

6.3.3 Time responses

A 225 kV cross-bonded cable commissioned by the French Transmission System Operator RTE has the layout in Figure 6.2 with 17 major sections and 64 km length. The sheaths are bonded and grounded at each major section through 5 Ω resistances and the cores are open-circuited at the receiving end. The cable is simulated in time domain using the alternative models in Figure 6.24 through Figure 6.27 for the energising from a balanced network of infinite power at t = 0 ms.

Figure 6.32 shows the receiving end voltage of phase-b. Model 2 cannot account for the high frequency oscillations caused by reflections between cross-bonding points and thus has the smoothest wave-shape. Models 3 and 4 present these high-frequency oscillations because they

model accurately the terminal major sections. However, these oscillations are more damped out than for model 1. If the cross-bonding is simply neglected, the response is similar to that of model 2.

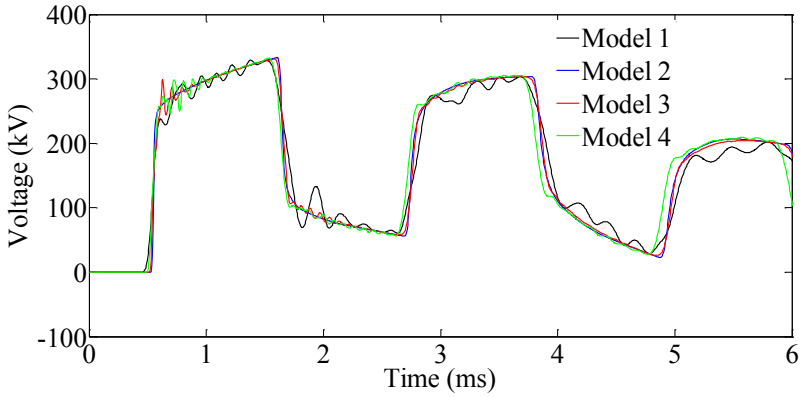

Figure 6.32 Receiving end phase-b voltage for 3-phase excitation of 17 major sections (64 km) for energising from a balanced network of infinite power [51].[17]

6.3.4 Simulation of a field test

The cable models in Figure 6.24 through Figure 6.27 are used to simulate the energising test presented in section 3.2.

Figure 6.33 shows the field test results of voltages at the cable sending end as well as the simulated results using models 1 and 2. Model 3 and Model 4 are omitted to avoid overloading the figures and because model 1 and model 2 already show nearly the same response. This is because the reflections transmitted from cross-bonding points are much more attenuated than in the case of the infinite power source used in section 6.3.3. In this case, if the cross-bonding the response would be the nearly the same as that of the full model (model 1)

[17] Circuit: CableSimulation_Files\EnergisingTest_RTECable\EMTP_circuit\Energization_Circuit.ecf
Plotting: Circuit:CableSimulation_Files\EnergisingTest_RTECable\EMTP_circuit\Plot_Energization.m

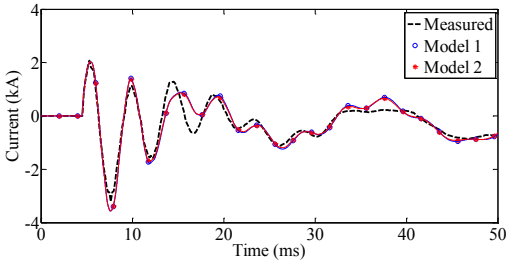

a) Phase-a sending end current.

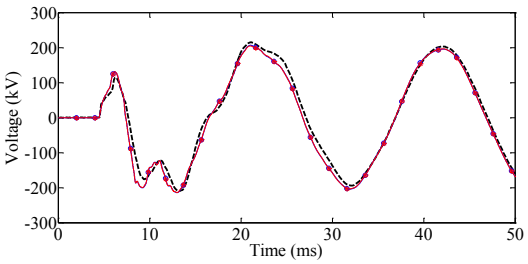

b) Phase-a sending end voltage.

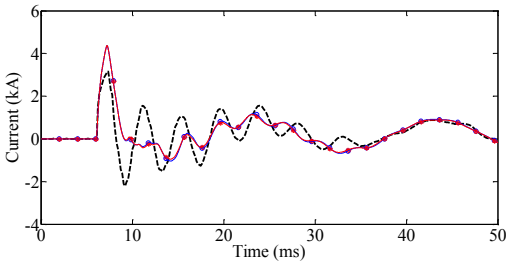

a) Phase-b sending end current.

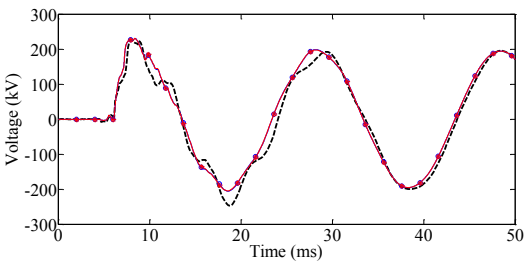

b) Phase-b sending end voltage.

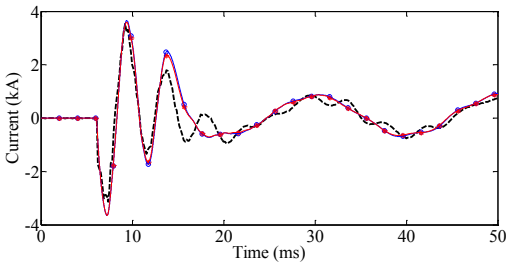

a) Phase-c sending end current.

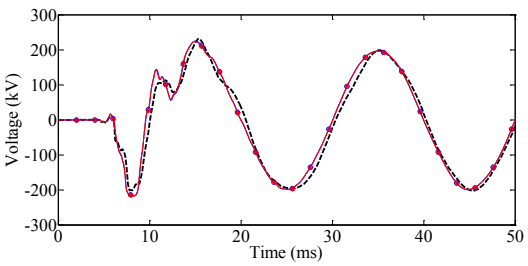

b) Phase-c sending end voltage.

Figure 6.33 Field test and simulation results of three-phase currents and voltages in a cross-bonded cable [51]. [17]

6.3.5 Performances of different cable models

The alternative models for cross-bonded cables, illustrated in Figure 6.24 through Figure 6.27 were tested in the previous sections with simulations in time and frequency domain.

In all tests, model 2 using homogeneous equivalents was the least accurate and the reason is that it cannot account neither for mode superposition caused by induced sheath currents nor for reflections at cross-bonding points. Models 3 and 4 perform substantially better because they model the terminal major sections accurately. Measurements at cable ends are mostly affected by the phenomena occurring in these sections because of proximity and because of sheath grounding which attenuates waves transmitted from distant sections.

The models also differ in CPU time required for time and frequency simulations. The values in Table 6.8 correspond to the relative CPU time required for each model to simulate a cross-bonded cable having 17 major sections and considering model 1 as the reference. Model 2 requires about 1/5 of the CPU time for model 1, while model 3 requires 1/3. However, the gains in CPU time are not linearly dependent on the number of modeled cable sections.

The cable models can also be compared in terms of the simulation time-step, limited by the shortest propagation delay on the cable. Models which go to the details of a minor section (models 1, 3 and 4) require a time-step 3 times smaller than model 2 and thus need 3 times more solution points. In Table 6, the time-step $\Delta t = 4$ μs is imposed by the minimum propagation delay of a minor section in the cable. However, model 2 could have been simulated using $\Delta t = 12$ μs (three times higher) which would further reduce the CPU time for the time domain simulation.

In summary, if computer resources are not a limitation, discrete modeling of each minor section (model 1) gives the most accurate results. If the number of major sections is high to the point of making simulations prohibitively long, then models 3 and 4 can be used and still give fairly accurate results. Further savings in memory and computation could be achieved if the intermediate major sections were modeled by a single homogeneous equivalent including the sheath grounding resistance in the admittance matrix as explained in [36]. The authors verified that this approximation affects mostly the earth-return mode which has little impact on the cable response due to high attenuation.

Table 6.8 Relative CPU time for simulating different models of a cross-bonded cable having 17 major sections.

Simulation type	Model 1	Model 2	Model 3	Model 4
Time domain ($\Delta t = 4$ μs, T = 0.1 s)	1 pu	0.22 pu	0.29 pu	0.39 pu
Freq. domain (1000 ppd, 1-10^6 Hz)	1 pu	0.18 pu	0.35 pu	0.49 pu

6.4 Application of frequency responses for calculation of propagation constants of cross-bonded cables

Since modal theory was first applied to the study of power transmission systems [48], the usual approach for calculating the propagation factors $\bar{\gamma} = \alpha + j\beta$ for a multi-phase system is to

calculate the eigenvalues of the product of per-unit-length matrices $\bar{\mathbf{Z}}\bar{\mathbf{Y}}$. For non-uniform systems such as cross-bonded cables or OHL's with multiply grounded shield wires, this usually requires deriving the per-unit-length parameters of a homogeneous equivalent [15], [34]-[36].

For a perfectly uniform structure, e.g. a cable minor section, $\bar{\gamma}$ is accurately calculated from the equivalent PI-model circuit representation of a mode, given by

$$\begin{bmatrix} \bar{I}_0 \\ \bar{I}_l \end{bmatrix} = \begin{bmatrix} \bar{A} & -\bar{B} \\ -\bar{B} & \bar{A} \end{bmatrix} \begin{bmatrix} \bar{V}_0 \\ \bar{V}_l \end{bmatrix} \tag{6.6}$$

$$\bar{A} = \bar{Y}_0 \coth(\bar{\gamma} l), \bar{B} = \bar{Y}_0 \operatorname{cosech}(\bar{\gamma} l) \tag{6.7}$$

where subscripts *0* and *l* are used for sending end and receiving end quantities and *l* is the total length of the system. In open-circuit $\bar{I}_l = 0$ and with voltage application $\bar{V}_0 = \bar{V}_{src}$. Under these conditions, (6.6) is reduced to give:

$$\bar{V}_l = \frac{1}{\cosh(\bar{\gamma} l)} \bar{V}_{src} \xrightarrow{\bar{V}_{src}=1\,\mathrm{V}} \bar{\gamma} = \frac{1}{l} \cosh^{-1}\left(\frac{1}{\bar{V}_l}\right) \tag{6.8}$$

From (6.8) it is possible to compute $\bar{\gamma}$ simply from the open-circuit receiving end voltage and cable length.

If one assumes that a representation such as (6.6) also applies for a non-uniform structure, e.g. a cross-bonded cable, then $\bar{\gamma}$ can be calculated from the receiving end voltage response of the cable by applying (6.8).

Figure 6.34 shows the propagation velocity $v = \omega/\beta$ with β the imaginary part of $\bar{\gamma}$ for 3 cases: 1) zero-sequence excitation of the cores giving the same result for normal-bonded and cross-bonded cables; 2) inter-core excitation as in Figure 6.5 (right circuit) applied to a cross-bonded (XB) cable; and 3) inter-core excitation as in Figure 6.5 (right circuit) applied to a normal-bonded (NB) cable. The inter-core mode velocity in a normal-bonded cable goes from purely inter-core to purely coaxial as the sheath skin depth becomes lesser than the sheaths thickness. The irregularity in inter-core mode velocity of a cross-bonded cable is due to a superposition of modes, as explained in section 6.1.2, and the spikes correspond to resonance in the cable length between sheath grounding points and the superposed mode wavelength.

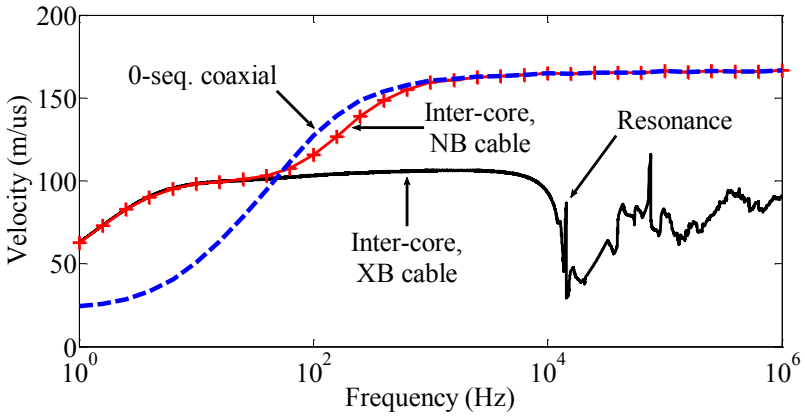

Figure 6.34 Propagation velocities calculated from the frequency scan of open-circuit response of normal-bonded and cross-bonded cables [51].[18]

6.5 Application of frequency responses for fault location in crossbonded cables

Methods for fault location in power cables can be divided into off-line and on-line methods according to whether the cable needs to be out-of-service to apply the method or not. Off-line methods have a long history and are well documented [79]. Though very accurate, off-line methods are highly demanding in man-power and time. This motivated the development of on-line methods, divided into impedance-based and travelling-based methods.

Online fault location methods developed for overhead lines or for cables with no bonding [80] may not be applicable to cross-bonded systems. Impedance-based methods are difficult to apply to cross-bonded cables because the loop impedance of the cable is discontinuous at cross-bonding points [45],[47]. Travelling-wave methods give accurate results on cross-bonded systems but require two or more observation points and good synchronization between measuring units [47],[81],[82].

---

[18] Circuit: CableSimulation_Files\FreqTimeResponses_Crossbonded\EMTP_Files\OC_Voltage.ecf
Computing and Plotting: CableSimulation_Files\MATLAB_routines\gamma_from_Voc.m

This chapter presents an alternative fault location method applicable to cross-bonded cables and requiring only one observation point. The method is based on the relation between the first resonant frequency of the system and the distance from the fault.

The method is illustrated by applying a solid core-to-sheath fault at the n^{th} minor section of the cable in Figure 6.2 with 6 major sections and a total length of 18 km, i.e. 1 km per minor section. The current source defined in equation (2.48) is applied to the faulted phase and the impedance response is calculated from the measured source voltage as in (2.49). The same test is applied to normal-bonded, cross-bonded and transposed cables.

The short-circuit cable response has an initial peak corresponding to the wavelength λ being equal to 4 times the length of the cable, or in this case the distance d to the fault point. Therefore, the distance to the fault can be calculated as

$$\lambda = c/f_0 = 4d \rightarrow d = c/(4f_0) \tag{6.9}$$

where c is the velocity of propagation and f_0 is the frequency of the first peak in the cable response. Though not shown, the modal velocities for this cable system becomes nearly constant above 100 Hz. Therefore, the values in Table 6.3 can be used to estimate the fault location using (6.9).

Though the interest is to calculate the location of the fault, eq. (6.9) can also be used inversely i.e. use the fault location d and the fundamental frequency f_0 observed from the cable response to calculate the velocity as

$$c = 4 f_0 d \tag{6.10}$$

The interest of this exercise is to verify which mode creates the resonance.

Table 6.9 shows the fundamental resonant frequencies of normal-bonded, cross-bonded and transposed cables when the fault is located at different points and the corresponding modal velocities estimated with (6.10). As expected, in the case of normal-bonding the coaxial mode velocity is obtained for all fault locations. For the cases of cross-bonded and transposed cables the velocity is 119 m/μs which corresponds to the inter-core mode in Table 6.3. An exception if found for a fault located within the first minor section in which the dominant modes are purely coaxial

(fault on the 1st minor section) and inter-sheath (fault on 2nd and 3rd minor sections). Although the cables are cross-bonded or transposed, the inter-sheath mode velocities obtained are those of a normal-bonded cable because at the first and second minor sections, the sheaths and cores have not been completely transposed yet. Even for a fault in the 4th minor section the error (deviation from the velocities in Table 6.3) is relatively high – 5.2% for cross-bonded and 6.8% for transposed cables. For faults located at the 5th minor section or further from the source, it is clearly the inter-core mode which is associated to the first resonant frequency in the cable response.

Figure 6.36 shows the impedance amplitude and phase of the cross-bonded cable for different fault locations. The location of the fault can be identified either from the first peak in impedance amplitude or the first zero-crossing of impedance phase.

Table 6.9. Measured frequencies and calculated velocities for fault detection on a cable with 6 major sections and 18 km [51].

Fault		Normal-bonded		Cross-bonded		Transposed	
Major	Minor	f_0 (Hz)	v (m/μs)	f_0	v	f_0	v
1	1	41400	166	41418	166	41400	166
	2	20559	164	12370	99	12560	100
	3	13772	165	8205	98	8337	100
2	4	10257	164	7820	125	7943	127
	5	8222	164	6007	120	6053	121
	6	6939	167	5078	122	5082	122
3	9	4560	164	3296	119	3350	121
4	12	3412	164	2414	116	2466	118
5	15	2716	163	1969	118	1995	120
6	17	2393	163	1768	120	1786	121
	18	2254	162	1645	118	1679	121

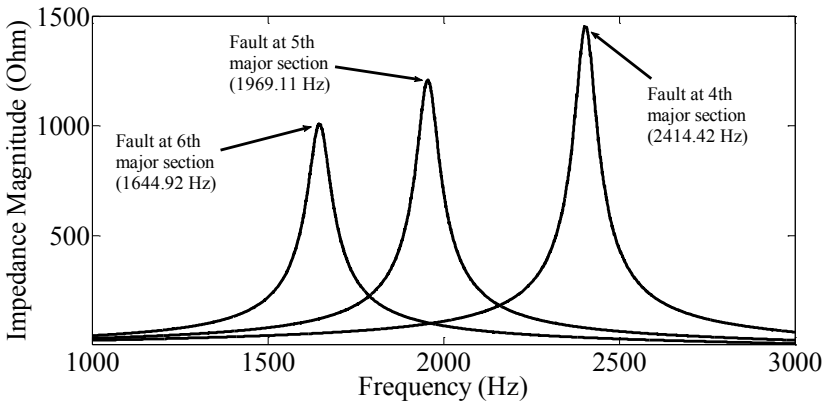

Figure 6.35 Simulated frequency response (magnitude of input impedance) of a cross-bonded cable with 6 major sections with a fault placed at 3 different locations [51].[19]

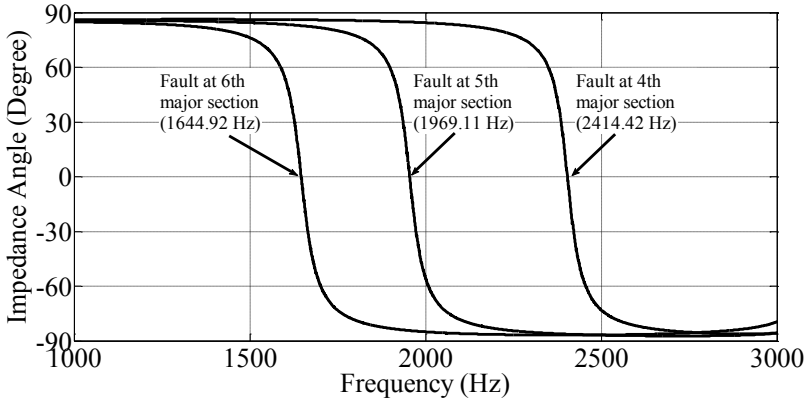

Figure 6.36 Simulated frequency response (angle of input impedance) of a cross-bonded cable with 6 major sections with a fault placed at 3 different locations [51]. [19]

This approach can also be verified in time-domain. The simulation test consists of applying a fault at t = 1 ms to the cross-bonded cable with 18 major sections. The cable is constantly fed by a balanced 225 kV source. Figure 6.37 shows the sending end current when a phase-to-phase fault occurs at two points in the cable: end of the 4th major section and end of the 6th major section. It can be observed that the period of oscillations is 149.7 μs for a fault at the 4th major section and 225.6 μs for the fault at the 6th major section. The ratio between oscillating periods $149.7/225.6 = 0.66$ is similar to the inverse of the frequency ratio $1644.92/2414.42 = 0.68$ which

[19] Circuit: CableSimulation_Files\FreqTimeResponses_Crossbonded\FreqDomain_DiffBonding.ecf

shows that the different between fault locations can be observed in frequency-domain as well as in time-domain.

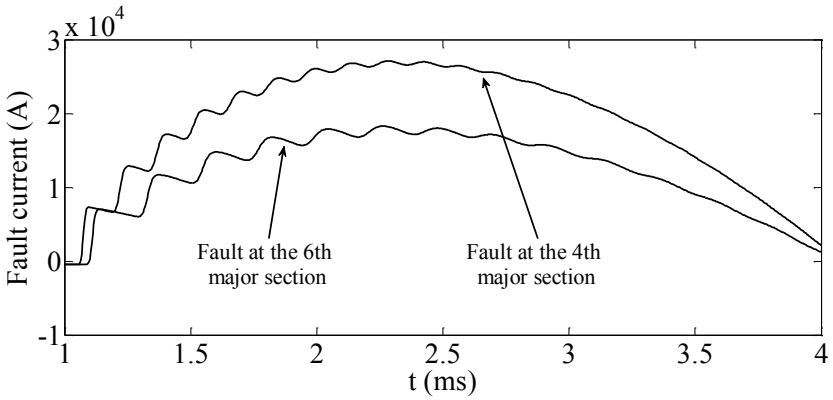

Figure 6.37 Sending end current for phase-to-phase short-circuit in a 225 kV cable with 18 major sections.[20]

6.6 Conclusion

In this chapter a study of cross-bonded cables for HVAC power transmission was presented with the following conclusions.

Single-core coaxial modes cannot propagate in cross-bonded systems because the sheaths change phase within each major section. Instead, these systems will have two inter-core modes which are slower and more attenuated.

Core modes, both of coaxial or inter-core nature, are unaffected by the grounding of the sheaths at each major section. This occurs because the penetration depth becomes lesser than the sheath thickness after a certain frequency. Thus the sheaths provide full shielding of the phase conductors to any external phenomenon. On the other hand, core modes are affected by the bonding of the sheaths at each major section.

Inter-core modes on cross-bonded cables are generally accompanied of induced inter-sheath modes. The superposition of modes is particularly noticeable when resonance between one major

[20] Circuit: CableSimulation_Files\FreqTimeResponses_Crossbonded\EMTP_Files\TimeDomain_DiffBonding.ecf

section and the inter-sheath mode wavelength occurs. This is generally observed at high frequencies, depending on the length of the major section.

Modeling cross-bonded systems through homogeneous equivalents is inaccurate both in time and frequency domain because the equivalent cannot represent the abovementioned superposition modes nor the reflections created at cross-bonding points which affect the core voltages and currents. The two phenomena have an important impact on the cable response to switching, fault and lightning transients.

Accurate modeling of first and last major sections greatly reduces the simulation times compared to full discrete modeling and gives more accurate results both in frequency and time domain compared to using homogeneous equivalents alone. The approach showed good accuracy in the simulation of a field test on a 225 kV underground cross-bonded cable with 64 km and 17 major sections.

Propagation constants of cross-bonded cables can be calculated without recurring to homogeneous equivalents, based only on the open-circuit response of the system.

A single-terminal method can accurately locate faults in cross-bonded cables based on their frequency response and characteristic wave velocity. The method was demonstrated in a cross-bonded system with 18 major sections for different fault locations.

CHAPTER 7 CONCLUSION AND RECOMMENDATIONS

7.1 Summary of this thesis

The main objective of this thesis was to investigate the behavior, modeling and simulation of underground cables used for HVAC power transmission. The main trigger for this project was the field test carried out by the French TSO Réseaux de Transport d'Électricité on a 64 km underground cable meant to measure the cable characteristics and to validate a cable model for transient studies. The study of the test results lead to the development of a method for calculating PUL resistance, inductance and capacitance from measured voltage and current waveforms which provides valuable additional information for validating the cable model. Another important trigger was the rare measurements of cable discharge courteously provided by National Grid, UK which allowed a validation of a cable model for discharge studies and the estimation of the typical time required to discharge a HVAC cable. Finally, this PhD project also filled a gap in the literature by demonstrating very important aspects of cross-bonded cables which differentiate them from simple normal-bonded cables. The most important remarks of this PhD project are summarized as follows.

Calculation of per-unit-length cable parameters from field test results

The usual practice when using field tests for validation of cable model for transients studies is to calculate modal attenuations, velocities and characteristic impedances from the voltages and currents measured at the cable terminals and to compare them to the cable model parameters. However, this method of validation is limited when the source of discrepancies between field test and simulation results needs to be identified. It was shown in this thesis that further information can be extracted from the results of cable surge testing namely the PUL resistance, the inductance and the capacitance for each modal excitation. The advantage of using these additional data to validate the cable model is that they allow a better identification of the sources of deviation between field test and simulation results. For example, the approach can be useful in identifying the impact of external factors, such as the grounding resistance or the inductance of a bonding wire into the measured results.

Cable discharge

The discharge of a power transmission cable to safe voltage levels can take many hours to complete if equipment for forced discharging is not used. Being a quasi-DC phenomenon, the time required for the discharge is mainly determined by the cable shunt parameters, i.e. the per-unit-length capacitance and conductance, as well as the leakage resistance of the insulators connected to the cable. The cable parameters are nearly unaffected by external factors. On the other hand, insulator equipment exposed to air are highly affected by air temperature, humidity and contamination. The cable capacitance can be easily calculated using available cable data. On the other hand, the leakage resistances of the cable and the external circuit are in general not easily available but can be estimated from measured time responses of cable voltage during discharge, as demonstrated in this thesis, which follow well-known formulas of RC circuits. Typical ranges of properties for cable insulation, cable capacitance and insulator equipment have been collected to estimate the typical discharge times required to lower the cable voltage to safe limits once the cable is out of service. This can go from a few minutes in case of a leaky system to several days if very little leakage is observed. A correction to the leakage resistance of insulators that accounts for changes in the air humidity was defined based on a field test result.

Cross-bonded cables

The main difference between cross-bonded and normal-bonded cables which was clearly demonstrated in this thesis is that coaxial modes cannot propagate in cross-bonded cables. Instead, inter-core modes will propagate. These modes have in general very different characteristics than those of coaxial modes, i.e. different attenuation, propagation velocity and characteristic impedance. This difference is extremely important when performing harmonic, fault location and transient studies. Furthermore, these inter-core modes are always accompanied by induced inter-sheath modes and they are thus affected by the non-uniformities in the sheaths. Because the skin effect depth becomes lesser than the sheath thickness above a certain frequency, the transient cable response will not be affected by the grounding of the sheath. However, it will be affected by the sheath cross-bonding and by the bonding of the three-phase sheaths at the end of each major section. Due to this bonding, each major section will have a separate circuit for the sheaths. When

the inter-sheath mode wave resonates inside a major section it will have a magnified impact on the overall cable response.

Modeling of cross-bonded cables using homogeneous equivalents is thus inaccurate not only in time domain but also in frequency domain because these standing wave phenomenon occurring in the sheaths is not represented. However, the accuracy of simulations can be improved if the terminal sections of the cable system are accurately represented, even if the remainder of the cable is modeled by a homogeneous equivalent. Still, if the purpose of the study is the estimation of sheath overvoltage the full cable length should be modeled in the most accurate manner, i.e. each minor section with each core and sheath conductor modeled separately and the cross-bonding and sheath groundings explicitly represented.

Another important aspect demonstrated in this thesis is that a homogeneous equivalent is not required to calculate the propagation characteristics of a cross-bonded cable because these can simply be calculated from the cable open-circuit and short-circuit responses. This approach is however limited to frequencies at which the cable length is lesser than half wavelength, after which the standing-wave effect becomes important. Finally it was also demonstrated that the frequency response of the cross-bonded cable can also be used for fault location.

The conclusions drawn from this PhD project have direct application in the simulation of electromagnetic transients involving HVAC underground cables, in particular the validation of cable models. The typical values of cable discharge time, cable insulation and insulator leakage resistances that have been provided in this thesis are useful for evaluating the need for special discharge equipment. Finally, the remarks on the behavior, modeling and simulation of cross-bonded cables can be applied to transient electromagnetic studies, harmonic studies and fault location in cables. A list of the journal and conference publications derived from this PhD project can be found in appendix C.

7.2 Future work

Considering the general scope of this thesis, which is the modeling of HVAC cables and simulation of electromagnetic transients, possible developments are as follows.

Investigation of impedance and admittance formulas for finite cable

The impedance and admittance formulas currently used in EMTP (Schelkunoff, Carson, Pollaczek) assume infinite conductors and are thus defined as per-unit-length. This assumption can be inaccurate particularly at frequencies for which the wavelength becomes comparable to the cable length. The impact of infinite conductor assumption on the accuracy of cable parameters has not been clearly identified.

Impact of grounding and earth return impedance during a field test of surge in a cable

During a field test, if the testing site is not located in a substation a local grounding has to be installed for protection of staff and equipment and to provide a voltage reference. The quality of a manually installed grounding is in general not as good as the grounding of a substation and it may have a magnified impact in the measurements. Moreover, the grounding and earth-return impedances are likely to be highly frequency dependent. The impact of grounding and frequency dependency of earth-return impedance in field test measurements is a subject to be further clarified.

Implement proximity effect aware formulas

Several publications have demonstrated the impact of proximity effect in the transient response of long cross-bonded cables [14] as well as submarine cables [84]. Due to the close proximity of the phases, this impact can be particularly important in submarine cables which are more and more often used for overseas interconnections (e.g. intercontinental links and off-shore wind farms). At the same time, the application of numerical methods (in particular the finite-elements method and the method of moments) for the calculation of proximity aware cable parameters has been thoroughly tested and reported in several publications and particularly in a report of CIGRÉ [85]. The implementation of proximity aware cable parameter calculation into EMTP is a feature desired by many power utilities. However, further analysis of the actual impact of proximity effect with field tests and practical cases is still needed.

Improve earth-return impedance formula

Pollaczek's formula for the earth-return impedance uses several assumptions. For example, the relative permittivity of the soil is assumed to be 1, the conductor is assumed as infinitely thin and the propagation is assumed to be in transverse electromagnetic (TEM) mode. At high frequencies the assumption that the earth behaves as a conductor is no longer valid, i.e. $\sigma_{earth} \approx \omega\varepsilon_{earth}$ and the assumption of TEM propagation is no longer valid. In the case of OHL, it was demonstrated that accounting for the earth-return admittance allows representing this mode transition [86]. It would be desirable to achieve a similar solution for the case of the underground cable or simply to derive a full-wave solution capable of eliminating the limitations of Pollaczek's formula.

REFERENCES

[1] CIGRE WG C4.502, "Power System Technical Performance Issues Related to the Application of Long HVAC Cables," CIGRE, 2013.

[2] L. Colla, M. Rebolini and F. Iliceto, "400 kV AC new submarine cable links new between Sicily and the Italian mainland," in CIGRE 2008 General Session Paper C4-116, Paris, 2008.

[3] Energinet.dk, "Cable Action Plan," Energinet.dk, 2009.

[4] S. Palone and F. Lauria, "Optimal Operation of Long Inhomogeneous AC Cable Lines: The Malta–Sicily Interconnector," IEEE Trans. Power Delivery, vol. 29, no. 1, pp. 1036-1044, 2014.

[5] Réseaux de Transport d'Électricité, "Filet de sécurité PACA: pour une sécurisation électrique durable de la région. Dossier de Presse," Réseaux de Transport d'Électricité, [Online]. Available: www.rte-france.com/fr/projet/file-de-securite-paca-pour-une-securisation-electrique-durable-de-la-region. [Accessed 25 04 2015].

[6] Réseaux de Transport d'Électricité, "Tous les projets," Réseaux de Transport d'Électricité, [Online]. Available: http://www.rte-france.com/fr/tous-les-projets. [Accessed 25 04 2016].

[7] L. M. Wedepohl and D. J. Wilcox, "Estimation of transient sheath overvoltages in power-cable transmission systems," Proc. IEE, vol. 120, no. 8, pp. 877-882, 1973.

[8] N. Nagaoka and A. Ametani, "A development of a generalized frequency-domain transient program – FTP," Trans. Power Delivery, vol. 3, no. 4, pp. 1986-2004, 1988.

[9] A. Semlyen and A. Dabuleanu, "Fast and accurate switching transient calculations on transmission lines with ground return using recursive convolution," IEEE Trans. Power Apparatus and Systems, vol. 94, no. 2, pp. 561-571, 1975.

[10] B. Gustavsen, J. Sletbak and T. Henriksen, "Simulation of transient sheath overvoltages in the presence of proximity effects," IEEE Trans. Power Delivery, vol. 10, no. 2, p. 1066–1075, 1995.

[11] T. Noda, N. Nagaoka and A. Ametani, "Phase domain modelling of frequency-dependent transmission lines by means of an ARMA model," IEEE Trans. Power Delivery, vol. 11, no. 1, p. 401–411, 1996.

[12] A. Morched, B. Gustavsen and M. Tartibi, "A universal model for accurate calculation of electromagnetic transients on overhead lines and underground cables," IEEE Trans. Power Delivery, vol. 14, no. 3, p. 1032–1038, 1999.

[13] T. C. Yu and J. R. Marti, "zCable model for frequency dependent modelling of cable transmission systems," in International Conference on Power Systems Transients (IPST), Rio de Janeiro, 2001.

[14] U. S. Gudmundsdottir, Modelling of long High Voltage AC cables in Transmission Systems, Aaborg: Aalborg University, 2010.

[15] N. Nagaoka and A. Ametani, "Transient calculations on crossbonded cables," IEEE Trans. Power Apparatus and Systems, vol. 102, no. 4, pp. 779-787, 1983.

[16] U. S. Gudmundsdottir, B. Gustavsen, C. L. Bak and W. W. Wiechowski, "Field Test and Simulation of a 400-kV Cross-Bonded Cable System," IEEE Trans. Power Delivery, vol. 26, no. 3, pp. 1403-1410, 2011.

[17] A. Ametani, Distributed-Parameter Circuit Theory, Tokyo: Corona Pub. Co., 1990.

[18] A. Ametani, N. Nagaoka, Y. Baba and T. Ohno, Power System Transients, New York: CRC Press, 2014.

[19] IEE Japan Working Group, "Surge Phenomena and Countermeasures on Cable Systems (Report no. 336)," IEE Japan, 1991, 1991.

[20] I. Lafaia, A. Ametani, J. Mahseredjian, A. Naud, M. T. Correia de Barros and I. Koçar, "Field test and simulation of transients on the RTE 225 kV cable," IEEE Trans. Power Delivery, (to be published).

[21] Y. Watanabe, K. Kosugi and et. al., "Installation of 275 kV PT-POF cable in Tokyo – Part 3 After installation tests," Fujikura Densen Tech. Review, vol. 48, pp. 11-26, 1973.

[22] M. Takaoka and M. Siseki, "The potential distribution of direct current on cable," IEE Japan, vol. 91, no. 11, pp. 2126-2134, 1971.

[23] M. Takaoka, "The potential distribution of direct current oil-filled cable," IEEE Trans. Power Apparatus and Systems, vol. 90, no. 6, pp. 2622-2630, 1971.

[24] A. Ametani, T. Ohno and N. Nagaoka, Cable System Transients, New York: Wiley, 2015.

[25] IEC TC 20 - Electric Cables, "Tests on oil-filled and gas-pressure cables and their accessories - Part 1: Oil-filled, paper or polypropylene paper laminate insulated, metal-sheathed cables and accessories for alternating voltages up to and including 500 kV," International Electrotechnical Comission (IEC), 1993.

[26] JEC-3401, "Standard of Oil-Filled Cable Testing," Japanese Electrotechnical Comittee, 2006.

[27] D. Paul, P. R. Chavadarian and V. Haddadian, "Cable-capacitance discharge time with and without the application of grounding device," IEEE Trans. Industry Applications, vol. 47, no. 1, pp. 286-291, 2011.

[28] F. Ghassemi, "Effect of trapped charges on cable SVL failure," in International Conference on Power Systems Transients (IPST), Vancouver, 2013.

[29] Insulated Conductors Comittee, "IEEE Guide for Bonding Shields and Sheaths of Single-Conductor Power Cables Rated 5 kV through 500 kV, Std. 575," IEEE, 2014.

[30] E. H. Ball, E. Occhini and G. Luoni, "Sheath overvoltages in high-voltage cables resulting from special sheath-bonding connections," IEEE Trans. Power App. Syst., vol. 84, no. 10, pp. 974-988, 1965.

[31] D. J. Rhodes and A. Wright, "Induced voltages in the sheaths of cross-bonded ac cables," Proc. Inst. Elect. Eng., vol. 113, no. 1, pp. 99-110, 1966.

[32] C. Adamson, E. Taha and L. M. Wedepohl, "Comparative steady-state performance of cross-bonded cable systems," Proc. Inst. Elect. Eng., vol. 115, no. 8, pp. 1147-1155, 1968.

[33] A. G. Heaton, "Transient response of cross-bonded cable systems," Proc. Inst. Elect. Eng., vol. 117, no. 3, pp. 578-586, 1970.

[34] N. D. Dang, Transient performance of cross-bonded cable systems, Manchester: University of Manchester, 1972.

[35] L. M. Wedepohl and C. S. Indulkar, "Wave propagation in nonhomogeneous systems. Properties of the chain matrix," Proc. IEE, vol. 121, no. 9, pp. 997-1000, 1974.

[36] L. M. Wedepohl and C. S. Indulkar, "Switching overvoltages in short cross-bonded cable systems using the Fourier transform," Proc. IEE, vol. 122, no. 11, pp. 1217-1221, 1975.

[37] D. J. Wilcox and K. J. Lawler, "Implementation of nonhomogeneous theory in the transient analysis of cross-bonded cable systems," Proc. IEE, vol. 125, no. 10, pp. 993-998, 1978.

[38] D. J. Wilcox and K. J. Lawler, "Transient phenomena in cross-bonded cable systems: analytical results," Proc. IEE, vol. 125, no. 10, pp. 999-1005, 1978.

[39] W. Kersten, "Surge arresters for sheath protection in cross-bonded cable system," Proc. IEE, vol. 126, no. 12, pp. 1255-1262, 1979.

[40] L. M. Wedepohl and C. S. Indulkar, "Switching overvoltages in long cross-bonded cable systems using the fourier transform," IEEE Trans. Power App. Syst., vol. 98, no. 4, pp. 1476-1480, 1979.

[41] R. Jackson, A. Wilson and D. Giesner, "Partial discharges in power-cable joints: their propagation along a cross-bonded circuit and methods for their detection," IEE Proc. Gen. Trans. Dist., vol. 127, no. 6, pp. 420-429, 1980.

[42] W. Humpage, K. Wong and T. Nguyen, "Z-transform electromagnetic transient analysis of cross-bonded cable transmission systems," IEE Proc. Gen. Trans. Dist., vol. 128, no. 2, pp. 55-62, 1981.

[43] E. Kuffel and J. Poltz, "AC losses in cross-bonded and bonded at both ends high voltage cables," IEEE Trans. Power App. Syst., vol. 100, no. 1, pp. 369-374, 1981.

[44] T. Ohno, C. L. Bak, A. Ametani, W. Wiechowski and T. Sorensen, "Derivation of theoretical formulas of the frequency component contained in the overvoltage related to long EHV cables," IEEE Trans. Power Del., vol. 27, no. 2, pp. 866-876, 2012.

[45] C. L. Bak and C. F. Jensen, "Distance protection of cross-bonded transmission cable-systems," in 12th IET Int. Conf. on Dev. Power Sys. Protections (DPSP 2014), Copenhagen, 2014.

[46] C. F. Jensen, U. S. Gudmundsdottir, C. L. Bak and A. Abur, "Field test and theoretical analysis of electromagnetic pulse propagation velocity on cross-bonded cable systems," IEEE Trans. Power Del., vol. 29, no. 3, pp. 1028-1035, 2014.

[47] C. F. Jensen, Online Location of Faults on AC Cables in Underground Transmission Systems, Aalborg: Aalborg University, 2013.

[48] L. M. Wedepohl, "Application of matrix methods to the solution of traveling wave phenomena in polyphase systems," Proc. IEE, vol. 110, no. 12, pp. 2200-2212, 1963.

[49] F. F. da Silva and C. L. Bak, Electromagneitc Transients in Power Cables, Springer, 2013.

[50] I. Lafaia, Y. Yamamoto, A. Ametani, J. Mahseredjian, M. T. Correia de Barros, I. Koçar and A. Naud, "Propagation of intersheath modes on underground cables," Electric Power Systems Research (EPSR), vol. 138, pp. 113-119, September 2016.

[51] I. Lafaia, A. Ametani, J. Mahseredjian, M. T. Correia de Barros and I. Koçar, Y. Fillion, "Frequency and time domain responses of cross-bonded cables," IEEE Trans. Power Delivery, (awaiting the first revision).

[52] I. Lafaia, F. Ghassemi, A. Ametani, J. Mahseredjian, S. Dennis, M. Haddad and S. Robson, "Experimental and theoretical analysis of cable discharge," IEEE Trans. Power Delivery, (submitted after the first revision).

[53] T. Ohtani, A. Ametani and I. Fujita, Electric Circuit Theory, Shokondo Pub. Co., 1992.

[54] Good Fellow, "Polyimide (PI) – Material Properties," Good Fellow.

[55] DuPont, "Summary of Properties for Kapton® Polyimide Films," DuPont, [Online]. Available: www.dupont.com/content/dam/assets/ products-and-services/membranes-films/assets/DEC-Kapton-summary-of-properties.pdf. [Accessed January 2016].

[56] IEC TC 20 - Electric Cables, "Power cables with extruded insulation and their accessories for rated voltages from 1 kV up to 30 kV (60502-1)," International Electrotechnical Commission (IEC), 2004.

[57] Nexans, "60-500 kV High Voltage Underground Power Cables – XLPE Insulated Cables," Nexans, [Online]. Available: www.nexans.co.uk/eservice/UK-en_GB/fileLibrary/Download_540192183/UK/files/Nexans%20High%20Voltage%20Underground.pdf. [Accessed January 2016].

[58] Brugg Kabel AG, "High Voltage XLPE Cable Systems – Technical User Guide," Brugg Kable AG, 2006.

[59] R. S. Gorur and et al., "Surface Resistance Measurements on Nonceramic Insulators," IEEE Trans. Power Del., vol. 16, no. 4, pp. 801-805, 2001.

[60] L. Chmura and et al., "Use of Dissipation Factor for Life Consumption Assessment and Future Life Modeling of Oil-Filled High-Voltage Power Cables," IEEE Electrical Insulation Magazine, vol. 28, no. 1, pp. 27-37, 2012.

[61] A. Ametani, "A general formulation of impedance and admittance of cables," IEEE Trans. Power Apparatus and Systems, vol. 99, no. 3, pp. 902-910, 1980.

[62] H. Dommel, "EMTP Theory Book," Bonneville Power Administration, Portland, 1986.

[63] A. Ametani (editor), Numerical Analysis of Power Systems Transients and Dynamics, Institute of Engineering and Technology (IET), 2014.

[64] Brugg Kabel AG, "Outdoor Terminations," Brugg Kabel AG.

[65] J. Mahseredjian, S. Dennetière, L. Dubé, B. Khodabakhchian and L. Gérin-Lajoie, "On a new approach for the simulation of transients in power systems," Electric Power Systems Research (EPSR), vol. 77, no. 11, pp. 1514-1520, 2007.

[66] I. Koçar, J. Mahseredjian and G. Olivier, "Improvement of Numerical Stability for the Computation of Transients in Lines and Cables," IEEE Trans. Power Delivery, vol. 25, no. 2, pp. 1104-1111, 2010.

[67] I. Koçar, J. Mahseredjian and G. Olivier, "Weighting Method for Transient Analysis of Underground Cables," IEEE Trans. Power Delivery, vol. 23, no. 3, pp. 1629-1635, 2008.

[68] B. Gustavsen, J. A. Martinez and D. Durbak, "Parameter determination for modelling system transients—Part II: Insulated cables," IEEE Trans. Power Delivery, vol. 20, no. 3, pp. 2038-2044, 2005.

[69] A. Ametani, Y. Miyamoto and N. Nagaoka, "Semiconducting Layer Impedance and its Effect on Cable Wave-Propagation and Transient Characteristics," IEEE Trans. Power Delivery, vol. 19, no. 4, p. 2004, 1523-1531.

[70] A. Ametani, Y. Miyamoto and N. Nagaoka, "An investigation of a wave propagation characteristic on a cross-bonded cable," IEE Japan Trans. PE, vol. 123, no. 3, pp. 395-401, 2003.

[71] Z. Iwata, H. Shii, M. Kinoshita, H. Hirukawa and E. Kawai, "New modified polyethylene paper proposed for UHV cable insulation," IEEE Trans. Power Apparatus and Systems, vol. 96, no. 5, pp. 1573-1582, 1977.

[72] L. M. Wedepohl and R. G. Wasley, "Wave propagation in polyphase transmission systems. Resonant effects due to discretely bonded wires," Proc. IEE, vol. 112, no. 11, pp. 2113-2119, 1965.

[73] A. Semlyen, "Some frequency domain aspects of wave propagation on nonuniform lines," IEEE Trans. Power Delivery, vol. 18, no. 1, pp. 315-322, 2003.

[74] J. A. B. Faria and J. F. Borges da Silva, "The effect of randomly earthed ground wires on PLC transmission – a simulation experiment," IEEE Trans. Power Delivery, vol. 5, no. 4, pp. 1669-1677, 1990.

[75] J. A. B. Faria, "On the resonance effects due to ground wires in transmission lines with non-uniform soil conductivity and non-uniform tower resistance," IEEE Trans. Power Delivert, vol. 7, no. 1, pp. 29-38, 1992.

[76] J. A. B. Faria and M. V. G. Neves, "Resonance effects due to conductor transposition in three-phase power lines," in 14th Power Systems Computation Conference (PSCC), Sevilla, 2002.

[77] N. Nagaoka, Transient analysis of cable systems by means of a frequency-transform method, Doshisha: Doshisha University, 1992.

[78] A. Ametani and Y. Kasai, "Application of an equivalent homogeneous line model to a transient analysis of a distributed system," IEEJ Trans. PE, Vols. B-114, pp. 1059-1065, 1994.

[79] Insulated Conductors Committee, "IEEE Guide for Fault-Locating Techniques on Shielded Power Cable Systems, Std. 1234," IEEE, 2007.

[80] R. Razzaghi, G. Lugrin, H. M. Manesh, C. Romero, M. Paolone and F. Rachidi, "An efficient method based on the electromagnetic time reversal to locate faults in power networks," IEEE Trans. Power Delivery, vol. 28, no. 3, pp. 1663-1673, 2013.

[81] B. Sheng, W. Zhou, J. Yu and S. Meng, "On-line PD detection and localization in cross-bonded HV cable systems," IEEE Trans. Dielectr. Electr. Insul., vol. 21, no. 5, pp. 2217-2224, 2014.

[82] R. J. Hamidi and H. Livani, "A travelling wave-based fault location method for hybrid three-terminal circuits," in IEEE Power & Energy Society General Meeting 2015, Denver, 2015.

[83] I. Lafaia, N. Alatawneh, J. Mahseredjian, A. Ametani, M. T. Correia de Barros, I. Koçar and A. Naud, "Modeling of an Underground Cable Installed in a Poly-Ethylene Tube for Transient Simulations," in IEEJ Power and Energy Society Conference, Nagoya, 2015.

[84] C. H. Chien and R. Bucknall, "Harmonic calculations of proximity effect on impedance characteristics in subsea power transmission cables," IEEE Trans. Power Delivery, vol. 24, no. 4, pp. 2150-2158, 2009.

[85] WG C4.501, "Guide for numerical electromagnetic analysis methods: application to surge phenomena and comparison with circuit theory-based approach (TB543)," CIGRÉ, 2013.

[86] A. Ametani, Y. Miyamoto, Y. Baba and N. Nagaoka, "Wave propagation on an overhead multiconductor in a high-frequency region," IEEE Trans. Electromagnetic Compatibility, vol. 56, no. 6, pp. 1638-1648, 2014.

[87] A. Ametani and K. Imanishi, "Development of Exponential Fourier Transform and Its Application to Electrical Transients," Proc. IEE, vol. 126, no. 1, pp. 51-56, 1979.

[88] S. A. Schelkunoff, "The electromagnetic theory of coaxial transmission lines and cylindrical shields," Bell System Technical Journal, vol. 13, no. 4, pp. 532-579, 1934.

[89] D. K. Cheng, Field and Wave Electromagnetics, Addison-Wesley Publishing Company, 1989.

[90] G. W. Brown and R. G. Rocamora, "Surge propagation in three-phase pipe-type cables, Part I—Unsaturated pipe," IEEE Trans. Power Apparatus and Systems, vol. 95, no. 1, pp. 89-95, 1976.

[91] J. A. Tegopoulos and E. E. Kriezis, "Eddy current distribution in cylindrical shells of inifinite length due to axial currents. Part II : shells of finite thickness," IEEE Trans. Power Apparatus and Systems, vol. 90, no. 3, pp. 1287-1294, 1971.

[92] V. F. Pollaczek, "Über das feld einer unendlich langen wechselstromdurchflossenen einfachleitung," Elektrische Nachrichtentechnik, vol. 9, no. 3, pp. 339-360, 1926.

[93] L. M. Wedepohl and D. J. Wilcox, "Transient analysis of underground power-transmission systems. System-model and wave-propagation characteristics," Proc. IEE, vol. 120, no. 2, pp. 253-260, 1973.

[94] O. Saad, G. Gaba and M. Giroux, "A closed-form approximation for ground return impedance of underground cables," IEEE Trans. Power Delivery, vol. 11, no. 3, pp. 1536-1545, 1996.

[95] R. Carson, "Wave propagation in overhead wires with ground return," The Bell System Technical Journal, vol. 5, no. 4, pp. 539-554, 1926.

[96] F. A. Uribe, J. L. Naredo, P. Moreno and L. Guardado, "Algorithmic evaluation of underground cable earth impedances," IEEE Trans. Power Delivery, vol. 19, no. 1, pp. 316-322, 2004.

[97] X. Legrand, A. Xemard, G. Fleury, P. Auriol and C. A. Nucci, "A quasi-Monte Carlo integration method applied to the computation of the Pollaczek integral," IEEE Trans. Power Delivery, vol. 23, no. 3, pp. 1527-1534, 2008.

[98] G. C. Stone and S. A. Boggs, "Propagation of partial discharge pulses in shielded power cable," in Proceedings of the Conference on Electrical Insulation and Dielectric Phenomena, Washington DC, 1982.

APPENDIX A – CALCULATION OF CABLE PER-UNIT-LENGTH PARAMETERS IN EMTP-RV

Cable models available in EMT software such as EMTP-RV, ATP and PSCAD-EMTPDC are generally based on the frequency-dependent per-unit-length (PUL) impedance and admittance matrices $\bar{\mathbf{Z}}$ and $\bar{\mathbf{Y}}$:

$$\bar{\mathbf{Z}}(\omega) = \left(\mathbf{R}(\omega) + j\omega\mathbf{L}(\omega)\right) \tag{A.1}$$

$$\bar{\mathbf{Y}}(\omega) = \left(\mathbf{G}(\omega) + j\omega\mathbf{C}(\omega)\right) \tag{A.2}$$

$\mathbf{R}$ and $\mathbf{L}$ are PUL series resistance and inductance matrices. $\mathbf{G}$ and $\mathbf{C}$ are PUL shunt conductance and capacitance. These matrices have dimension $n \times n$, where n is the number of conductors in the system except the ground.

The following sections show the formulas used by cable parameter calculation routines of common EMT software for calculating the PUL matrices $\bar{\mathbf{Z}}$ and $\bar{\mathbf{Y}}$. Even though there exist many different cable designs, these software are usually limited to the cases of single-core (SC) and pipe-type (PT) systems [61],[62],[63], which formulas are presented in sections A.1 and A.2, with special reference to earth-return impedances in section A.3. The modeling of special features such as stranded cores, semiconducting layers and high-density-poly-ethylene (HDPE) tubes require modification of input data as explained in section A.4 [83].

A.1 Single-core cable

A.1.1 Input data

Figure A.1 illustrates a single-phase single-core (SC) cable composed of core and sheath. The three-phase system is shown in Figure A.2. The data required for calculating the PUL matrices, defined in the figure, are :

- inner and outer radii of core and sheath conductors and outer radius of the cable,
- resistivity, permeability and permittivity of core and sheath conductors,
- permittivity and loss factor of insulation layers,

- depth of burial,
- cable length,
- if the cable is multiphase, the horizontal coordinate for each phase is also required.

These are the data commonly required by cable parameter calculation routines in EMT software. The impedance formulas given in the following sections are valid for underground cables, i.e. a negative burial depth cannot be used to represent an overhead cable.

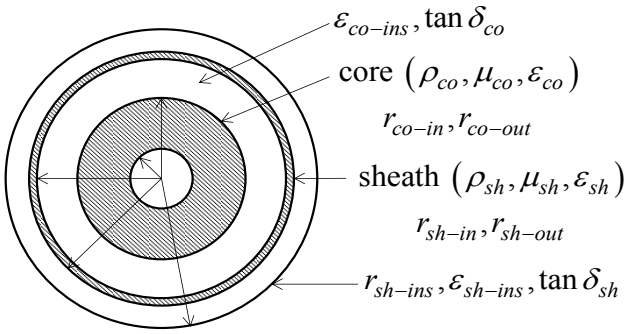

Figure A.1 One-phase single-core cable composed of core and sheath.

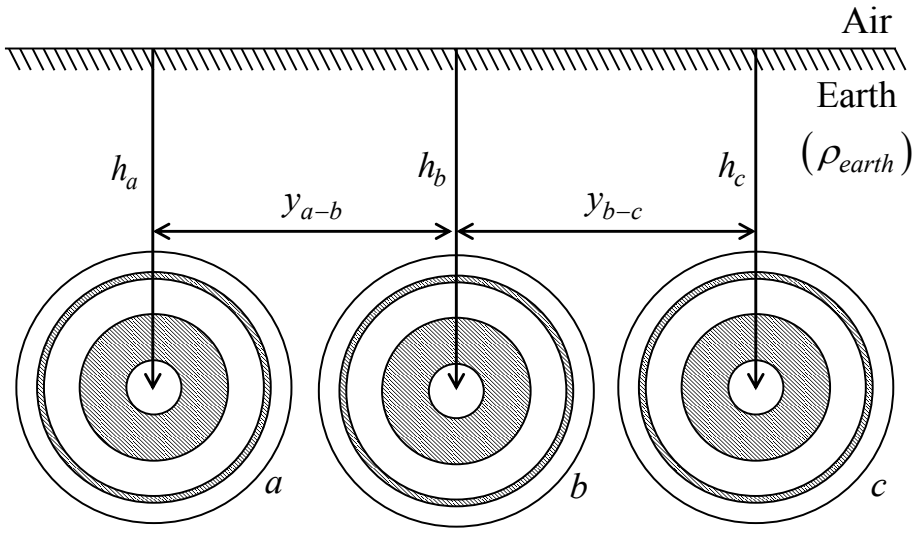

Figure A.2 Three-phase single-core underground cable.

A.1.2 **Series impedance matrix**

The series impedance matrix for the single-phase cable in Figure A.1 is defined from the ratio between the derivative of the voltage with respect to the direction of propagation $d\mathbf{V}/dx$ and the current $\mathbf{I}$ (the bar over complex quantities is dropped to simplify the notation)

$$-\frac{d\,\mathbf{V}}{dx} = \mathbf{ZI} \tag{A.3}$$

$$\mathbf{V} = \begin{bmatrix} V_{co} \\ V_{sh} \end{bmatrix}, \mathbf{I} = \begin{bmatrix} I_{co} \\ I_{sh} \end{bmatrix} \tag{A.4}$$

where V_{co}, I_{co} are the core-to-earth voltage and core current and V_{sh}, I_{sh} are the counterparts for the sheath. The PUL series impedance matrix $\mathbf{Z}$ can be expressed as the sum of an internal conductor impedance matrix $\mathbf{Z_i}$ and an earth-return impedance matrix $\mathbf{Z_0}$ as

$$\mathbf{Z} = \mathbf{Z_i} + \mathbf{Z_0} \tag{A.5}$$

Matrix $\mathbf{Z_i}$ has the following form :

$$\mathbf{Z_i} = \begin{bmatrix} Z_{i-11} & Z_{i-12} \\ Z_{i-12} & Z_{i-22} \end{bmatrix} \tag{A.6}$$

$$Z_{i-11} = \left[Z_{co-out} + Z_{co-ins} + Z_{sh-in} - 2Z_{sh-m}\right] + \left[Z_{sh-out} + Z_{sh-ins}\right] \tag{A.7}$$

$$Z_{i-22} = Z_{sh-out} + Z_{sh-ins} \tag{A.8}$$

$$Z_{i-12} = Z_{sh-out} + Z_{sh-ins} - Z_{sh-m} \tag{A.9}$$

and matrix $\mathbf{Z_0}$ is given as :

$$\mathbf{Z_0} = \begin{bmatrix} Z_{ea} & Z_{ea} \\ Z_{ea} & Z_{ea} \end{bmatrix} \tag{A.10}$$

The formula for the earth-return path impedance Z_{ea} is given in section A.3.

The impedances in (A.7) to (A.9) are defined as follows.

Z_{co-out} and Z_{sh-out} are the PUL impedance of core and sheath outer surfaces. The outer surface impedance of a tubular conductor is in general given as [87],[88]

$$Z_{out} = \frac{\rho\, m}{2\pi\, r_{out}\, D}\left\{I_0\left(m\, r_{out}\right) K_1\left(m\, r_{in}\right) + K_0\left(m\, r_{out}\right) I_1\left(m\, r_{in}\right)\right\} \tag{A.11}$$

$$D = I_1\left(m\, r_{out}\right) K_1\left(m\, r_{in}\right) - I_1\left(m\, r_{in}\right) K_1\left(m\, r_{out}\right) \tag{A.12}$$

$$m = \sqrt{j\omega\mu / \rho} \tag{A.13}$$

where ρ is the resistivity, μ is the magnetic permeability and r_{in}, r_{out} are the inner and outer radii of the tubular conductor. I_0, I_1, K_0, K_1 are modified Bessel functions.

Z_{sh-in} is the PUL impedances of inner surface of the sheath (the core is assumed to be solid). The inner surface impedance of a tubular conductor in general is [88]

$$Z_{in} = \frac{\rho m}{2\pi r_{in} D}\left\{I_0(m r_{in}) K_1(m r_{out}) + K_0(m r_{in}) I_1(m r_{out})\right\} \tag{A.14}$$

Z_{sh-m} is the PUL mutual impedance between inner and outer sheath surfaces. The mutual impedance of a tubular conductor is given in general as [88]

$$Z_m = \frac{\rho m}{2\pi r_{in} r_{out} D} \tag{A.15}$$

Z_{co-ins} and Z_{sh-ins} are PUL impedances of core and sheath insulations. The impedance of an insulation between two tubular concentric conductors is given in general as [89]

$$Z_{ins} = j\omega \frac{\mu_{ins}}{2\pi} \log \frac{r_{ins-out}}{r_{ins-in}} \tag{A.16}$$

where r_{ins-in} and $r_{ins-out}$ are inner and outer radii, and μ_{ins} the magnetic permeability of the specific insulation.

In the case of a three-phase cable system made up of three single-core cables as illustrated in Figure A.2, (A.3) is replaced by a 6-row equation

$$-\frac{d\,\mathbf{V}^{6\times1}}{dx} = \mathbf{Z}^{6\times6}\mathbf{I}^{6\times1} \tag{A.17}$$

$$\mathbf{V}^{6\times1} = \begin{bmatrix} V_{co-a} \\ V_{sh-a} \\ V_{co-b} \\ V_{sh-b} \\ V_{co-c} \\ V_{sh-c} \end{bmatrix}, \mathbf{I}^{6\times1} = \begin{bmatrix} I_{co-a} \\ I_{sh-a} \\ I_{co-b} \\ I_{sh-b} \\ I_{co-c} \\ I_{sh-c} \end{bmatrix} \tag{A.18}$$

$$\mathbf{Z}^{6\times6} = \mathbf{Z}_{\mathbf{i}}^{6\times6} + \mathbf{Z}_0^{6\times6} \tag{A.19}$$

$$\mathbf{Z}_{\mathbf{i}}^{6\times6} = \begin{bmatrix} \mathbf{Z}_{\mathbf{i}} & 0 & 0 \\ 0 & \mathbf{Z}_{\mathbf{i}} & 0 \\ 0 & 0 & \mathbf{Z}_{\mathbf{i}} \end{bmatrix} \tag{A.20}$$

$$\mathbf{Z}_{\mathbf{0}}^{6\times6} = \begin{bmatrix} \mathbf{Z}_{\mathbf{ea}} & \mathbf{Z}_{\mathbf{ea\text{-}m}} & \mathbf{Z}_{\mathbf{ea\text{-}m}} \\ \mathbf{Z}_{\mathbf{ea\text{-}m}} & \mathbf{Z}_{\mathbf{ea}} & \mathbf{Z}_{\mathbf{ea\text{-}m}} \\ \mathbf{Z}_{\mathbf{ea\text{-}m}} & \mathbf{Z}_{\mathbf{ea\text{-}m}} & \mathbf{Z}_{\mathbf{ea}} \end{bmatrix} \tag{A.21}$$

The diagonal matrices in (A.20) have the form of (A.6) and it is assumed that the three phases are equal. Otherwise, the three diagonal matrices in (A.20) would not be the equal. In (A.21), the diagonal matrices have the form in (A.10) and the off-diagonal matrices are as follows :

$$\mathbf{Z}_{\mathbf{ea\text{-}m}} = \begin{bmatrix} Z_{ea-m} & Z_{ea-m} \\ Z_{ea-m} & Z_{ea-m} \end{bmatrix} \tag{A.22}$$

The formula for the mutual earth-return impedance between any two conductors Z_{ea-m} is given in section A.3.

A.1.3 **Shunt admittance matrix**

The shunt admittance matrix for the single-phase cable in Figure A.1 is defined from the ratio of the current derivative with respect to the direction of propagation $d\mathbf{I}/dx$ and the voltage $\mathbf{V}$ as

$$-\frac{d\mathbf{I}}{dx} = \mathbf{Y}\mathbf{V} \tag{A.23}$$

where $\mathbf{V}$ and $\mathbf{I}$ are defined in (A.4). The shunt admittance matrix is conveniently expressed in terms of a potential coefficients matrix $\mathbf{P}$

$$\mathbf{P} = j\omega\mathbf{Y}^{-1} \tag{A.24}$$

$$\mathbf{P} = \mathbf{P}_{\mathbf{i}} \tag{A.25}$$

$$\mathbf{P}_{\mathbf{i}} = \begin{bmatrix} P_{co-ins} + P_{sh-ins} & P_{sh-ins} \\ P_{sh-ins} & P_{sh-ins} \end{bmatrix} \tag{A.26}$$

P_{co-ins} and P_{sh-ins} are the potential coefficients for the core and sheath insulations, respectively. In general, the potential coefficient for an insulation between two tubular concentric conductors is given as [89]

$$P = \frac{\log\left(r_{ins-out}/r_{ins-in}\right)}{2\pi\varepsilon} \tag{A.27}$$

where $\varepsilon = \varepsilon_0\varepsilon_r$ is the permittivity and r_{ins-in}, $r_{ins-out}$ are the inner and outer radii of the insulation.

In the case of a three-phase cable system as in Figure A.2, (A.23) is replaced by a 6-row equation

$$-\frac{d\mathbf{I}^6}{dx} = \mathbf{Y}^{6\times6}\mathbf{V}^6 \tag{A.28}$$

$$\mathbf{P}^{6\times6} = j\omega\left(\mathbf{Y}^{6\times6}\right)^{-1} = \mathbf{P}_\mathbf{i}^{6\times6} \tag{A.29}$$

$$\mathbf{P}_\mathbf{i}^{6\times6} = \begin{bmatrix} \mathbf{P_i} & 0 & 0 \\ 0 & \mathbf{P_i} & 0 \\ 0 & 0 & \mathbf{P_i} \end{bmatrix} \tag{A.30}$$

where it was assumed that the three phases are equal with $\mathbf{P_i}$ given in (A.26).

The above formulation considers lossless insulation, i.e. $\mathbf{Y} = j\omega\mathbf{C}$ with $\mathbf{C} = \mathbf{P}^{-1}$ the capacitance matrix. If insulation losses are accounted for, the admittance for the cable in Figure A.1 is instead written as :

$$\mathbf{Y}_{loss} = \mathbf{G} + j\omega\mathbf{C} \tag{A.31}$$

$$\mathbf{G} = \begin{bmatrix} G_{co-ins} & 0 \\ 0 & G_{sh-ins} \end{bmatrix} \tag{A.32}$$

Conductances G_{co-ins} and G_{sh-ins} represent the losses in the core and sheath insulations respectively, and they are generally accounted for by a so-called dielectric loss factor $\tan\delta$ defined at power frequency as

$$G = \omega C \tan\delta \tag{A.33}$$

(A.33) applies to each insulation, i.e. $G_{co-ins} = \omega C_{co-ins}\tan\delta_{co}$ and $G_{sh-ins} = \omega C_{sh-ins}\tan\delta_{sh}$. The capacitances are simply given as the inverse of respective potential coefficients in (A.27), i.e.

$$C = \frac{2\pi\varepsilon}{\log\left(r_{ins-out}/r_{ins-in}\right)} \tag{A.34}$$

Based on (A.33) an artificial complex permittivity can be defined:

$$\varepsilon = \varepsilon' - j\varepsilon'' \tag{A.35}$$

$$\varepsilon' = \varepsilon'' \tan\delta \tag{A.36}$$

Hence, the admittance of an insulation can be rewritten as :

$$Y_{loss} = \frac{j\omega 2\pi}{\log\left(\frac{r_{ins-out}}{r_{ins-in}}\right)}\left(\varepsilon' - j\varepsilon''\right) \tag{A.37}$$

A.2 Pipe-type cable system

A.2.1 Input data

Figure A.3 illustrates a pipe-type (PT) cable. Each phase inside the pipe is illustrated in Figure A.1. Additionally to the input data described in section A.1.1 for a single-core system, the computation of PUL matrices for a PT cable also requires :

- the inner and outer radii of pipe and the outer radius of pipe insulation,
- the depth of the pipe,
- the resistivity, permeability and permittivity of pipe conductor,
- the permittivity of insulation inside and outside the pipe,
- the location of each phase in relation to the center of the pipe i.e. distance to the center and angle.

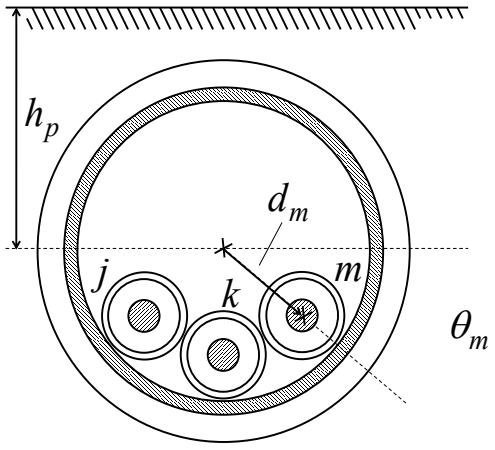

Figure A.3 Underground pipe-type cable.

A.2.2 Series impedance matrix

The series impedance matrix for a three-phase underground PT cable as illustrated in Figure A.3 (internal phases illustrated in Figure A.1) can be expressed as

$$\mathbf{Z}^{7\times7} = \mathbf{Z}_{\mathbf{i}}^{7\times7} + \mathbf{Z}_{\mathbf{p}}^{7\times7} + \mathbf{Z}_{\mathbf{c}}^{7\times7} + \mathbf{Z}_{\mathbf{0}}^{7\times7} \tag{A.38}$$

$$\mathbf{Z}_{\mathbf{i}}^{7\times7} = \begin{bmatrix} \mathbf{Z}_{\mathbf{i}} & \mathbf{0} & \mathbf{0} & \mathbf{0}' \\ \mathbf{0} & \mathbf{Z}_{\mathbf{i}} & \mathbf{0} & \mathbf{0}' \\ \mathbf{0} & \mathbf{0} & \mathbf{Z}_{\mathbf{i}} & \mathbf{0}' \\ \mathbf{0}'^{T} & \mathbf{0}'^{T} & \mathbf{0}'^{T} & 0 \end{bmatrix},\ \mathbf{0}' = \begin{bmatrix} 0 \\ 0 \end{bmatrix} \tag{A.39}$$

$$\mathbf{Z}_{\mathbf{p}}^{7\times7} = \begin{bmatrix} \mathbf{Z}_{\mathbf{p11}} & \mathbf{Z}_{\mathbf{p12}} & \mathbf{Z}_{\mathbf{p13}} & \mathbf{0}' \\ \mathbf{Z}_{\mathbf{p12}} & \mathbf{Z}_{\mathbf{p22}} & \mathbf{Z}_{\mathbf{p23}} & \mathbf{0}' \\ \mathbf{Z}_{\mathbf{p13}} & \mathbf{Z}_{\mathbf{p23}} & \mathbf{Z}_{\mathbf{p33}} & \mathbf{0}' \\ \mathbf{0}'^{T} & \mathbf{0}'^{T} & \mathbf{0}'^{T} & 0 \end{bmatrix} \tag{A.40}$$

$$\mathbf{Z}_{\mathbf{c}}^{7\times7} = \begin{bmatrix} \mathbf{Z}_{\mathbf{c1}} & \mathbf{Z}_{\mathbf{c1}} & \mathbf{Z}_{\mathbf{c1}} & \mathbf{Z}'_{\mathbf{c2}} \\ \mathbf{Z}_{\mathbf{c1}} & \mathbf{Z}_{\mathbf{c1}} & \mathbf{Z}_{\mathbf{c1}} & \mathbf{Z}'_{\mathbf{c2}} \\ \mathbf{Z}_{\mathbf{c1}} & \mathbf{Z}_{\mathbf{c1}} & \mathbf{Z}_{\mathbf{c1}} & \mathbf{Z}'_{\mathbf{c2}} \\ \mathbf{Z}'_{\mathbf{c2}}{}^{T} & \mathbf{Z}'_{\mathbf{c2}}{}^{T} & \mathbf{Z}'_{\mathbf{c2}}{}^{T} & Z_{c2} \end{bmatrix} \tag{A.41}$$

$$\mathbf{Z}_{\mathbf{0}}^{7\times7} = \begin{bmatrix} \mathbf{Z}_{\mathbf{ea}} & \mathbf{Z}_{\mathbf{ea\text{-}m}} & \mathbf{Z}_{\mathbf{ea\text{-}m}} & \mathbf{Z}'_{\mathbf{ea\text{-}m}} \\ \mathbf{Z}_{\mathbf{ea\text{-}m}} & \mathbf{Z}_{\mathbf{ea}} & \mathbf{Z}_{\mathbf{ea\text{-}m}} & \mathbf{Z}'_{\mathbf{ea\text{-}m}} \\ \mathbf{Z}_{\mathbf{ea\text{-}m}} & \mathbf{Z}_{\mathbf{ea\text{-}m}} & \mathbf{Z}_{\mathbf{ea}} & \mathbf{Z}'_{\mathbf{ea\text{-}m}} \\ \mathbf{Z}'_{\mathbf{ea\text{-}m}}{}^{T} & \mathbf{Z}'_{\mathbf{ea\text{-}m}}{}^{T} & \mathbf{Z}'_{\mathbf{ea\text{-}m}}{}^{T} & Z_{ea-m} \end{bmatrix},\ \mathbf{Z}'_{\mathbf{ea\text{-}m}} = \begin{bmatrix} Z_{ea-m} \\ Z_{ea-m} \end{bmatrix} \tag{A.42}$$

In (A.39), submatrix $\mathbf{Z_i}$ is the conductor internal impedance matrix of each SC cables inside the pipe given in (A.6). $\mathbf{Z}_{\mathbf{p}}^{7\times7}$ is the internal impedance matrix of the pipe, $\mathbf{Z}_{\mathbf{c}}^{7\times7}$ is the connection impedance between the pipe inner and outer surfaces, and $\mathbf{Z}_{\mathbf{0}}^{7\times7}$ is the earth-return impedance matrix.

If the pipe thickness is smaller than the skin depth, i.e. $r_{p-out} - r_{p-in} < \sqrt{2\rho_p / \omega\mu_p}$, the pipe can be regarded as being infinite, i.e. $r_{p-out} = \infty$. In that case, the last row and column in (A.39) to (A.42) can be dropped and (A.38) is rewritten as a 6×6 equation

$$\mathbf{Z}^{6\times6} = \mathbf{Z}_{\mathbf{i}}^{6\times6} + \mathbf{Z}_{\mathbf{p}}^{6\times6} \tag{A.43}$$

A sub-matrix of $\mathbf{Z}_{\mathbf{p}}^{7\times7}$ in (A.40) has the following form [61],[90],[91]

$$\mathbf{Z}_{\mathbf{pjk}} = \begin{bmatrix} Z_{p\,jk} & Z_{p\,jk} \\ Z_{p\,jk} & Z_{p\,jk} \end{bmatrix} \tag{A.44}$$

$$Z_{p_{jk}} = \frac{\rho\, m_p}{2\pi\, r_{p-in}} \frac{K_0\left(x_p\right)}{K_1\left(x_p\right)} + Q_{jk} + \frac{j\omega\mu_p}{2\pi} \sum_{n=1}^{\infty} \frac{2C_n}{n\left(1+\mu_p\right) + x_p\, K_{n-1}\left(x_p\right) \big/ K_n\left(x_p\right)} \tag{A.45}$$

$$Q_{jj} = \frac{j\omega\mu_0}{2\pi} \log\left[\frac{r_{p-in}}{r_j} \left(1 - \left(\frac{d_j}{r_{p-in}} \right)^2 \right) \right], r_1 = r_{p-in}, r_2 = r_{p-out}, r_3 = r_{p-ins} \tag{A.46}$$

$$Q_{jk} = \log\left(\frac{r_{p-in}}{\sqrt{d_j^2 + d_k^2 - 2 d_j\, d_k \cos\theta_{jk}}} \right) - \sum_{n=1}^{\infty} \frac{C_n}{n} \tag{A.47}$$

$$C_n = \left(\frac{d_j d_k}{r_{p-in}^2} \right)^n \cos\left(n\,\theta_{jk}\right) \tag{A.48}$$

$$x_p = r_{p-in} \sqrt{\frac{j\omega\,\mu_p}{\rho_p}} \tag{A.49}$$

In (A.45) K_i is the modified Bessel function of second class. Other parameters are defined in Figure A.3. The elements of matrix $\mathbf{Z}_{\mathbf{c}}^{7\times7}$ in (A.41) have the form

$$\mathbf{Z}_{\mathbf{c1}} = \begin{bmatrix} Z_{c1} & Z_{c1} \\ Z_{c1} & Z_{c1} \end{bmatrix},\ Z_{c1} = Z_{p-out} + Z_{p-ins} - 2Z_{p-m} \tag{A.50}$$

$$\mathbf{Z}_{\mathbf{c2}} = \begin{bmatrix} Z_{c2} \\ Z_{c2} \end{bmatrix},\ Z_{c2} = Z_{p-out} + Z_{p-ins} - Z_{p-m} \tag{A.51}$$

where is the impedance of the pipe outer surface calculated with (A.11), Z_{p-ins} is the impedance of the pipe insulation calculated with (A.16) and Z_{p-m} is the mutual impedance between the pipe inner and outer surface, calculated with (A.15).

A.2.3 Shunt admittance matrix

The potential coefficients matrix of a pipe-type as illustrated in Figure A.3 has the following form:

$$\mathbf{P}^{7\times7} = \mathbf{P}_{\mathbf{i}}^{7\times7} + \mathbf{P}_{\mathbf{p}}^{7\times7} + \mathbf{P}_{\mathbf{c}}^{7\times7} \text{ or } \mathbf{P}^{\mathbf{6\times6}} = \mathbf{P}_{\mathbf{i}}^{\mathbf{6\times6}} + \mathbf{P}_{\mathbf{p}}^{\mathbf{6\times6}} \text{ for infinite pipe} \tag{A.52}$$

Where

$$\mathbf{P}_{\mathbf{i}}^{7\times7} = \begin{bmatrix} \mathbf{P_i} & \mathbf{0} & \mathbf{0} & \mathbf{0}' \\ \mathbf{0} & \mathbf{P_i} & \mathbf{0} & \mathbf{0}' \\ \mathbf{0} & \mathbf{0} & \mathbf{P_i} & \mathbf{0}' \\ \mathbf{0}'^{T} & \mathbf{0}'^{T} & \mathbf{0}'^{T} & 0 \end{bmatrix} \tag{A.53}$$

$$\mathbf{P}_{\mathbf{p}}^{7\times7} = \begin{bmatrix} \mathbf{P_{p11}} & \mathbf{P_{p12}} & \mathbf{P_{p13}} & \mathbf{0}' \\ \mathbf{P_{p12}} & \mathbf{P_{p22}} & \mathbf{P_{p23}} & \mathbf{0}' \\ \mathbf{P_{p13}} & \mathbf{P_{p23}} & \mathbf{P_{p33}} & \mathbf{0}' \\ \mathbf{0}'^{\mathbf{T}} & \mathbf{0}'^{\mathbf{T}} & \mathbf{0}'^{\mathbf{T}} & 0 \end{bmatrix}, \mathbf{P_{jk}} = \begin{bmatrix} P_{p\,jk} & P_{p\,jk} \\ P_{p\,jk} & P_{p\,jk} \end{bmatrix}, P_{p\,jk} = \frac{Q_{jk}}{2\pi\varepsilon_0\varepsilon_{p1}} \tag{A.54}$$

$$\mathbf{P}_{\mathbf{c}}^{7\times7} = \begin{bmatrix} \mathbf{P_c} & \mathbf{P_c} & \mathbf{P_c} & \mathbf{P_c}' \\ \mathbf{P_c} & \mathbf{P_c} & \mathbf{P_c} & \mathbf{P_c}' \\ \mathbf{P_c} & \mathbf{P_c} & \mathbf{P_c} & \mathbf{P_c}' \\ \mathbf{P_c}'^{\mathbf{T}} & \mathbf{P_c}'^{\mathbf{T}} & \mathbf{P_c}'^{\mathbf{T}} & P_c \end{bmatrix}, \mathbf{P_c} = \begin{bmatrix} P_c & P_c \\ P_c & P_c \end{bmatrix}, \mathbf{P_c}' = \begin{bmatrix} P_c \\ P_c \end{bmatrix}, P_c = \frac{\log\left(2h/r_{p_3}\right)}{2\pi\varepsilon_0} \tag{A.55}$$

$P_{p\,jk}$ is the potential coefficient between inner conductors j and $j\ k$ with respect to the pipe inner surface. In (A.53) to (A.55) the last column and row of $\mathbf{P}_{\mathbf{i}}^{7\times7}$, $\mathbf{P}_{\mathbf{p}}^{7\times7}$ $\mathbf{P}_{\mathbf{c}}^{7\times7}$ correspond to the pipe conductor and should be dropped out when the pipe thickness is assumed to be infinite. In (A.53) $\mathbf{P_i}$ has the form of (A.26).

A.3 Earth-return impedance

Pollaczek developed the formulas for self and mutual earth-return impedances of underground conductors in (A.10) and (A.22). The self earth-return formula in (A.10), assuming $\mu_{ea} = \mu_0$ is as follows [92]

$$Z_{ea}(\omega) = j\omega\frac{\mu_0}{2\pi}\left[K_0(mr) - K_0(mR) + \int_{-\infty}^{+\infty} \frac{\exp\left\{-2h\sqrt{\alpha^2+m^2}\right\}}{|\alpha| + \sqrt{\alpha^2 - m^2}} \exp(j\alpha r)\, d\alpha \right] \quad \text{(A.56)}$$

where r is the outer radius of the cable outer insulation, h is the burial depth (positive value), $R = \sqrt{r^2 + (2h)^2}$ and $m = \sqrt{j\omega\mu_0/\rho_{ea}}$. In the above formula, Pollaczek assumed $\omega\mu_0/\rho_{ea} = \omega\mu_0\sigma_{ea} >> \omega^2\mu_0\varepsilon_{ea}$, i.e. that the earth behavior is largely closer to that of a conductor than to that of an insulator. It is clear that this assumption will hold only up to a certain frequency (generally above hundreds of MHz for typical values). If the assumption was not used, then $m' = \sqrt{j\omega\mu_0(\sigma_{ea} + j\omega\varepsilon_{ea})}$ should be used instead of m.

Pollaczek's formula for the mutual earth-return impedance between two underground conductors i and k is [92]

$$Z_{ea}(\omega) = j\omega\frac{\mu_0}{2\pi}\left[K_0(mr) - K_0(mR) + \int_{-\infty}^{+\infty} \frac{\exp\left\{-2h\sqrt{\alpha^2+m^2}\right\}}{|\alpha| + \sqrt{\alpha^2 - m^2}} \exp(j\alpha r)\, d\alpha \right] \quad \text{(A.57)}$$

where y is the horizontal distance between the two conductors, $d = \sqrt{(h_i - h_k)^2 + y^2}$ is the distance between two conductors and $D = \sqrt{(h_i + h_k)^2 + y^2}$ is the distance between one conductor and the image of the other.

The calculation of the integrals in (A.56) and (A.57) is not straightforward because of the highly oscillatory nature of integrands. This motivated the development of approximate formulas and series developments. One of the first approximate formulas developed was [93]

$$Z_{ea} = -\frac{j\omega\mu_0}{2\pi}\log\left(\frac{\gamma mr}{2} + \frac{1}{2} - \frac{4mh}{3}\right),\ \gamma = \lim_{n\to\infty}\sum_{k=1}^{n}\left[\frac{1}{k} - \log(n)\right] = 0.577215665 = e \quad \text{(A.58)}$$

This approximation gives less than 1% error up to 100 kHz but becomes less accurate for higher frequencies when the condition $|mr| < 1/4$ can no longer be fulfilled [61],[93].

Another approximate formula which was demonstrated to give only up to 3% error compared to Pollaczek's formula [94]

$$Z_{ea} = \frac{\omega\mu_0}{2\pi}\left[K_0(mr) + \frac{2}{4+(mr)^2} e^{-2hm} \right] \tag{A.59}$$

The formula for earth-return impedance used in EMTP is an approximation of (A.56) by Carson's earth-return impedance for overhead lines [95]. This approximation consists of replacing in (A.56) $\exp\left\{-(2h)\sqrt{\alpha^2+m^2}\right\}$ by $\exp\{-(2h)|\alpha|\}$ and accordingly in (A.57) replace $\exp\left\{-(h_i+h_k)\sqrt{\alpha^2+m^2}\right\}$ by $\exp\{-(h_i+h_k)|\alpha|\}$ [95]. The approximation is justified by the large penetration depth of earth at low frequencies and it is accurate up to 10 kHz [95].

Some authors also developed numerical methods to directly calculate the integrals in (A.56) and (A.57), for example [96],[97]. However these methods require a high number of computations and have not been implemented in EMTP-type software to this moment. However, they have been used to assess the accuracy of approximate formulas for the typical ranges of earth properties and system geometry and have confirmed the superiority of the approximate formula in [94].

A.4 Input data preparation for special cable features

Sections A.1and A.2 described the calculation of cable parameters applied in general by EMT software. The calculations have several limitations, e.g. conductors must be solid or cylindrical, and in direct contact with the respective insulation. However, it is quite common that real cable systems have stranded cores, and semiconducting layers. Also, in some countries it is common to bury the cable phases inside HDPE tubes which become a part of the cable outer insulation.

The modeling of special features which are not accounted for in cable parameter calculation routines require an adaptation of the data input to EMT software. The modifications required to model stranded cores, semiconducting layers and HDPE tubes are explained next.

A.4.1 Stranded cores

Cable parameter calculation routines assume solid or hollow cylindrical cores. In the case of stranded cores, the surface given by the outer radius is larger than the effective conducting surface because of space between the strands.

The modified resistivity ρ' to be input to the parameter calculation routine is calculated from the core nominal area $A_n = \pi r_{co-out}^2$ and the actual area of the copper strands A_c as follows [68]

$$\rho' = \rho \frac{\pi r_{co-out}^2}{A_c} \tag{A.60}$$

A.4.2 Semiconducting layers

Semiconducting layers can have substantial impact in the propagation of coaxial waves, particularly affecting the velocity, surge impedance and possibly also attenuation [68],[69]. The impedance of the semiconducting (SC) layers has minor impact on the cable series impedance, for which the conductor impedance is predominant, but it has an important effect on the shunt admittance [69],[98]. To account for SC layers, it is generally accurate enough to simply modify the permittivity of the insulation to account for the new thickness as follows [68],[69],[98]:

$$\varepsilon_r' = \varepsilon_r \frac{\log\left(r_{ins-out}/r_{ins-in}\right)}{\log\left[\left(r_{ins-out}-\Delta\right)/\left(r_{ins-in}+\Delta\right)\right]} \tag{A.61}$$

where r_{ins-in}, $r_{ins-out}$ are the inner and outer radii of insulation and semiconducting layers, Δ is the thickess of each semiconducting layer and ε_r is the relative permittivity of the insulation material.

A.4.3 High-density poly-ethylene tubes

Cable parameter calculation routines cannot account for a cable installed in high-density poly-ethylene (HDPE) tubes as in the system illustrated in Figure A.4 because the metallic sheaths are in fact wrapped in a three-layer insulation (composed of the cable outer insulation, an air gap and the HDPE tube) whereas parameter calculation routines can only model homogeneous cable insulation. Additionally, the air gap, and the HDPE tube are not concentric because the cable lies on the bottom of the tube. No analytical formula of impedance or admittance has been derived for such type of system. However, the air gap and HDPE tube can be accounted for by modifying the permittivity of the cable outer insulation as explained next [83].

Firstly, the eccentric system of insulation layers is transformed into a concentric one: the inner and outer radius $r'_{tube-in}$, $r'_{tube-out}$ for an equivalent HDPE tube concentric to the cable are calculated using the concept of geometrical mean distance (GMD) from the tube to the cable outer surface

$$r'_{tube-ins} = \exp\left\{\log\left(r_{tube-in}\right) + \frac{1}{2}\left(\frac{r_{sh-ins}}{r_{tube-in}}\right)^2 - \frac{1}{2}\right\} \tag{A.62}$$

$$r_{tube-out} = \exp\left\{\log\left(r_{tube-out}\right) + \frac{1}{2}\left(\frac{r_{sh-ins}}{r_{tube-out}}\right)^2 - \frac{1}{2}\right\} \tag{A.63}$$

where r_{sh-ins}, $r_{tube-in}$ and $r_{tube-out}$ are the sheath insulation outer radius and the HDPE tube real radius defined in Figure A.4. To obtain a concentric system composed of HDPE tube, air gap and cable outer insulation that is equivalent to the initial system it is still necessary to modify the permittivity of the HDPE tube to keep the same capacitance of the original HDPE tube, i.e.

$$\frac{2\pi\varepsilon_0\varepsilon_{tube}}{\log\left(r_{tube-out}/r_{tube-in}\right)} = \frac{2\pi\varepsilon_0\varepsilon'_{tube}}{\log\left(r'_{tube-out}/r'_{tube-in}\right)} \tag{A.64}$$

$$\varepsilon'_{tube} = \varepsilon_{tube}\frac{\log\left(r'_{tube-out}/r'_{tube-in}\right)}{\log\left(r_{tube-out}/r_{tube-in}\right)} \tag{A.65}$$

Secondly, the multi-layer insulation is transformed into a homogeneous one: The total capacitance C_{tot} of the multi-layer insulation is given by the series of the capacities for each layer

$$C_{tot} = \left(\frac{1}{C_{sh}} + \frac{1}{C_{air}} + \frac{1}{C_{tube}}\right)^{-1} \tag{A.66}$$

where C_{sh}, C_{air} and C_{tube} are the capacitances of sheath insulation, air gap and HDPE tube respectively. The permittivity ε'_{sh-ins} of the equivalent homogeneous insulation with radius r_{sh-ins} is then calculated from the total capacitance C_{tot} as

$$\varepsilon'_{sh-ins} = \frac{C_{tot}}{2\pi\varepsilon_0}\log\left(\frac{r_{sh-ins}}{r_{sh-out}}\right) \tag{A.67}$$

It is possible that a relative permittivity smaller than one results from (A.67) because of representing a multi-layer insulation by an equivalent homogeneous insulation having a smaller

thickness. This value is only artificial and has no effect on the accuracy of the cable model which depends only on the final values of the series impedance and shunt admittance matrices [83].

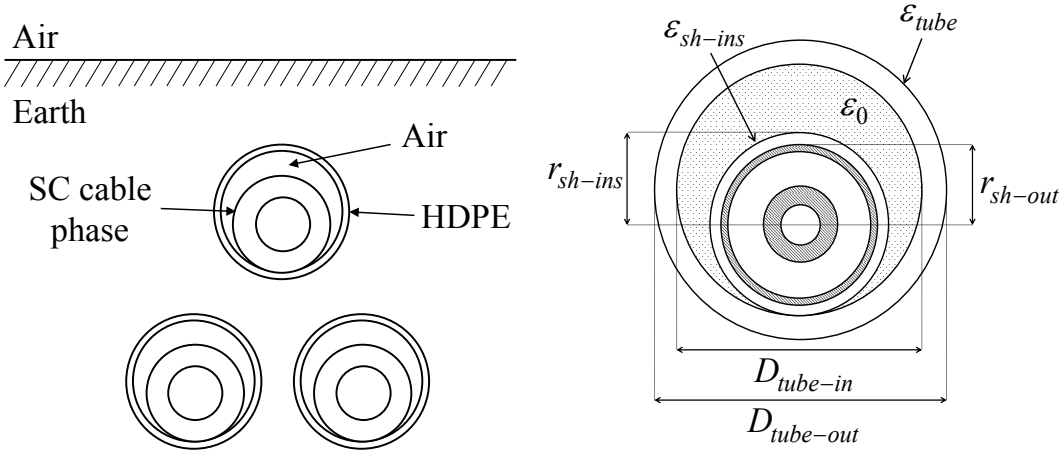

Figure A.4 Three-phase single-core cable buried inside high-density poly-ethylene tubes.

APPENDIX B – SCALING FACTOR BETWEEN THE RESISTANCE OF LUMPED- AND DISTRIBUTED- PARAMETER CIRCUITS

In chapter 4.1.2, it was demonstrated that there is a scaling factor between the inductance and capacitance of a lumped-parameter circuit and a distributed-parameter system having current responses with the same frequency of oscillations. In this appendix, it is demonstrated that the same scaling factor applies between the resistance of the two systems to ensure that both present the same attenuation in their current response.

Consider a single-phase distributed-parameter line of length l, propagation speed v, surge impedance Z_s and attenuation per-unit-length α'. The delay of propagation in this line is calculated as $\tau = l/v$. The line is connected to an ideal source at the sending end and it is open-circuited at the receiving end.

At t = 0:

- A voltage wave $V_{snd} = V$ is transmitted at the sending end, accompanied by a current impulse $I_{snd} = V/Z_s$.

At t = τ :

- The voltage wave arrives at the receiving end with as $Ve^{-\alpha' l}$ and is completely reflected back. The voltage at the receiving end becomes $V_{rcv} = 2Ve^{-\alpha' l}$. The arriving current wave $\frac{V}{Z_s}e^{-\alpha' l}$ is reflected back to the sending end as $-\frac{V}{Z_s}e^{-\alpha' l}$ resulting in $I_{rcv} = 0$

At t = 2τ :

- The backward travelling waves arrive further attenuated at the sending end. The current wave is totally reflected back due to the short-circuit. Thus, the current at the sending end becomes $I_{snd} = \frac{V}{Z_s} - 2\frac{V}{Z_s}e^{-2\alpha' l} \approx -\frac{V}{Z_s}e^{-2\alpha' l}$ (assuming that the wave attenuation after a two-way travel through the line is low).

Considering only the modulus of currents, the value at the sending end decreased from $\left|I_{snd}\right|_{t=0} = V/Z_s$ at t = 0 to $\left|I_{snd}\right|_{2\tau} \approx \frac{V}{Z_s} e^{-2\alpha' l}$ at t = 2τ .

If we model the current at the sending end through the response of a lumped-parameter circuit with attenuation constant α_l , then we can find a relation between the PUL α' and the lumped-parameter α_l as follows:

$$\alpha_l = \frac{\ln\left(\frac{V}{Z_s} \Big/ \frac{V}{Z_s} e^{-2\alpha' l}\right)}{2\tau} \rightarrow 2\tau\,\alpha_l = \ln\left(e^{2\alpha' l}\right) = 2\alpha' l \rightarrow \alpha' = \frac{\tau}{l}\alpha_l \tag{B.1}$$

Using the relations $\tau = l/v$, $\alpha_l = R/(2L)$ and $\alpha' = R'/(2Z_s)$ the above equation can be developed to:

$$\alpha' = \frac{\tau}{l}\alpha_l \rightarrow \frac{R'}{2Z_s} = \frac{1}{v}\frac{R}{2L} = \sqrt{L'C'}\,\frac{R}{2L} \tag{B.2}$$

Knowing that $L = \frac{2l}{\pi} L'$ (chapter 4.1.2), the above equation can be further developed:

$$\sqrt{L'C'}\,\frac{R}{2L} = \frac{\sqrt{L'C'}}{L'}\frac{\pi}{2l}\frac{R}{2} = \frac{\pi}{2l}\sqrt{\frac{C'}{L'}}\frac{R}{2} = \frac{\pi}{2l}\frac{R}{2Z_s} = \eta\frac{R}{2Z_s} \tag{B.3}$$

Finally,

$$\frac{R'}{2Z_s} = \eta\frac{R}{2Z_s} \rightarrow R' = \eta R \tag{B.4}$$

This shows that the relation between the resistances of lumped and distributed parameter circuits is the same as the relation between inductances and capacitances of the same circuits.

APPENDIX C – LIST OF PUBLICATIONS

The following is a list of journal and conference papers that derived from this PhD project.

Journal publications

[20] **I. Lafaia**, A. Ametani, J. Mahseredjian, A. Naud, M. T. Correia de Barros, I. Koçar, **"Field Test and Simulation of Transients on the RTE 225 kV Cable",** Special Issue on "Advances in the Simulation of Power System Transients", IEEE Transactions on Power Delivery (accepted for publication in Dec. 2015).

[52] **I. Lafaia**, F. Ghassemi, A. Ametani, J. Mahseredjian, S. Dennis, M. Haddad, S. Robson, **"Experimental and Theoretical Analysis of Cable Discharge"**, IEEE Transactions on Power Delivery (re-submitted after first review).

[51] **I. Lafaia**, A. Ametani, J. Mahseredjian, M. T. Correia de Barros, I. Koçar, Y. Fillion, **"Frequency and time domain responses of cross-bonded cables"**, IEEE Transactions on Power Delivery (submitted, awaiting first review).

[50] **I. Lafaia**, Y. Yamamoto, A. Ametani, J. Mahseredjian, M. T. Correia de Barros, I. Koçar, A. Naud, **"Propagation of intersheath modes on underground cables"**, Electric Power Systems Research, vol. 138, pp. 113-119, September 2016.

A. Ametani, **I. Lafaia**, Y. Miyamoto, T. Asada, Y. Baba, N. Nagaoka, **"High frequency wave propagation along overhead conductors by transmission line approach and numerical electromagnetic analysis"**, Electric Power Systems Research, vol. 136, pp. 12-20, July 2016.

Conference publications

I. Lafaia, Y. Yamamoto, A. Ametani, J. Mahseredjian, M. T. Correia de Barros, I. Koçar, A. Naud, **"Propagation of intersheath modes on underground cables"**, International Conference on Power Systems Transients (IPST'2015), June 2015, Cavtat, Croatia.

I. Lafaia, A. Ametani, J. Mahseredjian, A. Naud, M. T. Correia de Barros, **"Boutre-Trans Project: 225kV AC underground cable installed in the South-East of France"**, 9th International Conference on Insulated Power Cables (Jicable'2015), paper E4.6, June 2015, Versailles, France.

[83] **I. Lafaia**, N. Alatawneh, J. Mahseredjian, A. Ametani, M. T. Correia de Barros, I. Koçar, A. Naud, **"Modeling of an underground cable installed in a poly-ethylene tube for transient simulations"**, IEE Japan Power and Energy Society Meeting 2015 (IEEJ PES'2015), paper 5003, August 2015, Nagoya, Japan.

I. Lafaia, A. Ametani, J. Mahseredjian, A. Naud, **"Boutre-Trans project: 225kV AC underground cable installed in the South-East of France"**, 8th International Symposium on EMC and Transients in Infrastructures and International Student Session (ISET-ISS'2014), paper ISS-32, Danang, Vietnam.

I. Lafaia, N. Alatawneh, J. Mahseredjian, A. Ametani, A. Naud, **"Model for an underground cable installed in an HDPE tube"**, 8th International Symposium on EMC and Transients in Infrastructures and International Student Session (ISET-ISS'2014), paper ISS-33, Danang, Vietnam.

A. Ametani, **I. Lafaia**, J. Mahseredjian, A. Naud, **"Review of underground cable impedance and admittance formulas"**, 9th International Conference on Insulated Power Cables (Jicable'2015), paper E3.8, June 2015, Versailles, France.

Y. Yamamoto, **I. Lafaia**, A. Ametani, J. Mahseredjian, A. Naud, **"Inter-sheath modes on underground cables in particular reference to sheath grounding"**, IEE Japan Power and Energy Society Meeting 2015 (IEEJ PES'2015), paper 5001, August 2015, Nagoya, Japan.

A. Ametani, Y. Miyamoto, T. Asada, Y. Baba, N. Nagaoka, **I. Lafaia**, J. Mahseredjian, K. Tanabe, **"A study on high frequency wave propagation along overhead conductors by earth-return admittance/impedance and numerical electromagnetic analysis"**, International Conference on Power Systems Transients (IPST'2015), June 2015, Cavtat, Croatia.

T. Asada, Y. Baba, N. Nagaoka, A. Ametani, **I. Lafaia**, J. Mahseredjian, **"A study on basic characteristics of the proximity effect on conductors"**, IEE Japan Power and Energy Society Meeting (IEEJ PES'2015), August 2015, Nagoya, Japan.